Detailed studies of mid-ocean ridge volcanism at the Mid-Atlantic Ridge (45°N) and elsewhere

ISOBEL ALICE L YEO

Detailed studies of mid-ocean ridge volcanism at the Mid-Atlantic Ridge (45˚N) and elsewhere

Isobel A. Yeo

Department of Earth Sciences

Durham University

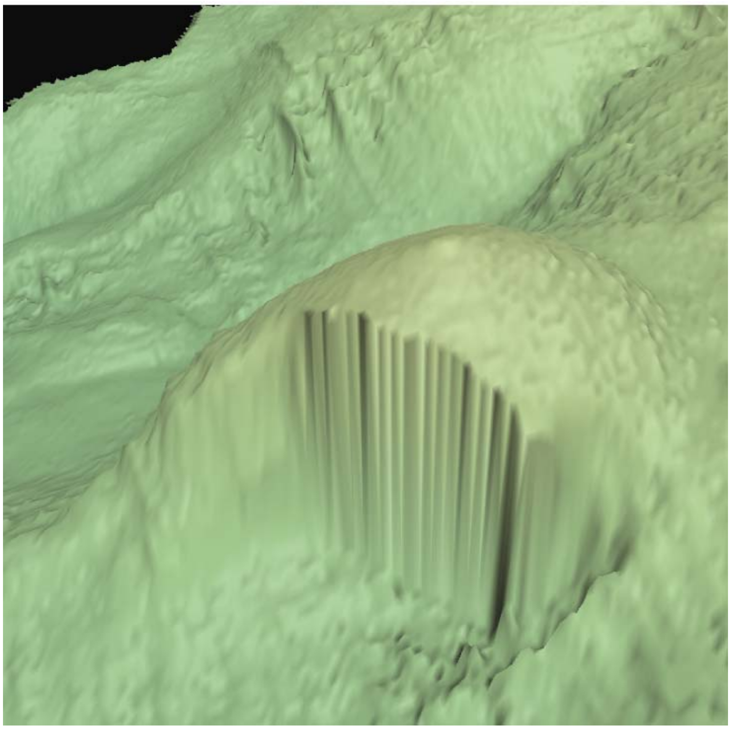

One volume

A thesis submitted in partial fulfilment of the degree of Doctor of Philosophy at the Department of Earth Sciences, Durham University

“If me no Google and you no Google…”

Matt Beer (2011)

Abstract

This thesis provides a comprehensive study of the Axial Volcanic Ridge (AVR) at 45˚30 N on the Mid-Atlantic Ridge. A number of datasets were collected over the area, including: EM120 ship based bathymetry, TOBI sidescan sonar, Isis high-resolution bathymetry, Isis video and sampling dives and crustal magnetisation surveys. In this thesis I seek to explore the questions of the volcanic building blocks of AVRs and their spatial and temporal evolution in a number of ways.

Very detailed volcanological mapping of the seafloor is used to provide semi-quantitative estimates of the relative proportions of different lava morphologies on and off the AVR and within the upper oceanic crust. I find that the AVR is characterised by predominantly pillow lavas while the flatter areas of seafloor around the AVR are covered by higher effusion rate lava morphologies. These observations are combined with the bathymetry and sidescan sonar datasets to elucidate the detailed nature of the building blocks of AVRs, which I find to be volcanic hummocks, composed predominantly of pillow lavas. These hummocks are morphologically the same as pillow mounds described at intermediate-spreading rate ridges. From these observations we identify common collapse scarps and associated talus deposits, which if buried may contribute significantly to increased porosity and lower seismic velocity in seismic layer 2A. Sediment cover is used as a proxy for seafloor age, and suggests that both the AVR and the flat seafloor around it are a similar age.

Statistical analysis of the distribution and size of volcanic hummocks on the AVR finds their numbers to have been vastly underestimated in previous studies. I also show that hummock density is very variable across the AVR, possibly corresponding to many discrete melt sources.

Evidence from 45˚N does not support either a uniform, long period life cycle model as has been proposed, or a steady state AVR. Instead I suggest that the AVR is the surface representation of robust magma supply, and irregular nature of this melt supply will control the surface appearance of the AVR

Declaration

This thesis is submitted for the degree of Doctor of Philosophy at Durham University. This thesis is my own work except where stated in the text and work division sections. No part of this thesis has been or is being submitted at this, or any other, university for a degree or any other qualification. This thesis does not exceed the word limit.

Isobel Yeo

Department of Earth Sciences

Durham University

May 2012

Acknowledgements

First and foremost I would like to thank my supervisor Roger Searle, for his guidance and support during my time at Durham, and for the superhuman patience he has displayed in all his dealings with my creative uses of English grammar. While I disagree that a sentence cannot be an entire page long[1], this thesis would almost certainly be unintelligible had it not benefitted repeatedly from his thorough editing. I must also thank my other supervisors: Jon Davidson (for fun in the lab and in the coffee room) and Ed Llewellin (for his statistical guidance and for not being too angry that time I spat Fanta all over him).

I extend my gratitude to David Clague, Jenny Paduan, Dave Caress and Julie Martin for being fabulous during my time at MBARI, for letting me use their data and go on their cruise, and for their continued work and support since then. I also thank Colin Devey for his belief in me and for giving me the opportunity to experience working in industry.

I would like to thank Kay Achenbach for her ideas and support (and for being completely hilarious), and Chris Mallows for his occasional help and continual sarcasm, without which Durham would not have been the same. I would also like to thank Nicole Schroth (for her input), Bramley Murton (for always being excellent to argue with) and Tim LeBas (for always managing to make things work). I would like to thank the rest of the JC24 science party: (in no particular order) Maurice Tivey, Peter Van Calteren, Kirsty Morris, Chris Waters, Pedro Ferreira, and the Officers and Crew of the RRS James Cook for their assistance in data collection.

I thank Geoff Nowell, Chris Ottley, Claire McLeod and Sarah Collins for their expertise, teaching and help in the lab (sorry about the beakers Geoff), and for being so supportive and positive when I briefly lost my faith in Strontium. I thank Karen Atkinson, Janice Oakes, Paula Elliott and all the administrative staff past and present for making sure I got paid, never booking me the wrong flight and being great company in the pub. I also thank Dave Stevenson, Gary Wilkinson and Matt Hepburn for answering my idiotic questions and not letting my computer explode.

[1]Roger has since informed me (with examples) that a sentence can indeed be a page long if it is written ‘properly’.

I would like to thank the Durham Volcanology group for their useful input, stimulating conversation and always knowing all the gossip (and the cake). I extend particular thanks to David Damby for help with volume calculations. In the same vein thank you to Simon Dixon for helping me make sense of even the most complex equations.

I would like to thank my family for their moral and occasionally financial support, as well as for the food parcels, lifts to IKEA and proof reading.

I would like to thank my friends, who have made my time here in Durham absolutely fantastic. Kathy, Claire, Sarah C, Harriet, Jenna, Yuan Yuan, Kirstie, Dean, Pete, Dave S, Leo, Amelie, Max, Dave D, Kay, Wanda, Sabina, Iona, Steve, Alex, James, Lisa, Ben F, Simon, Suzie, Boofy and really everyone in the department, thank you so much for everything. Special thanks to: Craig, Kay (again), Sabina (again) and Iona (again) for living with me - sorry about the kebabs and Lambrini Iona. I would also like to single out Sarah Porter for being the best fun, the best desk mate and the best friend I could have, and for running the best taxi service in Durham - I couldn't have done it without you Porty.

Finally I would like to thank Dave. Your humour, support and love are a source of constant inspiration, and your Dominos habit got me through the trickier bits.

This PhD was funded by the National Environmental Research Council (NERC). Further funding was obtained from The European Consortium for Ocean Research Drilling (ECORD), the Volcanic and Magmatic Studies Group (VMSG) and Durham University.

Contents

Appendices

List of figures

Chapter 1

Chapter 4

Chapter 5

Chapter 6

Chapter 7

List of tables

Introduction and Geological Setting 1

Chapter 1: Introduction and Geological Setting

1.1 Geological setting

1.1.1 Mid-ocean ridges

1.1.1.1 Introduction to mid-ocean ridges

Sea floor spreading, the mechanism by which plates move apart from each other to create new oceanic crust and mid-ocean ridges, was proposed by Hess in 1962 as a model to explain high heat flow and basaltic volcanism along the Mid-Atlantic Ridge.

Mid-ocean ridges are formed as a result of seafloor spreading, where tectonic plates are moving away from each other. This rifting causes adiabatic decompression in the mantle below the mid-ocean ridge producing decompression melting (Green and Ringwood, 1967; Kelemen et al., 1997a; McKenzie and Bickle, 1988; Turcotte and Ahern, 1978). This melt then percolates buoyantly upwards and is emplaced as intrusions or erupts as basaltic lava on the seafloor. Other evidence, such as symmetrical magnetic anomalies noted by Vine and Matthews (1963) and the elevation of the seafloor re-enforced these ideas and led to the concept of global plate tectonics (McKenzie and Parker, 1967). There are over 80,000 km of mid-ocean ridges currently active on the earth (Figure 1.1).

Spreading rate (the rate at which the tectonic plates are moving apart) exerts a strong control on the amount of decompression melting occurring beneath mid-ocean ridges, which in turn affects the seafloor morphology of the spreading segment. Ridges are classified as fast- (full spreading rate of 100 – 200 mm/yr), intermediate- (50 – 100 mm/yr), slow- (20 – 50 mm/yr) or ultraslow- (< 20 mm/yr) spreading ridges based on the rate at which the plates are separating. Each classification has a distinctive axial seafloor morphology with different proportions of extension being accommodated by faulting and volcanism (figure 1.2, figure 1.3). Mid-ocean ridges at all spreading rates are characterised by basaltic volcanism; however, the different volumes of melt supplied to fast and slow-spreading ridges mean that the typical eruption styles at different spreading rates differ.

1.1.1.2 Mid-ocean ridge offsets

Mid ocean ridges are broken up into segments by discontinuities that can offset the spreading centre by more than 30 km (Macdonald et al., 1991) (figure 1.4). These offsets may take the form of large transform faults (first order offsets) or more diffuse zones of faulting (second and third order offsets). Together first and second order discontinuities segment slow-spreading ridges every 50 km $\pm$ 30 km (Tucholke and Lin, 1994). Offsets are much less common at fast-spreading ridges (figure 1.5), which are characterised by much smaller, segment scale variations probably due to more uniform mantle upwelling beneath them (Bell and Buck, 1992; Gregg et al., 2007; Lin and Phipps Morgan, 1992; Macdonald et al., 1991).

Transform offsets are large, distinct transform faults (Wilson, 1965) that offset the ridge by 30 km or more (figure 1.4). They occur at 100-1000 km intervals (figure 1.5) along a spreading axis and break the spreading ridge up into segments. Transform faults are strike-slip and accommodate the movement of the two plates between different ridge segments (figure 1.4).

Non-Transform Offsets are second-order discontinuities (Grindlay et al., 1991) (figure 1.4), occurring far more frequently than first-order transform offsets at 10 – 100 km intervals, but with offsets < 30 km (figure

1.5). They are broad areas of offset between adjacent spreading segments, but have no significant transform faults, instead accommodating the horizontal shear stress over a broad area of strike slip, oblique slip and normal extensional faulting. In some places off axis evidence suggests that non-transform offsets can persist for millions of years (Macdonald et al., 1988), while in other areas they seem to be quite unstable over long periods of time (Gracia et al., 2000) and may migrate up and down the axis (Macdonald et al., 1988).

With some exceptions (e.g. small volcanoes, often with ‘rooster-comb’ distribution, have been observed at fast-slipping transforms (Gallo et al., 1986), and at the Garrett transform zone (Constantin, 1999)) very little volcanic activity is observed within a few tens of kilometres of both non-transform and transform offsets, and this decreased volcanism results in thinner crust towards both types of offset (figure 1.6).

1.1.1.3 Stresses at spreading centres

Earthquake focal mechanisms show that the horizontal stress field in the oceanic lithosphere at mid-ocean ridges consists predominantly of spreading parallel tensile stresses (Fujita and Sleep, 1978). These ridge perpendicular stresses are normally responsible for the strike of the ridge itself (although not always e.g. Reykjanes Ridge (Murton and Parson, 1993)), as well as the ridge parallel strike of the normal faults, which form the axial valley. Stress directions are similar at both fast- and slow-spreading ridges.

Stresses are usually only interrupted at or near segment offsets, where they may be rotated by up to 90°, usually with increased rotation closest to the offset (Fujita and Sleep, 1978; Neves et al., 2004). Here faults may be observed to bend towards the offset, or new faults with different strikes may form. The ridge itself may also curve (Neves et al., 2004), often corresponding to an observed bend in the volcanic expression of it at the surface.

1.1.2 Oceanic Crust

1.1.2.1 Structure of oceanic crust

From work on ophiolites (obducted sections of oceanic crust), rare seafloor exposures of the crustal section and seismic velocity experiments it was ascertained that oceanic crust is characterised by a recognizable crustal section 5 – 7 km thick (figure 1.7). Gabbroic to ultramafic plutonic complexes are found at the base, overlain by sheeted dyke complexes and erupted basalts at the top, all sitting on residual upper mantle peridotites, from which the melts that build the crustal section were sourced (Cann, 1974; Christensen and Salisbury, 1975; Dilek, 1998; Dilek et al., 1998; Karson, 2002; Kelemen et al., 1997b; Moores and Vine, 1971). It is suggested that these ophiolite lithological layers correspond to seismic layering observed in the oceanic crustal section, although this has only been demonstrated in few locations (Auzende et al., 1989; Bratt and Purdy, 1984; Dilek, 1998; Swift et al., 2008).

1.1.2.2 Seismic velocity in oceanic crust

Oceanic crust is composed of a number of different layers, which have characteristic P wave seismic velocities (figure 1.8). Layer 1 corresponds to the sedimentary layer, and thickens with distance off axis. It is characterised by P wave seismic velocities of 1.5 km s^{-1} at the top, which may increase with depth. Layer 2, which corresponds to the erupted and upper intrusive basaltic sections, is subdivided into two or three layers: layers 2a, 2b and sometimes 2c. Typical seismic P-wave velocities range from ~ 3.5 km s^{-1} (although may be as low as ~ 2 km s^{-1}) in seismic layer 2a, to 4.8 – 5.5 km s^{-1} in layer 2b, and 5.8 – 6.2 km s^{-1} in layer 2c. Layer 3, which is much more uniform in velocity than layer 2, is thought to correspond with the gabbroic section, and has seismic velocities of ~ 6.8 km s^{-1}. Finally layer 4, which corresponds to upper mantle peridotites at the base of the section, has a seismic p-wave velocity > 8 km s^{-1}.

It is not fully understood why the seismic velocity increases from layer 2a through layers 2b and 2c. Initially it was thought this marked the transition from the erupted basaltic lavas to the sheeted dyke complex (Christeson et al., 1992; Harding et al., 1993; Herron, 1982; Toomey et al., 1990); however drilling of the crustal section showed that the contacts between these subdivisions are very variable (Bratt and Purdy, 1984) . More recent studies suggests that in fact this boundary may relate to a depth at which cracks and pore spaces are sealed by hydrothermal mineralization and compaction, as porosity is directly correlated with reduced seismic velocity (Christeson et al., 2010). Others have correlated changing seismic velocities with changes in the metamorphic mineral assemblage (Karson, 2002).

1.1.2.3 Structure of oceanic crust as a function of spreading rate

The thickness of oceanic crust at most spreading rates (> 2 cm/yr) is fairly uniform at ~ 7 km $\pm$ 1 km (Bown and White, 1994). However, the differences in magma flux and segmentation at fast and slow spreading ridges affects eruption style, frequency and location, and the crustal structure is unlikely to be identical at different spreading rates. It is therefore important to test the seismic model of oceanic crust with in-situ observations. At fast-spreading and intermediate-spreading rate ridges, oceanic crustal drill cores and observations of major fault scarps have provided in situ constraints on the structure of oceanic crust (Auzende et al., 1989; Karson, 2002). These have allowed very detailed models of oceanic crustal structure to be produced (e.g. figure 1.9), which support these earlier models but provide more information on the exact locations of seismic velocity layer contacts and the detailed structure of the oceanic crustal section, as well as the structural variability of the crust (Karson, 2002).

Drilling of oceanic crust also makes it possible to constrain layer thicknesses and structures, and geochemical studies of drilled samples have shown that the accretionary processes in the lower crust differ at slow-spreading ridges to those at fast-spreading ridges, with less igneous layering and numerous small intrusive units (figure 1.10) (Atwater, 1979; Bryan and Thompson, 1979; Salisbury et al., 1979).

Structure of fast-spreading crust

Fast-spreading oceanic crust is typically fed by steady state magma chambers (e.g. (Detrick et al., 1987)), and therefore is structurally simpler than slow-spreading crust, as almost all extension is accommodated magmatically. As described in Karson (2002) fast-spread crust is characterised by an uppermost basaltic extrusive unit, composed of pillow lavas and sheet flows (see 1.1.4.3) (individual flows may be tens of cm to several meters thick). This upper layer overlies a layer of more compacted and deformed basaltic products. Both the upper and lower basaltic units are typically 0.5 - 1 km thick. This is underlain by a gradational contact with the sheeted dyke complex, typically more than 1 km thick. Seismic velocities typical of seismic layer 3 are reached at a depth of ~ 1500 m, within the sheeted dyke complex (correlated to a change in metamorphic mineral assemblage). The base of the sheeted dykes is underlain by a thin melt lens at the axis and gabbros off axis.

Porosity decreases deeper in the section, from substantial porosity (> 10 %) in the upper basaltic section to < 10 % in the lower basaltic section, to < 3% in the sheeted dyke complex (Karson, 2002).

Structure of intermediate- spreading crust

Intermediate-spreading oceanic crust has a similar upper oceanic crustal structure as fast-spreading crust, although the erupted basaltic unit has variable thickness, from 200 – 1000 m (Karson, 2002; McDonald et al., 1994). Additionally, the melt lens occurs deeper than at fast-spreading ridges due to the thermal structure (Karson, 2002), making the section different at depth.

Structure of slow-spreading crust

At slow-spreading ridges the magma flux is much lower, reducing eruption frequency and meaning that more extension is taken up by faulting. This will have a fundamental effect on the crustal structure, crustal thickness and duration and size of magma chambers. The Vema Transform fault at 11°N on the Mid-Atlantic Ridge is one of the few places that the exposed crustal section has been observed (Auzende et al., 1989) (figure 1.11). Here, mantle derived ultramafics (predominantly highly serpentinized peridotites) are found at the base of the section, overlain by 500 m of gabbros and 1100 m of axis-parallel sheeted dykes. The sheeted dyke section displays typical ‘dyke-in-dyke’ structures (where a new dyke intrudes through the centre of an older one) and is cut by a few sub-horizontal basaltic lava flows. The top of the section is composed of an 800 m thick upper unit of predominantly extrusive basaltic pillow lavas and breccias (Auzende et al., 1989).

Unfortunately, by their nature many of these sections are in a-typical areas (i.e. near transform zones). As a result there is little information available on the structure of oceanic crust on axis. The poor recovery of drill cores makes it difficult to identify the varying proportions of lavas in the upper crust and therefore the relative contributions to oceanic crust of different lava types remains poorly understood.

1.1.2.4 Crustal architecture and detachment faulting

Until recently oceanic core complexes were thought to be relatively discrete features, produced where only small amounts of extension could be accommodated by magmatism, and found predominantly near the ends of slow-spreading segments (Blackman et al., 1998; Tucholke and Lin, 1994; Tucholke et al., 1997). However some studies of the Mid-Atlantic Ridge between 12.5˚ and 35˚ N suggest detachment faulting may be much more common at slow-spreading mid-ocean ridges than previously thought (Blackman et al., 1998; Escartin et al., 2008). Evidence of 'asymmetrical accretion', whereby an active detachment fault forms one of the ridge flanks, is observed along ~ 50 % of the surveyed ridges and is associated with deeper microseismicity, curved volcanic ridges, geochemical variations and possibly increased hydrothermal activity.

1.1.3 Axial morphology

The surface expression of volcanic activity is extremely variable at different spreading rates, as a result of the differing eruption styles associated with different ridges (Heezen, 1960; Macdonald, 1982; Menard, 1960).

1.1.3.1 Fast-spreading ridge axial morphology

Fast-spreading ridges are characterised by a broad high at the axis with a narrow axial fissure through which eruptions are concentrated (Perfit and Chadwick, 1998; Small, 1998) (figure 1.2, figure 1.3). Most spreading can be accommodated through dyke intrusion and so faulting is minor but some small inward and outward facing normal faulting can be observed (Cowie et al., 1993; Escartin et al., 2007; Perfit and Chadwick, 1998; Small, 1998).

1.1.3.2 Slow-spreading ridge axial morphology

The low magma supply to slow-spreading ridges means that dyke intrusion is often not sufficient to accommodate all extension and more is accommodated by faulting than at fast-spreading ridges. As a result slow-spreading ridges are characterised by a number of large inward facing normal faults (figure 1.2, figure 1.3) with throws regularly upwards of several hundred metres. These faults form axial valleys, which may be tens of kilometres wide and more than a kilometre deep, bounded on either side by large normal faults or detatchment faults, which form the axial valley walls. Axial valleys and are typically hourglass shaped, narrower at the centre and wider at the ends (Escartín et al., 1999; Searle et al., 1998; Searle and Laughton, 1977). At slow-spreading ridges faulting is thought to accommodate an average of ~10 % of the strain under normal conditions, although this may vary by ~ 5 % (Escartín et al., 1999).

The axial valley floor also often displays a large degree of fissuring (Ballard and Van Andel, 1977; Lawson et al., 1996) and commonly an Axial Volcanic Ridge (AVR) (figure 1.12). AVRs are topographic highs tens of kilometres long by several kilometres wide which sit on the ridge axis (Ballard and Van Andel, 1977; Brown and Karson, 1988; Crane and Ballard, 1981).

1.1.3.3 Axial cross-section

Two mechanisms have been proposed to explain the existence of a deep, wide axial valley at slow-spreading mid-ocean ridges; hydraulic head loss and steady-state necking. The hydraulic head model states that axial rift valleys are too large to be normal isostatic grabens, but are instead the product of viscosity caused head loss beneath the axial valley which dominates at slow-spreading ridges because melt has to rise through a narrow conduit (Lin and Parmentier, 1990; Sleep, 1969; Sleep and Rosendahl, 1979). The recovery of head away from this central zone will lift blocks up to isostatic equilibrium, producing the axial valley wall faults

(Sleep, 1969). Alternatively, the necking model proposes a scenario in which the lithosphere is continually thinned at the ridge axis by tectonics but also thickened by cooling at the base and volcanism on the surface (Tapponnier and Francheteau, 1978). This series of 'neckings' occurs in the central section of the valley due to extension and the upwelling of hot material beneath it, but the valley as a whole is domed across the ridge, meaning the isostatic response away from the centre causes the uplift of the fault blocks which bound the axial valley (Lin and Parmentier, 1990; Tapponnier and Francheteau, 1978).

Both these models were combined into a single model by Chen and Morgan (1990) which accounts for deep, wide axial valleys at slow-spreading rates, a smaller relief axial valley at intermediate spreading rates and no axial valley at fast spreading rates. In this model, necking of the crust occurs in the ductile layer beneath the ridge at slow-spreading and intermediate-spreading rates, but at fast spreading rates the young, hot material beneath the ridge is not strong enough for necking to have much of an affect (Chen and Morgan, 1990). In these models the size of the axial rift valley decreases with thicker crust or increased mantle temperature, while thinner crusts and cooler mantle temperatures produce pronounced axial valleys. However Escartin et al. (1997) demonstrate that the wet dolerite rheology used in this model is actually unrealistically weak, and therefore the oceanic crust is unlikely to behave in this way.

Most recently Buck et al. (2005) suggested a model (now widely accepted) which does not depend on viscous flow beneath the ridge. They state that away from the area of active dyke emplacement the lithosphere is too strong to respond in an isostatic manner. Therefore, the accumulation of magma and lava on the plate at the axis will load the plate causing it to bend. As it moves away from the axis it unbends, developing faults. These faults will remain active until the plate has totally flattened out. Different magma supply regimes at the axis will dictate the throw and spacing of faults. At slow-spreading ridges the effect of stretching is greater, producing normal faulting as a result of cooling and contraction .

1.1.4 Axial volcanic ridges

1.1.4.1 Introduction to AVRs

Axial Volcanic Ridges or AVRs are found on ca. 90% of slow-spreading ridge segments (Smith and Cann, 1992). Where present, they represent the main observable large volume expression of magmatism on slow-spreading ridges (figure 1.12). As such, they are thought to be the main site of construction for the extrusive crustal section (seismic layer 2a) (Smith and Cann, 1992) . They are formed of successive small volume basaltic eruptions (Ballard and Van Andel, 1977; Ramberg and Van Andel, 1977; Sempere et al., 1993; Smith and Cann, 1993; Smith et al., 1995b), which build on top of each other to produce a topographic high.

Axial volcanic ridges are elongate, typically ridge parallel structures. They vary in size, although are typically a few km wide and tens of km long. They are often surrounded by areas of flatter seafloor, but may extend all the way to the axial valley fault scarp in other locations.

Their position, typically within the centre of an axial valley, is explained by models of mantle upwelling. They suggest that magma supply should be most robust at the centre of the segment where the extraction of melt is greatest (Cannat et al., 1997; Kelemen et al., 1995). Melt is extracted via dunite channels through depleted mantle rocks, which coalesce as they shallow towards the centre of the ridge axis (Kelemen et al., 1995). As a result, we would expect the central section of a segment, and furthermore the central section of an AVR, to be the most volcanically robust, as this is where most of the melt is being delivered. This is not always the case however as different sections of an AVR can be observed to have undergone different amounts of tectonic degradation (Mendel et al., 2003; Parson et al., 1993; Smith and Cann, 1992), suggesting episodic volcanism or that volcanism or faulting may move up and down the AVR through time.

Where detachment faults (normal faults active for > 1 m.y.) are active on slow-spreading ridges, the conjugate ridge flank typically displays volcanic morphology and typical abyssal hills, suggesting that detachment faulting is associated with some magmatic activity (Canales et al., 2004). Modelling of this situation undertaken by Tucholke et al. (2008) has shown that typical megamullion style detachment faulting is most likely to occur when 30 – 50 % of total plate separation is taken up by magmatic intrusion. Slip on a detachment will be terminated when either > 50 % of separation is taken up by magmatism, or if magmatism drops to account for < 30 %, in which case a new fault will initiate. Where < 20 % of the separation is accounted for by magmatism the seafloor may consist almost entirely of faults.

1.1.4.2 Lava morphology at mid-ocean ridges

Submarine volcanic eruptions differ from subaerial basaltic eruptions because lava is erupted into cold seawater at high hydrostatic pressures. Probably the most important effect of water interaction is the extremely quick rate at which the crusts of submarine lava flows cool. Water is a much better heat conductor than air and the rapid quenching of this outer surface results in the range of unique lava morphologies seen at the mid-ocean ridges.

Pillow lavas

Pillow lavas (figure 1.13, figure 1.14) are interconnected systems of a number of individual, typically bulbous, lobes of lava and were described comprehensively by Moore (1975) and Ballard and Moore (1977). They form as a result of rapid cooling of the outer crust to 700 – 800°C as lavas are extruded into water (figure 1.15). The pillows continue to expand as lava flows into them, causing the newly formed crust to crack and lava to be extruded through them to produce either pillow buds or a new pillow lava. These newly formed buds and pillows may form in any direction due to the pressure of the lava within the feeder pillow, although they may sag as they grow. Pillow growth may also be interrupted by implosions due to the contraction of gases cooling within the pillows and they may stop growing as lava drains downslope. Due to the rapid quenching of the outer surface of pillow lavas their surface tend to be glassy, becoming a mix of glass and small crystals and finally totally crystalline towards the centre. Outer surfaces may also show two types of ridges known as *corrugations*, which are produced as lava oozes through an irregularly shaped crack, and *fault slivers* (figure 1.15), which are produced parallel to the feeder crack at slow extrusion rates. Pillow lavas can also form when the initial frontal flow lobe of a more fluid submarine lava flow encounters an obstruction on the seafloor. The lobe cannot continue to travel horizontally but the flow of lava into the lobe is constant so it inflates and the crust cools until it ruptures feeding a new pillow. The crust on this pillow begins to cool as soon as it comes into contact with seawater, effectively damming the flow until it too ruptures, feeding the next pillow.

Rounded pillows are typically called *bulbous pillows* (figure 1.14; A), however pillow lavas have a variety of different forms caused by different slope angles, viscosities, effusion rates and other variables as described by Ballard and Moore (1977). These include:

Flattened Pillows (figure 1.14; E), like bulbous pillows, tend to be roughly equidimensional when viewed from above but are vertically flattened and do not stand above the terrain. They are probably produced in the same way as bulbous pillows but drained of lava while they are still plastic causing the thin, weak, unsupported crust to sag . They are typically associated with eruptive vents with high effusion rates.

Elongate Pillows (figure 1.14; B) are subcylindrical and generally have a length between ten and twenty times their diameter. They plunge downslope at angles from 10 degrees to almost vertical. They often branch and may change direction and tangle with other elongate pillows in the flow direction as long as they maintain a downslope component. They are characterised by "neck-and-knob" growth patterns formed from successive downslope pillow growth (Ballard and Moore, 1977). It is likely that elongate pillows form in the same way as subaerial pahoehoe, by progressive budding, producing irregular, sinuous tubes (Kennish and Lutz, 1998).

Both the pillow types listed above may also exist as *Hollow Pillows* (figure 1.14; D). Hollow Pillows have been drained of lava during their formation leaving only a solidified crust of between 1 and 15 cm thick (typically ~ 5 cm). Some hollow pillows may contain lava shelves (figure 1.14; D, figure 1.16) marking the height of the top surface of the lava flow running into the pillow when it was only partly full. Hollow pillows commonly collapse, exposing the interiors. Many collapse long after the eruption has ended and are characterised by fairly thick crusts. Those which break open when the crust is very thin tend to be fed by lavas with high, erratic delivery rates (Ballard and Moore, 1977).

In addition, both bulbous and elongate pillows may be *decorated* by numerous small buds (figure 1.14 C). These pillows, known as decorated or *knobby pillows*, are covered in small protrusions, between 2 and 10 cm in length, with a length to diameter ratio of around 1:3 (Ballard and Moore, 1977). Because of their size, buds cool very quickly and have thick glassy crusts. Decorated pillows are believed to be associated with intermediate flow rates, faster than those which produce regular pillows and slower than those that produce sheet flows.

Trapdoor Pillows (figure 15B) are a type of pillow bud formed where a circular crack forms in a pillow. They are usually short and stubby with striated sides parallel to the direction of extension. Where these pillows are more elongated and bent they are called Toothpaste Pillows (Ballard and Moore, 1977).

Lobate lava flows

Lobate Flows (figure 1.13) are characterised by a gentle, hummocky surface. Intact lobes superficially appear like flattened pillows, however they are purely surface features and do not define individual pillows. Crust thickness is dependant on the size of the lobes and varies between 5 and 15cm (Kennish and Lutz, 1998).

Sheet lava flows

Sheet flows (figure 1.13) are flat lying lava flows with slopes < 10° (Gregg and Fink, 1995), resulting from lavas being extruded at high rates. They may display a variety of surface textures and morphologies (Ballard and Moore, 1977), dependant on the characteristics of the lavas that produce them . Sheet flows range in thickness from a few centimetres to metres thick (Auzende et al., 1989), with glassy crusts from a few millimetres to ~ 10 cm (Perfit et al., 2003).

Folded Sheets show various degrees of surface deformation ranging from loosely deformed *curtain-folded sheets* to *rippled sheets* and, at shear zones active while lava flows are mobile, *whorly sheets*, where the surface lava coils into spirals 1-5m in diameter (Kennish and Lutz, 1998).

Hackly and *Jumbled Flows* (figure 1.13) are sheet flows which display no ordered structure and consist of metre sized blocks of irregular broken lava and glass. They have thin, very tightly folded glassy crusts. The surface is characterised by randomly orientated blades of glass and lava protruding through the folded crust and these flows produce an irregular surface, very similar in appearance to the aa flows produced subaerially (Kennish and Lutz, 1998; Lawson, 1996).

Fast-spreading ridges are typically characterised by both sheet flow and pillowed eruptions (Gregg et al., 1996; Perfit and Chadwick, 1998), however pillow lavas are much less common (Tominaga and Umino, 2010). Slow-spreading ridges are characterised predominantly by pillowed eruptions (Perfit and Chadwick, 1998), with rare larger volume sheet flow eruptions (Smith and Cann, 1990).

1.1.4.3 Effusion rate

'Effusion rate' is often used to describe eruption characteristics, and as a reason for the formation of different lava lithologies, however it's exact definition is important as it can be used in a number of ways. A full discussion of this is presented in Harris et al. (2007), however as it is a term used a number of times in this thesis a brief outline is included below.

Effusion rate influences the growth, shape, thickness, morphology and pressure conditions of a lava body. Originally defined by Walker et al. (1973) as the "instantaneous lava flow output by a vent", it differs from the 'eruption rate', which is equivalent to the average lava output for the entire eruption (although in many simulations effusion rate and eruption rate are the same). These terms are often used interchangeably or variably, with effusion rates being given for single vents versus entire systems, and being averaged across different timescales. Harris et al. (2007) conclude that: 1) eruption rate is defined as the total erupted volume, divided by the length of time since the eruption began (once an eruption has ended this is also the 'mean output rate'), and 2) that the definition of effusion rate is dependant on the timescale and spatial scale of the measurement, and that this information should be provided.

1.1.4.4 Large scale features of AVRs

A number of different volcanic edifices and volcanic styles are observed on AVRs and within the axial valley which are summarised in figure 1.17. The volcanic units that build up AVRs at slow spreading ridges have been described by a number of studies and have been given a number of different names shown in figure 1.17 (Allerton et al., 2000; Cannat et al., 2006; Head et al., 1996; Hess, 1962; Lawson et al., 1996; Magde and Smith, 1995; Mendel et al., 2003; Parson et al., 1993; Smith and Cann, 1992, 1993, 1999; Smith et al., 1995a). In this thesis I will use the terminology most common for the Mid-Atlantic Ridge (figure 1.17), to describe the common large scale features, summarised below.

Volcanic Hummocks

Hummocks (figure 1.17) are small volcanic edifices found all over the median valley floor (Batiza et al., 1989a; Smith and Cann, 1990; Smith and Cann, 1992; Smith et al., 1995b). They may be cone or dome shaped, are typically < 300m in height (Smith and Cann, 1990), with 50 – 200 m diameters (Briais et al., 2000). Hummocks often have steep flanks, commonly with slopes > 25° (Smith and Cann, 1990). They are the most common volcanic edifice observed on slow-spreading mid-ocean ridge segments and account for most of the volcanism observed on AVRs, contrasting with fast-spreading ridges where similar small seamounts are predominantly observed away from the ridge axis (Smith and Cann, 1990; Smith and Cann, 1992).

Due to their size, studies of volcanic hummocks have tended to focus mainly on larger hummocks, which can be seen in ship based bathymetric surveys. In one such study Smith and Cann (1990) measure average hummock densities of 80 per 1,000 km^2 for 'seamounts' over 50 m in height (although due to the low resolution of that study, the 'seamounts' they measured may include both large hummocks and hummocky seamounts) on the Mid-Atlantic Ridge between 24 and 30˚N. They also note that the AVR appears to be constructed entirely of coalesced hummocks and therefore this density probably represents a minimum. Magde et al. (1995) conducted a similar study on the Reykjanes Ridge and calculated a 'seamount density' (again, edifices > 50 m) of 310 $\pm$ 20 per 10^3 km^2, although they recognise the possibility of there being many more seamounts below 50 m in height and therefore state that their estimate is a minimum.

No detailed studies of specifically hummocky terrain have been carried out at slow-spreading mid-ocean ridges, and therefore their modes of formation are poorly understood. Hummocks are small, circular edifices and therefore are probably formed from point source pillow lava volcanism, fed from small to intermediate sized magma chambers (Smith and Cann, 1990). It is not known whether one or several hummocks is produced in a single eruption, although most models (e.g. Head et al. (1996)) predict that a number of hummocks will be produced along a fissure eruption, where the dyke connects to the seafloor.

Hummocky seamounts and ridges

Volcanic hummocks can coalesce together to form distinct edifices called hummocky seamounts or hummocky ridges (Briais et al., 2000; Head et al., 1996; Lawson, 1996; Smith and Cann, 1993; Smith et al., 1995a) (figure 1.17).

Hummocky ridges may either be formed by a linear arrangement of connected hummocks or an elongate composite pile of hummocks. Composed predominantly of pillow lavas, these linear features may be > 30 m high and several kilometres long (Head et al., 1996; Lawson, 1996; Smith and Cann, 1993; Smith et al., 1995a). Often aligned parallel to the ridge axis, their orientations are probably strongly constrained by the stress regime (Lawson, 1996; Smith and Cann, 1993) and are probably formed either by fissure eruptions, much like the 'curtain of fire' eruptions seen on fissures in Iceland (Smith and Cann, 1993; Smith et al., 1995a), or volcanism focused on a single, syn-magmatic fault (Briais et al., 2000; Lawson, 1996; Smith and Cann, 1993), both of which would produce their elongate form. Hummocky seamounts are very similar to hummocky ridges but with no sense of alignment of the hummocks (Lawson, 1996; Magde and Smith, 1995). Large numbers of individual hummocks and/or hummocky ridges and seamounts may be described as *hummocky terrain*.

Both hummocky seamounts and ridges are very similar to the pillow mound eruptions described on intermediate spreading rate ridges, which are composed almost entirely of pillow lavas (Chadwick and Embley, 1994; Chadwick et al., 1998; Embley et al., 1991), although no studies have so far imaged them in sufficient resolution to see if they are identical.

Flat-seafloor

There is a clear difference between hummocky morphology (as described above) and distinctive smooth terrains which are composed of low relief extrusives (figure 1.17). These areas of flat-seafloor are identified as uniformly backscattering areas in sidescan sonar data. They tend to be several kilometres in length and width and irregularly shaped (Parson et al., 1993). They may be bounded or dammed by other features such as hummocky ridges, volcanoes or faults (Briais et al., 2000; Lawson, 1996). Flat-seafloor is regularly interpreted as a sheet-like extrusive surface (Parson et al., 1993), however sidescan resolution isn't good enough to distinguish between low relief pillow flows and sheet flows or distinguish between different sheet flow morphologies (Cann and Smith, 2005), and therefore it is currently unknown whether these flat areas actually are 100% sheet flows.

Where smooth volcanic terrains are composed of sheet flows, they may be associated with *Lava Tubes* – pipes through which melt has travelled, and *Tumuli* – small blister like structures created by gas beneath a smooth lava flows solidified surface causing swelling and cracking of the upper surface (Ballard and Van Andel, 1977; Lawson, 1996).

Smooth terrains over large areas are most commonly associated with fast-spreading ridges, such as the East Pacific Rise (e.g. Sinton et al. (2002)), however smaller areas are common at slow-spreading ridges (Smith et al., 1995a). The textural differences between hummocky terrain (seafloor covered by lots of hummocks) and the flat-seafloor is probably related to lower eruption effusion rates in the hummocky areas producing pillow lava flows (Ballard et al., 1979; Griffiths and Fink, 1992a, b; Perfit and Chadwick, 1998), which are capable of building taller, narrower edifices. Underlying slope may also be important (Tominaga and Umino, 2010), with observations from the East Pacific Rise suggesting that pillow lavas are more likely to be formed that sheet flows on slopes of > 5˚. Viscosity and crystal content may also affect lava morphology, but are less likely (Briais et al., 2000; Gregg and Fink, 1995; Griffiths and Fink, 1992b; Perfit and Chadwick, 1998).

Flat-topped seamounts

Flat-topped seamounts (figure 1.17) are observed at all spreading rates. They make up ≤ 5 % of AVRs, but are more common outside them on the axial valley floor, on top of the axial valley wall faults and at the ends of segments (Lawson et al., 1996; Smith et al., 1995a). They have a distinctive table-top shape with steep sides and a very slightly domed summit (Smith et al., 1995a). They are usually almost perfectly circular in shape and often have central pit craters which may be up to 200m in diameter, both of which indicate they may be fed by a central conduit (Smith et al., 1995a). They are usually 1 – 2 km wide and 50 – 300 m high and have typical height to diameter rations of around 1:10 (Smith et al., 1995a). Dredging and submersible studies suggest they are composed mainly of pillow lavas, with sheet flows on their summits (Lawson, 1996). Seamount frequency tends to decrease almost exponentially with increasing height and are similar in shape, although on average slightly smaller on slow-spreading ridges, than those found on the fast spreading East Pacific Rise (Smith and Cann, 1992). In places they seem to be surrounded by areas of flat-seafloor, which may be composed of low relief pillow fields or sheet flow (Searle et al., 2010; Smith and Cann, 1993).

A number of different formation mechanisms have been proposed for flat-topped seamounts. It is possible that they begin as hummocks but that the eruptions which feed them have larger volumes than typical hummock forming eruptions, causing the cone to grow upwards until it reaches a critical height, controlled by the magmastatic head and volatile content, and then outwards (Head et al., 1996; Lawson, 1996; Magde and Smith, 1995; Smith et al., 1995a). As flat-topped seamounts have larger volumes than the smaller hummocks, it follows that it is eruption volume that predominantly controls whether or not a hummock will reach its critical height. In this model the degree of flatness of the top should increase and the flanks should become steeper the larger the seamount grows (Rabain et al., 2001), although this was not observed either on the Mid-Atlantic Ridge (Rabain et al., 2001) or on similar features around Hawaii (Clague et al., 2000).

Alternatively, the observed combination of simple vent structure and relatively small volumes may point to a monogenetic origin (Clague et al., 2000), in which cycles of levee formation and overflowing would build the characteristic flat topped seamount shape. However, this method of formation requires the existence of what is essentially a lava lake on the seafloor, and there is little evidence for lava lakes at slow-spreading mid-ocean ridges, except for at those effected by nearby hotspots (e.g. Lucky Strike (Scheirer et al., 2000)).

Flat-tops could also be produced by a stack of radially spreading flows which pile on top of one another to form a roughly circular volcanic edifice as a result of flow focusing along a fissure (Head et al., 1996; Magde and Smith, 1995). In this case the degree of flatness of the summit depends only on how the flow lengths change during the period in which the edifice is being constructed, with repeated flows of similar run out required to produce the characteristic seamount shape. In this situation, a greater degree of summit flatness would require a very quick decrease in flow lengths at the end of the eruption (Rabain et al., 2001).

Other authors suggest that some seamounts are simply flat-topped megatumuli (Bryan et al., 1994) – swellings on flat-lying lava flows caused by lava pressure forcing a solidified lava upper surface upwards and extruding pillow lavas through cracks in the sides and summit (Guest et al., 1984).

1.1.4.5 Lava properties and morphology

The different lava forms mentioned above are due to the different properties of the lavas being erupted. Studies have shown no correlation between the lava morphology and its chemistry (Batiza et al., 1989b) and therefore other properties such as effusion rate, viscosity and slope must be responsible (Gregg and Fink, 1995).

A variety of analogue experiments have been carried out to try and examine which properties are responsible for morphological variations. Laboratory wax analogue experiments have shown that different wax morphologies (similar to different lava morphologies) are produced as a result of a balance between the rate at which wax is flowing and the rate at which a hardened crust can form on the outside (Gregg and Fink, 1995;

Griffiths and Fink, 1992b). These experiments demonstrated that with increasing effusion rate they were able to produce recognizable seafloor lava morphologies, progressing from pillow lavas, to lobate lavas to sheet flows with increasing effusion rate and to a lesser extent, decreasing viscosity (figure 1.18).

The most comprehensive study of the effect of slope on lava morphology was conducted in a laboratory using molten wax as an analogue for erupting lavas (Gregg and Fink 2000). They were able to create recognisable submarine lava flow morphologies and found that at any given slope pillow lavas were formed by the lowest effusion rates and sheeted flows by the highest. However, at constant effusion rates they recognised that varying slope could control changes in lava morphology. With slopes between 10° and 30° they noted that increasing the slope had an effect similar to increasing the effusion rate, increasing the length of the run out and producing slightly higher effusion rate morphology. At slopes of 40° or more the solidified crust of the lava exerted a stronger control on morphology than effusion rate, and the flow divided into lobes rather than forming a smooth sheeted flow. They also noted that in pillowed flows the length to width ratio of pillows increases with increasing slope and the width of the flow decreases with increasing slope.

Viscosity is directly tied to the temperature, composition and crystal percentage of the erupted lava, and will increase as the lava cools with distance from the vent (Bonatti and Harrison, 1988). As such, viscosity is related to effusion rate, as more viscous lavas are less able to effuse quickly (Fink and Griffiths, 1992; Gregg and Fink, 1995; Griffiths and Fink, 1992b). A rough correlation has been found between lower eruptive temperatures producing pillows and higher temperatures tending to produce sheets, (Bonatti and Harrison, 1988). It has also been suggested that more viscous lavas are likely to erupt on slow-spreading ridges as they have no steady state magma chamber and therefore no stratified melt and mush zones (Sinton and Detrick, 1992) (although this may not always be the case as the RAMASSES study (Peirce and Navin, 2002) showed some evidence of stratification of a melt lens on the Reykjanes Ridge). This makes the eruption of crystal rich magmas from a slowly cooling mush more likely than at fast-spreading ridges, where they are more likely to tap the predominantly molten lens formed at the top of a long lasting magma chamber.

Some caution must be taken when using lab-based experimental data as a direct equivalent for real systems. For example in the experiments above it is assumed that the ratio for time taken to form a crust on the wax against the time taken for it to spread outwards is the same for basaltic lavas, which may not be the case. Additionally their experiments were conducted predominantly on slopes of < 10° (Gregg and Fink, 1995), which is flatter than a lot of the slopes observed on slow-spreading mid-ocean ridges (discussed in chapters 3 and 4). However gravitational forces are not predicted to exert control on morphology until slopes exceed 25° (Gregg and Smith, 2003) so the results should be broadly applicable to submarine lava flows (Gregg and Fink, 1995; Griffiths and Fink, 1992b). This is supported by comparison of these results to real life scenarios (e.g. Malin (1980) and Walker et al. (1973)) produce a good correlation between predicted and observed results.

1.1.4.6 Controls on edifice height

The maximum height to which a submarine volcanic edifice can grow depends on the hydraulic head of the fluid magma or the *magmastatic head* (Smith and Cann, 1992) (figure 1.19). For an eruption to begin the magmastatic pressure must exceed the confining pressure of the overlying rock and water; this usually occurs when the rock above the chamber fractures. Conversely, to stop erupting, the magmastatic pressure in the column of lava must become less than the lithostatic and hydrostatic pressure being exerted on the chamber so the forces balance. The magmastatic pressure within a magma body is a function of the depth of the magma chamber below the seafloor as the weight of the overlying rocks provides an overburden pressure. It therefore follows that deeper magma chambers will be subject to greater overburdens and therefore larger magmastatic pressures (as a result of buoyancy) are required to exceed the overburden. Therefore eruptions fed by deeper magma chambers should be capable of building taller edifices. This is described by the Smith and Cann (1992) equation:

$$h_s = [(\rho r(z) - \rho m)/(\rho m - \rho w)]z$$

Where h_s is the height of the seamount, $\rho r(z)$ is the mean density of the rock overlying the magma chamber, ρm is the density of the magma, ρw is the density of seawater and *z* is the depth.

However not all volcanic edifices will necessarily reach their maximum possible height as other factors, such as eruption volumes and geometries, can also affect the height to which an edifice builds below this maximum (Mitchell, 2001).

The level of neutral buoyancy for magma is within the brittle lid, and therefore it is unlikely that this controls the depth of the magma chamber, as the magma cannot penetrate the brittle lid (Smith and Cann, 1992). It is more likely that magma ponds at the deeper brittle/ductile transition, which can be a variable depth. Therefore AVRs with taller seamounts are probably a sign of a deeper brittle-ductile transition (Lawson, 1996; Smith and Cann, 1992).

1.1.4.7 Observed eruptions

The rarity and brevity of eruptions (compared with the huge length of mid-ocean ridges on earth) and the expense of surveying them, means very few active eruptions have been observed. Those that have include those in the Brimstone Pit Crater on the Marianas Arc in 2006 (Chadwick et al., 2008) and in the Lau Basin in 2010 (Resing et al., 2011). These, plus other eruptions that have been detected acoustically typically have durations of a few days to a month (Chadwick et al., 1998; Embley et al., 2000; Resing et al., 2011). Eruptions are believed to occur along fissures parallel with the regional stress field, and probably erupt along the length of the fissure, before focusing down to a number of discrete points as the effusion rate wanes (Head et al., 1996; Wylie et al., 1999).

The Brimstone pit crater eruption occurred at shallow depths (540 m) and was extremely explosive (rare at mid-ocean ridges). Due to the very gassy nature of this eruption and its extremely shallow water depth (resulting in it's explosive nature), this eruption is likely to have little in common with mid-ocean ridge eruptions, which are compositionally different (lower volatile concentrations) and usually much deeper.

The Lau Basin eruption consisted of the eruption of boninitic composition lavas to form pillow lavas at a depth of 1200 m (Resing et al., 2011). The Lau basin is a back arc spreading centre rather than a mid-ocean ridge, however with the exception of composition, these pillow lavas are indistinguishable from mid-ocean ridge pillow lavas and therefore the mechanism by which they are being produced – through inflation and cracking of the crust – is applicable everywhere. Back-arc magmas contain higher concentration of volatiles. These volatiles exsolve as the lavas approach the seafloor and in the case of the Lau basin drive explosive eruptions, which fragmented magmas. Exsolving gases were also observed producing large lava bubbles at the vent, which expanded and then exploded, producing glassy fragments. Such a mechanism may, on a smaller scale, be the mechanism by which similar glassy fragments are produced where they are observed on mid-ocean ridges (e.g. (Lackschewitz et al., 1994; Sohn et al., 2008)).

The only direct observations of a mid-ocean ridge lava flow were not visual but were made by an instrument that became entrapped in a sheet lava flow at Axial Seamount on the Juan de Fuca Ridge (Fox et al., 2001). This instrument, a bottom pressure recorder, recorded a sheet flow eruption lasting only 72 minutes, characterised by two periods of uplift, with rates of uplift as great as 73 cm/min. Uplift slowed suddenly, probably as effusion dropped off at the vent, but continued at a much lower rate for another 20 minutes. The instrument then measured slow subsidence relating to drain-back of the lava into the vent over a period of a few hours, which left only 1m thickness on the seafloor (the maximum height reached was 3.5 m). Estimated effusion rates from this eruption per 1 m length of effusive fissure are calculated to be between 0.016 m^3/s and 2.7 m^3/s, with a drain-back rate of 0.17m^3/s. Summed along the entire fissure, the instantaneous total eruption rate may have reached as high as 7,000 m^3/s during the early stages of the eruption, or 550 m^3/s if averaged over 72 minutes (Fox et al., 2001). The depth of the magma chamber was estimated from ground deformation measurements to be 3.8 km.

High-resolution pre and post eruption surveys have also been undertaken at Axial Seamount, covering an eruption that occurred in April 2011. Axial seamount is not a typical mid-ocean ridge setting (Rhodes et al., 1990), sitting at the current centre of the hotspot and being underlain by a steady state, continuously replenished magma chamber. As described by Caress et al. (2012), the April 2011 eruption lasted 6 days, and had a volume of 27×10^6 m^3. It erupted from multiple, discontinuous en-echelon fissures forming < 5m thick sheet and lobate lava flows and one, or possibly two, several kilometre long pillowed ridges. These pillowed ridges, composed of a number of pillow mounds, is believed to have taken longer to form and may be produced after the initial high effusion rate eruption depleted the magma stored at shallow depths of volatiles. Interestingly, in this eruption there is evidence of old fissures having been reactivated as conduits for the magma.

1.1.5 Magma plumbing

1.1.5.1 Magma supply at mid-ocean ridges

As the amount of decompression melting occurring beneath a spreading centre is a product of the rate at which the plates are spreading apart, much more magma is produced beneath fast-spreading ridges than slow-spreading ones (Fowler, 2005). Spreading rate has a fundamental effect on the dimensions of a magma chamber, with large magma chambers only being produced at ridges spreading faster than the critical spreading rate of 5 cm/yr full rate (Phipps Morgan and Ghen, 1993). Below this, thermal modelling has shown that heat flux into the crust is insufficient to maintain a steady state magma chamber of any size (Sleep, 1975). Seismic studies of the East Pacific Rise have regularly identified low velocity zones and narrow sub-axial reflections corresponding to steady state magma chambers (Orcutt et al., 1976). Thus the magma supply to the seafloor at fast-spreading ridges is much more continuous and voluminous.

The method of delivery within the crust differs very little between the fast and slow ridges. Magma is stored in magma chambers beneath the ridge until a dyking event occurs (Smith and Cann, 1993). Melt then travels upwards and laterally along a dyke erupting as a fissure eruption on the surface, similar to the 'fire fountain' eruptions commonly observed on Iceland and Hawaii (Head et al., 1996). These eruptions may focus down to a number of (and eventually a single) point sources as the magma flow through the fissure wanes (Wylie et al., 1999).

Evidence supports mantle upwelling beneath mid-ocean ridges as melt is extracted, predominantly studies of crystal preferred orientation in seafloor peridotites (e.g. (Achenbach et al., 2011)) and seismic measurements (Forsyth, 1992). At fast-spreading ridges, the large volume of melt being produced, combined with the relatively small number of transform offsets, sustains a steady state magma chamber beneath most of the length of a segment (Sinton and Detrick, 1992). This means that crustal thickness (as a result of magmatism) is only really affected near large-offset transforms. As discussed in Lin and Phipps Morgan (1992) and Cannat (1993), at more magma-starved slow-spreading ridges, melt production is too low to sustain large steady state magma chambers anywhere along the ridge and plume-like mantle upwelling beneath the segment centres is thought to exert a stronger control on the location of magmatism. In these situations mantle upwelling away from the segment centre is likely to be negligible (although, as pointed out by Cannat et al. (1996), the thickness of crust here may not be directly proportional to the melt supply as the modelled temperature field would allow some melts to crystalise in the mantle) and therefore it is unlikely that eruptions occurring at the distal ends of a slow-spreading segment are being fed by magma chambers extracted from mantle directly beneath those areas (Sauter et al., 2002), and more likely that melt is travelling laterally along the ridge from the more melt-rich centre (Smith and Cann, 1999). This is supported by Abelson et al. (2001) who showed the magnetic fabric of the Troodos ophiolite is compatible with melt flow along axis, and Magde et al. (2000) who infer lateral transport at the Mid-Atlantic Ridge from seismic tomography imagery.

1.1.5.2 Magma chambers at slow-spreading ridges

A number of segments of the Mid-Atlantic Ridge have been surveyed for the presence of a magma chamber. In 1997 Sinha et al. conducted a variety of seismic and electromagnetic experiments on a volcanically active section of the Iceland Hotspot influenced Reykjanes Ridge at 57°N and found convincing evidence for a thin, centrally 100 m thick, sill-like melt lens 2.5 km below the seafloor at the top of the body and a crystal mush zone containing 20 % melt surrounding it (Sinha et al., 1998; Sinha et al., 1997). Other similar experiments in hot-spot influenced areas were also able to identify magma chambers (e.g. Singh et al., (2006) at Lucky Strike 37°17.5'N MAR). However similar studies on normal sections of the Mid-Atlantic Ridge have found no evidence for magma chambers beneath segment centres (Detrick et al., 1990; Purdy and Detrick, 1986), suggesting they are either small, short lived or do not exist at all (Detrick et al., 1990).

Overall, with the exception of ridges influenced by hotspots, if magma bodies do exist below slow-spreading ridges then they are likely to be < 1 – 2 km wide (Sinton and Detrick, 1992). Such small magma chambers would have a high surface area to volume ratio and would be subject to more rapid cooling, increasing the rate at which they would solidify. With a fairly low magma supply at slow-spreading ridges, it is likely that these small magma chambers will solidify before they are recharged, and thus are probably transient rather than long-lived features (see section 1.1.6.2) (Bideau et al., 1998; Calvert, 1995; Peirce et al., 2007; Singh et al., 2006). There may be exceptions where there is a strong basal lithosphere gradient that focuses melt migration towards one shallow area (Magde et al., 1997; Rabain et al., 2001) or during periods of above average melt flux to the surface (Bryan et al., 1994).

1.1.6 AVR Life-Cycles

1.1.6.1 Life cycle models

The observation of en-echelon volcanic ridges (synonymous to AVRs) at the Reykjanes ridge displaying apparently different levels of tectonic degradation led to the theory of AVR life cycles (Mendel et al., 2003; Parson et al., 1993; Peirce et al., 2005) (figure 1.20). They are believed to begin with a short focused magmatic stage during which progressively more evolved lavas are erupted at decreasing flow rates (due to dropping magmastatic pressure within the magma chamber). This leads to an evolution from sheet to lobate to pillow flow morphologies during the period of formation (Parson et al., 1993). This evolution is also represented in a switch in large-scale volcanic morphology from the large, flat-lying sheet flows to hummocky ridges and mounds (Briais et al., 2000; Parson et al., 1993). This initially active stage is then followed by a much longer period during which the AVR is broken up, and eventually destroyed, by amagmatic extension through faulting. The old AVR becomes part of the new axial valley bounding walls (it is suggested that abyssal hills may be the remnants of old AVRs (Briais et al., 2000; Mendel et al., 2003), which develop during this period. Eventually very little of the original AVR remains on the axis (Parson et al., 1993; Peirce et al., 2005). Parson et al. (1993) suggests that the AVR shape could be a function of the stage of its life cycle it is in, with a broad, convex AVR only developing as it reaches the mature stage. Four representative stages are shown in figure 1.20, although the AVR is envisaged to evolve smoothly between them.

Evidence cited for AVR life cycles includes the discovery of fresh lavas found across an entire graben superimposed on previously faulted terrain (Ondreas et al., 1997), and the observation of different ridges displaying different levels of magmatic robustness and tectonic degradation (Mendel et al., 2003; Parson et al., 1993; Peirce et al., 2005). Additionally, fault scarps providing cross sections have been observed to show periodic switches from sheet flow production to pillow lavas (Ondreas et al., 1997), although both these lithologies may form during the same cycle, as pillows and sheet flows have been observed to form during the same eruptive phase in the AMAR Valley (Stakes et al., 1984).

There are a number of variants of this model. Crane and Ballard (1981) suggested a model in which an AVR life cycle consists of 4 stages, similar to those in figure 1.20. The difference between this model and others is that it suggests that extension does not occur centrally but to one side of the AVR, hence the AVR would never become split in half by faulting but the entire thing would be faulted off to one side (Crane and Ballard, 1981). Parson et al (1993) suggest that cyclicity is a product of tectonic focusing of magma supply (in which tectonic accommodation of extension initiates decompression melting beneath that section of the ridge) while Briais et al. (2000) suggests that cycles are controlled by temporal variations in melt supplied from the mantle. They also suggest that the length of an AVR's life cycle is controlled by the extent and strength of the mantle upwelling.

Alternatively, Murton et al. (2012, in prep) suggest that AVRs are steady state features. They propose a model in which AVRs are present all the time at slow-spreading segments, erupting lavas at their summits, which are then faulted down their sides. In this model sheet flows observed around the base of an AVR are suggested to episodically bury the hummocky terrain and explain the reduced relief off axis. A steady state AVR would require almost steady state volcanism.

1.1.6.2 Life Cycles and Magma Chambers

The cyclicity of magmatism on the AVR is intrinsically linked to the presence of a magma chamber. Sinha et al. (1997) argue that cycles like these are produced because of the solidification of the underlying magma chamber. They put forward the idea that the magmatically robust phase on an AVR lasts only a small proportion of its life cycle and that it is only underlain by a magma chamber during this magmatic phase. This is supported by evidence from the Reykjanes ridge where imagine of a crustal magma chamber showed it to contain volumes of magma equivalent to 20,000 years of crustal accretion in the area, yet the magma body would solidify in less than 2000 years, and therefore magmatism must be episodic (Sinha et al., 1998). This is not compatible with the steady state magmatism proposed by Murton et al (2012, in prep).

Alternatively, smaller magma chambers delivered regularly to the seafloor could maintain a steady state AVR. Smith and Cann (1993) argue that different parts of AVRs often appear to be undergoing different amounts of volcanic and tectonic activity and that this is evidence that entire segments do not go through evolutionary cycles simultaneously. They suggest that discrete small pockets of magma rise to become trapped at the brittle/plastic rheological boundary, where most solidify before a dyking event occurs, except those that are delivered at the right time, which erupt to feed individual axial volcanoes. Thus, the AVR remains a steady state feature underlain by a number of small plutons, and eruptions only occur where one of these plutonic bodies is in the right place and molten when a dyking event occurs (Smith and Cann, 1993). This is supported by geochemical evidence that suggests that lavas sampled from a single AVR were probably produced by more than one discrete magma chamber (Nisbet and Fowler, 1978; Stakes et al., 1984).

1.1.7 Tectonic Processes

Extension at mid-ocean ridges is not only accommodated through dyke injection but also through faulting, which is particularly important at slow spreading ridges where typically ~ 10 % of plate separation (although it may be much more) is accommodated on normal faults (Escartín et al., 1999; MacLeod et al., 2009; Mutter and Karson, 1992). The axial valley wall faults are typically 5 – 50 km in length, with offsets of hundreds of metres (figure 1.2). The upfaulted ridge flanks reach their highest point between 10 and 15 km away from the ridge axis before progressively deepening again (Laughton and Searle, 1979; Shaw, 1992). Fault spacing also varies along the ridge, with many small faults near segment centres and fewer larger faults towards segment ends (Shaw and Lin, 1993). Fissuring may be weak on the AVR but more intense on the surrounding median valley floor (Lawson et al., 1996).

Faults probably begin as fissures at or near the ridge axis, and develop increasing offsets as they are rafted away from the axis (Laughton and Searle, 1979). These small faults and fissures gradually merge together through fault tip propagation and linkage (Cowie, 1998; Searle et al., 1998; Shaw, 1992) to form larger faults, which eventually become the axial valley wall faults (Cann and Smith, 2005). At this point their direction of throw is probably determined by the asymmetry of lithospheric stretching (Laughton and Searle, 1979).

Strain at spreading centres initially localizes on faults at, or close to, the ridge axis and these faults remain active as they are rafted away, until it becomes easier to initiate a new fault close to the ridge axis (Behn and Ito, 2008). Faulting style varies both along the strike as well as across it and the rift valley structure may vary from heavily fissured to unfissured terrain within a few kilometres, indicating that accommodation of plate separation along the axis does not take place everywhere at the same time (Cann and Smith, 2005; Searle et al., 1998).

1.1.8 Petrogenesis of MOR lavas

The dominant erupted rock type found at mid-ocean ridges is mid-ocean ridge basalt (MORB), with phenocrysts of olivine, plagioclase and occasionally clinopyroxene (Kay et al., 1970). These basalts form new oceanic crust and are produced by the adiabatic decompression partial melting of mantle lherzolite in upwelling mantle beneath a ridge segment (Wilson, 1989) (figure 1.21). The chemical composition of MORB depends on the source of the melt, the degree of partial melting of this source, the depth of magma segregation and the extent of fractional crystallisation (Wilson, 1989). In some situations (predominantly when associated with hotspots) melts may be derived from more enriched sources (i.e. more enriched in incompatible components), in this case they are called enriched MORB (E-MORB) (Schilling, 1973; Schilling et al., 1983; Wilson, 1989). Under typical conditions MORB can be produced from 15 – 25 % partial melting (Ahern and Turcotte, 1979; Kushiro, 2001; Wilson, 1989), although percentage melt is affected by depth and the initial composition of the decompressing mantle (Ahern and Turcotte, 1979). Partial melting depth can be obtained from geophysical studies of P and S wave attenuation and, while only available for a few segments, probably starts at a depth of 60 – 80 km, segregating into batches at around 20 km (Hekinian, 1982), a finding supported by the East Pacific Rise MELT experiment (Forsyth et al., 1998), which identified a low velocity zone, probably caused by partial melt, between 70 and 20 km depth beneath the ridge.

Variations in N-MORB composition, common on the northern Mid-Atlantic Ridge, are probably due to variations in the degree of partial melting of 10 – 15% as well as compositional variations in the source (Michael and Bonatti, 1985).

Additionally the basalts at 45˚N on the Mid-Atlantic Ridge (where my study is conducted) are more enriched than typical N-MORB (Sun et al., 1979; White and Schilling, 1978) and it has been suggested that this area was underlain by a hotspot (Mello et al., 1999; Searle and Whitmarsh, 1978).

1.1.9 Summary

Slow-spreading ridges are characterized by broad axial valleys, typically > 1 km deep and bounded by a series of normal faults (Laughton and Searle, 1979). At slow-spreading ridges ~ 10 % of plate separation is accommodated by this faulting rather than dyke injection (Mutter and Karson, 1992).

Most slow-spreading ridge segments contain an AVR, which are the main sites of extrusive volcanism in the axial valley (Ballard and Van Andel, 1977; Ramberg and Van Andel, 1977; Sempere et al., 1993; Smith and Cann, 1993; Smith et al., 1995a). They are typically several tens of kilometres long by a few kilometres wide, but may vary in shape and size, and may even be discontinuous along a ridge (Head et al., 1996; Smith et al., 1995a). They are composed almost entirely of volcanic hummocks, which are small volcanic domes or cones, composed predominantly of pillow lavas (Smith and Cann, 1990), and these hummocks may coalesce to form hummock ridges or larger mounds (Head et al., 1996; Lawson et al., 1996; Smith and Cann, 1993; Smith et al., 1995a).

Axial valleys also contain areas of smooth lava flows, typically composed of sheet or lobate lava flows (Ballard and Moore, 1977; Ballard and Van Andel, 1977) and flat-topped seamounts, which are found all around axial valleys, but rarely on the AVR (Lawson et al., 1996; Smith et al., 1995a). These different lithologies, as well as different degrees of tectonism, may be explained by the AVR life cycle hypothesis, whereby a pulse of magma is supplied to the ridge resulting in a short period of focused magmatism producing high effusion rate sheet and lobate lava flows (Parson et al., 1993; Sinha et al., 1998; Sinha et al., 1997). This will be followed by a period of pillow lava construction due to dropping magmastatic pressures and finally, as the magma chamber stops erupting and solidifies, by a longer period of tectonic dismemberment, where all the extension is accommodated tectonically and the AVR is broken up by normal faulting (Parson et al., 1993; Peirce et al., 2005). Alternatively they may be steady state features. As described by Murton et al. (2012) in the steady state scenario an AVR will be present at the axis all the time, fed by near steady state volcanism. Lavas will be erupted near the AVR summit and then faulted down the sides of the AVR by outward facing normal faults, before being buried by higher effusion rate sheet flows which occur periodically around its base.

1.2 Summary of thesis aims and structure

1.2.1 Thesis Aims

The MAR at 45°N is a typical ocean spreading centre with a well defined axial volcanic ridge, making it an ideal location in which to investigate the formation of these near ubiquitous features, the presence or lack of life cycles and the implications of these processes to the formation of upper oceanic crust. This thesis sets out to answer the following two main questions:

- **What is the detailed volcanological structure of slow-spread oceanic crust?** Axial volcanic ridges are the only large volume expression of volcanism on slow-spreading ridges, making them the most likely site for the production of the extrusive volcanics which we know form the upper oceanic crust. If this is the case, the building blocks of AVRs are also the building blocks of oceanic crust. By studying their eruptive characteristics and morphology on the AVR where they are being produced, it should be possible to define fully what the upper oceanic crust is made of, and also assess the importance of other lithologies (e.g. flat lava flows) observed in the axial valley.

- **Is the model of AVR development as proposed by Parson et al. (1993) correct?** The model presented in Parson et al. (1993) suggests a four-stage model of life cycles for AVRs, through which they constantly evolve. This model consists of a period of fissure eruption which forms the flat lying flows, followed by a period of robust magmatism producing the body of the AVR and the flat-topped seamounts. As magmatism wanes, tectonic extension takes over and this breaks the AVR up. However AVRs are observed on 90 % of mid-ocean ridges, suggesting they are present most of the time (Murton et al., 2012, in prep). With detailed coverage of an entire slow-spreading segment, it should be possible to test whether this model matches observations, and examine whether AVRs really are episodic features.

Within these questions there are a number of smaller subsidiary questions which will also be addressed.

- **What are the volcanic units at slow-spreading ridge segments? How are they distributed spatially at slow-spreading mid-ocean ridge segments containing an AVR?** A number of different volcanic units are observed on slow-spreading mid-ocean ridges, however few studies have covered an entire ridge segment in sufficient detail to accurately map the distribution of these units across an entire ridge segment.

- **What form do volcanic eruptions at AVRs take? How large are they and how long do the last?** It is not currently known whether individual volcanic eruptions at slow-spreading ridges produce one, or many hummocks. Volumes of hummocks and mid-ocean ridge eruptions have not been quantified, neither have eruption durations or periodicity.

- **How are volcanic eruptions related to each other? Is one section of the AVR more active than the rest? Do flat-topped seamounts begin as hummocks?** It is not known how many volcanic hummocks comprise a single eruption, nor how far from a fissure a lava flow can reach. It is also not known whether sheet flows and hummocks are produced by the same eruption, or if they are separate processes, nor how flat-topped seamounts are related to the other eruptive products at mid-ocean ridges. Furthermore, the hypothesis of magma transport along axis can also be tested. If one section of an AVR is far more active than another, or if all the recent activity is concentrated in a single area then magma transport along axis is unlikely to be occurring along great distances.

- **Are the styles of volcanism similar at faster spreading rates?** It is not known how volcanic eruptions at intermediate-spreading rate ridges differ from those at slow spreading ridges in terms of size, periodicity and form. Descriptions of pillow mound eruptions at intermediate spreading rates are similar to those of hummocky seamounts observed at slow-spreading mid ocean ridges. Are they the same features?

- **How many melts are combined in each magma chamber? Are isotopic ratios the same as those measured by White and Schilling (1978)?** Detailed isotopic studies of the composition and zoning of crystals could tell us how many melts the crystals come from and how the melts evolve through time. Additionally, by carrying out analyses on a range of samples from across the axis, we could see if the E-MORB type ratios observed by White and Schilling (1978) are ubiquitous, and if not, how they are distributed. In the event problems with contamination prevented me from completing this part of the study.

1.2.2 Thesis outline

Section 1.1 has provided an overview of the state of research into axial volcanism and AVRs on the Mid-Atlantic Ridge, which are the most common and voluminous volcanic features on slow-spreading ridges and the most likely site for the production of upper oceanic crust. The central part of the thesis is split into five data chapters, which cover five separate projects I have undertaken to tackle the questions set out is section 1.2.1. Each of these chapters begins with a ‘Rationale’ section, explaining why it was carried out and how it related to the central questions presented above in section 1.2.1. The chapters are laid out like scientific papers, with individual introduction, methods, discussion and conclusion sections. Chapter two deals with the ROV video observations and mapping of the AVR. Chapter three concentrates on the volumes of eruptions and distribution of volcanic features observed with sidescan sonar and high-resolution bathymetric studies. Chapter four discusses the importance of collapse features observed from the high-resolution bathymetry and their implications for upper oceanic crustal construction. Chapter five focuses on intermediate spreading ridges, with mapping of three historic eruptions from high-resolution datasets, and comparison with those at 45°N. The results of these chapters are linked together and discussed in chapter six, which is divided into two themes, based around answering the two main questions in section 1.2.1: "What is the oceanic crust made of?" and "Is the model of AVR development as proposed by Parson et al. (1993) correct?". Chapter six discusses conclusions from the previous chapters to try and answer these questions, as well as setting them in the context of current literature. The thesis conclusions for these, and all the questions presented in section 1.2.1 are presented in chapter seven, which also covers possibilities for future work.

Additionally an attempt to study $^{87}Sr/^{86}Sr$ isotopic zoning in plagioclase crystals from a subset of the 45˚N samples was also carried out and is included in appendix 9.10. This study attempted to use micromilling of zoned plagioclases to investigate melt mixing or magma chamber wall assimilation within magma chambers beneath the ridge (as changing Sr isotopic ratios within an evolving magma will be recorded by minerals crystallising from the melt). Additionally, I aimed to compare the measured isotopic ratios with other studies (e.g. Schilling et al., 1983), which have suggested that unusually high $^{87}Sr/^{86}Sr$ ratios have been observed . Unfortunately, due to contamination, many of the results were clearly unrealistic and I was unable to investigate magma chamber processes using them. As such, this work is included as an appendix for methodology and comparison only.

1.2.3 Papers

I have written a number of papers based on this thesis work, which are in varying stages of completion. One paper, "Eruptive Hummocks: Building blocks of the upper oceanic crust" has so far been published from this thesis and is contained in the appendices. It forms a part (eruption volume and timing sections) of chapter 3 and most of chapter 4, although the chapter contains an extended discussion on potential collapse mechanisms. I also contributed to the Searle et al. (2010) paper. This is also included in the appendices.

Drafts of two further papers are currently being prepared, one (on the distribution of lava lithologies within an axial valley) is being prepared from chapter two. This paper, entitled "High Resolution ROV Mapping of a

Slow-Spreading Ridge: Mid-Atlantic Ridge 45˚N" is in preparation for *Geochemistry, Geophysics, Geosystems* and should be submitted June/July 2012. The second (on eruption volumes and discontinuous dykes) is being prepared from chapter 6. This paper, which came out of work done during an internship at MBARI entitled New Insights into Diking Processes from High-Resolution Bathymetry of Historic Pillow Ridges on the Juan de Fuca and Gorda Ridges", is also in preparation for *Geochemistry, Geophysics, Geosystems* and should be submitted June 2012. I am also in the early stages of writing a paper with Nicole Schroth (NOC Southampton, who has been doing a range of geochemical analyses on the 45˚N samples), which aims to combine the physical volcanology and geochemistry of the southern high resolution study area to look at a single lava flow in detail, attempting to accurately estimate its spatial extent, changing effusion rate, feeding systems and duration.

The draft of a paper by Murton et al (2012, under review) paper, which I also contributed to and which is discussed in detail in chapter 7, is also included in the appendices.

1.3 Data

The Mid-Atlantic Ridge sections of this thesis (chapters 2, 3, 4, 5) are based on data collected on cruise JC24 in June/July 2008. The data discussed in chapter 6, from the Juan de Fuca and North Gorda Ridges were collected on several cruises run by the Monterey Bay Aquarium and Research Institute (MBARI) in 2009. The different data sets collected and discussed in this thesis are outlined below.

1.3.1 JC24 cruise

1.3.1.1 EM120 bathymetry

The EM120 bathymetry was collected with a Simrad EM120 multibeam echosounder (figure 1.22). Data was processed by T P LeBas in CARIS HIPS version 6.1, to produce a 50 m grid with a navigational precision of 50 m (Searle et al., 2008). Data was corrected for heave, pitch, roll and gyro.

1.3.1.2 TOBI sidescan sonar

Sidescan sonar was collected using the Towed Ocean Bottom Instrument (TOBI), operated by the National Oceanography Centre, Southampton (Flewellen et al., 1993). 30 kHz sidescan sonar was collected as 6 km swaths, with a pixel size of 3m (Searle et al., 2008). Complete coverage of the axial valley was obtained in the north and south looking directions from 1.5 km spaced lines (figure 1.23). East and west looking side-scan was obtained from the two N-S tracks. Data was processed by T P LeBas using PRISM (LeBas, 2005), yielding data with estimated post-processed navigational precision of ~100m. The north looking mosaic is shown in figure 1.24.

1.3.1.3 SM2000 Isis bathymetry

Two areas were chosen for detailed study. Bathymetry was collected using the ROV Isis (German et al., 2003), operated by the National Oceanography Centre, Southampton. Data was collected with a Simrad SM2000 bathymetry system, yielding bathymetry with a horizontal and vertical resolution of ~1 – 2 m.

The southern high-resolution study area was surveyed on dive JC24-91 (figure 1.25, dive number 91) on the eastern flank of the magmatically robust southern part of the AVR. It covers ~5 km^2 from the AVR crest to its base at the eastern axial valley wall (figure 1.26). The northern high-resolution study area, surveyed on dive JC24-87 (figure 1.25, dive number 87) provides an almost complete (~5.7 km) oblique transect across the lower-lying, probably older AVR, north of 45°32'N (figure 1.27).

Raw SM2000 bathymetry was processed in CARIBES version 3.4 by T P LeBas (Searle et al., 2008). Further renavigation of the processed data was carried out by K L Achenbach in MATLAB yielding final, post processed horizontal and vertical resolution of 1 – 2 m.

1.3.1.4 Isis dive track video and sampling

Video data was recorded on all Isis sampling dives (JC24-79, JC24-80, JC24-81, JC24-82, JC24-83, JC24-84/5, JC24-88, JC24-89, JC24-90, JC24-92, and JC24-93). These dive tracks are shown in figure 1.25. The following cameras were used:

An Atlas 3-chip 850-line colour video camera with a 14x optical zoom.
A pan and tilt camera (Pegasus), a 560 TV line, low light, colour video camera with 12x zoom. It is mounted on a pan and tilt unit, which was available for science operation during the dive.

Stills were taken with the Scorpio camera, a 3.34 Mega pixel digital still camera with a 4x zoom. It was used to take publication-quality pictures of both geology and biology.

The science party elected to record video data from the Atlas 3-chip camera and the Pegasus Pan and Tilt camera, with the exception of one watch, which used the Aft Cam (the rear looking, black and white camera) for several hours to record footage while the ROV was travelling down a slope. We recorded onto DV Cam tapes lasting 3 hours and tape changes were staggered so one set of tapes was always recording.

Samples were taken on all the video dives using the manipulator arm. Samples were typically pillow buds or crusts which were easier to snap off with the ROV arm than in-tact pillows. Sheet flow samples were typically taken where tectonism had made it possible to snap off pieces with the manipulator arm. Sample locations can be seen in figure 1.28.

1.3.1.5 Crustal magnetisation

Maps of crustal magnetisation were produced by M Tivey using both the TOBI magnetic field data (figure 1.29) and the data recorded by Isis in the southern (figure 1.30) and northern (figure 1.31) study areas (Searle et al., 2008).

1.3.2 MBARI data

1.3.2.1 AUV bathymetry

High-resolution bathymetry was collected by the MBARI autonomous underwater vehicle (AUV) on cruises in 2009. Data was collected at using 200KHz multibeam sonar (Caress et al., 2008) and processed using MB System (described in Caress and Chayes (1996) yielding final maps with an ~ 1 m horizontal and vertical resolution. Data from the North Gorda (figure 1.32), and from the CoAxial (figure 1.33) and North Cleft (figure 1.34) segments of the Juan de Fuca ridge are used in this thesis.

1.3.2.2 ROV video observations

Video footage was recorded on high resolution video cameras. These cameras were mounted on the MBARI ROVs Tiburon (using Panasonic 3- chip pan and tilt colour cameras recording to Digital BetacamTM) and Doc Ricketts (using a ROS PT-25 pan and tilt HDTV) operated from the R/V Western Flyer on cruises in 2005 and 2009.

1.4 References

Abelson, M., Baer, G., and Agnon, A., 2001, Evidence from gabbro of the Troodos ophiolite for lateral magma transport along a slow-spreading mid-ocean ridge: Nature, v. 409, p. 72-75.

Achenbach, K.L., Cheadle, M.J., Faul, U., Kelemen, P., and Swapp, S., 2011, Lattice-preferred orientation and microstructure of peridotites from ODP Hole 1274A (15°39′N), Mid-Atlantic Ridge: Testing models of mantle upwelling and tectonic exhumation: Earth and Planetary Science Letters, v. 301, p. 199-212.

Ahern, J.L., and Turcotte, D.L., 1979, Magma migration beneath an ocean ridge Earth and Planetary Science Letters, v. 45, p. 115-122.

Allerton, S., Escartín, J., and Searle, R.C., 2000, Extremely asymmetric magmatic accretion of oceanic crust at the ends of slow-spreading ridge segments: Geology, v. 28, p. 179-182.

Atwater, T., 1979, Constraints from the Famous Area concerning the structure of th oceanic section, *in* Talwani, M., Harrison, C.G.A., and Hayes, D.E., eds., Deep drilling results in the atlantic ocean: Oceanic crust: Maurice Ewing Series: Washington D. C., American Geophysical Union.

Auzende, J.M., Bideau, D., Bonatti, E., Cannat, M., Honnorez, J., Lagabrielle, Y., Malavieille, J., Mamaloukas-Frangoulis, V., and Mevel, C., 1989, Direct observation of a section through slow-spreading oceanic crust: Nature, v. 337, p. 726-729.

Ballard, R.D., Holcomb, R.T., and Vanandel, T.H., 1979, Galapagos Rift at 86-degrees-W .3. Sheet flows, collapse pits and lava lakes of the rift valley Journal of Geophysical Research, v. 84, p. 5407-5420.

Ballard, R.D., and Moore, J.G., 1977, Photographic Atlas of the Mid-Atlantic Ridge Rift Valley: New York, Springer-Verlag, 114 p.

Ballard, R.D., and Van Andel, T.H., 1977, Morphology and tectonics of inner rift valley at lat 36degree50'N on Mid-Atlantic Ridge Geological Society of America Bulletin, v. 88, p. 507-530.

Batiza, R., Fox, P.J., Vogt, P.R., Cande, S.C., Grindlay, N.R., Melson, W.G., and O'Hearn, T., 1989a, Morphology, Abundance, and Chemistry of Near-Ridge Seamounts in the Vicinity of the Mid-Atlantic Ridge ~26°S: The Journal of Geology, v. 97, p. 209-220.

Batiza, R., Smith, T.L., and Niu, Y.L., 1989b, Geological and petrological evolution of seamounts near the EPR based on submersible and camera study Marine Geophysical Researches, v. 11, p. 169-&.

Behn, M.D., and Ito, G., 2008, Magmatic and tectonic extension at mid-ocean ridges: 1. Controls on fault characteristics: Geochemistry Geophysics Geosystems, v. 9, p. 22.

Bell, R.E., and Buck, W.R., 1992, Crustal control of ridge segmentation inferred from observations of the Reykjanes Ridge: Nature, v. 357, p. 583-586.

Bellaich, G., Cheminee, J.L., Franchet.J, Hekinian, R., Lepichon, X., Needham, H.D., and Ballard, R.D., 1974, Inner floor of rift valley - First submersible study Nature, v. 250, p. 558-560.

Bideau, D., Hekinian, R., Sichler, B., Gracia, E., Bollinger, C., Constantin, M., and Guivel, C., 1998, Contrasting volcanic-tectonic processes during the past 2 Ma on the Mid-Atlantic Ridge: submersible mapping, petrological and magnetic results at lat. 34 degrees 52 ' N and 33 degrees 55 ' N: Marine Geophysical Researches, v. 20, p. 425-458.

Blackman, D.K., Cann, J.R., Janssen, B., and Smith, D.K., 1998, Origin of extensional core complexes: Evidence from the Mid-Atlantic Ridge at Atlantis Fracture Zone: J. Geophys. Res., v. 103, p. 21315-21333.

Bonatti, E., and Harrison, C.G.A., 1988, Eruption styles of basalts in oceanic spreading ridges and seamounts - Effect of magma temperature and viscosity Journal of Geophysical Research-Solid Earth and Planets, v. 93, p. 2967-2980.

Bown, J.W., and White, R.S., 1994, Variation with spreading rate of oceanic crustal thickness and geochemistry: Earth and Planetary Science Letters, v. 121, p. 435-449.

Bratt, S.R., and Purdy, G.M., 1984, Structure and Variability of Oceanic Crust on the Flanks of the East Pacific Rise Between 11° and 13°N: J. Geophys. Res., v. 89, p. 6111-6125.

Briais, A., Sloan, H., Parson, L.M., and Murton, B.J., 2000, Accretionary processes in the axial valley of the Mid-Atlantic Ridge 27 degrees N-30 degrees N from TOBI side-scan sonar images: Marine Geophysical Researches, v. 21, p. 87-119.

Brown, J., and Karson, J., 1988, Variations in axial processes on the Mid-Atlantic Ridge: The median valley of the MARK area: Marine Geophysical Researches, v. 10, p. 109-138.

Bryan, W.B., Humphris, S.E., Thompson, G., and Casey, J.F., 1994, Comparitive volcanology of small acial eruptive centres in the MARK area Journal of Geophysical Research-Solid Earth, v. 99, p. 2973-2984.

Bryan, W.B., and Thompson, G., 1979, Petrologic character of the Atlantic crust from DSDP and IODP drill sites, *in* Talwani, M., Harrison, C.G.A., and Hayes, D.E., eds., Deep drilling results in the Atlantic Ocean: Ocean Crust: Maurice Ewing Series: Washington, American Geophysical Union, p. 273 - 284.

Buck, W.R., Lavier, L.L., and Poliakov, A.N.B., 2005, Modes of faulting at mid-ocean ridges: Nature, v. 434, p. 719-723.

Calvert, A.J., 1995, Seismic evidence for a magma chamber beneath the slow-spreading Mid-Atlantic Ridge: Nature, v. 377, p. 410-414.

Canales, J.P., Tucholke, B.E., and Collins, J.A., 2004, Seismic reflection imaging of an oceanic detachment fault: Atlantis megamullion (Mid-Atlantic Ridge, 30°10′N): Earth and Planetary Science Letters, v. 222, p. 543-560.

Cann, J.R., 1974, A Model for Oceanic Crystal Structure Developed: Geophysical Journal International, v. 39, p. 169-187.

Cann, J.R., and Smith, D.K., 2005, Evolution of volcanism and faulting in a segment of the Mid-Atlantic Ridge at 25 degrees N: Geochemistry Geophysics Geosystems, v. 6, p. 20.

Cannat, M., 1993, Emplacement of Mantle Rocks in the Seafloor at Mid-Ocean Ridges: J. Geophys. Res., v. 98, p. 4163-4172.

—, 1996, How thick is the magmatic crust at slow spreading oceanic ridges?: J. Geophys. Res., v. 101, p. 2847-2857.

Cannat, M., Lagabrielle, Y., Bougault, H., Casey, J., de Coutures, N., Dmitriev, L., and Fouquet, Y., 1997, Ultramafic and gabbroic exposures at the Mid-Atlantic Ridge: geological mapping in the 15°N region: Tectonophysics, v. 279, p. 193-213.

Cannat, M., Sauter, D., Mendel, V., Ruellan, E., Okino, K., Escartin, J., Combier, V., and Baala, M., 2006, Modes of seafloor generation at a melt-poor ultraslow-spreading ridge: Geology, v. 34, p. 605-608.

Caress, D.W., and Chayes, D.N., 1996, Improved processing of Hydrosweep DS multibeam data on the R/V Maurice Ewing: Marine Geophysical Researches, v. 18, p. 631-650.

Caress, D.W., Clague, D.A., Paduan, J.B., Martin, J.F., Dreyer, B.M., Chadwick, W.W., Denny, A., and Kelley, D.S., 2012, Repeat bathymetric surveys at 1-metre resolution of lava flows erupted at Axial Seamount in April 2011: Nature Geosci, v. 5, p. 483-488.

Caress, D.W., Thomas, H., Kirkwood, W.J., McEwen, R., Henthorn, R., Clague, D.A., Paull, C.K., and Paduan, J., 2008, High-Resolution Multibeam, Sidescan, and Subbottom Surveys Using the MBARI AUV: Marine Habitat Mapping Technology for Alaska.

Chadwick, W.W., and Embley, R.W., 1994, Lava flows from a mid-1980s submarine eruption on the Cleft Segment, Juan de Fuca Ridge Journal of Geophysical Research-Solid Earth, v. 99, p. 4761-4776.

Chadwick, W.W., Embley, R.W., and Shank, T.M., 1998, The 1996 Gorda Ridge eruption: geologic mapping, sidescan sonar, and SeaBeam comparison results: Deep-Sea Research Part Ii-Topical Studies in Oceanography, v. 45, p. 2547-2569.

Chadwick, W.W., Jr., Cashman, K.V., Embley, R.W., Matsumoto, H., Dziak, R.P., de Ronde, C.E.J., Lau, T.K., Deardorff, N.D., and Merle, S.G., 2008, Direct video and hydrophone observations of submarine explosive eruptions at NW Rota-1 volcano, Mariana arc: J. Geophys. Res., v. 113, p. B08S10.

Chadwick, W.W., Scheirer, D.S., Embley, R.W., and Johnson, H.P., 2001, High-resolution bathymetric surveys using scanning sonars: Lava flow morphology, hydrothermal vents, and geologic structure at recent eruption sites on the Juan de Fuca Ridge: Journal of Geophysical Research-Solid Earth, v. 106, p. 16075-16099.

Chen, Y., and Morgan, W.J., 1990, A Nonlinear Rheology Model for Mid-Ocean Ridge Axis Topography: J. Geophys. Res., v. 95, p. 17583-17604.

Christensen, N.I., and Salisbury, M.H., 1975, Structure and constitution of the lower oceanic crust: Rev. Geophys., v. 13, p. 57-86.

Christeson, G.L., Karson, J.A., and McIntosh, K.D., 2010, Mapping of seismic layer 2A/2B boundary above the sheeted dike unit at intermediate spreading crust exposed near the Blanco Transform: Geochemistry Geophysics Geosystems, v. 11, p. Q03015.

Christeson, G.L., Purdy, G.M., and J., F.G., 1992, Structure of young upper crust at the East Pacific Rise near 9° 30′N: Geophysical Research Letters, v. 19, p. 1045-1048.

Clague, D.A., Moore, J.G., and Reynolds, J.R., 2000, Formation of submarine flat-topped volcanic cones in Hawai'i: Bulletin of Volcanology, v. 62, p. 214-233.

Constantin, M., 1999, Gabbroic intrusions and magmatic metasomatism in harzburgites from the Garrett transform fault: implications for the nature of the mantle–crust transition at fast-spreading ridges: Contributions to Mineralogy and Petrology, v. 136, p. 111-130.

Cowie, P.A., 1998, Normal Fault Growth in three dimensions in Continental and Oceanic crust, *in* Buck, R., Delaney, J.R., Karson, J.A., and Lagabrielle, Y., eds., Faulting and Magmatism at Mid-Ocean Ridges: Geophysical Monograph: Washington D. C., Americal Geophysical Union, p. 348.

Cowie, P.A., Scholz, C.H., Edwards, M., and Malinverno, A., 1993, Fault strain and seismic coupling on midocean ridges: Journal of Geophysical Research-Solid Earth, v. 98, p. 17911-17920.

Crane, K., and Ballard, R.D., 1981, Volcanics and structure of the FAMOUS Narrowgate Rift - Evidence for cyclic evolution - AMAR - 1 Journal of Geophysical Research, v. 86, p. 5112-5124.

Detrick, R.S., Buhl, P., Vera, E., Mutter, J., Orcutt, J., Madsen, J., and Brocher, T., 1987, Multichannel seismic imagin of a crustal magma chamber alqong the East Pacific Rise Nature, v. 326, p. 35-41.

Detrick, R.S., Mutter, J.C., Buhl, P., and Kim, II, 1990, No evidence from multichannel reflection data for a crustal magma chamber in the MARK area in the Mid-Atlantic Ridge Nature, v. 347, p. 61-64.

Dilek, Y., 1998, Structure and Tectonics of Intermediate-Spread Oceanic Crust Drilled at DSDP/ODP Holes 504B and 896A, Costa Rica Rift: Geological Society, London, Special Publications, v. 131, p. 177-197.

Dilek, Y., Moores, E.M., and Furnes, H., 1998, Structure of modern oceanic crust and ophiolites and implications for faulting and magmatism at oceanic spreading centers, *in* Buck, R., Delaney, J.R., Karson, J.A., and Lagabrielle, Y., eds., Faulting and Magmatism at Mid-Ocean Ridges: Geophysical Monograph: Washington, American Geophysical Union, p. 348.

Embley, R.W., Chadwick, W., Perfit, M.R., and Baker, E.T., 1991, Geology of the Northern Cleft Segment, Juan de Fuca Ridge - Recent lava flows, sea-floor spreading, and the formation of megaplumes Geology, v. 19, p. 771-775.

Embley, R.W., Chadwick, W.W., Perfit, M.R., Smith, M.C., and Delaney, J.R., 2000, Recent eruptions on the CoAxial segment of the Juan de Fuca Ridge: Implications for mid-ocean ridge accretion processes: Journal of Geophysical Research-Solid Earth, v. 105, p. 16501-16525.

Escartín, J., Cowie, P.A., Searle, R.C., Allerton, S., Mitchell, N.C., MacLeod, C.J., and Slootweg, A.P., 1999, Quantifying tectonic strain and magmatic accretion at a slow spreading ridge segment, Mid-Atlantic Ridge, 29°N: J. Geophys. Res., v. 104, p. 10421-10437.

Escartín, J., Hirth, G., and Evans, B., 1997, Effects of serpentinization on the lithospheric strength and the style of normal faulting at slow-spreading ridges: Earth and Planetary Science Letters, v. 151, p. 181-189.

Escartin, J., Smith, D.K., Cann, J., Schouten, H., Langmuir, C.H., and Escrig, S., 2008, Central role of detachment faults in accretion of slow-spreading oceanic lithosphere: Nature, v. 455, p. 790-794.

Escartin, J., Soule, S.A., Fornari, D.J., Tivey, M.A., Schouten, H., and Perfit, M.R., 2007, Interplay between faults and lava flows in construction of the upper oceanic crust: The East Pacific Rise crest 9 degrees 25 '-9 degrees 58 ' N: Geochemistry Geophysics Geosystems, v. 8.

Fink, J.H., and Griffiths, R.W., 1992, A laboratory analog study of the surface morphology of lava flows extruded from point and line sources: Journal of Volcanology and Geothermal Research, v. 54, p. 19-32.

Flewellen, C., Millard, N., and Rouse, I., 1993, TOBI, A Vehicle for Deep Ocean Survey Electronics & Communication Engineering Journal, v. 5, p. 85-93.

Forsyth, D.W., 1992, Geophysical Constraints on Mantle Flow and Melt Geneation Beneath Mid-Ocean Ridges, *in* Phipps Morgan, J., Blackman, D.K., and Sinton, J.M., eds., Mantle Flow and Melt Generation at Mid-Ocean Ridges: Washington, American Geophysical union, p. 1-65.

Forsyth, D.W., Webb, S.C., Dorman, L.M., and Shen, Y., 1998, Phase Velocities of Rayleigh Waves in the MELT Experiment on the East Pacific Rise: Science, v. 280, p. 1235-1238.

Fowler, C.M.R., 2005, The Solid Earth: An Introduction to Global Geophysics (Second Edition): Cambridge, Cambridge University Press, 685 p.

Fox, C.G., Chadwick, W.W., and Embley, R.W., 2001, Direct observation of a submarine volcanic eruption from a sea-floor instrument caught in a lava flow: Nature, v. 412, p. 727-729.

Fox, C.G., Murphy, K.M., and Embley, R.W., 1988, Automated display and statistical analysis of interpreted deep-sea bottom photographs: Marine Geology, v. 78, p. 199-216.

Fujita, K., and Sleep, N.H., 1978, Membrane stresses near mid-ocean ridge-transform intersetions Tectonophysics, v. 50, p. 207-221.

Gallo, D.G., Fox, P.J., and Macdonald, K.C., 1986, A Sea Beam Investigation of the Clipperton Transform Fault: The Morphotectonic Expression of a Fast Slipping Transform Boundary: J. Geophys. Res., v. 91, p. 3455-3467.

German, C., Tyler, P., and Griffiths, G., 2003, The maiden voyage of UK ROV "Isis": Ocean Challenge, v. 12, p. 16-18.

Gracia, E., Charlou, J.L., Radford-Knoery, J., and Parson, L.M., 2000, Non-transform offsets along the Mid-Atlantic Ridge south of the Azores (38 degrees N-34 degrees N): ultramafic exposures and hosting of hydrothermal vents: Earth and Planetary Science Letters, v. 177, p. 89-103.

Green, D.H., and Ringwood, A.E., 1967, The genesis of basaltic magmas: Contributions to Mineralogy and Petrology, v. 15, p. 103-190.

Gregg, P.M., Lin, J., Behn, M.D., and Montesi, L.G.J., 2007, Spreading rate dependence of gravity anomalies along oceanic transform faults: Nature, v. 448, p. 183-U5.

Gregg, T.K.P., and Fink, J.H., 1995, Quantification of submarine lava-flow morphology through analog experiments Geology, v. 23, p. 73-76.

Gregg, T.K.P., Fornari, D.J., Perfit, M.R., Haymon, R.M., and Fink, J.H., 1996, Rapid emplacement of a mid-ocean ridge lava flow on the East Pacific Rise at 9 degrees 46'-51'N: Earth and Planetary Science Letters, v. 144, p. E1-E7.

Gregg, T.K.P., and Smith, D.K., 2003, Volcanic investigations of the Puna Ridge, Hawai'i: relations of lava flow morphologies and underlying slopes: Journal of Volcanology and Geothermal Research, v. 126, p. 63-77.

Griffiths, R.W., and Fink, J.H., 1992a, The morphology of lava flows in planetary environments - Predictions from analog experiments Journal of Geophysical Research-Solid Earth, v. 97, p. 19739-19748.

—, 1992b, Solidification and morpholoy of submarine lavas - A dependence on extrusion rate Journal of Geophysical Research-Solid Earth, v. 97, p. 19729-19737.

Grindlay, N.R., Fox, P.J., and Macdonald, K.C., 1991, 2nd-order ridge axis discontinuities in the South Atlantic - morphology, structure, and evolution Marine Geophysical Researches, v. 13, p. 21-49.

Guest, J.E., Wood, C., and Greeley, R., 1984, Lava tubes, terraces and megatumuli on the 1614–24 pahoehoe lava flow field, Mount Etna, sicily: Bulletin of Volcanology, v. 47, p. 635-648.

Harding, A.J., Kent, G.M., and Orcutt, J.A., 1993, A multichannel seismic investigation of upper crustal structure at 9°N on the East Pacific Rise: Implications for crustal accretion: Journal of Geophysical Research, v. 98, p. 13,925–13,944.

Harris, A.J.L., Dehn, J., and Calvari, S., 2007, Lava effusion rate definition and measurement: a review: Bulletin of Volcanology, v. 70, p. 1 - 22.

Head, J.W., Wilson, L., and Smith, D.K., 1996, Mid-ocean ridge eruptive vent morphology and substructure: Evidence for dike widths, eruption rates, and evolution of eruptions and axial volcanic ridges: Journal of Geophysical Research-Solid Earth, v. 101, p. 28265-28280.

Heezen, B.C., 1960, The rift in the ocean floor: Scientific American, v. 203, p. 98-110.

Hekinian, R., 1982, Petrology of the Ocean Floor: Amsterdam, Elsevier.

Herron, T.J., 1982, Lava flow layer-East Pacific Rise: Geophysical Research Letters, v. 9, p. 17-20.

Hess, H.H., 1962, History of Ocean Basins: Petologic Studies: A Volume to Honor, p. 599-620.

Karson, J.A., 2002, Geologic structure of the uppermost oceanic crust created at fast- to intermediate- rate spreading centres Ann. Rev. Earth Planet Sci., v. 30, p. 347-384.

Kay, R., Hubbard, N.J., and Gast, P.W., 1970, Chemical Characteristics and Origin of Oceanic Ridge Volcanic Rocks1: J. Geophys. Res., v. 75, p. 1585-1613.

Kelemen, P.B., Hirth, G., Shimizu, N., Spiegelman, M., and Dick, H.J., 1997a, A review of melt migration processes in the adiabatically upwelling mantle beneath oceanic spreading ridges: Philosophical Transactions of the Royal Society of London. Series A: Mathematical, Physical and Engineering Sciences, v. 355, p. 283-318.

Kelemen, P.B., Koga, K., and Shimizu, N., 1997b, Geochemistry of gabbro sills in the crust-mantle transition zone of the Oman ophiolite: implications for the origin of the oceanic lower crust: Earth and Planetary Science Letters, v. 146, p. 475-488.

Kelemen, P.B., Shimizu, N., and Salters, V.J.M., 1995, Extraction of mid-ocean ridge basalt from the upwelling mantle by focused flow of melt in dunite channels: Nature, v. 375, p. 747-753.

Kennish, M.J., and Lutz, R.A., 1998, Morphology and distribution of lava flows on mid-ocean ridges: a review: Earth-Science Reviews, v. 43, p. 63-90.

Kushiro, I., 2001, Partial melting experiments on peridotite and origin of mid-ocean ridge basalt: Annual Review of Earth and Planetary Sciences, v. 29, p. 71-107.

Lackschewitz, K.S., Dehn, J., and Wallrabe-Adams, H.-J., 1994, Volcaniclastic sediments from mid-oceanic Kolbeinsey Ridge, north of Iceland: Evidence for submarine volcanic fragmentation processes: Geology, v. 22, p. 975-978.

Laughton, A., and Searle, R.C., 1979, Tectonic Processes on Slow Spreading Ridges, *in* Talwani, M., Harrison, C.G., and Hayes, D.E., eds., Deep drilling results in the Atlantic Ocean: ocean crust: Washington, American Geophysical Union, p. 431.

Lawson, K., Searle, R.C., Pearce, J.A., Browning, P., and Kempton, P., 1996, Detailed volcanic geology of the MARNOK area, Mid-Atlantic Ridge north of Kane transform: Geological Society, London, Special Publications, v. 118, p. 61-102.

Lawson, N.K., 1996, Crustal Accretion Near Ridge-Transform Intersections: Kane Fracture Zone, Mid-Atlantic Ridge: Durham, University of Durham.

LeBas, T.P., 2005, PRISM - Processing of Remotely-sensed Imagery for Seafloor Mapping - Version 4.0, Southampton, National Oceanography Centre.

Lin, J., and Parmentier, E.M., 1990, A Finite Amplitude Necking Model of Rifting in Brittle Lithosphere: J. Geophys. Res., v. 95, p. 4909-4923.

Lin, J., and Phipps Morgan, J., 1992, The Spreading-Rate Dependance of Three-Dimensional Mid-Ocean Ridge Gravity Structure: Geophysical Research Letters, v. 19, p. 13 - 16.

Lowrie, W., 1997, Fundamentals of Geophysics: Cambridge, Cambridge University Press, 354 p.

Macdonald, K.C., 1982, Mid-Ocean Ridges - Fine Scale Tectonic, Volcanic and Hydrothermal Processes within the Plate Boundary Zone: Annual Review of Earth and Planetary Sciences, v. 10, p. 155-190.

Macdonald, K.C., Fox, P.J., Perram, L.J., Eisen, M.F., Haymon, R.M., Miller, S.P., Carbotte, S.M., Cormier, M.H., and Shor, A.N., 1988, A new view of the mid-ocean ridge from the behaviour of ridge-axis discontinuities: Nature, v. 335, p. 217-225.

Macdonald, K.C., Scheirer, D.S., and Carbotte, S.M., 1991, Mid-Ocean Ridges: Discontinuities, Segments and Giant Cracks: Science, v. 253, p. 986-994.

MacLeod, C.J., Searle, R.C., Murton, B.J., Casey, J.F., Mallows, C., Unsworth, S.C., Achenbach, K.L., and Harris, M., 2009, Life cycle of oceanic core complexes: Earth and Planetary Science Letters, v. 287, p. 333-344.

Magde, L.S., Barclay, A.H., Toomey, D.R., Detrick, R.S., and Collins, J.A., 2000, Crustal magma plumbing within a segment of the Mid-Atlantic Ridge, 35 degrees N: Earth and Planetary Science Letters, v. 175, p. 55-67.

Magde, L.S., and Smith, D.K., 1995, Seamount volcanism at the Reykjanes Ridge - Relationship to the Iceland hot-spot Journal of Geophysical Research-Solid Earth, v. 100, p. 8449-8468.

Magde, L.S., Sparks, D.W., and Detrick, R.S., 1997, The relationship between buoyant mantle flow, melt migration, and gravity bull's eyes at the Mid-Atlantic Ridge between 33°N and 35°N: Earth and Planetary Science Letters, v. 148, p. 59-67.

Malin, M.C., 1980, Lengths of Hawaiian lava flows: Geology, v. 8, p. 306-308.

McDonald, M.A., Webb, S.C., Hildebrand, J.A., Cornuelle, B.D., and Fox, C.G., 1994, Seismic structure and anisotropy of the Juan de Fuca Ridge at 45°N: J. Geophys. Res., v. 99, p. 4857-4873.

McKenzie, D., and Bickle, M.J., 1988, The Volume and Composition of Melt Generated by Extension of the Lithosphere: Journal of Petrology, v. 29, p. 625-679.

McKenzie, D.P., and Parker, R.L., 1967, North Pacific - An example of tectonics on a sphere Nature, v. 216, p. 1476-&.

Mello, S.L.M., Cann, J.R., and Fowler, C.M.R., 1999, Anomalous mantle at 45 degrees N Mid-Atlantic Ridge?: Journal of Geophysical Research-Solid Earth, v. 104, p. 29335-29349.

Menard, H.W., 1960, East pacific Rise: Science, v. 132, p. 1737-1746.

Mendel, V., Sauter, D., Rommevaux-Jestin, C., Patriat, P., Lefebvre, F., and Parson, L.M., 2003, Magmato-tectonic cyclicity at the ultra-slow spreading Southwest Indian Ridge: Evidence from variations of axial volcanic ridge morphology and abyssal hills pattern: Geochemistry Geophysics Geosystems, v. 4.

Michael, P.J., and Bonatti, E., 1985, Peridotite composition from the North-Atlantic - Regional and tectonic variations and implications for partial melting Earth and Planetary Science Letters, v. 73, p. 91-104.

Mitchell, N.C., 2001, Transition from circular to stellate forms of submarine volcanoes: J. Geophys. Res., v. 106, p. 1987-2003.

Moore, J.G., 1975, Mechanism of Formation of Pillow Lava: Pillow lava, produced as fluid lava cools underwater, is the most abundant volcanic rock on earth, but only recently have divers observed it forming: American Scientist, v. 63, p. 269-277.

Moores, E.M., and Vine, F.J., 1971, The Troodos Massif, Cyprus and other Ophiolites as Oceanic Crust: Evaluation and Implications: Philosophical Transactions of the Royal Society of London. Series A, Mathematical and Physical Sciences, v. 268, p. 443-467.

Murton, B.J., and Parson, L.M., 1993, Segmentation, volcanism and deformation of oblique spreading centres - A quantitative study of the Reykjanes Ridge Tectonophysics, v. 222, p. 237-257.

Murton, B.J., Schroth, N., Le Bas, T.P., Van Calsteren, P., Searle, R.C., and Yeo, I., 2012, Formation of oceanic crust at slow spreading ridges by continuous Axial Volcanic Ridge processes: In prep, p. in prep.

Mutter, J.C., and Karson, J.A., 1992, Structural processes at slow-spreading ridges Science, v. 257, p. 627-634.

Neves, M.C., Bott, M.H.P., and Searle, R.C., 2004, Patterns of stress at midocean ridges and their offsets due to seafloor subsidence: Tectonophysics, v. 386, p. 223-242.

Nisbet, E.G., and Fowler, C.M.R., 1978, Mid-Atlantic Ridge at 37-degrees and 45-degrees N - Some geophysical and petrological constraints: Geophysical Journal of the Royal Astronomical Society, v. 54, p. 631-660.

Ondreas, H., Fouquet, Y., Voisset, M., and RadfordKnoery, J., 1997, Detailed study of three contiguous segments of the Mid-Atlantic Ridge, South of the Azores (37 degrees N to 38 degrees 30' N), using acoustic imaging coupled with submersible observations: Marine Geophysical Researches, v. 19, p. 231-255.

Orcutt, J.A., Kennett, B.L.N., and Dorman, L.M., 1976, Structure of East Pacific Rise from and ocean bottom seismometer survey Geophysical Journal of the Royal Astronomical Society, v. 45, p. 305-320.

Parson, L.M., 1993, Sidescan sonar and swath bathymetry investigation of the Reykjanes Ridge, southwest of Iceland, R/V Maurice Ewing EW9008 Cruise Report (unpublished).

Parson, L.M., Murton, B.J., Searle, R.C., Booth, D., Evans, J., Field, P., Keeton, J., Laughton, A., McAllister, E., Millard, N., Redbourne, L., Rouse, I., Shor, A., Smith, D., Spencer, S., Summerhayes, C., and Walker, C., 1993, En-echelon axial volcanic ridges at the Reykjanes Ridge- A life-cycle of volcanism and tectonics Earth and Planetary Science Letters, v. 117, p. 73-87.

Peirce, C., Gardiner, A., and Sinha, M., 2005, Temporal and spatial cyclicity of accretion at slow-spreading ridges - evidence from the Reykjanes Ridge: Geophysical Journal International, v. 163, p. 56-U31.

Peirce, C., and Navin, D.A., 2002, The RAMESSES experiment - V. Crustal accretion at axial volcanic ridge segments - a gravity study at 57 degrees 45 ' N on the slow spreading Reykjanes Ridge: Geophysical Journal International, v. 149, p. 76-94.

Peirce, C., Sinha, M., Topping, S., and Gill, C., 2007, Morphology and genesis of slow-spreading ridges - seabed scattering and seismic imaging within the oceanic crust: Geophysical Journal International, v. 168, p. 59-89.

Perfit, M.R., Cann, J.R., Fornari, D.J., Engels, J., Smith, D.K., Ian Ridley, W., and Edwards, M.H., 2003, Interaction of sea water and lava during submarine eruptions at mid-ocean ridges: Nature, v. 426, p. 62-65.

Perfit, M.R., and Chadwick, W., 1998, Magmatism an Mid-Ocean Ridges: Constraints from Volcanological and Geochemical Investigations, *in* Buck, R., ed., Faulting and Magmatism at Mid-Ocean Ridges, Americal Geophysical Union.

Phipps Morgan, J., and Ghen, Y.J., 1993, Dependence of ridge-axis morphology on magma supply and spreading rate: Nature, v. 364, p. 706-708.

Purdy, G.M., and Detrick, R.S., 1986, Crustal structure of the Mid-Atlantic Ridge at 23-degrees-N from seismic refraction studies Journal of Geophysical Research-Solid Earth and Planets, v. 91, p. 3739-3762.

Rabain, A., Cannat, M., Escartin, J., Pouliquen, G., Deplus, C., and Rommevaux-Jestin, C., 2001, Focused volcanism and growth of a slow spreading segment (Mid-Atlantic Ridge, 35 degrees N): Earth and Planetary Science Letters, v. 185, p. 211-224.

Ramberg, I.B., and Van Andel, T.H., 1977, Morphology and tectonic evolution of the rift valley at LAT 36DEGREES30'N, Mid-Atlantic Ridge Geological Society of America Bulletin, v. 88, p. 577-586.

Resing, J.A., Rubin, K.H., Embley, R.W., Lupton, J.E., Baker, E.T., Dziak, R.P., Baumberger, T., Lilley, M.D., Huber, J.A., Shank, T.M., Butterfield, D.A., Clague, D.A., Keller, N.S., Merle, S.G., Buck, N.J., Michael, P.J., Soule, A., Caress, D.W., Walker, S.L., Davis, R., Cowen, J.P., Reysenbach, A.L., and Thomas, H., 2011, Active submarine eruption of boninite in the northeastern Lau Basin: Nature Geoscience, v. 4, p. 799-806.

Rhodes, J.M., Morgan, C., and Liias, R.A., 1990, Geochemistry of Axial Seamount Lavas: Magmatic Relationship Between the Cobb Hotspot and the Juan de Fuca Ridge: J. Geophys. Res., v. 95, p. 12713-12733.

Salisbury, M.H., Stephen, R., Christensen, N.I., Franchet.J, Hamano, Y., Hobart, M., and Johnson, D., 1979, The physical state of the upper levels of cretaceous oceanic crust from the results of logging, laboratory studies and the oblique seismic experiment at DSDP sites 417 and 418, *in* Talwani, M., Harrison, C.G.A., and Hayes, D.E., eds., Deep drilling results in the Atlantic ocean: Ocean crust: Maurice Ewing Series: Washington, American Geophysical Union, p. 113 - 134.

Sauter, D., Parson, L., Mendel, V., Rommevaux-Jestin, C., Gomez, O., Briais, A., Mével, C., and Tamaki, K., 2002, TOBI sidescan sonar imagery of the very slow-spreading Southwest Indian Ridge: evidence for along-axis magma distribution: Earth and Planetary Science Letters, v. 199, p. 81-95.

Scheirer, D.S., Fornari, D.J., Humphris, S.E., and Lerner, S., 2000, High-resolution seafloor mapping using the DSL-120 sonar system: Quantitative assessment of sidescan and phase-bathymetry data from the Lucky Strike segment of the Mid-Atlantic Ridge: Marine Geophysical Researches, v. 21, p. 121-142.

Schilling, J.G., 1973, Iceland Mantle Plume: Geochemical Study of Reykjanes Ridge: Nature, v. 242, p. 565-571.

Schilling, J.G., Zajac, M., Evans, R., Johnston, T., White, W., Devine, J.D., and Kingsley, R., 1983, Petrologic and geochemical variations along the Mid-Atlantic Ridge from 29 degrees N to 73 degrees N: American Journal of Science, v. 283, p. 510-586.

Searle, R.C., Cowie, P.A., Mitchell, N.C., Allerton, S., MacLeod, C.J., Escartin, J., Russell, S.M., Slootweg, P.A., and Tanaka, T., 1998, Fault structure and detailed evolution of a slow spreading ridge segment: the Mid-Atlantic Ridge at 29 degrees N: Earth and Planetary Science Letters, v. 154, p. 167-183.

Searle, R.C., and Laughton, A.S., 1977, Sonar Studies of the Mid-Atlantic Ridge and Kurchatov Fracture Zone: J. Geophys. Res., v. 82, p. 5313-5328.

Searle, R.C., Murton, B.J., Achenbach, K., LeBas, T., Tivey, M., Yeo, I., Cormier, M.H., Carlut, J., Ferreira, P., Mallows, C., Morris, K., Schroth, N., van Calsteren, P., and Waters, C., 2010, Structure and development of an axial volcanic ridge: Mid-Atlantic Ridge, 45°N: Earth and Planetary Science Letters, v. 299, p. 228-241.

Searle, R.C., Murton, B.J., and Shipboard Scientific Party, 2008, Cruise Report: The Axial Volcanic Ridge of the Mid-Atlantic Ridge, 45º30'N, p. 134.

Searle, R.C., and Whitmarsh, R.B., 1978, The structure of King's Trough, Northeast Atlantic, from bathymetric, seismic and gravity studies: Geophysical Journal International, v. 53, p. 259-287.

Sempere, J.C., Lin, J., Brown, H.S., Schouten, H., and Purdy, G.M., 1993, Segmentation and morphotectonic variations along a slow-spreading centre - the Mid-Atlantic Ridge (24-DEGREES-00'N-30-DEGREES-40'N): Marine Geophysical Researches, v. 15, p. 153-200.

Shaw, P.R., 1992, Ridge segmentation, faulting and crustal thickness in the Atlantic Ocean: Nature, v. 358, p. 490-493.

Shaw, P.R., and Lin, J., 1993, Causes and Consequences of Variations in Faulting Style at the Mid-Atlantic Ridge: J. Geophys. Res., v. 98, p. 21839-21851.

Singh, S.C., Crawford, W.C., Carton, H., Seher, T., Combier, V., Cannat, M., Canales, J.P., Dusunur, D., Escartin, J., and Miranda, J.M., 2006, Discovery of a magma chamber and faults beneath a Mid-Atlantic Ridge hydrothermal field: Nature, v. 442, p. 1029-1032.

Sinha, M.C., Constable, S.C., Peirce, C., White, A., Heinson, G., MacGregor, L.M., and Navin, D.A., 1998, Magmatic processes at slow spreading ridges: implications of the RAMESSES experiment at 57 degrees 45 ' N on the Mid-Atlantic Ridge: Geophysical Journal International, v. 135, p. 731-745.

Sinha, M.C., Navin, D.A., MacGregor, L.M., Constable, S., Peirce, C., White, A., Heinson, G., and Inglis, M.A., 1997, Evidence for accumulated melt beneath the slow-spreading Mid-Atlantic ridge: Philosophical Transactions of the Royal Society of London Series a-Mathematical Physical and Engineering Sciences, v. 355, p. 233-253.

Sinton, J., Bergmanis, E., Rubin, K., Batiza, R., Gregg, T.K.P., Gronvold, K., Macdonald, K.C., and White, S.M., 2002, Volcanic eruptions on mid-ocean ridges: New evidence from the superfast spreading East Pacific Rise, 17 degrees-19 degrees S: Journal of Geophysical Research-Solid Earth, v. 107.

Sinton, J.M., and Detrick, R.S., 1992, Midocean ridge magma chambers Journal of Geophysical Research-Solid Earth, v. 97, p. 197-216.

Sleep, N.H., 1969, Sensitivity of Heat Flow and Gravity to the Mechanism of Sea-Floor Spreading: J. Geophys. Res., v. 74, p. 542-549.

—, 1975, Formation of oceanic crust - Some thermal constraints Journal of Geophysical Research, v. 80, p. 4037-4042.

Sleep, N.H., and Rosendahl, B.R., 1979, Topography and Tectonics of Mid-Oceanic Ridge Axes: J. Geophys. Res., v. 84, p. 6831-6839.

Small, C., 1998, Global Systematics of Mid-Ocean Ridge Morphology, *in* Buck, R., Delaney, J.R., Karson, J.A., and Lagabrielle, Y., eds., Faulting and magmatism at mid-oean ridges: Geophysical Monograph: Washington, Americal Geophysical Union, p. 348.

Smith, D.K., and Cann, J.R., 1990, Hundreds of small volcanoes on the median valley floor of the Mid-Atlantic Ridge at 24-30[deg] N: Nature, v. 348, p. 152-155.

—, 1992, The role of seamount volcanism in crustal construction and the Mid-Atlantic Ridge (24-degrees-30-degrees-N) Journal of Geophysical Research-Solid Earth, v. 97, p. 1645-1658.

—, 1993, Building the crust at the Mid-Atlantic Ridge Nature, v. 365, p. 707-715.

—, 1999, Constructing the upper crust of the Mid-Atlantic Ridge: A reinterpretation based on the Puna Ridge, Kilauea Volcano: Journal of Geophysical Research-Solid Earth, v. 104, p. 25379-25399.

Smith, D.K., Cann, J.R., Dougherty, M.E., Lin, J., Spencer, S., Macleod, C., Keeton, J., McAllister, E., Brooks, B., Pascoe, R., and Robertson, W., 1995a, Mid-Atlantic Ridge volcanism from deep-towed side-scan sonar images, 25-degrees-29degrees-N Journal of Volcanology and Geothermal Research, v. 67, p. 233-262.

Smith, D.K., Humphris, S.E., and Bryan, W.B., 1995b, A comparison of volcanic edifices at the Reykjanes Ridge and the Mid-Atlantic Ridge at 24-degrees-30degrees-N Journal of Geophysical Research-Solid Earth, v. 100, p. 22485-22498.

Sohn, R.A., Willis, C., Humphris, S., Shank, T.M., Singh, H., Edmonds, H.N., Kunz, C., Hedman, U., Helmke, E., Jakuba, M., Liljebladh, B., Linder, J., Murphy, C., Nakamura, K.I., Sato, T., Schlindwein, V., Stranne, C., Tausenfreund, M., Upchurch, L., Winsor, P., Jakobsson, M., and Soule, A., 2008, Explosive volcanism on the ultraslow-spreading Gakkel ridge, Arctic Ocean: Nature, v. 453, p. 1236-1238.

Stakes, D.S., Shervais, J.W., and Hopson, C.A., 1984, The volcanic-tectonic cycle of the FAMOUS and AMAR valleys, Mid-Atlantic Ridge (36-degrees-47'N) - Evidence from basalt glass and phenocryst compositional variations for a steady-state magma chamber beneath the valley midsections, AMAR-3 Journal of Geophysical Research, v. 89, p. 6995-7028.

Sun, S.-S., Nesbitt, R.W., and Sharaskin, A.Y., 1979, Geochemical characteristics of mid-ocean ridge basalts: Earth and Planetary Science Letters, v. 44, p. 119-138.

Swift, S., Reichow, M., Tikku, A., Tominaga, M., and Gilbert, L., 2008, Velocity structure of upper ocean crust at Ocean Drilling Program Site 1256: Geochemistry Geophysics Geosystems, v. 9, p. Q10O13.

Tapponnier, P., and Francheteau, J., 1978, Necking of the Lithosphere and the Mechanics of Slowly Accreting Plate Boundaries: J. Geophys. Res., v. 83, p. 3955-3970.

Tominaga, M., and Umino, S., 2010, Lava deposition history in ODP Hole 1256D: Insights from log-based volcanostratigraphy: Geochemistry Geophysics Geosystems, v. 11, p. Q05003.

Toomey, D.R., Purdy, G.M., Solomon, S.C., and Wilcock, W.S.D., 1990, The three-dimensional seismic velocity structure of the East Pacific Rise near latitude 9°30′N: Nature, v. 347, p. 639–645.

Tucholke, B.E., Behn, M.D., Buck, W.R., and Lin, J., 2008, Role of melt supply in oceanic detachment faulting and formation of megamullions: Geology, v. 36, p. 455-458.

Tucholke, B.E., and Lin, J., 1994, A geological model for the structure of ridge segments in slow-spreading ocean crust Journal of Geophysical Research-Solid Earth, v. 99, p. 11937-11958.

Tucholke, B.E., Lin, J., Kleinrock, M.C., Tivey, M.A., Reed, T.B., Goff, J., and Jaroslow, G.E., 1997, Segmentation and crustal structure of the western Mid-Atlantic Ridge flank, 25°25 - 27°10 N and 0 - 29 m.y.: J. Geophys. Res., v. 102, p. 10203-10223.

Turcotte, D.L., and Ahern, J.L., 1978, A Porous Flow Model for Magma Migration in the Asthenosphere: J. Geophys. Res., v. 83, p. 767-772.

Vine, F.J., and Matthews, D.H., 1963, Magnetic Anomalies Over Oceanic Ridges: Nature, v. 199, p. 947-949.

Walker, G.P.L., Huntingdon, A.T., Sanders, A.T., and Dinsdale, J.L., 1973, Lengths of Lava Flows [and Discussion]: Philosophical Transactions of the Royal Society of London. Series A, Mathematical and Physical Sciences, v. 274, p. 107-118.

White, W.M., and Schilling, J.-G., 1978, The nature and origin of geochemical variation in Mid-Atlantic Ridge basalts from the Central North Atlantic: Geochimica et Cosmochimica Acta, v. 42, p. 1501-1516.

Wilson, J.T., 1965, A new class of faults and their bearing on continental drift Nature, v. 207, p. 343-&.

Wilson, M., 1989, Igneous Petrogenesis: London, Unwin Hyman.

Wylie, J.J., Helfrich, K.R., Dade, B., Lister, J.R., and Salzig, J.F., 1999, Flow localization in fissure eruptions: Bulletin of Volcanology, v. 60, p. 432-440.

1.5 Figures

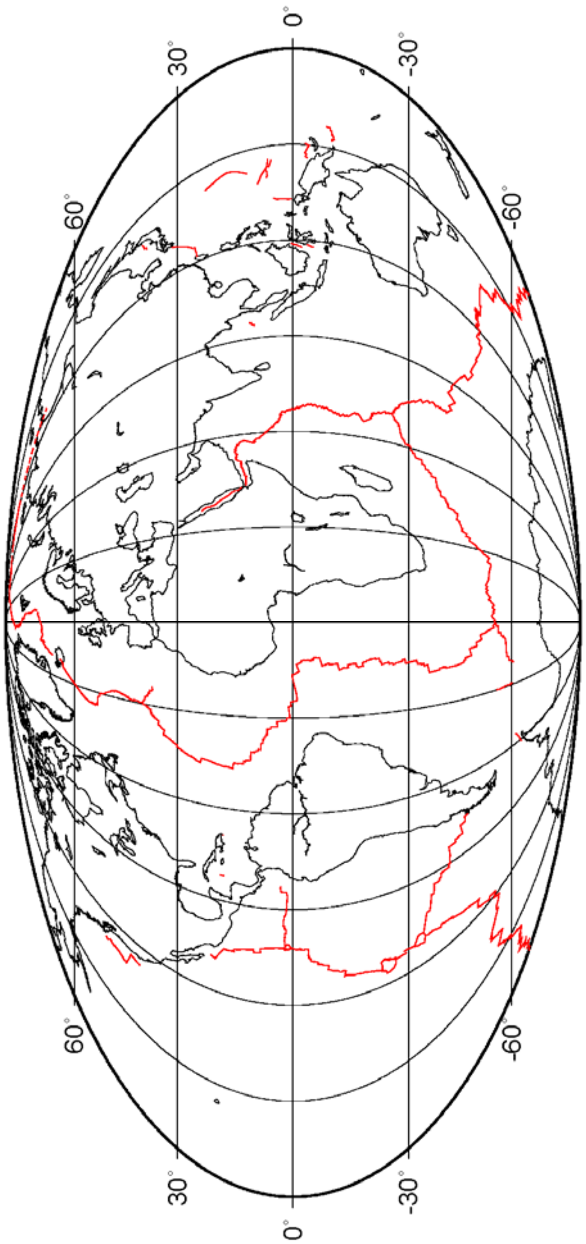

Figure 1.1: Global map of mid-ocean ridges (in red).

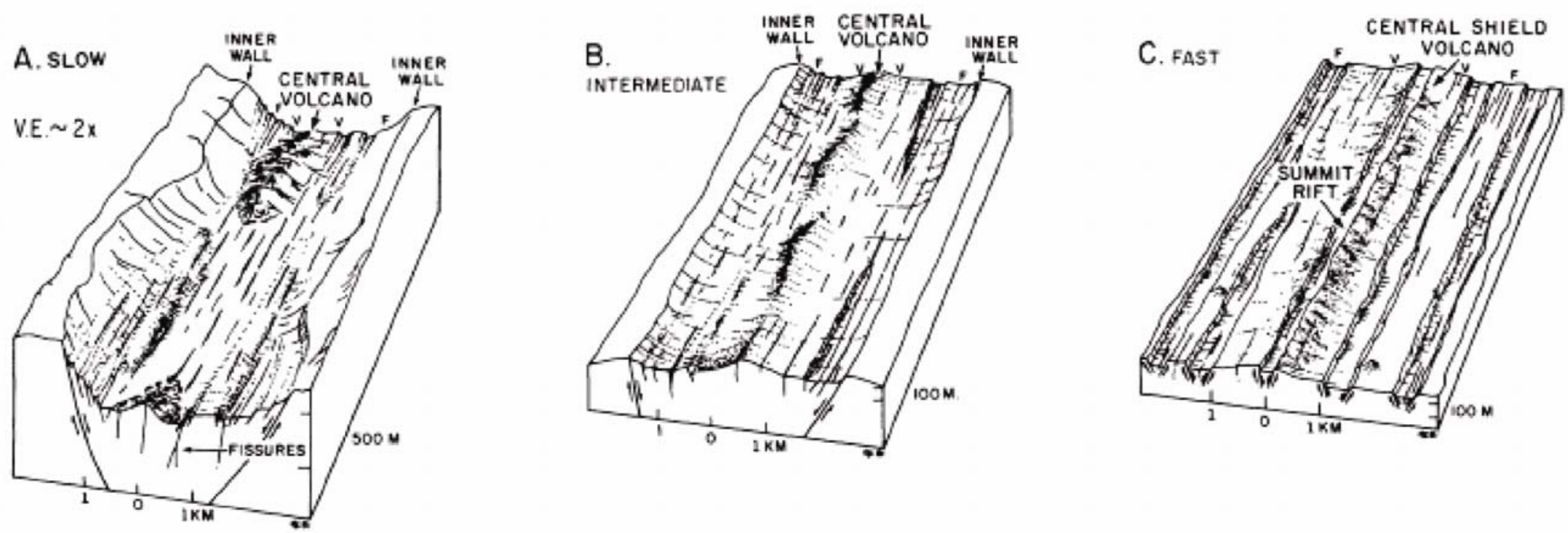

Figure 1.2: Schematic illustrations of the ridge axis and neovolcanic zone at (A) Slow –spreading (B) Intermediate –spreading and (C) fast –spreading rates, from Macdonald (1982). The central volcano is discontinuous at slow-spreading ridges, become more continuous with increasing spreading rate. In contrast, the axial valley is best developed t slow rates, and is replaced by an axial high at fast-spreading.

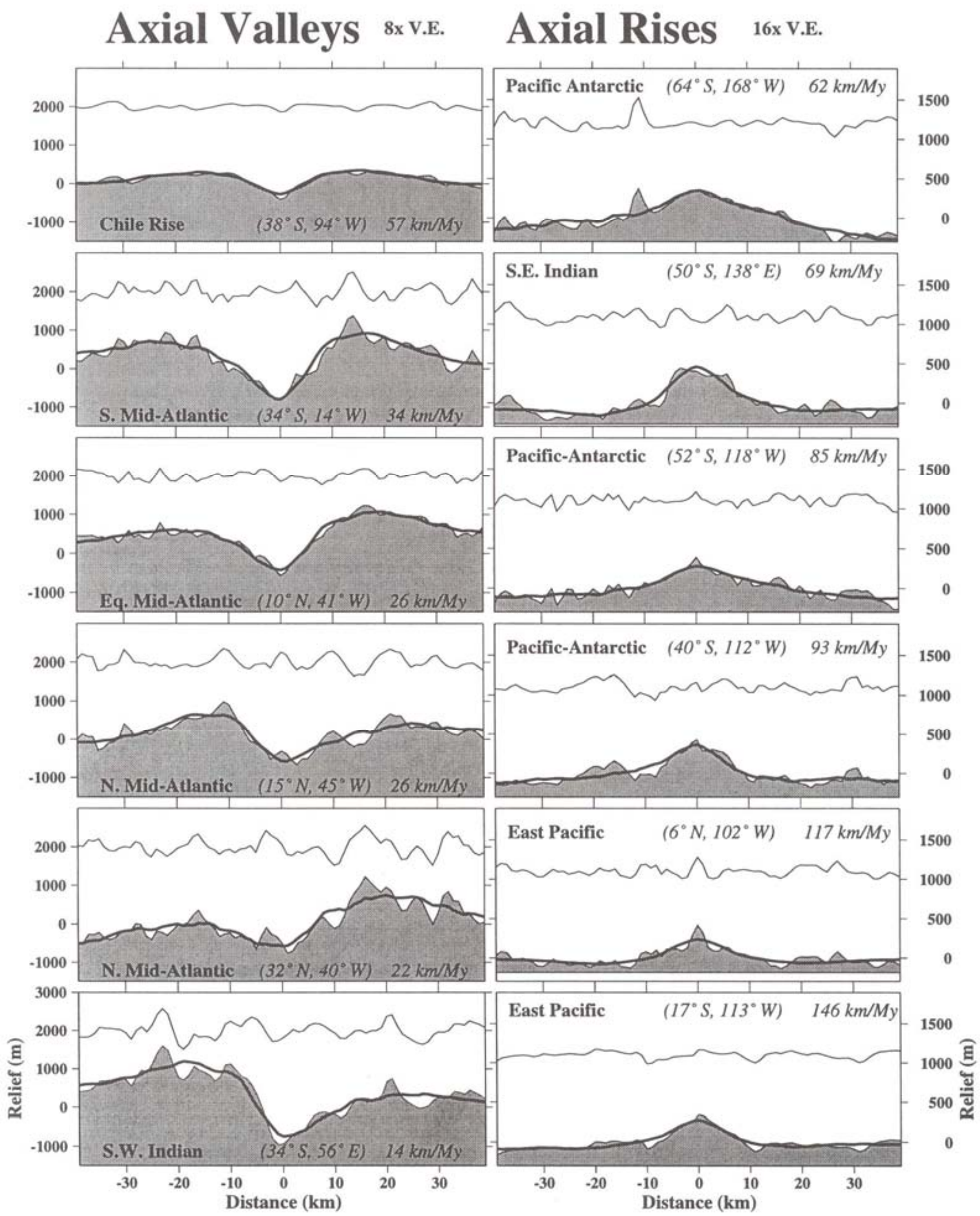

Figure 1.3: Examples of profiles of mid-ocean ridges at a range of slow – and fast – spreading rates from Small (1998). These profiles clearly illustrate the different typical profiles for fast – and alow – spreading ridges, with all theose spreading at rates < 57 km/my (5.7 cm/yr) displaying axial valleys superimposed on a broad high and those at faster spreading rates just showing the broad high. Axial valleys and axial rises are shown at different vertical exaggeration. The heavy curve is the deterministic component of the topography (roughly described as an averaged profile) and the paler line is the stochastic component (representing the changes in topography above or below the deterministic component. The deterministic component + the stochastic component = bathymetry.

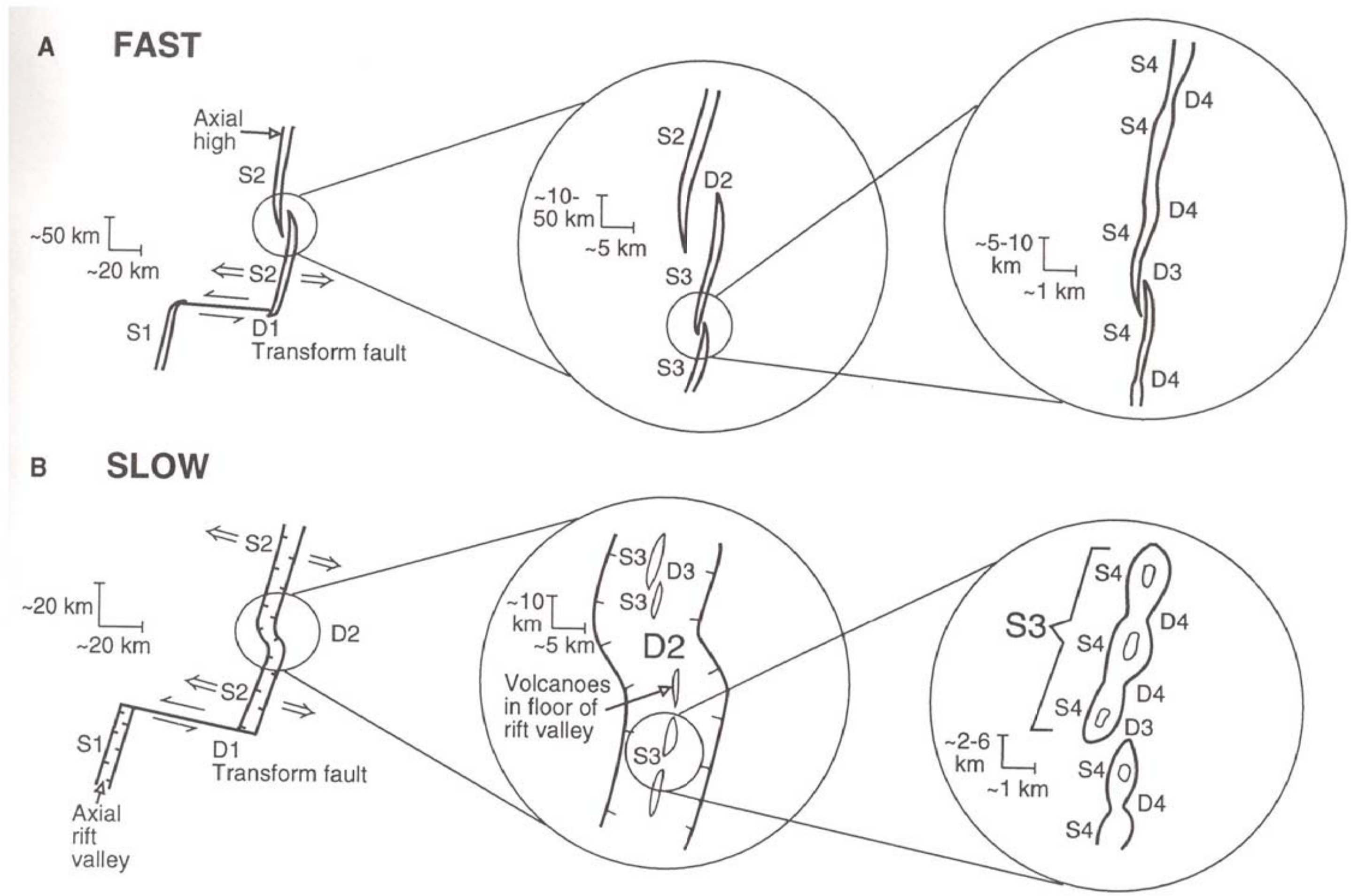

Figure 1.4: The hierarchy of ridge segmentation at (A) fast and (B) slow – spreading ridges from Macdonald (1998) (after Macdonald et al. (Cannat et al., 2006; 1991)). S1 – S$ are ridge segments of order 1 – 4 and D1 – D4 are ridge axis discontinuities of order 1 – 4. First order discontinuities are transform faults. Second order discontinuities may be overlapping spreading centres at fast spreading ridges, or oblique shear zones on slow-spreading ridges. Third order discontinuities are small overlapping spreading centres on fast-spreading ridges. Fourth order discontinuities are slight bends or deviations in the strike of the segment of less than 1 km.

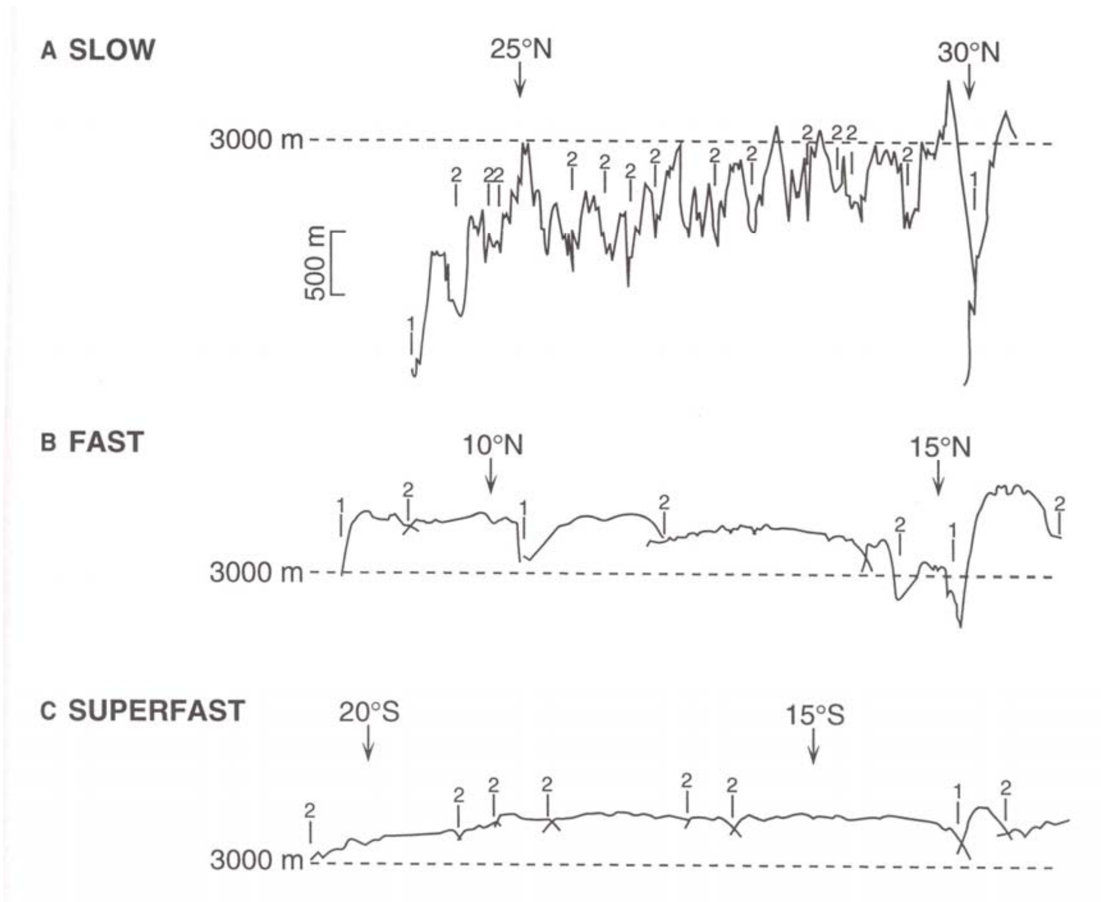

Figure 1.5: Axial depth profiles for (A) slow-spreading, (B) fast-spreading and (C) ultrafast-spreading ridges from Macdonald (1991). Order 1 (transform faults) and 2 (diffuse zones of faulting and extension) discontinuities are marked and typically cause a deepening of the topography. The segments at fast and ultrafast spreading ridges are smoother and interrupted less frequently by discontinuities than those at slow-spreading ridges.

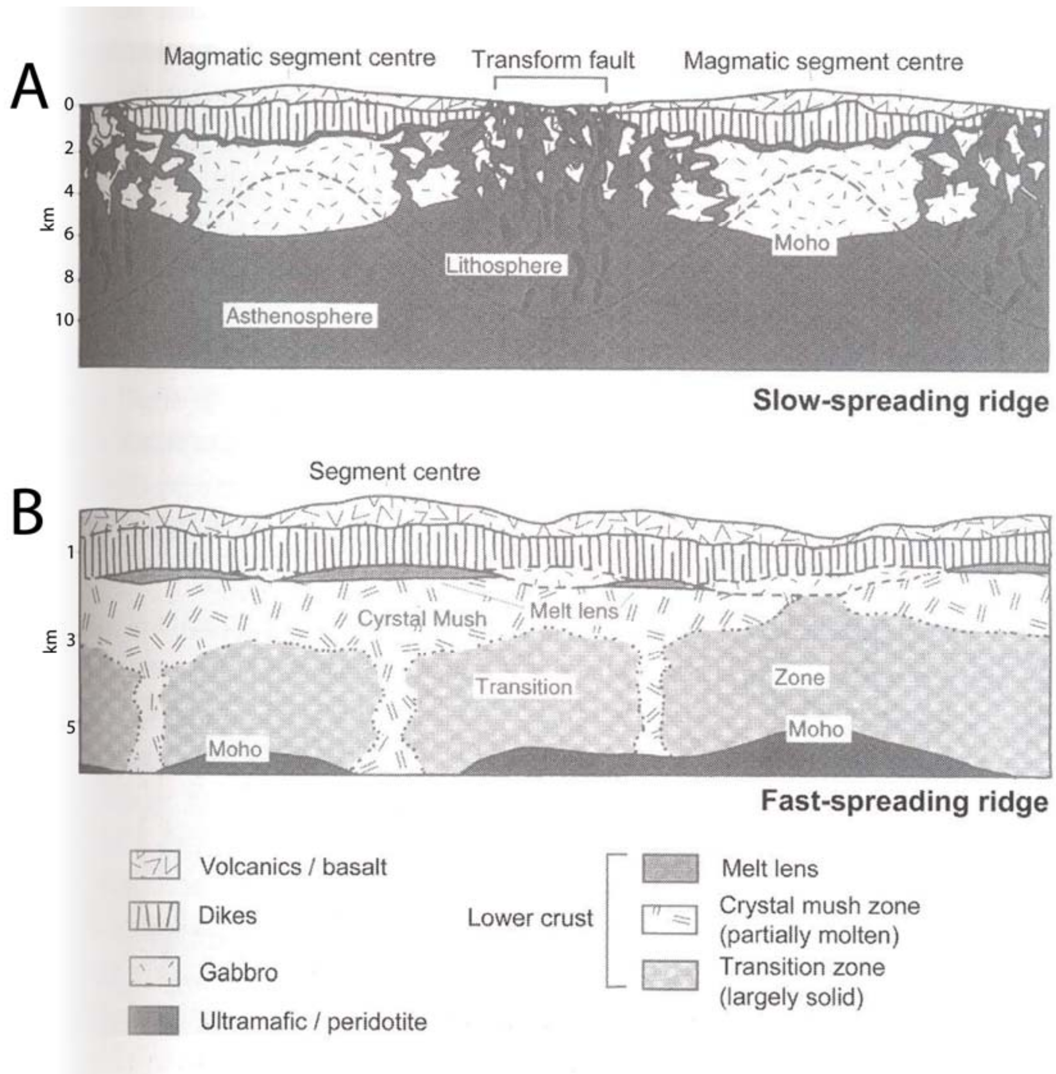

Figure 1.6: Along axis profiles of slow-spreading crust (A) and fast-spreading crust (B)showing crustal thickness variations along axis. Modified from Cannat et al. (1997) and Sinton and Detrick (1992) in Dilek at al. (1998)

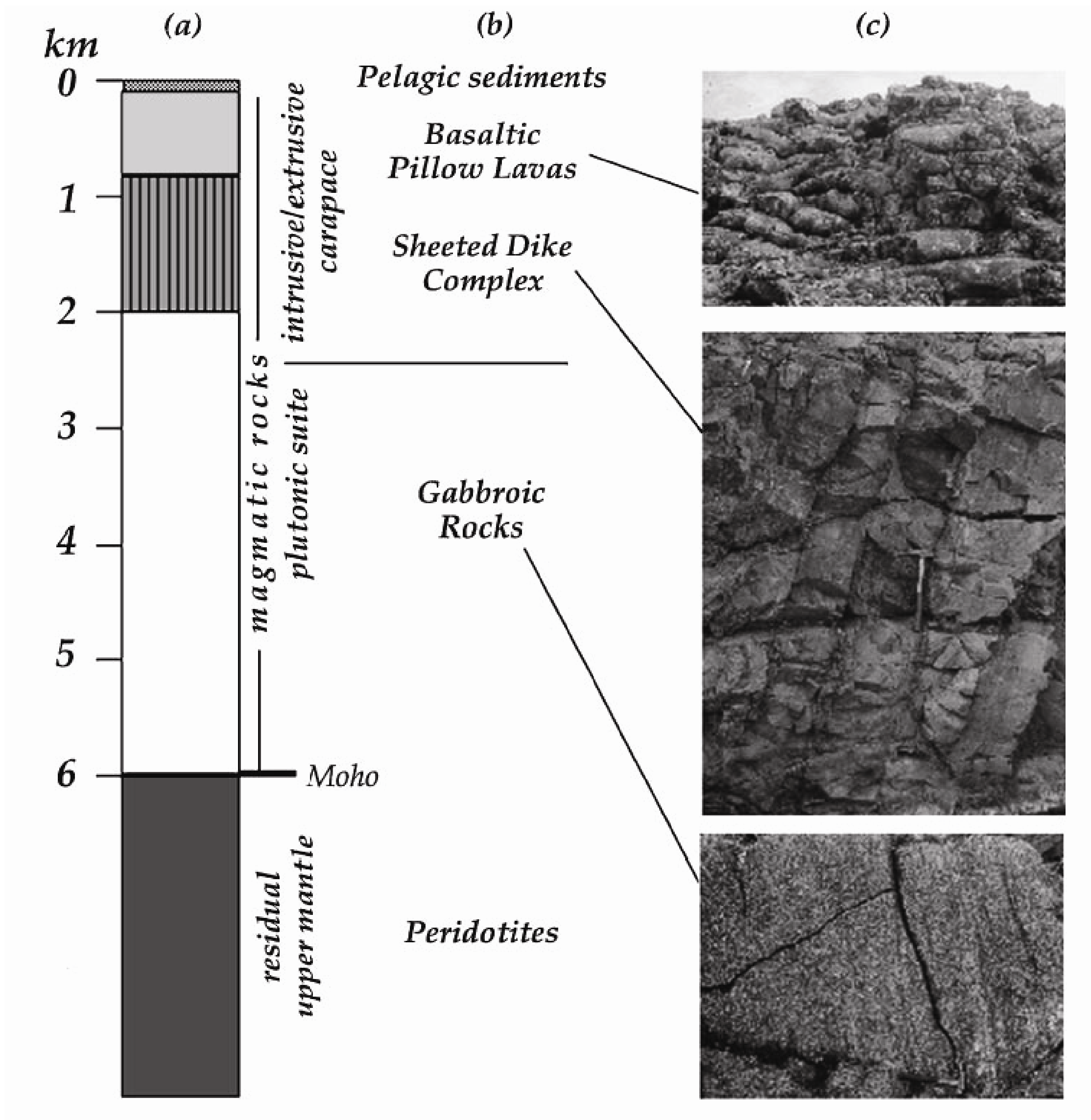

Figure 1.7: Oceanic crustal section from Karson et al. (2002). Section (a) shows the generalized internal structure, (b) the interpretation of oceanic crust from ophiolite complexes and (c) outcrop photos from ophiolites. For seismic layering refer to figure 5.

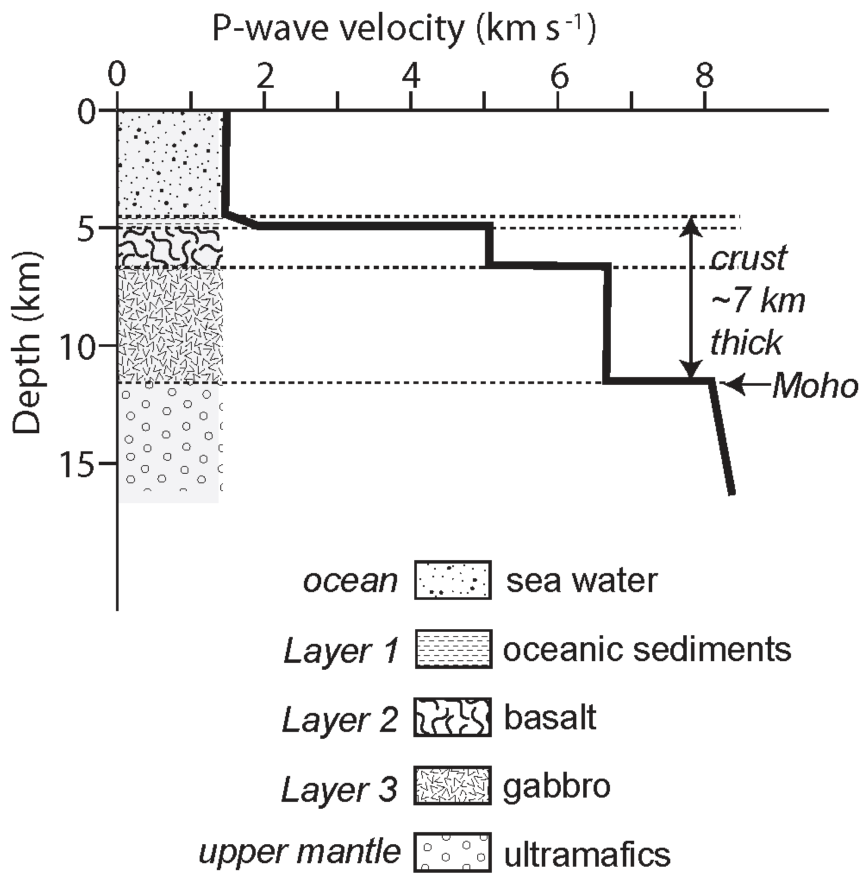

Figure 1.8: Model of P-wave velocity against depth for a generalized oceanic crustal section. Redrawn from Lowrie (1997) p157.

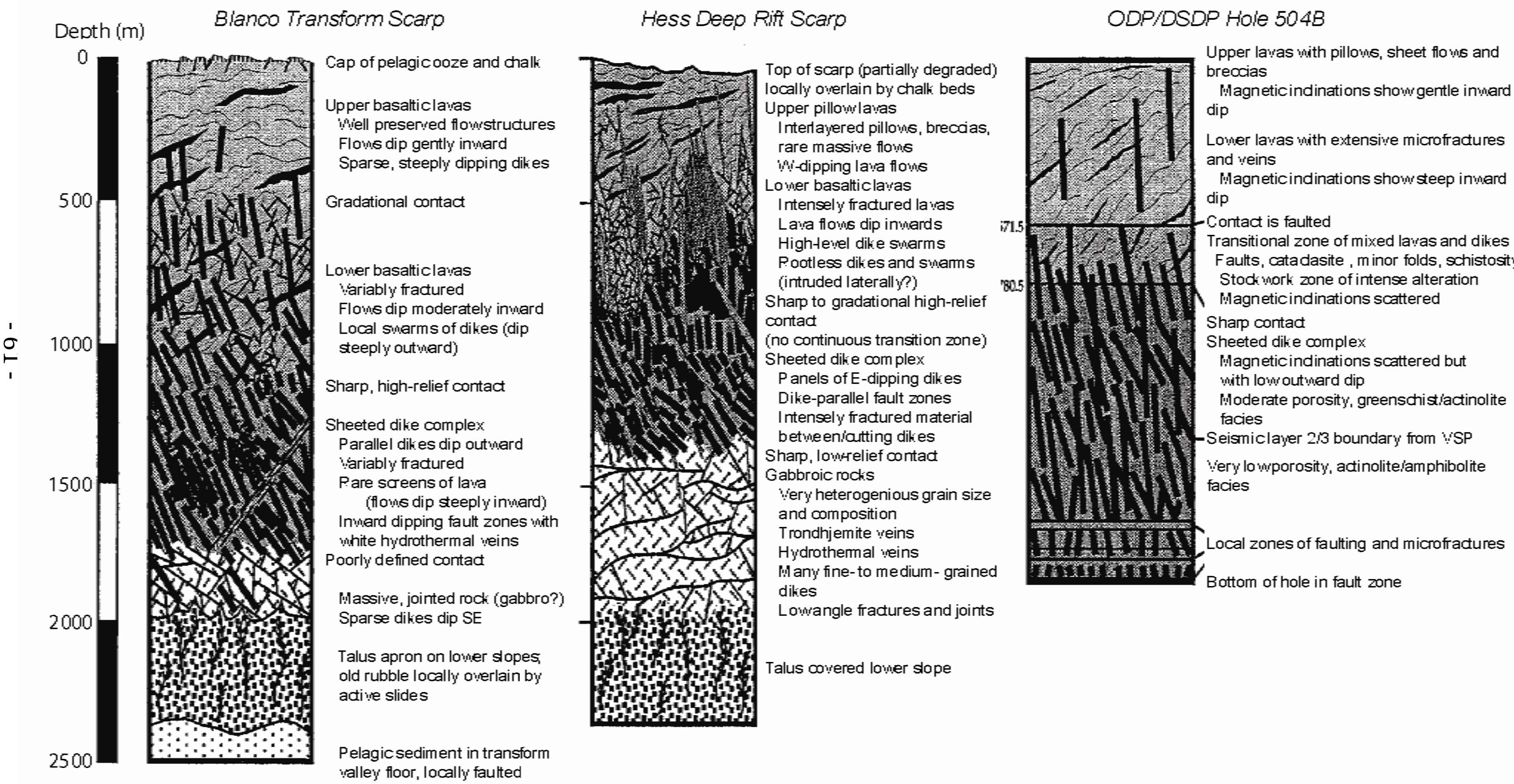

Figure 1.9: Detailed structure of the upper oceanic crust at The Blanco Transform Scarp spreading half rate of 30 mm/yr at the Juan de Fuca Ridge), Hess Deep (spreading half rate of 66 mm/yr at the EPR) and DSDP/ODP hole 504B (spreading rate 36 mm/yr at the Cost Rica Rift) from Karson (2002). Note the generalized geological structure of the crust is similar in all three sections despite differences in spreading rate and history.

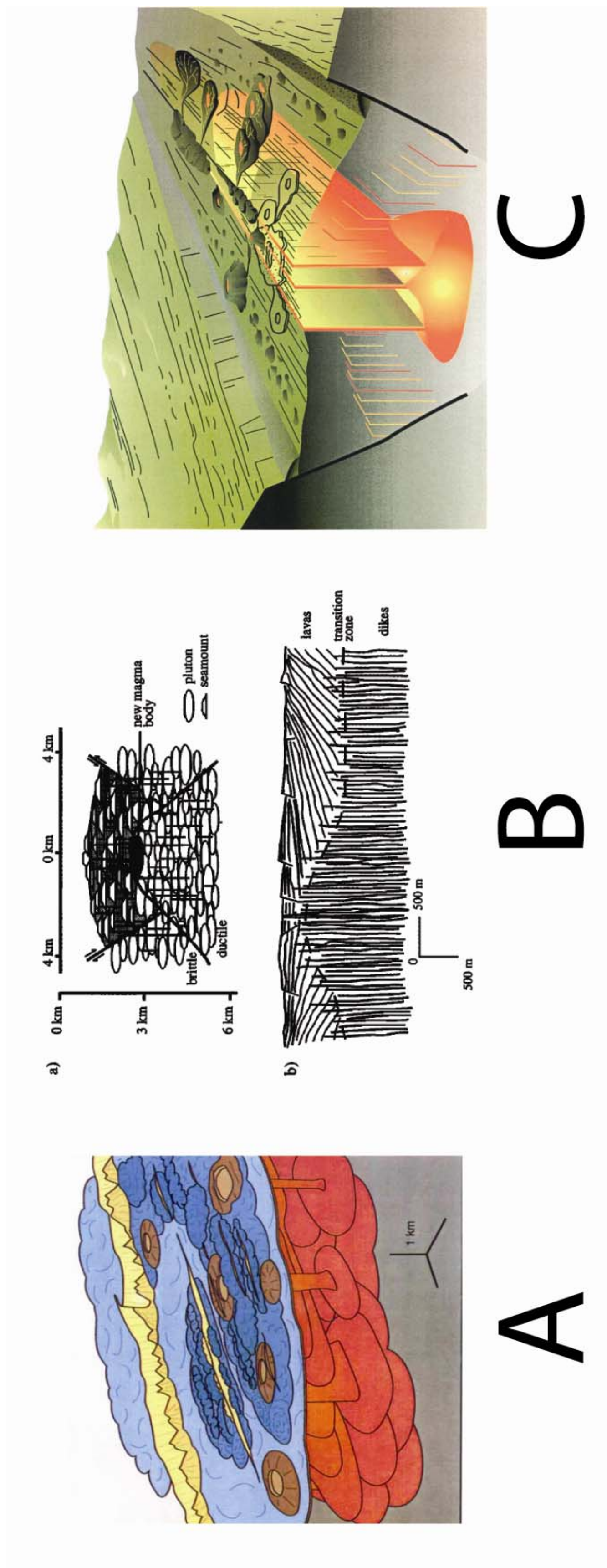

Figure 1.10: Models for crustal accretion and structure at slow spreading ridges from (A) Smith and Cann (1993), (B) Smith and Cann (1992), and (C) Smith and Cann (1999). They show a crustal section where the extrusive volcanics are fed by dykes connecting a host of small, ephemeral magma chambers, trapped at the brittle ductile transition to the surface.

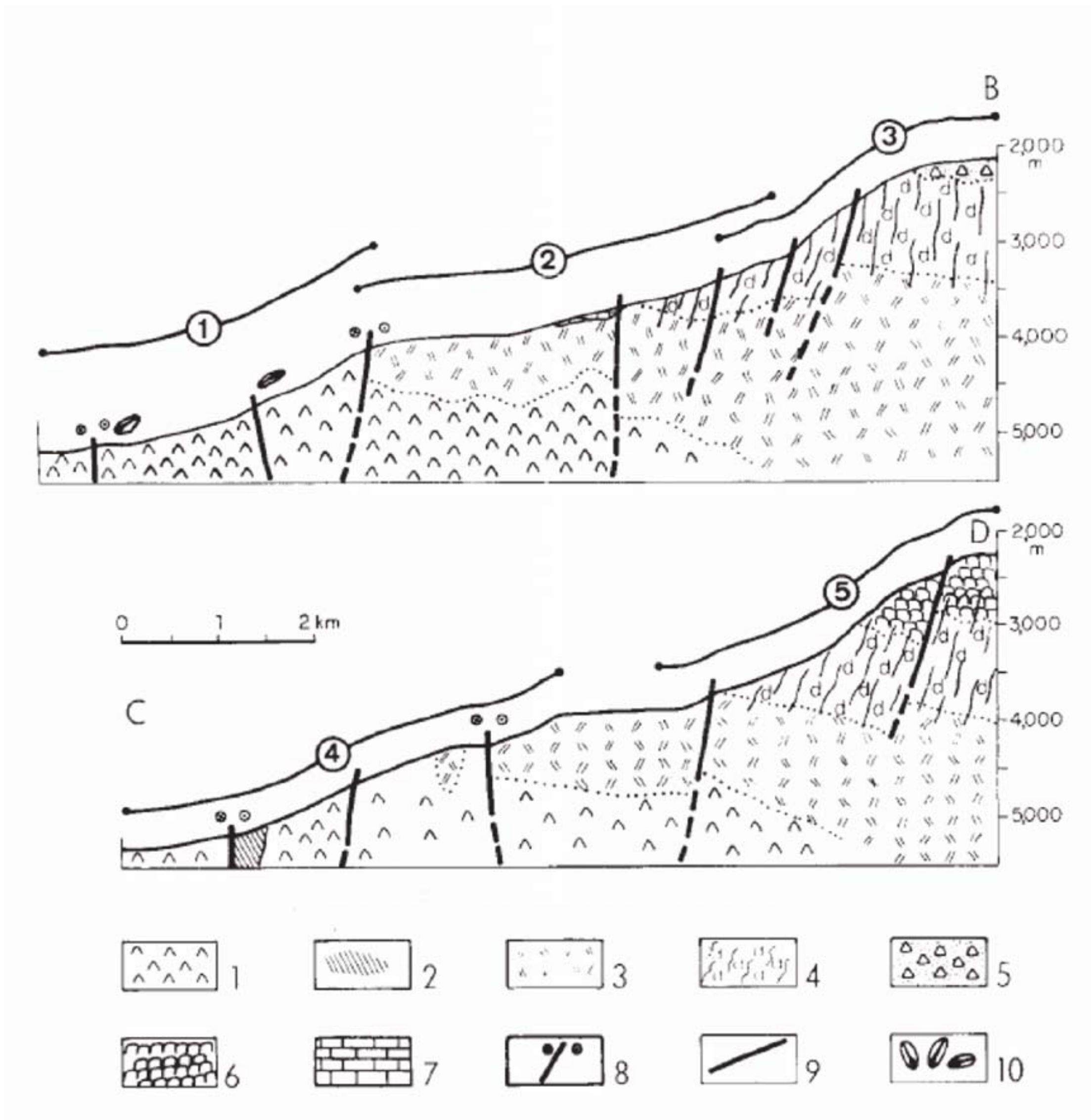

Figure 1.11: Observed slow-spreading crustal section from Vema transform, from Auzende et al., (1989). Synthetic geological sections A – B and C – D. 1: Serpentinites, 2: Amphibolites, 3: Gabbros, 4: Dykes, 5: Basalt Pavements, 6: Pillows, 7: Indurated Sediments, 8: Strike-Slip Faults, 9: Normal Faults, 10: Clams

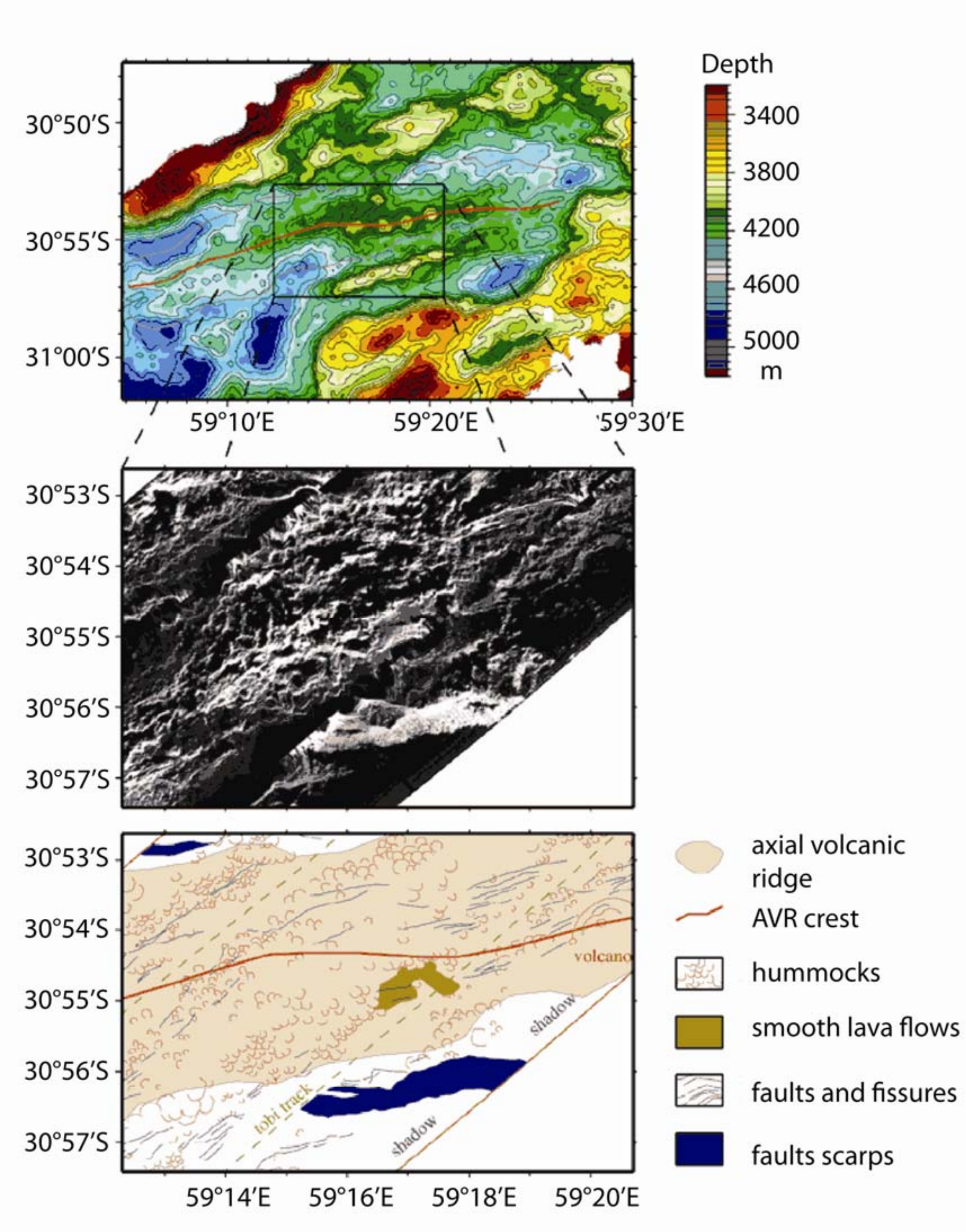

Figure 1.12: An example of a robust AVR on the ultraslow-spreading Southwest Indian Ridge, from Mendel et al. (2003). The top map shows the bathymetry, the central panel shows TOBI sidescan sonar and the bottom panel shows geological interpretation.

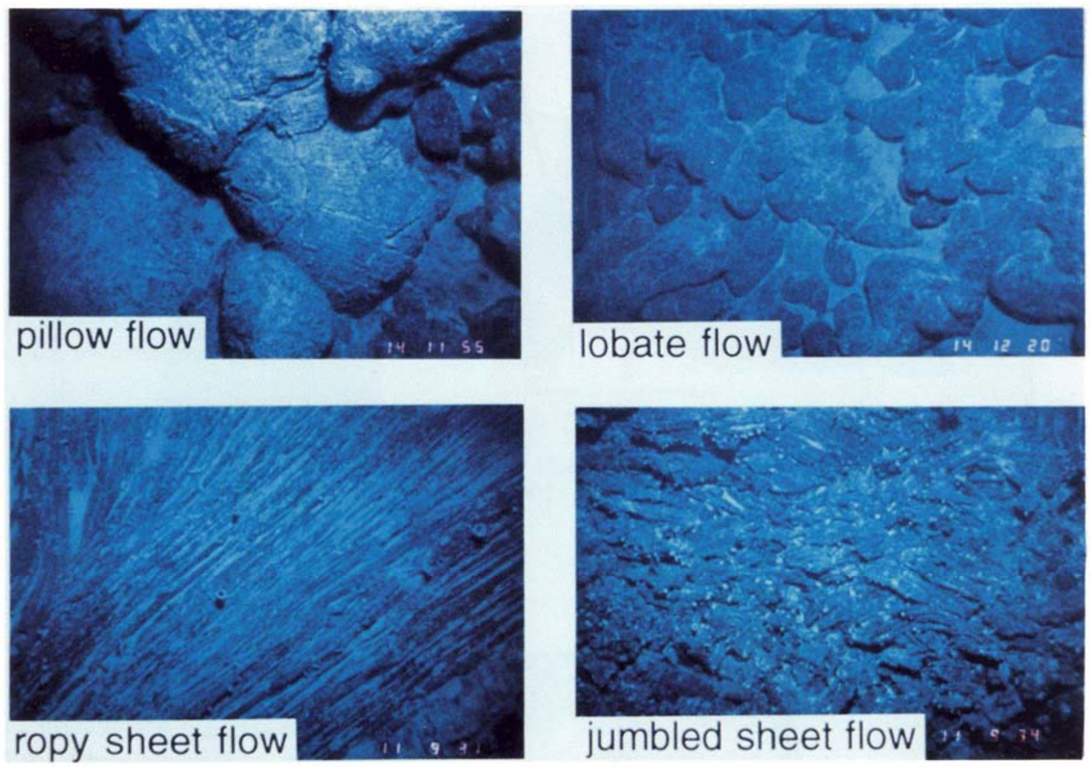

Figure 1.13: Main lava lithologies observed on mid-ocean ridges adapted from Fox et al. (1988) in Perfit and Chadwick (1998).

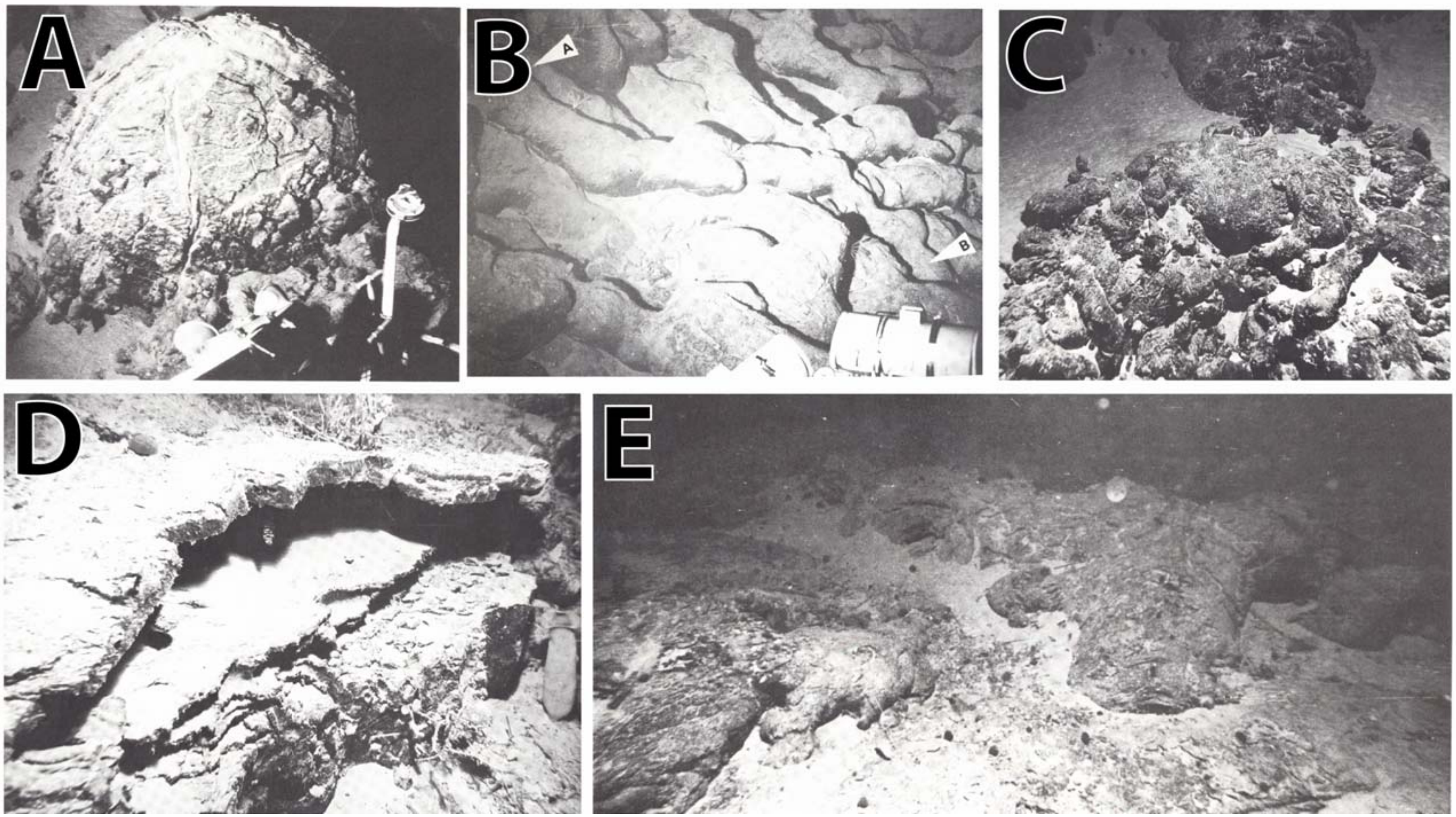

Figure 1.14: Pillow lava types from Ballard and Moore (1977; Hess, 1962). A: a bulbous pillow, B: elongate pillow lavas, C: decorated or knobby pillow, D: hollow pillow showing shelves of previous lava levels, E: flattened pillows

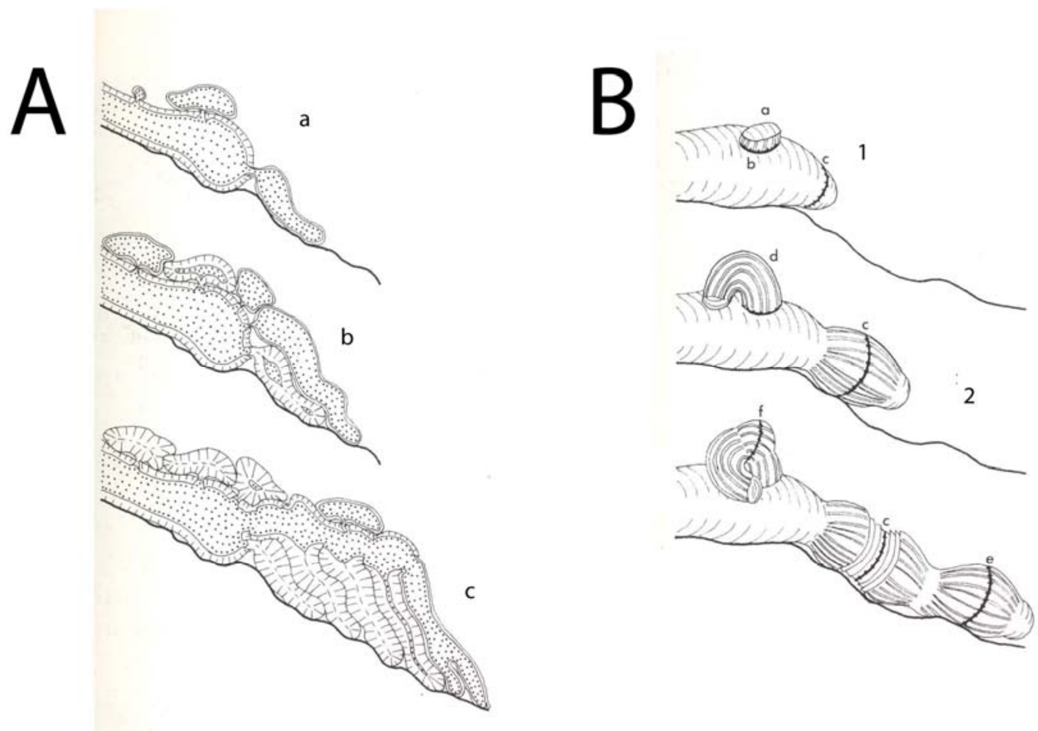

Figure 1.15: Diagrams showing (A) formation of pillow lavas on an irregular slope and (B) the interconnected nature of pillows and development of common features of pillowed crust. From Ballard and Moore (1997). The left hand panel (A) shows three stages of forest pillow development: (a) the lobe travelling downslope inflates, ruptures and feeds a small pillow which drapes the slope, (b) this original pillow inflates, cools and dams the flow, causing the flow lobe to rupture again feeding a second pillow. This repeats producing more pillows, which drape over the first pillow, creating a near horizontal surface on which more bulbous pillows develop, (c) these more bulbous pillows form a feeding channel near the top of the flow which feeds pillows further downslope. The right hand panel (B) shows: (1) a large pillow lobe fed from a flow ruptures along a ring fracture forming a trapdoor pillow, (2) continued extrusion from this ring crack produces a toothpaste pillow, while the original pillow lobe cracks and spreading is accommodated on this crack, causing development of a corrugated surface, (3) as lava continues to flow into the lobe it may fracture again, producing a new corrugated section and slowing expansion at the first crack which will produce a more faulted, constricted surface. Fault slivers are produced parallel to the crack and are shown by the letter c in diagrams B2 and B3.The toothpaste pillow may also crack and expand. This process of cracking and extension of pillows produces the typical 'neck and knob' pillow lithology commonly observed.

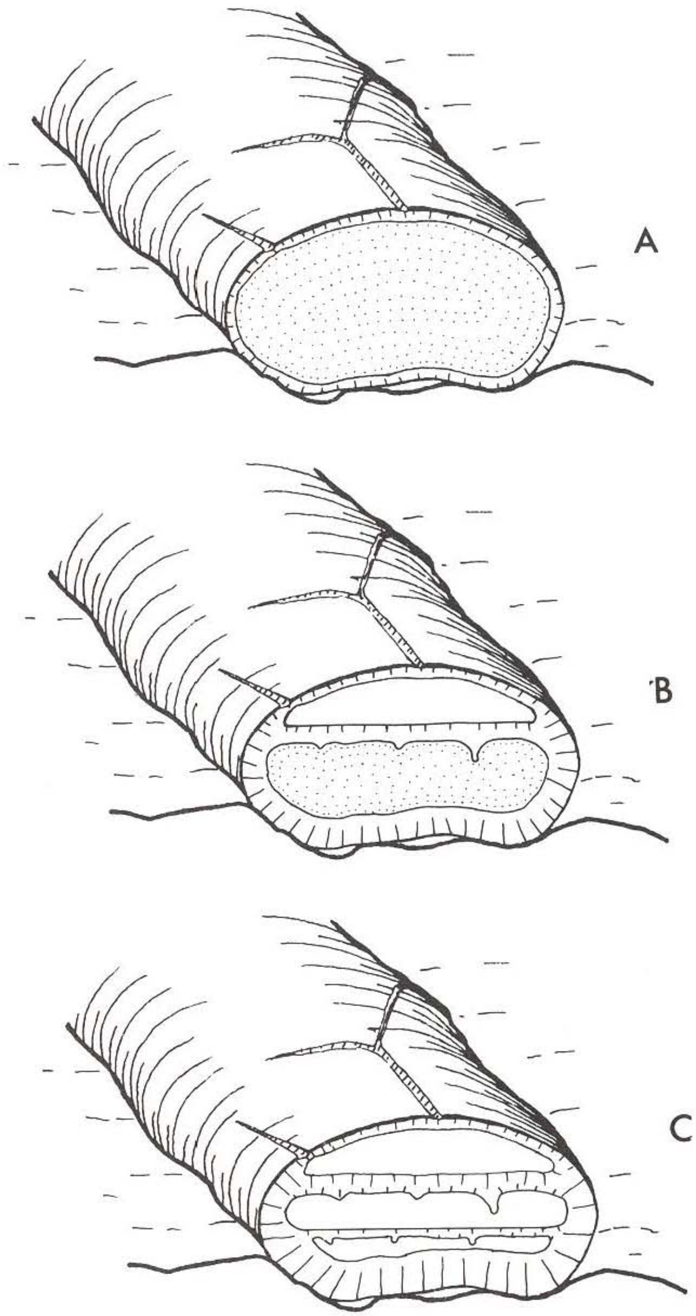

Figure 1.16: Sketch showing development of shelves in a pillow from Ballard and Moore (1977). (A) An elongate pillow filled with molten lava (dotted) and a solidified thin outer crust. (B) The lava level in the pillow drops due to a reduction in magma flux and water enters the space created, causing the upper surface of this new lave level to solidify. Further chilling of the lava through the pillow wall thickens the pillow crust below this level. (C) Further drops in lava level and subsequent filling with water create a number of shelves. If lava level drops quickly enough small drips (septa) may be left hanging from the lower surface of shelves.

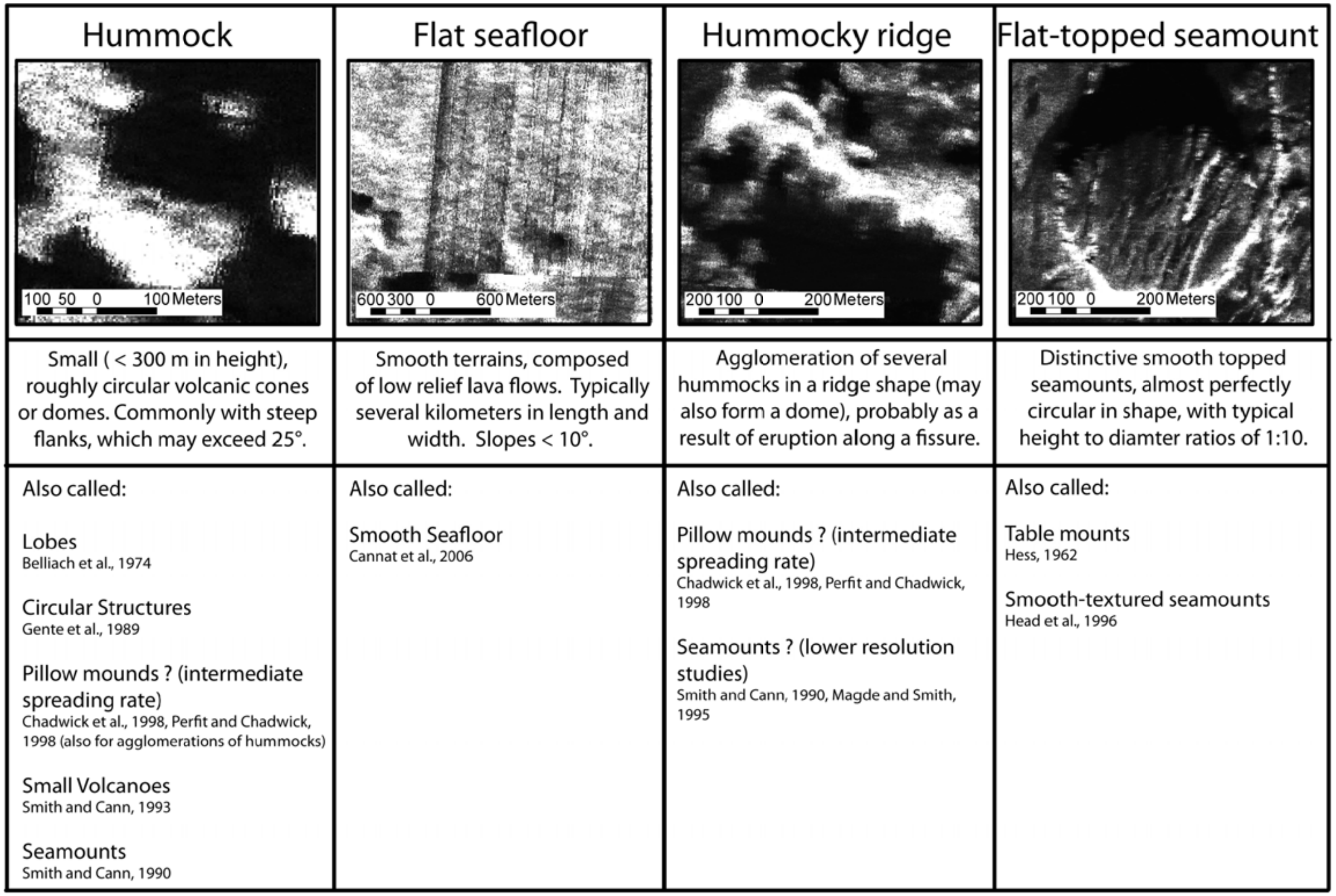

Figure 1.17: Large scale volcanic morphologies observed at slow-spreading ridges. As the same features have been described a number of times in different studies (Bellaich et al., 1974; Chadwick et al., 2001; Head et al., 1996; Magde and Smith, 1995; Perfit and Chadwick, 1998; Smith and Cann, 1990) many have been given a variety of names. Images are sidescan sonar as described in section 1.3.1.2. The hummocky ridge is south looking, all others are north looking.

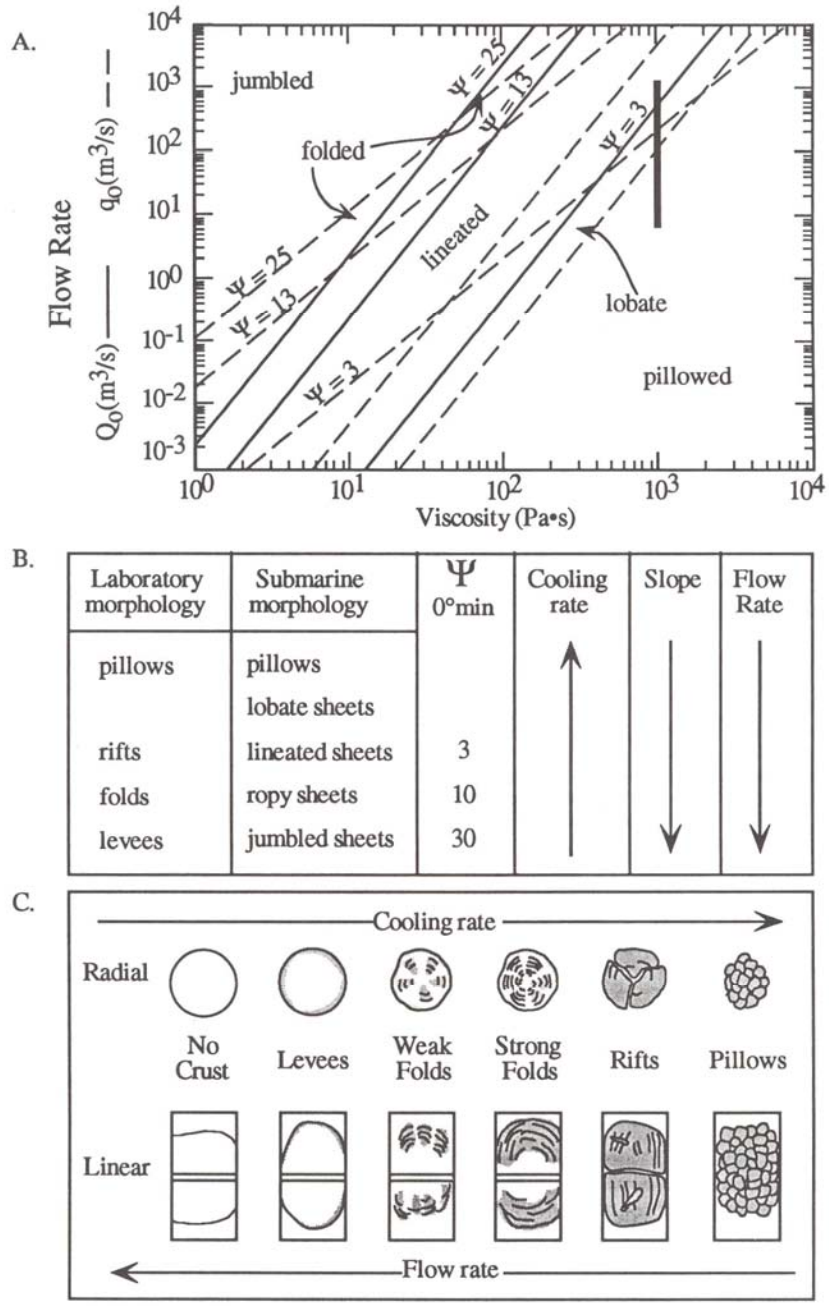

Figure 1.18: Results of seafloor and wax experiments investigating effect of effusion rate and viscosity on lava morphology from Gregg and Fink (1995) and Fink and Griffiths (1992). (A) Seafloor effusion rate and lava viscosity against lava flow morphology for basaltic lavas on a 10° slope. Dashed lines separate fields for a linear source and solid lines fields for a point source showing effusion rate is probably the dominant controlling factor on lava lithology. (B) Laboratory wax experiment results for lava morphology with varying factors. ψ is the ratio of time required for a crust to form on the surface of a flow against the rate at which it spreads out. (C) Characteristic wax lava morphologies with changes in cooling/effusion rate. Radical and Linear represent the upper and lower limits of geometry in experiments. Crust is shown by shading.

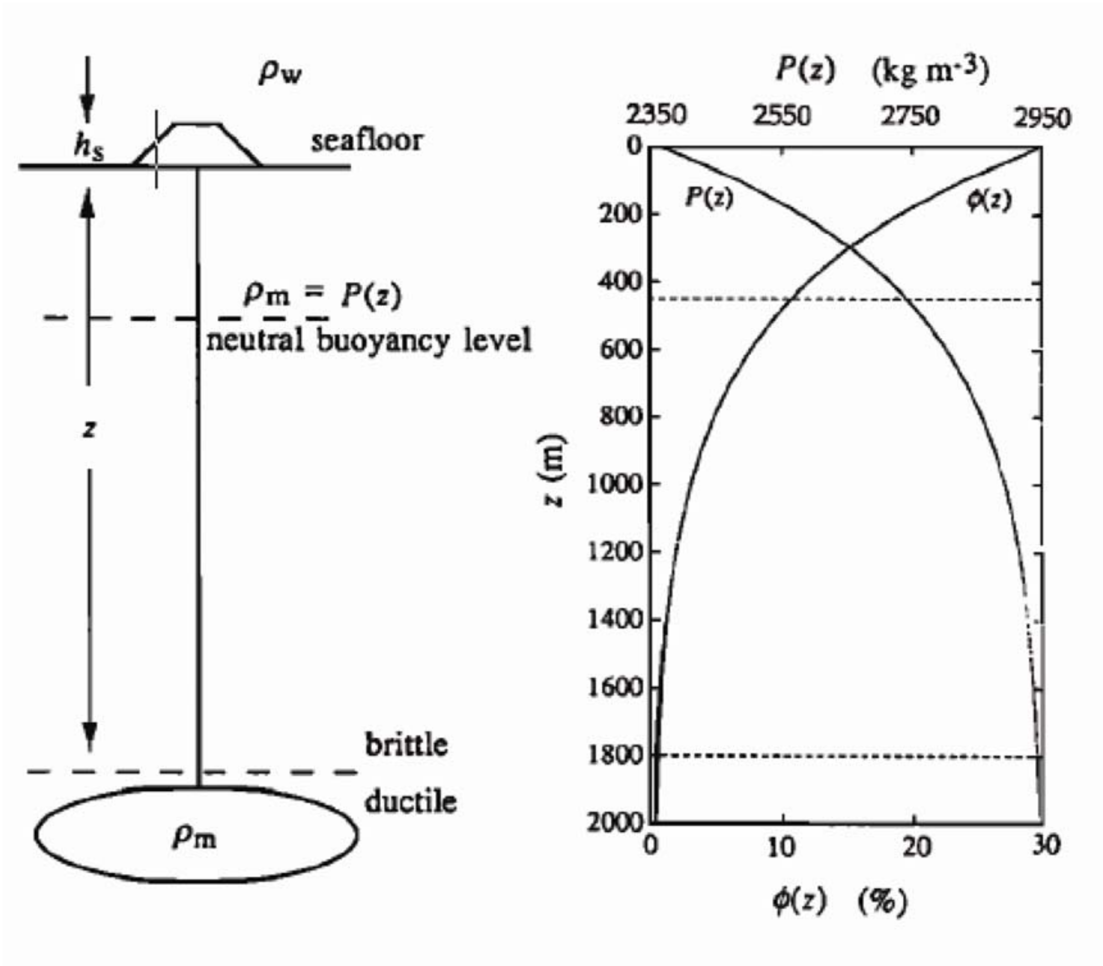

Figure 1.19: A flat topped seamount and its associated magma body trapped at the brittle/ductile transition from Smith and Cann (1992). The left hand panel shows a schematic diagram, while the right hand panel shows the rock porosity Φ*(z)*, as a function of depth below the seafloor, against rock density ρ (z) and depth. Dashed lines show the levels of the brittle/ductile transition and neutral buoyancy, which lies above the brittle dutile/transition.

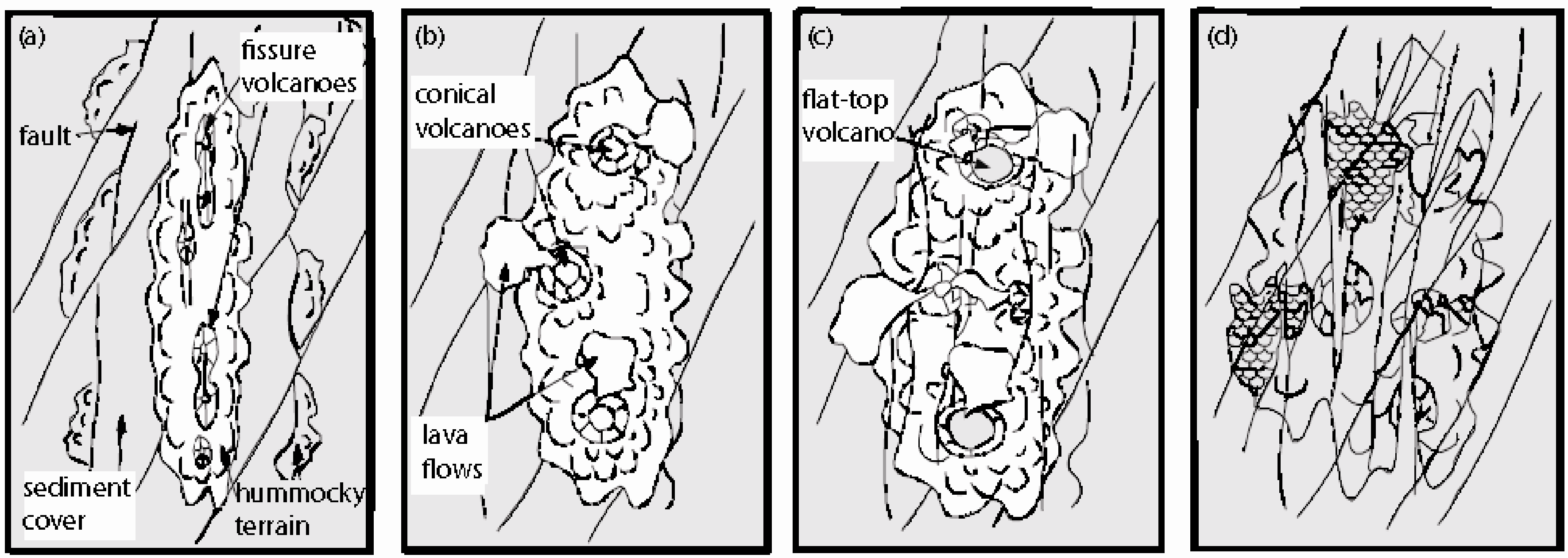

Figure 1.20: Life cycle model from Pierce et al. (2005) adapted from Parson et al. (1993). The first stage (a) shows the overprinting of a previously tectonised terrain by new volcanics erupted from fissures. This magmatic outpouring becomes more focussed as the eruption continues producing the seamounts appearing in (b). As the high magmatic flux wanes the AVR is cut by faults and broken up as shown in (c) and (d).

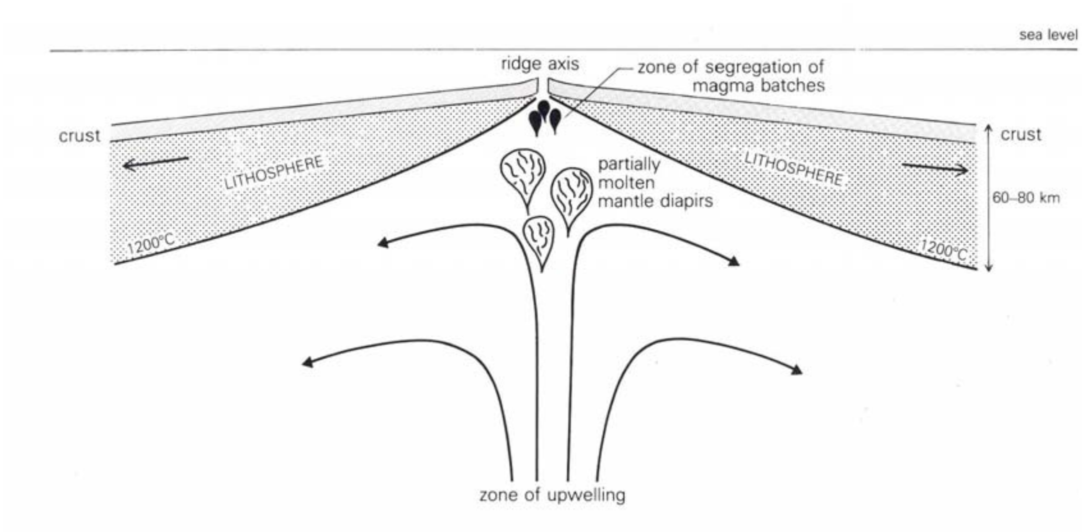

Figure 1.21: Schematic cross section of a mid-ocean ridge showing zone of mantle upwelling and melting zones from Wilson (1988). The base of the lithosphere is represented by the 1200°C isotherm.

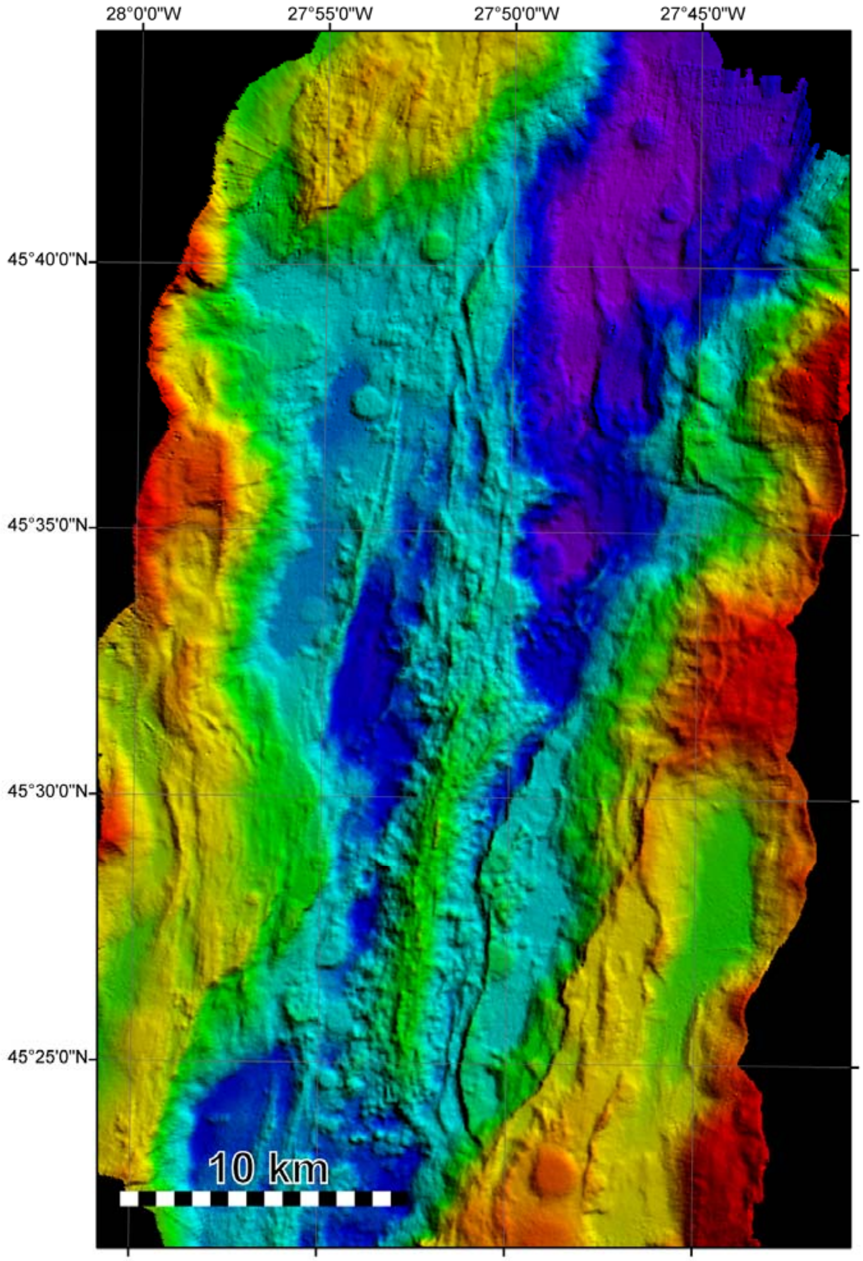

Figure 1.22: EM120 bathymetry of the axial valley at 45°30'N on the Mid-Atlantic Ridge.

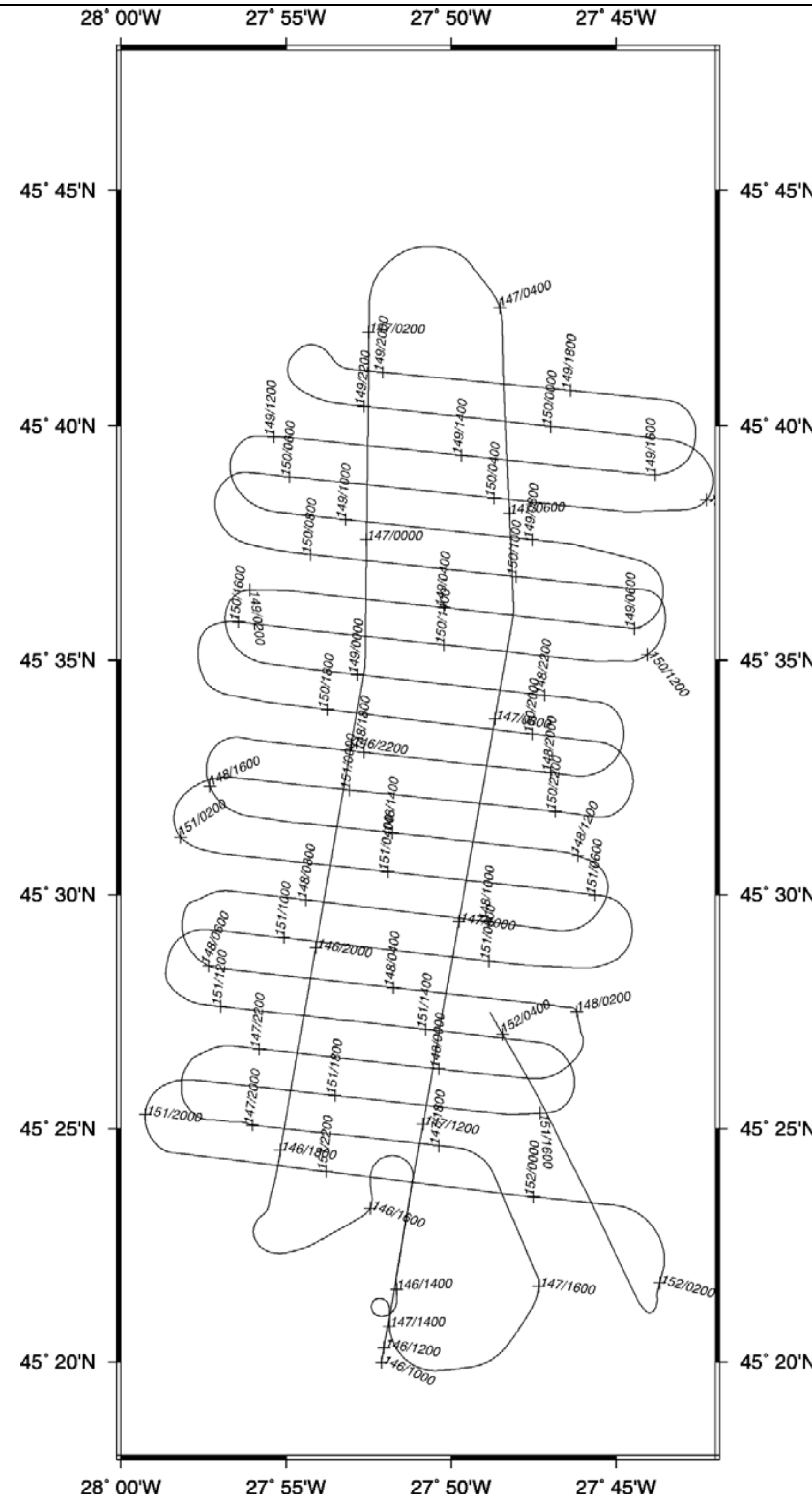

Figure 1.23: TOBI tracks from Searle et al. (2008)

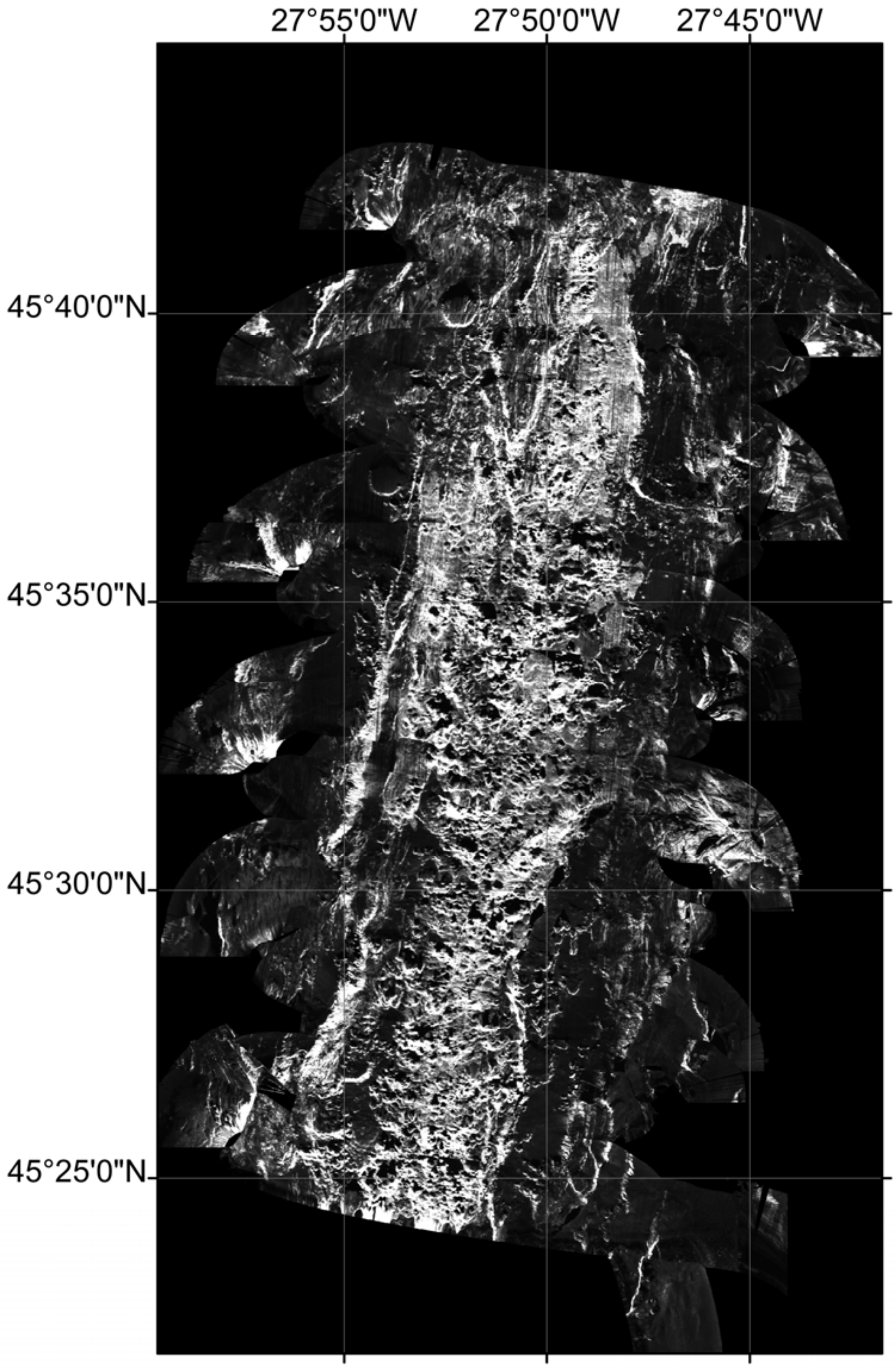

Figure 1.24: North looking TOBI sidescan sonar data

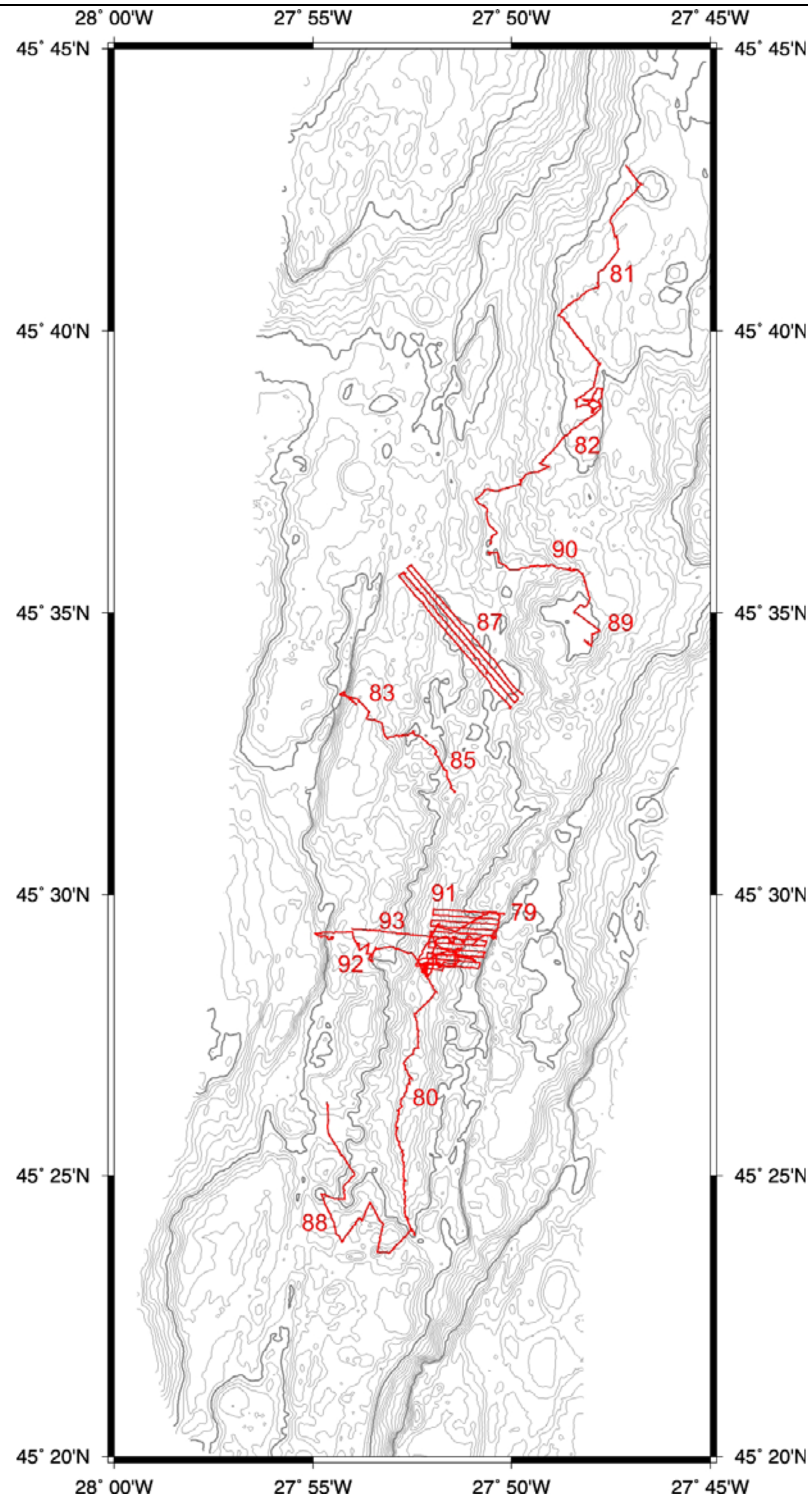

Figure 1.25: Isis dive tracks from Searle et al. (2008). Tracks 91 and 87 are the high-resolution study areas (the grid like tracks). All others were video and sampling dives

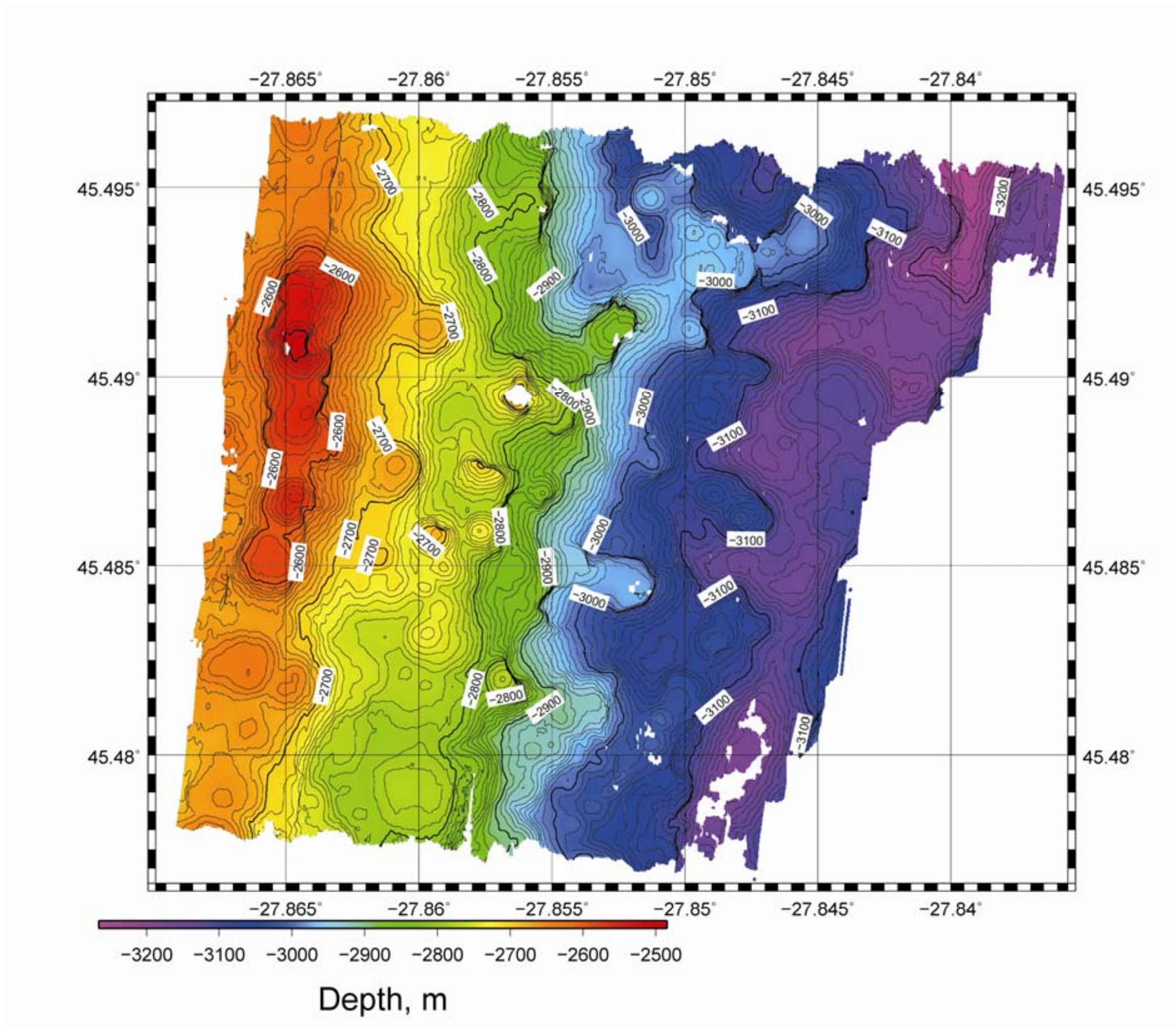

Figure 1.26: Southern area high-resolution Isis bathymetry. Contours at 10 m.

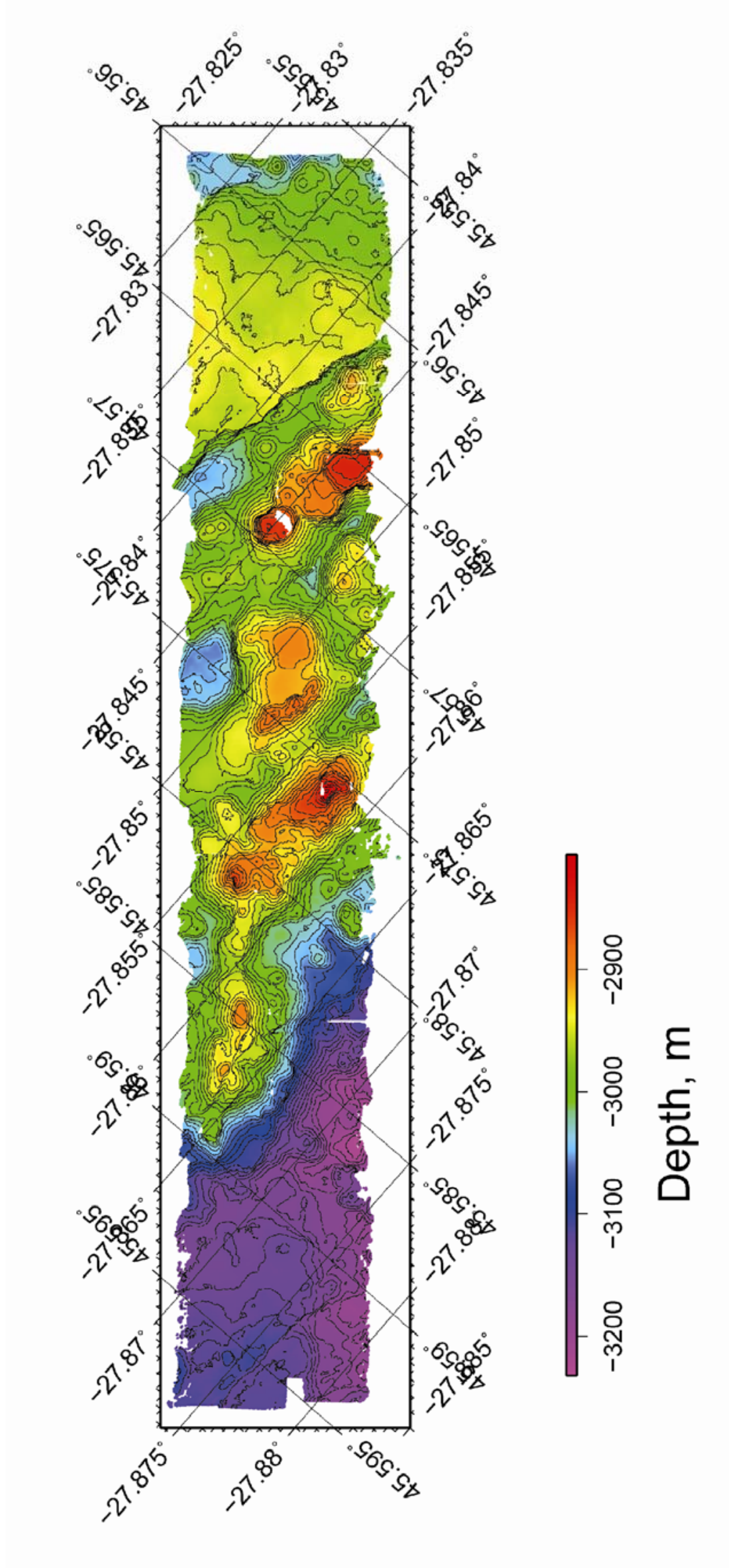

Figure 1.27: Northern area of Isis high-resolution bathymetry. Contours at 10 m.

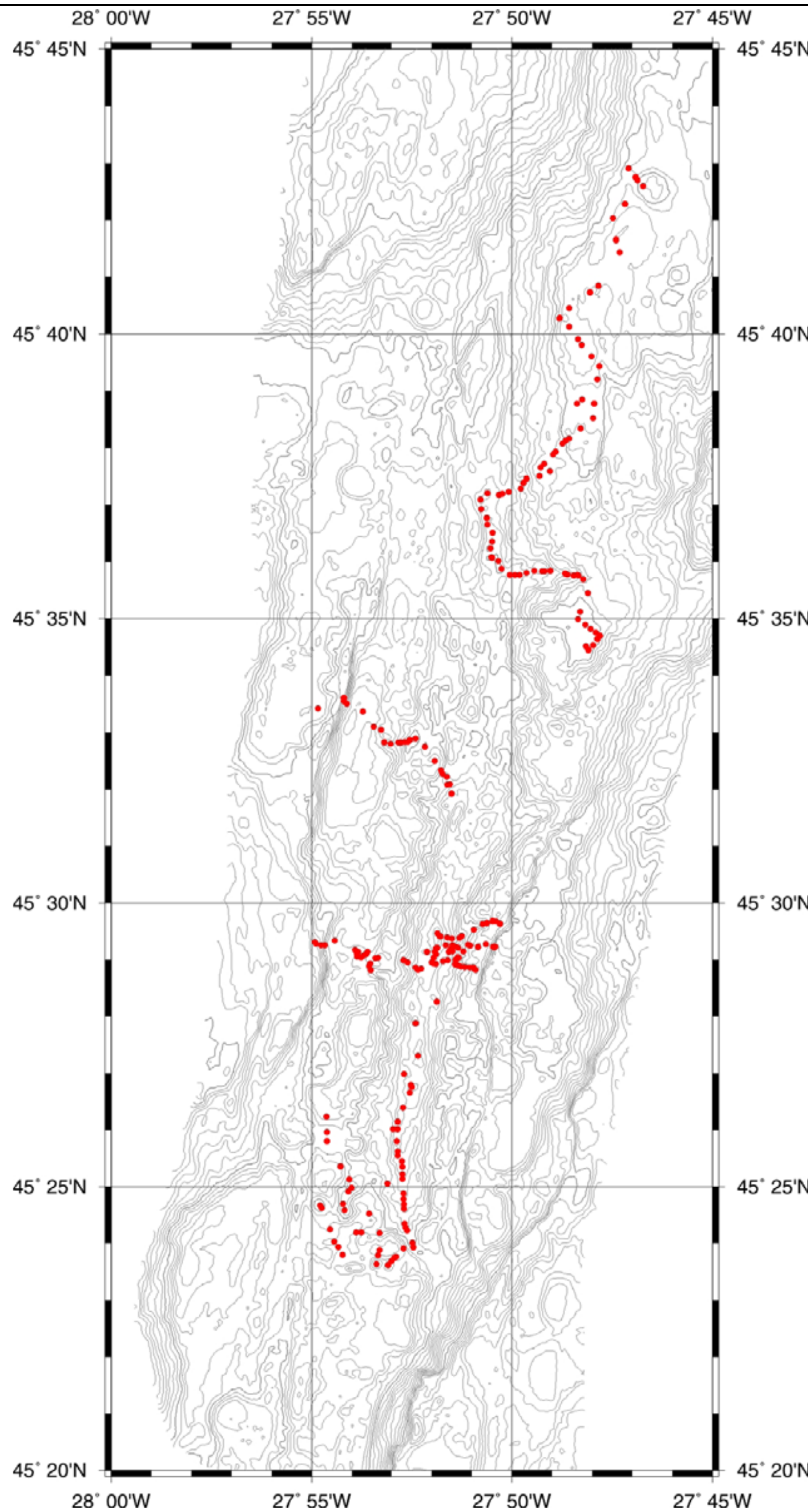

Figure 1.28: Sample locations from Searle et al. (2008)

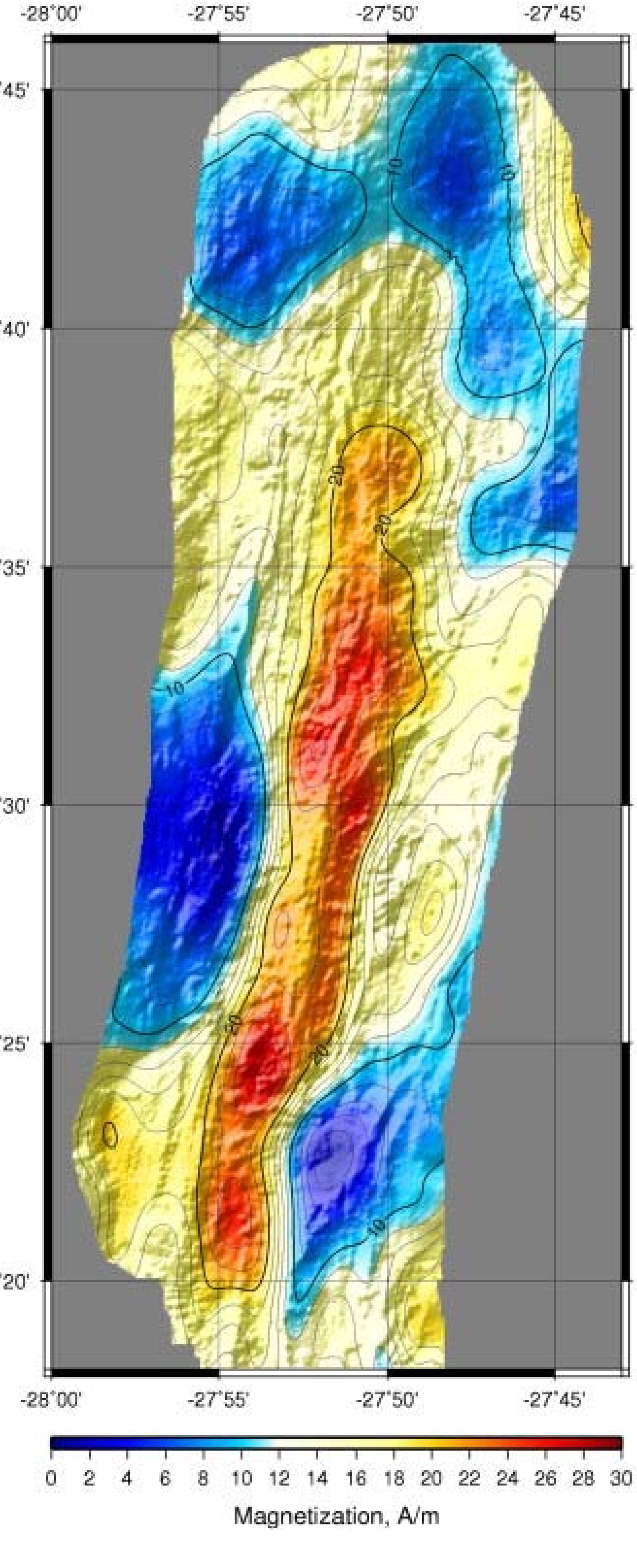

Figure 1.29: Crustal magnetization deduced from inversion of the measured TOBI magnetic field from Searle et al. (2010). Contour interval is 2 A m^{-1}.

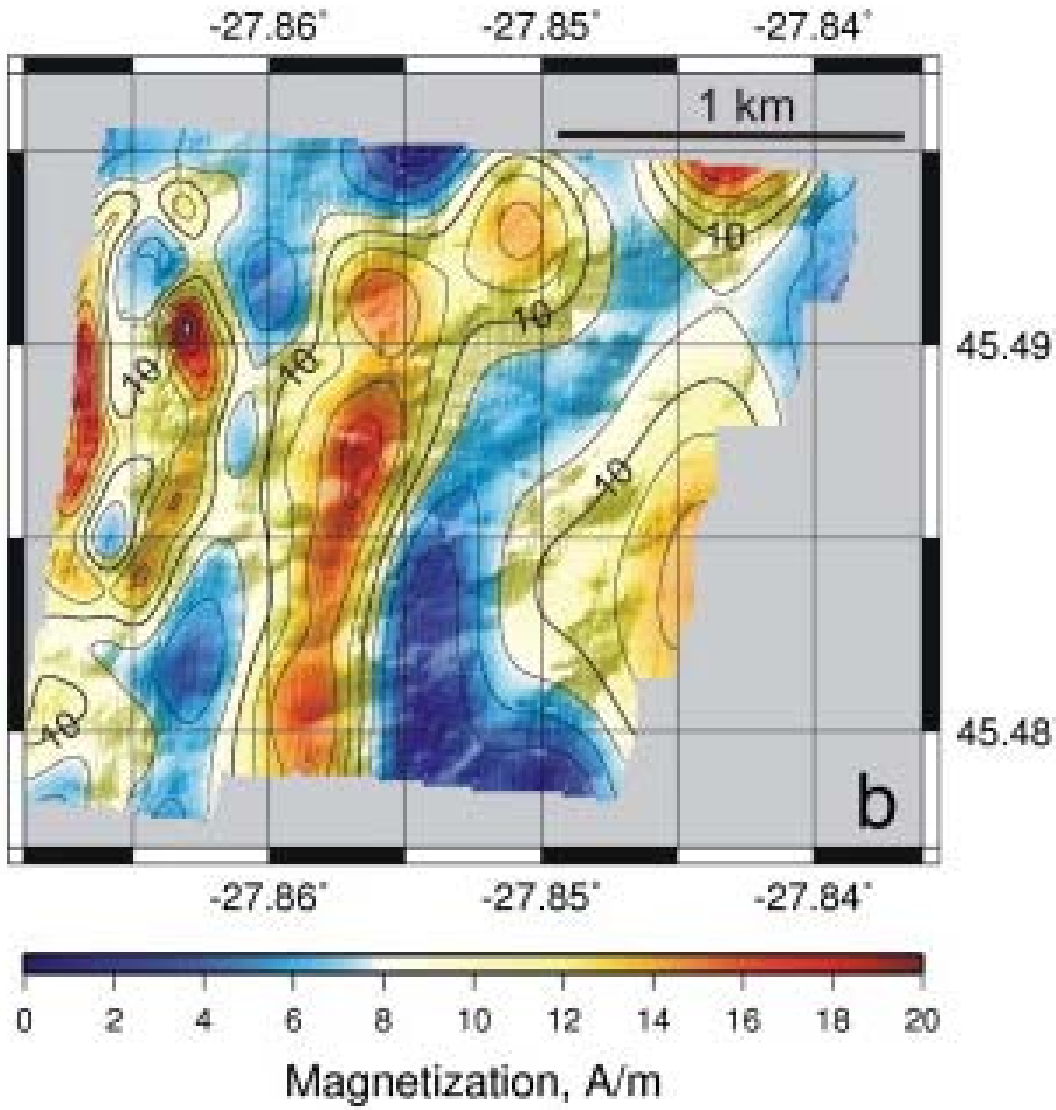

Figure 1.30: High-resolution Isis crustal magnetization of southern high-resolution study area draped over shaded bathymetry (9 times annihilator). From Searle et al. (2012). Contour interval is 2 A m^{-1}.

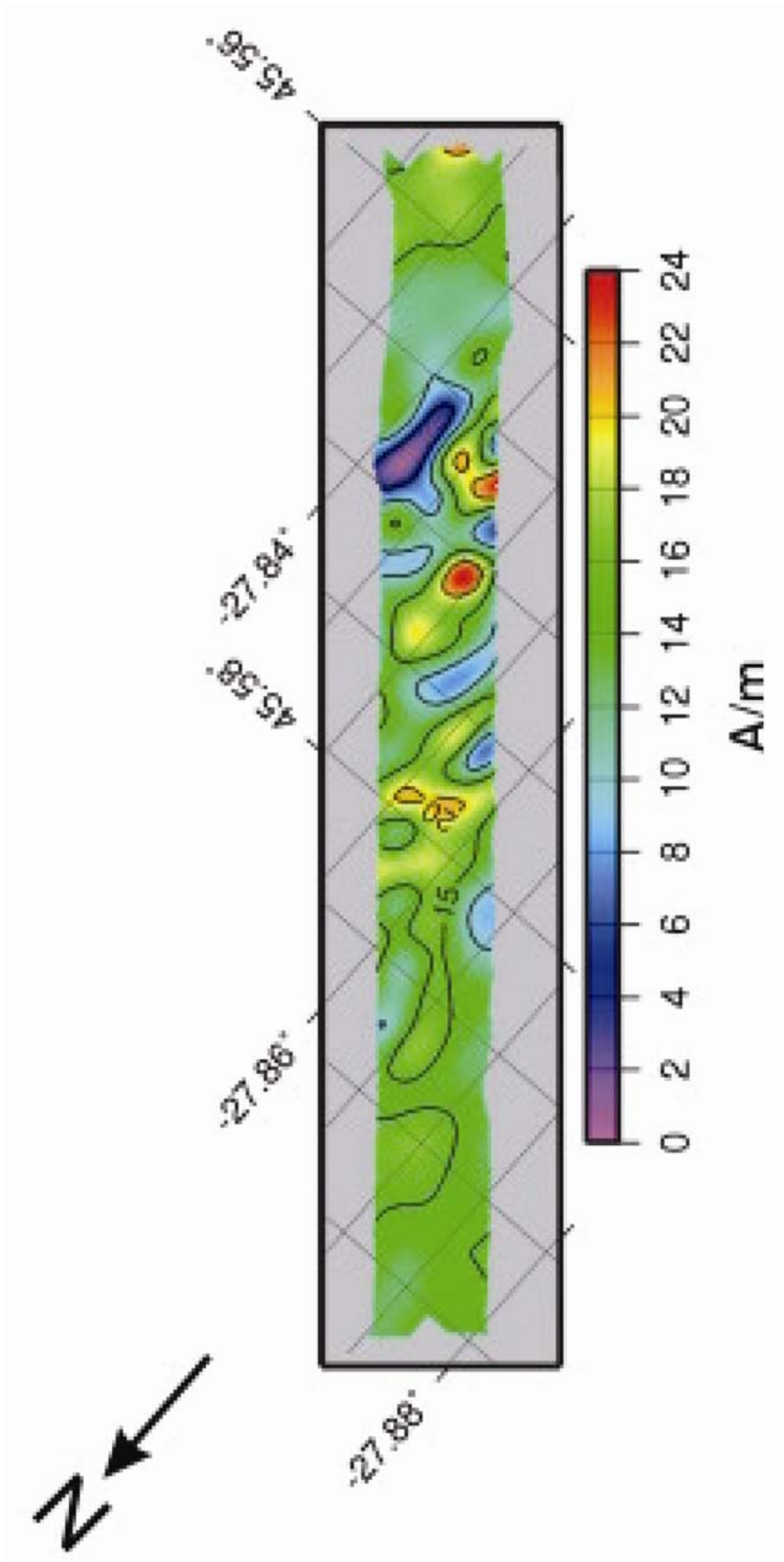

Figure 1.31: High-resolution Isis crustal magnetization of the northern area (fifteen times annihilator). From Searle et al. (2010). Contour interval is 5 A m^{-1}

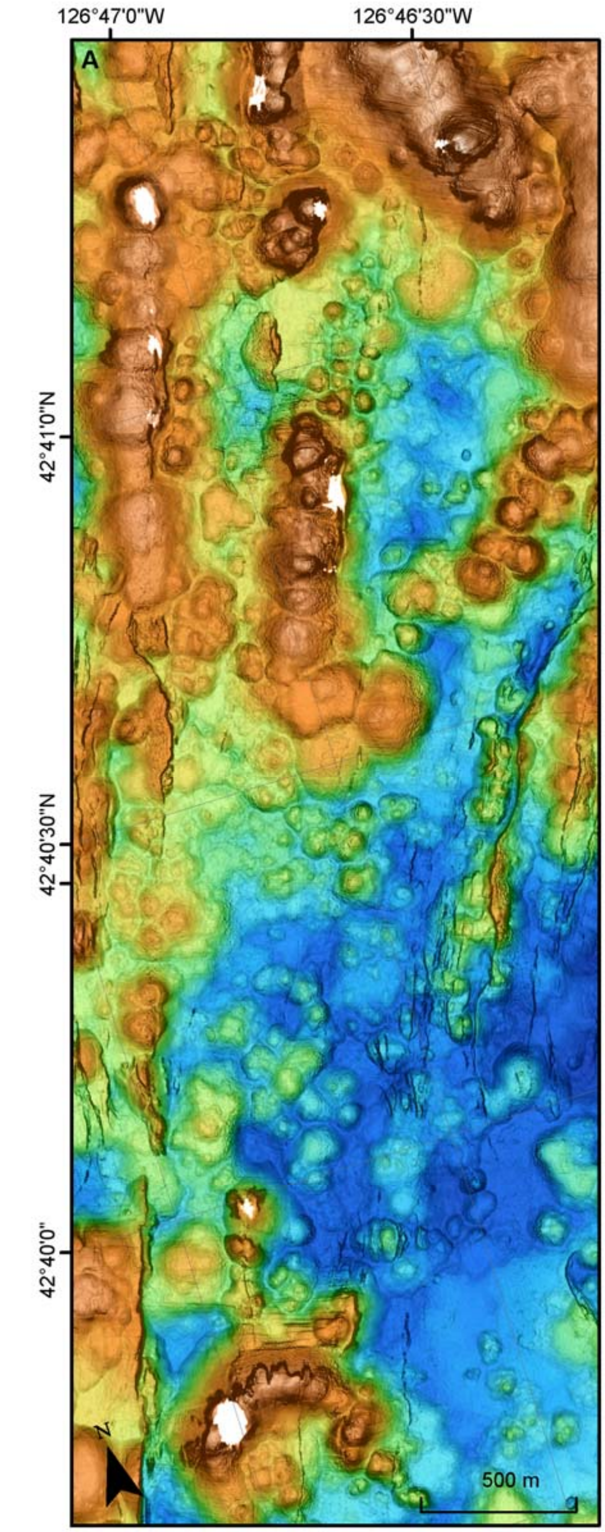

Figure 1.32: AUV bathymetry for the North Gorda Ridge.

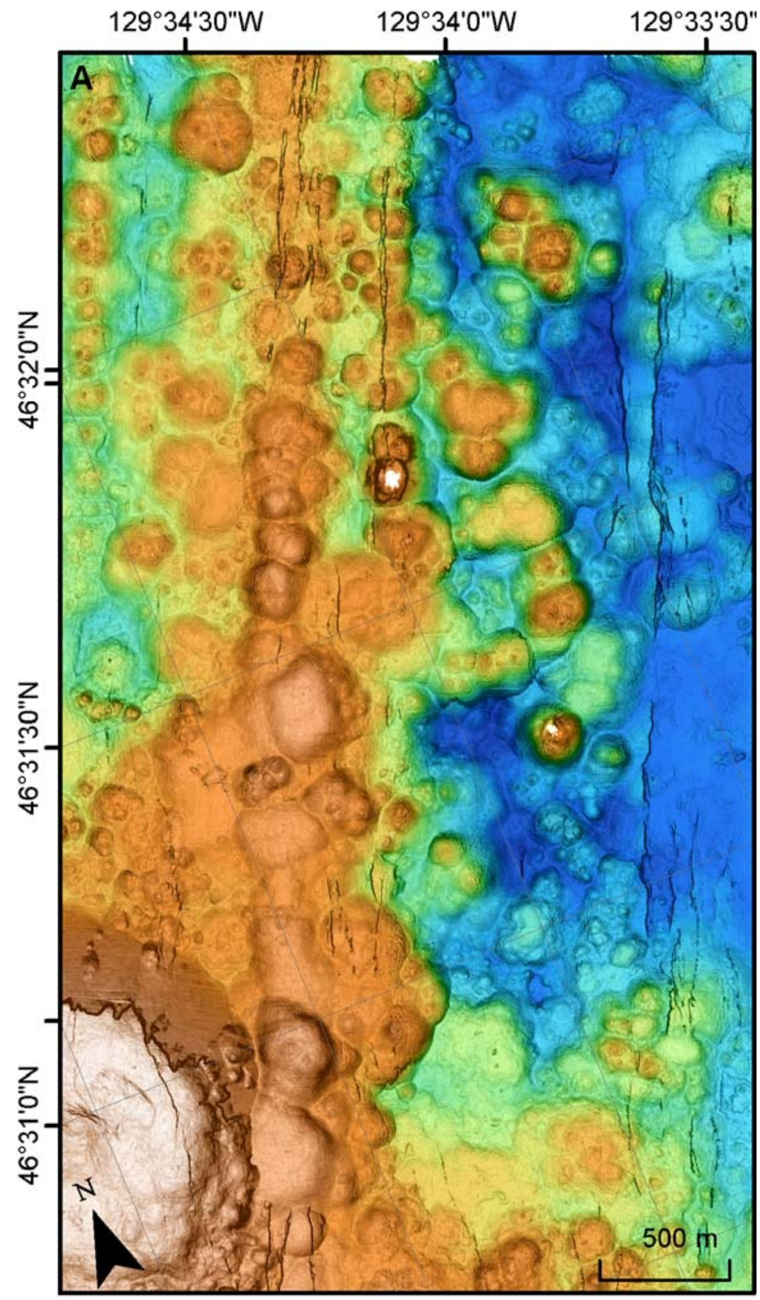

Figure 1.33: AUV bathymetry for Coaxial Segment of Juan de Fuca Ridge.

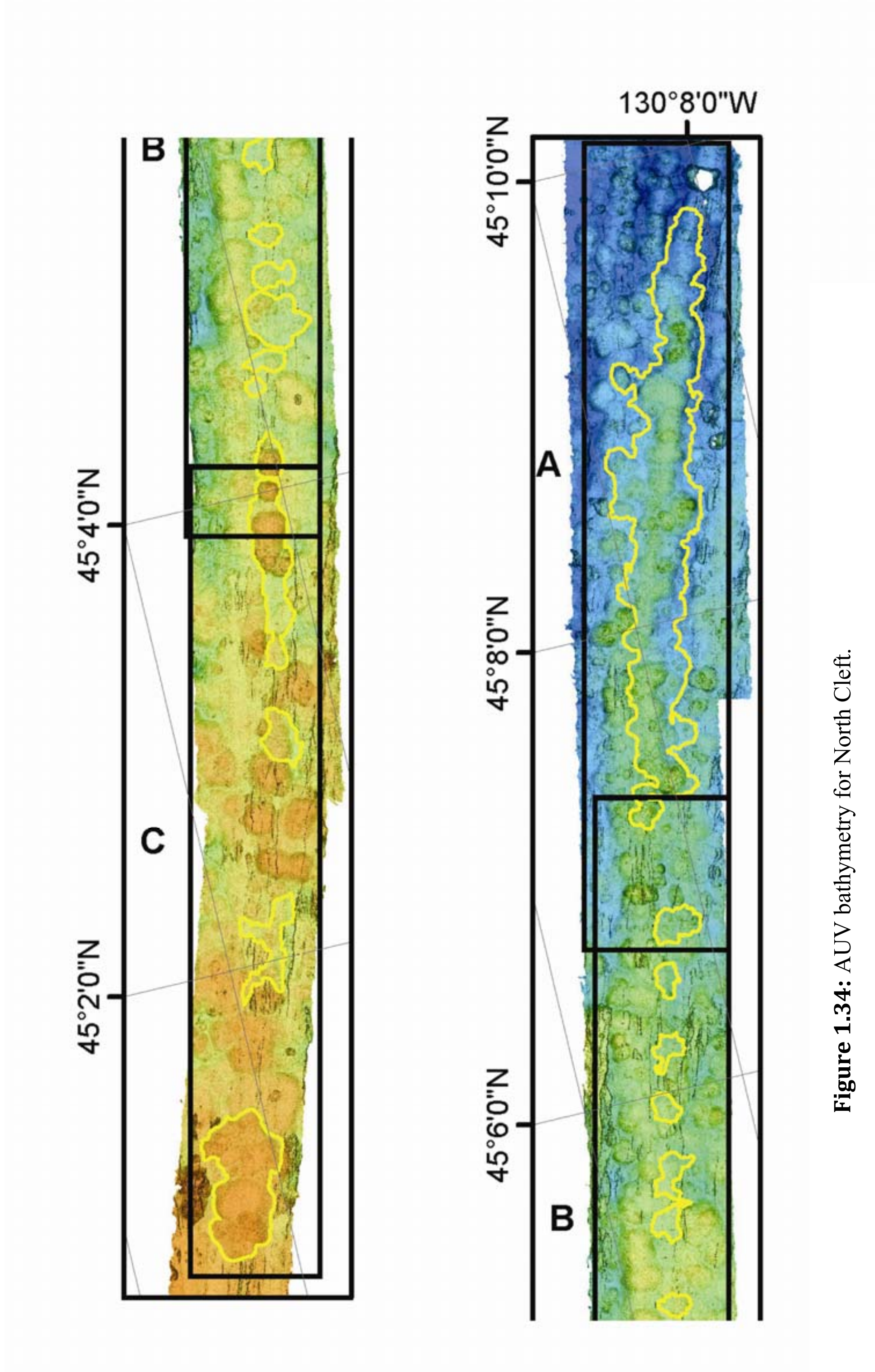

Figure 1.34: AUV bathymetry for North Cleft.

Chapter 2: Mapping the AVR

2.1 Rationale

It would be unthinkable to undertake a geological project on land without the aid of a geological map to provide the spatial and stratigraphic context for any sampling or measurement. Currently very little is know about the geographical distribution of lava flows and geological features on Axial Volcanic Ridges (AVRs) and no detailed maps of these features have been produced on a large scale. In order to address the questions of AVR construction it is important to know the spatial distribution and relative proportions of the volcanic units that build these features, and ideally provide at least some relative estimates of age. In addition, a geological map helps put other data, such as geochemical analyses and crustal magnetisation maps, in context. Until recently, high-resolution observation vehicles did not exist which were able to cover large areas of seafloor. The recent introduction of remote operated vehicles (ROVs) to mid-ocean ridge studies provides us with the opportunity to cover longer distances that were possible with manned submersibles, making producing a comprehensive, well-ground-truthed map of an axial volcanic ridge possible. In this chapter I present maps of the geology along the 11 video and sampling dives carried out on cruise JC24. I then use this data to address what axial volcanic ridges are built of, examine the spatial distribution of different lava lithologies and examine the relationship of these lava morphologies to each other. Distribution of sediment is also used to estimate the duration and periodicity of volcanic activity.

Observation tables can be found in appendix 9.5.

2.2 Work Division

EM120 bathymetry and sidescan sonar maps were produced by T P LeBas, while the SM2000 maps were renavigated and plotted by K L Achenbach. All lithological and sedimentary mapping was done solely by I Yeo and all maps, figures and statistics included here are based on this work. The paper 'High Resolution ROV Mapping of a Slow-Spreading Ridge: Mid-Atlantic Ridge 45˚N', which constitutes the rest of this chapter was written by I Yeo based on the above work and co-authored with R C Searle.

2.3 PAPER: High Resolution ROV Mapping of a Slow-Spreading Ridge: Mid-Atlantic Ridge 45˚N

I. A. Yeo[1] and R. C. Searle[1]

[1] *Department of Earth Sciences, Durham University, South Road, Durham, DH1 3LE*

Submitted to *Geochemistry, Geophysics, Geosystems*

2.3.1 Abstract

Axial Volcanic Ridges (AVRs) are found on most slow spreading mid-ocean ridges and are thought to be the main locus of volcanism there. In this study we present high-resolution mapping of a typical, well-defined AVR on the Mid-Atlantic Ridge at 45°N. The AVR is characterised by 'hummocky terrain', composed typically of pillowed or elongate pillowed flanks with pillowed or lobate lava flow summits, often with small haystacks sitting on their highest points. The AVR is surrounded by several areas of 'flat seafloor', composed of lobate and sheet lava flows. The spatial and morphological differences between these areas indicate different eruption processes or effusion rates operating on and off the AVR. Volcanic fissures are found all around and on the AVR, although those with the greatest horizontal displacement are found on the ridge crest and flat seafloor. Clusters of fissures, associated with areas of typically high effusion rate lavas, may represent volcanic vents. Extremely detailed comparisons of sediment coverage and examination of contact relations around the AVR suggest that many of the areas of flat seafloor are a similar age or younger than the hummocky terrain of the AVR. Additionally, all the lavas surveyed have similar degrees of sediment cover, suggesting that the AVR was either built or resurfaced in the same 10 ka timeframe as the flat seafloor.

2.3.2 Introduction

Axial Volcanic Ridges (AVRs) are found on most slow spreading mid-ocean ridges and are thought to be the main locus of volcanism there. In this study we present high-resolution mapping of a typical, well-defined AVR on the Mid-Atlantic Ridge at 45°N. The AVR is characterised by ‘hummocky terrain’, composed typically of pillowed or elongate pillowed flanks with pillowed or lobate lava flow summits, often with small haystacks sitting on their highest points. The AVR is surrounded by several areas of ‘flat seafloor’, composed of lobate and sheet lava flows. The spatial and morphological differences between these areas indicate different eruption processes or effusion rates operating on and off the AVR. Volcanic fissures are found all around and on the AVR, although those with the greatest horizontal displacement are found on the ridge crest and flat seafloor. Clusters of fissures, associated with areas of typically high effusion rate lavas, may represent volcanic vents. Extremely detailed comparisons of sediment coverage and examination of contact relations around the AVR suggest that many of the areas of flat seafloor are a similar age or younger than the hummocky terrain of the AVR. Additionally, all the lavas surveyed have similar degrees of sediment cover, suggesting that the AVR was either built or resurfaced in the same 10 ka timeframe as the flat seafloor.

2.3.3. Data Acquisition and Detailed Study Areas

2.3.3.1 Data Acquisition

Data were collected during RRS James Cook cruise 24 in May and June 2008.

Sidescan sonar data was acquired using TOBI (Flewellen et al., 1993). TOBI is fitted with 30kHz sidescan sonar which measures 6km wide swaths with a pixel size of ~3m (LeBas, 2005). Post-processed data has an absolute precision of 100m. Twenty-two E-W, 2-km-spaced tracks provided 100 % N – and S – looking sonar coverage. Attenuation of TOBI backscatter can be used as a proxy for sediment thickness and therefore age. Data was interpreted by Searle et al. (2010).

Video data were captured by two cameras using the ROV Isis (operated by NOC, Southampton, UK; (German et al., 2003). Video was recorded at all times during 11 sampling dives. Three dives (centred on 45˚29.00 N 27˚51.50 W) were in an area of Simrad SM2000 microbathymetry collected by the ROV. It has post-processed horizontal and vertical resolution of ~1 – 2 m (Searle et al., 2010).

Video and sampling dives were carried out in both the robust southern AVR and the tectonised north, on the axial valley floor (figure 2.1, figure 2.2) and up the axial valley wall fault scarps (figure 2.3). Sediment was recorded from visual observations (figure 2.4). The dive positions were chosen based on the TOBI sidescan sonar and, where it was available, high resolution SM2000 bathymetry.

2.3.3.2 Mapping

Lava lithology was spilt into seven categories, including pillow lavas (figure 2.5; A and D), elongate pillow lavas (G), lobate lavas (B), and sheet flows (E and H). Total sediment cover (I), talus (F) and scarps (C) were also recoded. Frequently two lava types would occur close together, and where there were two within a 10 m^2 area we used the additional categories pillow and elongate pillow lavas, pillow and lobate lavas, and lobate and sheet flows.

Sheeted lava flows were not divided further (i.e. into ropey, lineated etc) as they are more easily buried by sediment and exposures were typically not large enough to be representative of the whole flow. Scarps were defined as any broken vertical or near vertical face. Fissures were defined as any crack cutting the seafloor, and were subdivided into those which were purely eruptive, i.e. those that were narrow, sinuous, surrounded by pillow lavas and formed a local high, and those which were linear, purely tectonic cracks or previously eruptive fissures with large horizontal separation. We also mapped haystacks, cone shaped features < 5 m high, composed of pillows and elongate pillows, and collapse pits.

In order to cover all the scientific objectives it was occasionally necessary for the ROV to fly above topography, which was not of scientific interest, in order to travel at its maximum speed. These are referred to as ‘blue-jumps’ and are represented by a dashed line in figure 2.2.

The first order along-track mapping was done using the Adelie-Otus ArcGIS extension developed by L'Institut Français de Recherche pour l'Exploitation de la Mer (IFREMER), Brest, mounted on an ArcGIS 9.1 platform. Further maps were produced using ArcGIS and Adobe Illustrator CS3. Lithology was recorded at one minute intervals during dives, which, with a typical ROV speed of ~1 km/hr, equates to one observation every ~17 m. This is the smallest scale at which meaningful lithological changes can be observed and is similar to the resolution of the TOBI survey. Strikes were recorded for structural features observed. These have variable accuracy as some were measured with the ROV while others are estimated relative to the vehicle heading. Estimated strikes have an estimated accuracy of ± 020˚.

2.3.3.3 Sediment Cover

In order to compare the sedimentation along and between dives (Ballard et al., 1981; Francheteau and Ballard, 1983; Mitchell, 1995), we devised a sedimentation scale. Sediment Cover (SC) categories were assigned with divisions at: 0 (No sediment cover), 1 (< 10% Sediment Cover – light dusting of sediment), 2 (10 – 50% sediment cover – sediment on surfaces but no joined sediment pockets between lavas), 3 (50 – 90% sediment cover – heavy sediment cover with interconnected sediment pockets) and 4 (> 90 % sediment cover). These categories do not represent regular divisions of sediment thickness, but are the clearest divisions observable from the video footage, as cross sections of sediment thickness are not usually visible. As with the lithology mapping, observations of sediment cover were made every minute along the video dives, except on vertical or near vertical slopes where sediment is unable to settle. When using sediment cover to estimate relative dates for lava flows we compared only similar areas (pillowed terrain) to minimise the problems associated with differing lava relief. In areas where there were no pillows, sediment thickness was also compared where it was observed in cross section (i.e. at fissures/scarps). This was the main method of comparing the relative dates of the flat and hummocky seafloor. There is no way to remove errors associated with currents or differing deposition rates, so broad comparisons of lavas tens of km apart are difficult, however local comparisons between lavas close to each other should be more reliable.

2.3.4. Mapping Observations

In the following sections, I describe each video and sampling dive separately. A summary of the features and lava morphologies described can be found in chapter 1 (sections 1.1.4.2 and 1.1.4.3).

2.3.4.1 Dive JC24-79

Dive JC24-79 followed a 5.1km long track beginning at 45°29.32 N, 29°50.58 W, and ending at 45°28.88 N, 27°52.35 W (figure 2.2i and 2.2xii), forming a rough transect from the axial valley wall and then across hummocky terrain up to the AVR crest at one of its shallowest points. Excluding scarps, talus flows, blue jumps and areas of 100% sediment cover, in-situ lavas were observed along 2.5 km of the dive, consisting of predominantly pillow and elongate pillow lava lithologies (table 2.1).

The first section of the dive covered the innermost eastern axial valley wall, a 250m high, near vertical scarp. The seafloor farthest from the base of the scarp was flat with a thick sediment covering. As the ROV approached the scarp this flat seafloor gave way to a slope of heavily sedimented old talus, which became less sedimented at the top, suggesting that there have been numerous wall collapses of different ages. The scarp was stepped in places by short (< 5m) benches. Scarp faces displayed primarily truncated pillows (broken along a plane rather than converted to talus), which ranged in size from 0.3 to 1.5 m in diameter. Three small sheet flows were identified from the video, the first (lowermost) was 1.4 m thick (3033 m depth; figure 2.3), the second 12m thick (2960 m) and the third (uppermost) 9m thick (2923 m). A single 20 cm sediment bed (2990 m) was also observed. The seafloor at the top of the scarp was flat and covered with sediment (A; figure 2.2i). The ROV tracked along the scarp with a blue jump for a further 750 m, before dropping back down to the seafloor and heading towards the base of the AVR (point B).

The ROV then climbed ~ 600 m across sloping pillowed terrain to the crest of the AVR (G). It followed an oblique, NE-trending spur, composed of a cluster of hummocks (seen in sidescan). This terrain had variable slopes, ranging from 10˚ to 45˚, and was mostly covered by pillows and elongate pillows. The contacts between hummocks were not clear, as no noticeable sharp change in sediment, lithology or slope could be discerned from the video, and sediment cover was similar. Hummock summits were either pillowed or covered by lobate lava flows; those with lobate flows tended to be flatter (> 15°). On the summit of this hummock (C) we also observed a small eruptive fissure with an orientation of 199˚, roughly parallel to the spreading axis.

Hummocks (seen in sidescan) along the remainder of the dive displayed flanks with pillows and steeper elongate pillowed sections, and lobate hummock summits. A small haystack (F) was observed along with three near vertical or vertical scarps and their associated talus deposits (D, E). The haystack was a 2 m tall, steep-sided pile of elongate pillow lavas and sat on a narrow area of lobate lava flows on the summit of a small hummock. The first three scarps (D, E) had a combined throw of 206 m, and both faced outwards from the ridge axis. Neither can be observed clearly in the sidescan sonar due to the N –S insonification direction, nor in the lower quality E – W insonified data [appendix A], although the scarp at D may correspond to a brighter area that crosscuts the hummock. None of these scarps correspond to observable faults that extend beyond the hummock in the sidescan sonar data or in the low-resolution bathymetry. However the scarp at G, which is also outward facing, does correspond with a steepening in the depth contours and a scarp that is clearly observable in the E – W insonified sidescan [appendix A], where it is visible cutting along the ridge axis for at least 4 km. The scarp face was composed entirely of broken pillow lavas and was 117 m high at this point, all of which appears to be tectonic offset. The top of this scarp was followed by a short, sloped section of pillows and elongate pillows to the crest of the AVR (G), which with a depth of 2497 m lay 657 m above the flat, sedimented seafloor on which the dive began.

The final section of dive JC24-79 covered the AVR crest. This area of hummocky terrain (from the sidescan) was similar to that observed on the AVR flank (mainly pillow lavas, elongated pillows and occasional lobate flows), however was characterised by an increased number of roughly ridge-parallel fissures (H). These fissures were a combination of eruptive and open fissures, and may join up along the axis, although this was not observed.

2.3.4.2 Dive JC24-80

Dive JC24-80 (figure 2.2ii) is a 10.4km long dive which began at the southernmost point of the AVR (45°23.92 N, 27°52.04 W), climbed up to the ridge crest and then followed it for 5.8 km before deviating down the eastern flank of the AVR then climbing back to meet the end of dive JC24-79 (45°28.83 N, 27°52.38 W). This dive aimed to investigate changing ridge crest morphology across hummocky terrain from the southern tip of the AVR. The dive covered predominantly pillow and elongate pillows with some lobate lava flows (table 2.1).

The start of the dive covered hummocky terrain, similar to that observed during dive JC24-79. Starting at a depth of 2975 m (A; figure 2.2ii) the ROV climbed up and along the crest of the AVR to 2700 m across 3 km of hummocky terrain (D). This terrain was composed of pillowed and elongate pillowed lava flows, with the elongate pillows forming the steeper sections (> ~ 20°) of the hummock flanks. Summits were covered by a combination of pillows and lobate lava flows and most hummocks sat directly in contact with others (a few were separated by flatter, SC 4 areas of seafloor; figure 2.4). Contact relationships were not clear as pillows had similar dimensions and degrees of sediment cover. This section of the dive crossed three haystacks, and two groups of ridge parallel fissures (B, C).

Between D and F lithology remained the same; however, the SC dropped slightly (corresponding to slightly higher backscatter levels north of 45˚25.30 N), suggesting that the flows covered between D and the end of the dive are younger than those at the start (figure 2.4). Five further clusters of fissures were observed on the AVR axis and several small scarps.

At F the ROV turned east and covered 1 km off axis terrain. This terrain was similar to the hummocky terrain observed earlier in the dive. The ROV then climbed back towards the AVR axis. As it approached the AVR crest it encountered the long fault observed just off the AVR summit in dive JC24-79, which here is 51 m high.

2.3.4.3 Dive JC24-81

Dive JC24-81 covers 11.1km of deep seafloor in the north-eastern section of the axial valley between 45°42.97 N, 27°47'.17 W and 45°38.47 N, 27°47.97 W, near the non-transform offset (figure 2.2iii). The seafloor covered was predominantly very flat (< 5˚ for most of the dive), however the dive also took in part of a small (1km diameter) flat-topped seamount (A; figure 2.2iii), the base of the AVR flank (E), and a section of the eastern axial valley fault scarp (F). The dive covered a combination of pillow, lobate and sheet lava lithologies, but with a much greater proportion of sheet and lobate lava flows than dives JC24-79 and JC24-80 (table 2.1).

On the approach to the flat-topped seamount the seafloor was very flat (< 5˚) and for the most part 100% covered with sediment. Pillow lavas were observed only twice on the approach to the seamount and in both cases appeared to be forming small mounds (~ 10 m across), which had a higher relief than the surrounding lavas. They were both heavily sedimented.

The seamount flanks (A; figure 2.2iii) were composed predominantly of pillows and elongate pillows, which flowed down the < 45° flanks from above. The top of the seamount was composed almost entirely of lobate and sheet flows where observed. Both the flanks and the lobate and sheet flows on the summit were SC 3 – 4 (figure 2.4).

The ROV then covered approximately 5 km of flat seafloor (< 5˚), composed of a combination of sheet flows, lobate flows and low relief pillow fields (B - E). The sheet flows were often so flat that a few cm of sediment was enough to bury them completely, thus the majority of observed sheet flow outcrops were tumuli (blisters on the surface of the flow caused by gas pressure beneath it), which formed small local highs of a few metres (C). Many sheet flow outcrops had distinctive ropy textures visible on the surface. Just north of D the dive crossed an area of sedimented collapse pits up to 10 m across and 5 m deep. The pits had steep, heavily sedimented sides, although occasionally sheet flow cross sections were observed.

Most of the sheet flow areas were characterised by one or more single pillow lavas, which sit above the upper crust of the flow. Pillow lavas were also observed in small groups within the sheet flows, which appear to correlate to hummocks (possibly partially buried), observed in the sidescan sonar (e.g. D).

As the dive approached the base of the AVR eastern flank (E), the seafloor continued to be covered predominantly by lobate and sheet flows, with pillows appearing as the gradient steepened onto the AVR. The flat seafloor was mostly buried by sediment and the pillows appeared sparsely at first, becoming progressively more common until they were the main lithology observed. The contact relationship was not directly observed due to the sediment cover, however as there is no sudden appearance of a pillowed flow and appears more consistent with the high effusion rate lavas slowing, producing progressively more pillows, and onlapping the AVR.

The ROV then covered a further 2 km of flat seafloor (E – F), composed of lobate and sheet flows, between the edge of the AVR and the axial valley wall scarp. Pillow lavas were observed near the base of the scarp and the scarp face was mainly broken pillow lavas with rarer sheet flow layers (F).

The ROV then returned to the median valley floor, where further pillowed flows were observed. The seafloor here appeared broken up, with a large number of open fissures striking roughly north – south. The ROV covered further sheet and lobate flows as it moved south, before covering a small 880 m x 800 m area in detail (G). This southern area was again cut by many open fissures with varying orientations. In some places the lavas were very crumbly and altered and occasionally patches of what may be bacterial mats were observed, possibly indicating a nearby hydrothermal source.

The entire dive was characterised by high sediment cover, with almost all lavas north of E having an SC of 3.5 or above and lavas to the south SC of around 3 (figure 2.4). As expected, higher sediment cover categories were allocated for sheet flows than higher relief pillow lavas.

2.3.4.4 Dive JC24-82

Dive JC24-82 (figure 2.2iv) covered a 7.9 km long track from the end point of dive JC24-81, southwest across flat seafloor to and then up the north eastern flank of the AVR to its crest (45˚36.12 N, 27˚50.55 W). In-situ lavas were exposed along 6 km of the dive length, comprising mainly sheet flow, lobate flow and pillow lavas (table 2.1).

As on previous dives, the flat seafloor was composed of low relief sheet, lobate and occasionally pillow flows (A – C; figure 2.2iv), exposed predominantly as small tumuli or in fissures. A number of small eruptive fissures were observed, again trending predominantly N – S (B). SC was mostly 3 – 4 (figure 2.4).

As the ROV reached the AVR flank (C, figure 2.2iv) pillows in association with lobate and elongate pillows were observed forming ~ 25 ˚ to > 40˚ slopes, with SCs of 3 – 3.5 (figure 2.4). Many fissures were observed on the 2.2 km of hummocky terrain between C and D, trending approximately 160°. The ROV then climbed a series of talus flows and small scarps < 10 m high (D). These appeared to correlate with a N – S orientated, east facing fault scarp, visible in the ship-based bathymetry and the N – S insonified sidescan sonar.

The final 3.3 km (D onwards) covered more pillowed hummocky terrain with variable SC, mostly 2 – 3 (figure 2.4). There were three < 100 m wide areas of sheet flow, all of them associated with fissured terrain (E, F, G). This association of high effusion rate lithology and a cluster of fissures may indicate the proximity of a lava vent, although fissures were observed all along the final 1.7 km of the dive.

2.3.4.5 Dive JC24-83

Dive JC24-83 (figure 2.2v) began at 45˚33.63 N, 27˚53.90 W in an area of flat seafloor to the west of the AVR, with a transect up the median valley wall to the west (A – B; figure 2.2v). It then took a 'blue water jump' eastwards, to resume near 45˚33.43 N, 27°53.85 W (C) whence it traversed to and up the AVR flank, following a NW – SE trending spur to 45˚33.38 N, 27˚53.22 W, approximately halfway up the AVR flank (C - F). Approximately 1.5 km of the track were characterised by in-situ lavas, and these were mainly pillow and lobate lava flows (table 2.1).

The first section of the dive, over flat seafloor near the base of the axial valley wall scarp, traversed heavily sedimented sheet flow outcrops (A; figure 2.2v) with SCs of 3.8 – 4.

The scarp itself (a 157 m talus deposit and a 277 m scarp) was characterised mostly by broken pillow faces (figure 2.3). Two thin sheet flow units, which were 5 and 6 m thick respectively, were observed at a depth of approximately 3120 m, separated by a 3m pillow flow. A 7m thick pillow and lobate unit lay above the sheet flow units at a depth of 3066 m. The rest of the scarp was composed of broken pillow faces. The seafloor at the top of the scarp had SC 4 (figure 2.4).

The ROV then dropped down onto the flat seafloor again (C) where moderately sedimented (SC 3 - 4) pillows and lobate flows were observed (figure 2.4) – the pillows forming slightly higher areas of topography. At D the ROV climbed a gentle, pillowed slope with an SC of 3, which formed a small ridge-like structure trending roughly N – S across the flat seafloor. The slope was gently stepped with flatter areas covered by primarily lobate with some pillow flows. The top of this area was covered by sheet flows and was cut by numerous eruptive fissures trending between 10° and 22°, parallel with the structure itself. This combined with its elevation and similar sediment covers to the surrounding sheet and lobate flows suggests it may have been their source. Beyond this ridge the dive crossed a further 600 m of flat sheet, lobate and pillowed terrain.

The base of the AVR slope is initially gentle (E), but becomes a small NW – SE orientated, W - facing 20 m scarp towards the top of the spur (F), which may be a small gravitational collapse (Yeo et al., 2012). Between F and the end of the dive there are pillows and elongate pillows with SCs of 3 (figure 2.4), forming gentle and moderate slopes, similar to previous dives.

2.3.4.6 Dive JC24-85

Dive JC24-85 covered a 3.9 km long track continuing on from the end point of dive JC24-83 at 45˚32.80 N, 27˚53.15 W, up a W – E orientated lateral spur and then up the western flank of the AVR to the summit at 45˚31.82 N, 27˚51.42 W (figure 2.2vi). In-situ lavas, predominantly pillows, were exposed along 2.1 km of the track (table 2.1).

The ROV crossed a 250 m gentle slope of pillow lavas (A; figure 2.2vi) before climbing a talus deposit and 20 m high scarp that appear in the sidescan sonar to form part of the side of a hummock. The ROV then crossed a further 1.9 km of pillowed, elongate pillowed and occasionally lobate lavas (A - C; hummocky terrain in the sidescan), crossing one small scarp at B. From C to D it climbed a series of talus deposits and scarps, which ranged from 3 to 62 m in height, with a total climb of 132 m.

Between D and the end of the dive the ROV climbed a further 158 m across sloping pillowed and elongate pillowed terrain, cut by two small (< 35 m high) roughly ridge-parallel scarps. The final hummock was characterised by an E – W orientated scarp on its southern side (E). This scarp is perpendicular to the regional N – S aligned pattern of faulting and is not associated with any faults observed in the sidescan sonar, suggesting it is a collapse feature (Yeo et al., 2012). Sediment ages on this section appeared slightly younger than those observed on other areas of pillowed terrain on the dive, with SCs between 2.5 and 3 on the pillowed hummock flanks (figure 2.4).

2.3.4.7 Dive JC24-88

Dive JC24-88 (figure 2.2vii) covered an 11.5 km track beginning at 45˚26.32 N, 27˚54.65 W on flat seafloor to the south west of the AVR. It crossed 2 flat-topped seamounts (at A and west of C), then skirted around the base of the AVR, crossing some individual hummocks, before meeting the start of dive JC24-80 at the southern end of the AVR at 45˚24.07N, 27˚52.50 W. In-situ lavas were exposed along 7.4 km of the track. The dive set out to explore an area of relatively high crustal magnetisation (indicative of recent volcanism) which lay just south west of the southern tip of the AVR (Searle et al., 2010).

The first 650 m of dive JC24-88 (A – B; figure 2.2vii) covered highly sedimented seafloor, predominantly of SC 4 (figure 2.4). Where there was exposure, pillows were observed with SCs of 3. The ROV then climbed a gentle, 47 m high, sedimented slope (the wall of an old (poorly backscattering) slightly irregular, flat-topped seamount seen in the sidescan sonar (A). The summit of the seamount was heavily sedimented, with rare, isolated pillow lavas across its 950m wide summit. However as the ROV crossed its south eastern flank, sediment cover decreased to SC 3.5 and pillow lavas were observed (B).

As the ROV reached the base of the seamount flank it crossed into an area of much more brightly backscattering hummocky terrain. This increase in backscatter correlates well with an instant decrease in sediment cover to SC 1.5 – 2.5 (figure 2.4). These younger inferred ages characterised the whole of the brightly reflecting seafloor in this 1.7 km wide, hummocky area. With the exception of the younger sediment ages this hummocky area was morphologically indistinct from hummocks elsewhere.

As the ROV moved back into the more darkly reflective area of low lying seafloor (C – D), sediment cover increased (up SC 4 in places, figure 2.4). The terrain was similar to flat seafloor observed on dives JC24-81 and JC24-83. Some texture could be observed in the sidescan sonar data, and although the seafloor appears flat, the ROV recorded depth fluctuations of up to 15m, so these structures may represent small hummocky features (possibly buried), or flow surface features due to inflation.

The ROV then crossed back into brightly backscattering terrain (D). This correlated with a drop in SC to < 3 (figure 2.4). This area of younger looking hummocky terrain, composed of pillows, elongate pillows and lobate flows, extended for 5 km (D - E). Three haystacks were observed on the summits of three separate hummocks and two small fissures at high angles to the strike of the AVR occurred on areas of lobate lava flows. Two small scarps were also observed. The final 450 m of the dive (E to end) covered more pillowed hummocky terrain. The SC remained < 3.

2.3.4.8 Dive JC24-89

Dive JC24-89 (figure 2.2viii) covered a 4.4 km long track across an area of mostly flat seafloor east of the AVR from 45˚34.52 N, 27˚48.15 W north to 45˚35.75 N, 27˚48.47 W. In-situ lavas were exposed along 3.2 km of the dive, comprising mainly pillow, elongate pillow and lobate lava flows (table 2.1).

The start of the dive covered a flat, pillowed area 8 m above lower, flat lying seafloor. This appears to correspond with faint hummocky texture in the flat seafloor (seen in the sidescan sonar). The flat seafloor was covered by both lobate and sheet flow lavas and met steeper pillowed terrain to the east, where a small scarp was observed (A; figure 2.2viii).

The ROV then followed the edge of a large area of flat seafloor that borders higher hummocky ground to the east (A - B). The hummocky terrain was composed of pillow lavas, elongate pillows and transitional lavas, which range from pillows to lobate lava flows. Some sections of the boundary were formed by scarps, as a result of gravitational collapse or faulting. All the lavas between A and B had SC > 3 (figure 2.4).

The ROV then crossed the 900 m wide area of flat seafloor (B – C), which was predominantly lobate lava flows with some pillow and sheet flow sections. The western side of the flat area was ~ 20 m shallower than the eastern side. The flat flow had similar sediment cover to the lavas on its boundary, with nothing younger than SC 3 (figure 2.4).

West and north of the flat flow was heavily sedimented (C – D) with small outcrops of lobate and sheet flow lavas and a ~ 1 m diameter lava tube (C). The final 1.2 km of the dive from D to the end covered hummocky terrain to the north of the flat area, composed of pillow lavas, lobate lavas and elongate pillow slopes. An increase in brightness in the sidescan sonar data (E) correlates with a slight decrease in sediment cover, from SC 3.5 – 4 to SC 2 – 3.5 (figure 2.4). The ROV crossed a final small collapse scarp on the southern side of a large hummock (F).

2.3.4.9 Dive JC24-90

Dive JC24-90 (figure 2.2ix) covered a 3.8 km long east – west transect across the northern section of the AVR, linking dives JC24-82 and JC24-89. It ran from 45˚35.75 N, 27˚48.40 W up a large spur on the eastern AVR flank and across the summit region to the top of the western flank at 45˚36.05 N, 27˚50.52 W. In-situ lavas were observed along 3.5 km of the dive track, comprising mainly pillow and elongate pillow lava morphologies (table 2.1).

The first 850 m of the dive covered regular, pillowed, elongate pillowed and occasionally lobate, hummocky terrain. The area covered is fairly bright in the sidescan sonar maps, and has lower sediment cover (SC 2 – 3; figure 2.4) than observed on dive JC24-89 on the median valley floor.

The ROV then crossed what looks like a 550 m wide flat-topped seamount or lava terrace in the north insonified sidescan sonar (A – B; figure 2.2ix), although this is less clearly defined in the south looking dataset (appendix B). The ROV climbed a 20° - 40° slope (possibly the seamount flank) composed entirely of pillows and elongate pillows (A). The summit plateau sloped < 10˚ and was covered by pillow and elongate pillow lavas, with areas of lobate flow on the eastern half. The flat area was cut by a small N – S orientated, 13 m high scarp, which displayed broken pillow lava faces. The central point of the flat area is characterised by a 25 m high pillowed/elongate pillowed mound with steep sides. This mound extends for 50 m east of the centre of the flat area, but almost the entire way to its western flank at B, possibly representing the final lava flow from a central vent (similar to a haystack on a hummock). Sediment cover on the flat area was SC 2.5 – 3, similar to that observed on the surrounding hummocky terrain (figure 2.4).

The last 1.3 km of the dive (B - end) covered typical hummocky terrain composed of pillow and elongate pillow lavas. Sediment cover was relatively low in this area compared to the rest of the AVR (SC mostly ranged from 2 – 3). The SC increased to 3.5 for the last 215 m of the dive (C), which corresponds to a decrease in brightness in the sidescan sonar data and may represent a boundary between different flows. A number of eruptive fissures were observed near the AVR crest (C) and may correspond to summit fissures observed on dive JC24-79, JC24-81 and JC24-92.

2.3.4.10 Dive JC24-92

Dive JC24-92 (figure 2.2x and 2.2xii) covered a 13.5 km long track, from the western valley-wall fault scarp across the median valley floor and up onto the summit of the AVR, which it then investigated in detail (in one of the two areas of high-resolution SM2000 mapping). Beginning at 45˚29.25 N, 27˚54.80 W it covered flat seafloor near the base of the western axial valley wall scarp, the scarp itself, and then the hummocky terrain forming the AVR, to the dive end at 45˚28.87 N, 27˚51.92 W. In-situ lavas were observed along 9.2 km of the dive, composed mainly of pillow, elongate pillow and lobate lava flows (table 2.1).

The ROV began by climbing the 90 m talus slope covering the base of the axial valley wall scarp (A; figure 2.2x). It then travelled up the 192 m scarp, which forms the lower section of the western axial valley wall. The scarp face displayed 0.2 – 0.5 m broken pillow faces. Five sheet flow units were observed in the face with thicknesses of 5 m, 3 m, 8 m, 2m and 10 m respectively, although the upper two were separated by talus and therefore may form part of the same flow, which would be upwards of 30 m thick (figure 2.3).

The ROV then dropped back down the scarp, onto a small pillowed hummock area (B) and crossed a smoother sloping area with 100% sediment cover before dropping down another, smaller scarp. The base of this second scarp was similarly characterised by a talus deposit and a gently sloping area of 100% sediment cover.

The ROV then dropped into a collapse pit in sheeted lava flows. This collapse pit connected with a series of fissures (C), which it followed. It then climbed 27 m out of the fissure, up a vertical wall of broken pillows, to emerge on a 180 m wide, flat area of lobate lavas and sedimented seafloor (SC 3.5 – 4). The ROV then crossed a small, less sedimented (SC 2), pillowed hummock (D). This hummock was flanked on its east side by older lobate and sheet flows.

The ROV then met a scarp of broken sheet flows orientated SW –NE, which it followed for 150 m before climbing a N – S orientated, 8 m high slope of broken up pillow and sheet flow lavas. The top of the slope was covered by pillow lavas, which formed a N-S orientated spur (E; spur is obscured by the track). The spur was cut by a scarp and the ROV dropped down onto sedimented and then further pillowed seafloor. The dive then covered 2.5 km of typical hummocky terrain (SC 3.5 – 4) between E and G, and a small, 150 m wide, flat lobate lava flow with SC 3 (F).

The ROV then investigated in detail a 2 km x 1 km area of hummocky terrain, which was also covered by the SM2000 bathymetry (G – O). All the hummocks encountered had a similar level of sediment cover, with typical SCs of 3 (figure 2.4). Pillows and elongate pillows were the most common lava lithologies observed, while lobate flows were more common on hummock summits. Thirteen scarps were observed, most of which were outward (east) facing, suggesting either small outward facing normal faulting, or collapse down slope. Due to the small field of view it is impossible to distinguish between faulting and ridge parallel volcano flank collapse from the video data. A number of the hummocks in this area had flanks with slopes up to 45˚. A number of fissures were observed in this area, typically on hummock summits.

2.3.4.11 Dive JC24-93

Dive JC24-93 (figure 2.2xi and 2.2xii) covered 7.7 km of seafloor in the form of two, approximately 500 m spaced, transects up the eastern AVR flank, just south of dive JC24-79. Both transects started on the low-lying seafloor near the base of the eastern axial valley wall fault (the first at 45˚29.25 N, 27˚50.60 W) and climbed to the crest (the second one finishing at 45˚29.10 N, 27˚51.90 W). Excluding a substantial blue jump between the two transects, a second smaller blue jump, talus flows and heavy sediment cover on the far eastern side meant that in-situ lavas were observed along only 4.0 km of the dive track (table 2.1).

Both transects crossed hummocky terrain just north of that covered by dive JC24-92. The first (northern) one covered 9 hummocks, composed predominantly of pillow lavas and elongate pillows. Four of these hummocks were cut by scarps, predominantly outward facing (A, B, C, E; figure 2.2xi). Lobate lava flows were only observed on the summit of one hummock (D), close to the end of the first transect and the crest of the AVR.

The second transect covered a further 9 hummocks, 5 of which were cut by outward facing scarps (F, G, H, I, J). Again, the most common lava lithologies observed were pillow lavas and elongate pillows, although lobate flows were more common on this southern transect than the northern one, observed on 5 hummocks, both near and away from the AVR crest. A transect across one of these broken faces (I), shows elongate pillows dipping gently (10 – 20 ˚) away from the central conduit.

On both transects the sediment cover appeared to be distributed similarly (figure 2.4). The most sedimented hummocks (SC 3.5 – 4) lay at the eastern ends of the transects, close to the eastern axial valley wall, suggesting these lavas were older. Between these older looking lavas and the AVR crest sediment ages were predominantly SC 3 on pillowed terrain, although the talus flows associated with the scarps were less sedimented (figure 2.4). This may be because faulting and collapse are more recent processes, because talus deposits are regularly resurfaced by additional lavas falling off the scarp, or because sediment is easily shaken off these deposits during tremors. The apparently youngest hummocks, with SC 2 – 2.5, lay on the crest of the AVR (figure 2.4).

2.3.5. General Observations

2.3.5.1 Volcanic morphology

Volcanic hummocks with diameters 30 – 350 m were observed all over the AVR and on parts of the surrounding lower lying terrain. Slopes on the flanks of hummocks were typically 20° to 40° and their summits ranged from almost flat to > 20°. Many were characterised by summit haystacks (figure 2.5; P).

Flat seafloor, composed mainly of sheet and lobate lava flows, was observed around the AVR, particularly in the north. In some places pillow lavas can be observed forming on the top surfaces of sheet and lobate flows (figure 2.5; O). Pillow lavas were also observed in small discrete areas within the sheet flows, which appear to correlate to small hummocks observed in the sidescan sonar.

Nineteen flat-topped seamounts are imaged in the EM120 data as mapped by Searle et al. (2010). Flat-topped seamounts are predominantly observed around the AVR rather than on it (7 of the seamounts lie outside the axial valley floor, only 2 lie on the AVR) and are distributed fairly evenly from north to south. Three flat-topped seamounts were dived on, two near 45˚25.85 N, 27˚54.45 W (dive JC24-88) and one at 45˚42.58 N, 27˚46.52 W (dive JC24-81). All of these were characterised by sloping (15 – 40˚) pillowed or elongate pillowed lava flows on their flanks and high effusion rate sheet flow or lobate flows on their flat (< 10˚) tops.

2.3.5.2 Fissures

Eruptive fissures consist of narrow, sinuous fissures with less than a metre of separation and pillows and lobate flows spilling out of them (figure 2.5; J). The linear, or ‘tectonic’ fissures (K) are straighter and much wider (up to 15 m) and deeper (> 30 m) with vertical walls composed of broken pillow lava or broken sheet flow faces. This classification is purely given as a way to distinguish two separate morphologies of fissure. Linear fissures may have erupted in the past and many had a mix of talus and pillows in their bases and pillows on their edges, which were probably erupted from the fissure. In some cases these larger fissures have small vertical offsets. Fissures are predominantly ridge parallel (figure 2.6) with 70% of measured strikes lying within $\pm$ 025˚ of the AVR strike; the distribution of orientations of the purely eruptive and large linear fissures is very similar.

Trapdoors (figure 2.5; L) and heavily sedimented collapse pits (M) (which were the same size and may be the sedimented trapdoors) were also observed associated with the sheet and lobate lava lithologies.

2.3.5.3 Fault scarps

Faults were observed on the axial valley walls, consisting of stepped vertical or near vertical sections, from 5 m to several hundred metres in height, of broken lavas separated by small 2-5 m flat benches that were usually fairly heavily sedimented. These wall scarps produced quite extensive talus deposits extending away from their bases for up to 300m. Smaller scarps, usually < 100 m in height, are also observed on the AVR as both faults and gravitational collapse scars on hummocks (Yeo et al., 2012).

2.3.5.4 Sediment distribution

While flatter lying lava flows often appeared more sedimented (typically between SC 3 and 4), where broken surfaces were exposed this sediment cover was shown to be usually < 10 cm, which would be comparable to SC 2 to 3 (30 – 90 % cover) for the AVR pillow lavas. The apparently youngest observed lavas were seen on dive JC24-88 on the southern and south western section of the AVR and surrounding seafloor, with sediment cover of 10% - 60 % (SC as young as 1-2) being observed. Lavas with sediment cover < 10% (SC 0) were not observed anywhere.

2.3.6 Discussion

2.3.6.1 Eruption products

The building blocks of the AVR at the MAR 45˚N are pillow, lobate and very rarely sheet lava flows, as found elsewhere on the MAR (Ballard and Moore, 1977; Ballard and Van Andel, 1977; Briais et al., 2000; Brown and Karson, 1988; Sinton and Detrick, 1992; Smith and Cann, 1990; Smith and Cann, 1993).

Pillow lavas form the main building blocks of hummocks and were additionally observed on the flanks of flat-topped seamounts and in areas of flat seafloor, suggesting that multiple lava morphologies can be produced by the same flow. Elongate pillow lavas are observed only on slopes over 15˚ and predominantly on those > 20˚, consistent with observations elsewhere (Kennish and Lutz, 1998; Wells et al., 1979).

Sheet lava flows were observed only around the edges of the AVR (Searle et al., 2010) or on the summits of flat-topped seamounts, where the seafloor is flat or very gently sloping (< 5˚), suggesting that they are only produced on areas of low gradient seafloor, or that they produce such seafloor as a result of faster effusion rates. Some areas of the flat seafloor appeared slightly hummocky, suggesting that they did have some (normally less than 10 m) relief. This may be due to the burial of hummocky terrain beneath these flows (as suggested by Murton et al. (2012) or be due to inflation (as evidenced by the observation of numerous tumuli) or deflation of the flow surface during the eruption.

2.3.6.2 Relative proportions of lithologies

Relative abundances of each observed lava lithology were estimated by measuring the length of exposure of each along the dive track in comparison to the total dive length (table 2.1). Since the dives were not randomly allocated but chosen to cover specific features, this is not a completely unbiased estimate of different lava abundances, but does provide a rough indication of the percentage of seafloor that is currently being produced by each flow type. Purely pillow lava flows (pillows + elongate pillows) cover 51% of the seafloor but are observed either alone or with other lava morphologies on over 77 % of seafloor surveyed. This makes them by far the most common lava lithology and suggests that they are probably also the most common current eruptive product on the AVR. The sheeted flows by comparison were observed on only 6 - 10 % of the surveyed seafloor (> 30 % in areas of flat-seafloor), but are probably slightly under-represented in the observations as they are buried so easily by sediment. Lobate flows are also observed less frequently than pillows, covering 13 – 43 % of the observed seafloor. Sheet flows and lobate flows together are observed on > 80% of areas of flat seafloor (table 2.2). Both sheet flows and lobate flows are considered to result from higher effusion rates (Griffiths and Fink, 1992) and are much less common than pillow lavas. As we see them only on low gradient seafloor and they form recognisable flat-looking, uniformly medium-level backscatter seafloor on the 45˚N sidescan sonar maps, it is unlikely that the AVR itself has any sheet flows at all on its surface (excluding flat-topped seamounts), while lobate flows occur only on the flatter summits of hummocks. This difference in lithology between hummocky terrain and flat-seafloor suggests that the two types of seafloor are produced by lavas erupting at different effusion rates, suggesting there is a difference in eruption effusion rate, and therefore potentially magma properties, magma chamber depth or feeding mechanism.

It is possible there are two types of hummocks, and that those with lobate summits would have a higher degree of flatness. Alternatively, the degree of flatness may grade, increasing with increasing effusion rate. However, we only have accurate height and diameter information in the high resolution study area, and summit morphology was only observed on 24 hummocks in this area, which is too small a sample to be representative of the ~ 3000 hummocks observed on the surface of the AVR (Yeo et al., 2012). This is discussed further in Chapter 3, section 3.4.2.3.

2.3.6.3 Relative ages

Where pillow and sheet flows can be observed in cross section the sheet flows appear to have a similar thickness of sediment (usually < 10 cm) lying on their surfaces. It is therefore likely that both types of volcanism are occurring in a similar time frame (although not necessarily at the same time). The low exposure of the flat lying lava flows makes examining the contact relationships between them and the edge of the AVR flank very difficult. Where such contacts are covered by dives, the flat seafloor appears to grade into pillows, appearing first sparsely as single pillows on the surface of the flat lava flow and becoming more common as you get closer to the steep AVR flank. However, there is no evidence of a pillowed flow flowing over the sheet flow, which would cause a sudden change in lithology and gradient, and therefore it seems likely that the flat-lying flows here on-lap the pillowed flows.

With a regional sedimentation rate ~5 cm/ky (Keen and Manchester, 1970) the observed sediment cover on the eastern side of the AVR and in the JC24-83 area, which we observe in cross section, suggests that these sheet flows were erupted less than 2000 years ago. The other flat lying lava flow, covered by dive JC24-88, was not observed in cross section so may be older, as mapped by Searle et al. (2010). Since parts of the AVR appear to be as old as 12 ky (Searle et al., 2010), these young, flat-lying lavas were erupted either during AVR construction or, if the AVR is no longer being built, very shortly afterwards.

There is no evidence for them being the earliest eruptive products, preceding AVR construction, as suggested elsewhere (e.g. Parson et al. (1993).

While the SC scale is not a quantitative one, the differences between SC categories is probably equivalent to between 25 and 50 cm of sediment thickness, which equates to between 5 and 10 thousand years of sediment deposition. It therefore seems likely that, with the exception of the younger lava flows observed on the southern tip of AVR, all the lavas observed during the dives, and probably most of those on the surface of the AVR, were erupted in a single 5 – 10 thousand year period.

These observations are more or less consistent with the observations of sediment cover and the palaeointensity dates for the AVR (Searle et al., 2010).

2.3.6.4 Feeding lava flows

The pillow lavas and elongate pillow lavas mainly form the eruptive hummocks, which are the main building blocks of AVRs (Smith and Cann, 1990; Yeo et al., 2012). These hummocks are often characterised by small haystacks which are located on their summits, commonly at their highest points. Haystacks have steep sides formed of elongate pillows, and as they sit right on the top of the hummocks, they probably represent the very last lavas to be erupted in this location. As such they give us an indication of the location of the vent and this, combined with the fact that the hummocks are fairly circular in shape, suggests that hummocks are centrally fed. Where observed in cross section (as the result of gravitational collapse) the elongate pillows exposed in the collapse face appear to dip gently downwards by 10 – 20˚ away from the centre of the hummock (observed on dive JC24-93). No conduits are exposed by collapses. However, the hummock at 27˚51 W, 45˚29 N has undergone a collapse ~ 20 m from the summit haystack. The collapse face was comprehensively surveyed by the ROV video dives and no conduit is exposed, indicating that for this hummock (typical of those observed in the area) the conduit, if there is one, must be < 40 m in diameter (twice the distance between the scarp and the summit haystack).

The largest and most comprehensively surveyed area of lobate and sheet flows lies in dive JC24-81 area, northeast of the AVR. As lavas do not flow uphill the highest point on this flow should be at the source, as long as no tectonic uplift has occurred post eruption. There is no suggestion from our medium-resolution bathymetry or high-resolution side-scan that the lava flow is extensively faulted, with the exception of two small NNW – SSE orientated faults at 45˚40.13 N, 27˚46.97 W and 45˚39.62 N, 27˚47.68 W. Bathymetry of the area (figure 2.1) shows that the deepest area of flat seafloor lies roughly in the middle of the flat area (at 45˚41.84 N, 27˚47.03 W at a depth of 3641 m), close to the base of the western axial valley wall fault in the non-transform offset and just south of a flat-topped seamount. The shallowest depths (~ 3540 m) are found at the southern end of the flow at 45˚38.80 N, 27˚47.97 W,. This is also the area in which the greatest number and densest spacing of eruptive fissures is observed (dive JC24-81), suggesting it may have fed an eruption. These results must be treated with some caution though as inflation and deflation of the flow surface could cause irregularities of a few metres and therefore the slope of the area may not be directly related to the flow direction (Fox et al., 2001). If this entire flat area was produced by a single eruption sourced from the south, it should slope gently away from this point and this is not the case. In fact some of the deeper terrain (45˚39.83 N, 27˚48.24 W) lies just north of this high area, directly between the high and the rest of the flow. In addition, a number of highs and lows are observed across its surface.

Alternatively, Murton et al. (2012, in prep) suggest, partly on the basis of geochemical affinities, that the sheet flows in these areas are being fed by the flat-topped seamounts, but as not all the flat seafloor is associated with a flat-top (e.g. the flat area covered by dive JC24-83), this cannot be the only explanation.

The second area of flat seafloor studied in detail was on the western side of the AVR and covered by dive 83 (figure 2.1). Here a small elongate high with lows on either side is observed aligned ~ 020˚. This elongate high may represent a fissure along which the eruption was fed, the mechanism suggested to feed eruptions at this mid-ocean ridge (Searle et al., 2010; Yeo et al., 2012) and correlates with an area of slightly more pillowed hummocky terrain on the dives and a number of fissures with similar alignments. However, no such features are observed on any of the other flat seafloor areas.

I am therefore unable to conclude where the sheet flows forming the flat seafloor were fed from, but suggest that these raised, fissured areas may correspond to sheet flow vents. There may be multiple eruption sites for the flat area of seafloor, or more than one eruption. Hopefully further geochemical work (being carried out at NOC, Southampton) will help to answer these questions.

2.3.6.5 Fissuring

The role of fissures in feeding both flat and hummocky lava flows appears to be quite a complex one. The fissures that were obviously eruptive were all very small, meaning that either all of the lavas are erupted through single short, narrow fissures or, as seems more likely, that more than one fissure was active at a time, or that the true fissure sources are buried under the lavas. Eruptive fissures were observed both on the hummocky terrain of the AVR (mainly on the summits of hummocks displaying lobate flows) and on the flat areas of sheet and lobate flows around the AVR. Interestingly in the sheet and lobate flow areas the fissures are not only found on the shallowest parts of the flow (although commonly cluster in such areas) , where they were most likely erupting from, but occur fairly randomly distributed all over them. This suggests either that there are a large number of flows occurring, each being fed by a small fissure or series of fissures, or that these fissures are superficial features, possibly formed by overpressure in certain parts of the flow or tearing of the crust. Some of the tectonic fissures also showed evidence of having once erupted, so it is possible that these larger fissures also fed eruptions.

2.3.6.6 Flat-topped seamounts

Our observations show that the flat-topped seamounts have moderately sloping flanks of between 10 and 40˚, characterised by pillow and elongate pillow lavas. Their summits have high effusion rate sheet and lobate flows which appear to feed the pillows forming the flanks. The pillowed flanks are all fairly heavily sedimented, suggesting that they predate the younger looking pillowed flows on the AVR. Summits are very slightly domed, with the highest point at the centre, suggesting they are centrally fed. Summits are also very simple: the only features observed were small tumuli exposing sheet flows; no fissures were observed. This lack of complexity suggests either a monogenetic origin for such seamounts (Clague et al., 2000), or that they have been completely resurfaced during their last eruption. None of the seamounts showed any evidence of summit depressions, although these have been seen at other locations (Head et al., 1996; Smith et al., 1995a), suggesting that at 45°N draining did not occur prior to solidification.

Eighteen of the 19 imaged flat-topped seamounts lie at least 2 km from the axis, representing an age of more than ~20,000 yr at the segment half spreading rate of 1.1 cm/yr. Seven of the 19 lie more than 5 km away from the segment axis representing ages of more than 50,000 yr. These ages are as old as or older than the estimated age of the AVR of ~10,000 yr from palaeointensity dating (Searle et al., 2010; Yeo et al., 2012) or the ~18,000 yr age of the AVR calculated using half spreading rate. While it is possible that these flat-topped seamounts were produced off axis, as documented on the MAR at 24°N (Lawson et al., 1996), the fact that we see one flat-topped seamount (at 27˚50.00 W, 45˚33.50 N) sitting almost directly on the AVR axis suggests that this is an equally viable location for their construction. This latter seamount also has the highest acoustic backscatter of the seamounts imaged by this TOBI survey, suggesting it is the youngest.

2.3.6.7 Sediment Cover

The youngest sediment ages inferred from pillow lavas were on the southern sections of dive JC24-88. This corresponds with a high in the crustal magnetization inferred from TOBI data (Searle et al., 2010). Since near-axis magnetisation is closely related to age (Hussenoeder et al., 1996; Searle et al., 2010), this suggests that the most recent eruptions on the AVR were at its southernmost point. The most complete sediment cover by area was observed on the flat seafloor at the northern end of the AVR (dive JC24-81), although in cross section the cover here is not noticeably thicker than elsewhere on the AVR and the higher SC is due to the low topography on these flows being easily buried. The more tectonised northern AVR does appear to have marginally older SCs than the southern section when comparing pillowed terrain, corresponding with the observed lower crustal magnetisation of the northern area as described in Searle et al. (2010).

The fact that most of the AVR has a similar degree of sediment cover suggests that much of it, at least on the surface, is of a similar age, particularly on the more robust southern section. While the SC scale is not a quantitative one, the differences between SC categories is probably equivalent to between 25 and 50 cm of sediment thickness, which, with the sediment accumulation rate of 5cm/ka (Keen and Manchester, 1970), equates to between 5 and 10 thousand years of sediment deposition. It therefore seems likely that, with the exception of the younger lava flows observed on the southern tip of AVR, all the lavas observed during the dives, and probably most of those on the surface of the AVR, were erupted in a single 5 – 10 thousand year period.

2.3.7 Conclusions

The main building blocks of AVRs are small hummocks composed almost entirely of pillows and occasional lobate flows. Similar degrees of sediment on hummocks and no obvious overlapping contact relationships suggest that more than one hummock is formed at the same time. The flat-seafloor and the hummocky terrain are composed of different morphologies, with the hummocky terrain being composed of mostly pillow and elongate pillow lavas with small amounts of lobate lava flows. The flat-seafloor is characterised by higher percentages of higher effusion rate sheet and lobate lava flows suggesting that there is a difference in magma properties, magma chamber depth or eruption mechanism on and off the AVR.

Pillow lavas are by far the most common form of volcanism in the 45°N axial valley and are observed almost everywhere, either as pure pillow lava flows, or in association with higher effusion rate lava morphologies. Sheet flow lithologies are confined to the summits of the large flat-topped seamounts and to areas of flat seafloor surrounding the AVR. Both the pillow lava flows in the AVR and the sheet flows around the AVR have similar degrees of sediment cover, suggesting that they were erupted at approximately the same time. There is little variation in the inferred ages of flows on the AVR surface and no obviously contrasting contact relations between different flows, although observations are consistent with the flat-seafloor onlapping the AVR flanks. This suggests that most of the lavas observed, particularly those observed on the AVR itself, were erupted in a single period lasting < 10,000 yr, and that at least some of the flat-seafloor is younger than the hummocky AVR.. No very fresh lavas were observed on the AVR, however the apparently most recent eruptions occurred at the southern tip of the AVR.

Eruptions appear to be fed by clusters of small fissures, probably above a feeder dyke, although small, single eruptive fissures are also observed distributed all over the AVR, often on the summits of hummocks. Similar fissures may feed linear rows of hummocks in hummocky terrain (Searle et al., 2010) or elongate highs in the sheet and lobate flows.

The flat-topped seamounts appear to be the oldest features observed within the axial valley, with the exception of the single young seamount observed on the axis, suggesting they were formed before or during the early phases of AVR construction. We cannot say whether they formed on or off axis from this dataset, although they do not appear very broken up and I therefore suggest they can form both on and off axis.

2.3.8 Acknowledgements

This work was funded by the Natural Environment Research Council (NERC). Yeo acknowledges receipt of an NERC postgraduate studentship. We thank the shipboard scientific party, officers, crew, and technicians of RRS *James Cook* cruise 24 for their dedication and professionalism in assisting in the data acquisition.

2.4 References

Aumento, F., Loncarev.Bd, and Ross, D.I., 1971, Hudson Geotraverse - Geology of the Mid-Atlantic Ridge at 45 Degrees N Philosophical Transactions of the Royal Society of London Series a-Mathematical and Physical Sciences, v. 268, p. 623.

Ballard, R.D., Francheteau, J., Juteau, T., Rangan, C., and Normark, W., 1981, East Pacific rise at 21°N: The volcanic, tectonic, and hydrothermal processes of the central axis: Earth and Planetary Science Letters, v. 55, p. 1-10.

Ballard, R.D., and Moore, J.G., 1977, Photographic Atlas of the Mid-Atlantic Ridge Rift Valley: New York, Springer-Verlag, 114 p.

Ballard, R.D., and Van Andel, T.H., 1977, Morphology and tectonics of inner rift valley at lat 36degree50'N on Mid-Atlantic Ridge Geological Society of America Bulletin, v. 88, p. 507-530.

Bellaich.G, Cheminee, J.L., Franchet.J, Hekinian, R., Lepichon, X., Needham, H.D., and Ballard, R.D., 1974, Inner floor of rift valley - First submersible study Nature, v. 250, p. 558-560.

Bideau, D., Hekinian, R., Sichler, B., Gracia, E., Bollinger, C., Constantin, M., and Guivel, C., 1998, Contrasting volcanic-tectonic processes during the past 2 Ma on the Mid-Atlantic Ridge: submersible mapping, petrological and magnetic results at lat. 34 degrees 52 ' N and 33 degrees 55 ' N: Marine Geophysical Researches, v. 20, p. 425-458.

Briais, A., Sloan, H., Parson, L.M., and Murton, B.J., 2000, Accretionary processes in the axial valley of the Mid-Atlantic Ridge 27 degrees N-30 degrees N from TOBI side-scan sonar images: Marine Geophysical Researches, v. 21, p. 87-119.

Brown, J., and Karson, J., 1988, Variations in axial processes on the Mid-Atlantic Ridge: The median valley of the MARK area: Marine Geophysical Researches, v. 10, p. 109-138.

Bryan, W.B., Humphris, S.E., Thompson, G., and Casey, J.F., 1994, Comparitive volcanology of small acial eruptive centres in the MARK area Journal of Geophysical Research-Solid Earth, v. 99, p. 2973-2984.

Clague, D.A., Moore, J.G., and Reynolds, J.R., 2000, Formation of submarine flat-topped volcanic cones in Hawai'i: Bulletin of Volcanology, v. 62, p. 214-233.

Flewellen, C., Millard, N., and Rouse, I., 1993, TOBI, A Vehicle for Deep Ocean Survey Electronics & Communication Engineering Journal, v. 5, p. 85-93.

Fox, C.G., Chadwick, W.W., and Embley, R.W., 2001, Direct observation of a submarine volcanic eruption from a sea-floor instrument caught in a lava flow: Nature, v. 412, p. 727-729.

Francheteau, J., and Ballard, R.D., 1983, The East Pacific Rise near 21°N, 13°N and 20°S: inferences for along-strike variability of axial processes of the Mid-Ocean Ridge: Earth and Planetary Science Letters, v. 64, p. 93-116.

Gente, P., Mevel, C., Auzende, J.M., Karson, J.A., and Fouquet, Y., 1989, An example of a recent accretion on the Mid-Atlantic Ridge - The Snake Pit neovolcanic ridge (MARK area, 23-degrees-22'N) Symp at the 5th Biennial Meeting of the European Union of Geosciences (Eug-5) : The Geology, Geophysics and Metallogeny of the Present-Day Oceans: Strasbourg, France, Elsevier Science Bv, p. 1-29.

Gràcia, E., Parson, L.M., Bideau, D., and Hekinian, R., 1998, Volcano-tectonic variability along segments of the Mid-Atlantic Ridge between Azores platform and Hayes fracture zone: evidence from submersible and high-resolution sidescan sonar data: Geological Society, London, Special Publications, v. 148, p. 1-15.

Griffiths, R.W., and Fink, J.H., 1992, Solidification and morpholoy of submarine lavas - A dependence on extrusion rate Journal of Geophysical Research-Solid Earth, v. 97, p. 19729-19737.

Head, J.W., Wilson, L., and Smith, D.K., 1996, Mid-ocean ridge eruptive vent morphology and substructure: Evidence for dike widths, eruption rates, and evolution of eruptions and axial volcanic ridges: Journal of Geophysical Research-Solid Earth, v. 101, p. 28265-28280.

Hussenoeder, S.A., Tivey, M.A., Schouten, H., and Searle, R.C., 1996, Near-bottom magnetic survey of the Mid-Atlantic Ridge axis, 24°–24°40′N: Implications for crustal accretion at slow spreading ridges: J. Geophys. Res., v. 101, p. 22051-22069.

Karson, J.A., Thompson, G., Humphris, S.E., Edmond, J.M., Bryan, W.B., Brown, J.R., Winters, A.T., Pockalny, R.A., Casey, J.F., Campbell, A.C., Klinkhammer, G., Palmer, M.R., Kinzler, R.J., and Sulanowska, M.M., 1987, Along-axis variations in sea-floor spreading in the MARK area Nature, v. 328, p. 681-685.

Keen, M.J., and Manchester, K.S., 1970, The Mid-Atlantic Ridge near 45ºN. X. Sediment distribution and thickness from seismic reflection profiling: Canadian Journal of Earth Sciences, v. 7, p. 735-747.

Keeton, J.A., and Searle, R.C., 1996, Analysis of Simrad EM12 multibeam bathymetry and acoustic backscatter data for seafloor mapping, exemplified at the Mid-Atlantic Ridge at 45 degrees N: Marine Geophysical Researches, v. 18, p. 663-688.

Kennish, M.J., and Lutz, R.A., 1998, Morphology and distribution of lava flows on mid-ocean ridges: a review: Earth-Science Reviews, v. 43, p. 63-90.

Kong, L.S.L., Detrick, R.S., Fox, P.J., Mayer, L.A., and Ryan, W.B.F., 1989, The morphology and tectonics of the MARK area from sea marc-I observations (Mid-Atlantic Ridge 23-degrees-N) Marine Geophysical Researches, v. 10, p. 59-90.

Lawson, K., Searle, R.C., Pearce, J.A., Browning, P., and Kempton, P., 1996, Detailed volcanic geology of the MARNOK area, Mid-Atlantic Ridge north of Kane transform: Geological Society, London, Special Publications, v. 118, p. 61-102.

LeBas, T.P., 2005, PRISM - Processing of Remotely-sensed Imagery for Seafloor Mapping - Version 4.0, Southampton, National Oceanography Centre.

Mello, S.L.M., Cann, J.R., and Fowler, C.M.R., 1999, Anomalous mantle at 45 degrees N Mid-Atlantic Ridge?: Journal of Geophysical Research-Solid Earth, v. 104, p. 29335-29349.

Mitchell, N.C., 1995, Characterising the extent of volcanism at the Galapagos Spreading Centre using Deep Tow sediment profiler records: Earth and Planetary Science Letters, v. 134, p. 459-472.

Murton, B.J., Schroth, N., Le Bas, T.P., Van Calsteren, P., Searle, R.C., and Yeo, I., 2012, in prep, Formation of oceanic crust at slow spreading ridges by continuous Axial Volcanic Ridge processes: In prep.

Parson, L.M., Murton, B.J., Searle, R.C., Booth, D., Evans, J., Field, P., Keeton, J., Laughton, A., McAllister, E., Millard, N., Redbourne, L., Rouse, I., Shor, A., Smith, D., Spencer, S., Summerhayes, C., and Walker, C., 1993, En-echelon axial volcanic ridges at the Reykjanes Ridge- A life-cycle of volcanism and tectonics Earth and Planetary Science Letters, v. 117, p. 73-87.

Searle, R.C., Murton, B.J., Achenbach, K., LeBas, T., Tivey, M., Yeo, I., Cormier, M.H., Carlut, J., Ferreira, P., Mallows, C., Morris, K., Schroth, N., van Calsteren, P., and Waters, C., 2010, Structure and development of an axial volcanic ridge: Mid-Atlantic Ridge, 45°N: Earth and Planetary Science Letters, v. 299, p. 228-241.

Sempere, J.C., Purdy, G.M., and Schouten, H., 1990, Segmentation of the Mid-Atlantic Ridge between 24-degrees-N and 30-degrees-40'N Nature, v. 344, p. 427-431.

Sinton, J.M., and Detrick, R.S., 1992, Midocean ridge magma chambers Journal of Geophysical Research-Solid Earth, v. 97, p. 197-216.

Smith, D.K., and Cann, J.R., 1990, Hundreds of small volcanoes on the median valley floor of the Mid-Atlantic Ridge at 24-30[deg] N: Nature, v. 348, p. 152-155.

—, 1992, The role of seamount volcanism in crustal construction and the Mid-Atlantic Ridge (24-degrees-30-degrees-N) Journal of Geophysical Research-Solid Earth, v. 97, p. 1645-1658.

—, 1993, Building the crust at the Mid-Atlantic Ridge Nature, v. 365, p. 707-715.

Smith, D.K., Cann, J.R., Dougherty, M.E., Lin, J., Spencer, S., Macleod, C., Keeton, J., McAllister, E., Brooks, B., Pascoe, R., and Robertson, W., 1995a, Mid-Atlantic Ridge volcanism from deep-towed side-scan sonar images, 25-degrees-29degrees-N Journal of Volcanology and Geothermal Research, v. 67, p. 233-262.

Smith, D.K., Humphris, S.E., and Bryan, W.B., 1995b, A comparison of volcanic edifices at the Reykjanes Ridge and the Mid-Atlantic Ridge at 24-degrees-30degrees-N Journal of Geophysical Research-Solid Earth, v. 100, p. 22485-22498.

Wells, G., Bryan, W.B., and Pearce, T.H., 1979, Comparative Morphology of Ancient and Modern Pillow Lavas: The Journal of Geology, v. 87, p. 427-440.

Yeo, I., Searle, R.C., Achenbach, K.L., Le Bas, T.P., and Murton, B.J., 2012, Eruptive hummocks: Building blocks of the upper ocean crust: Geology, v. 40, p. 91-94.

2.5 Figures

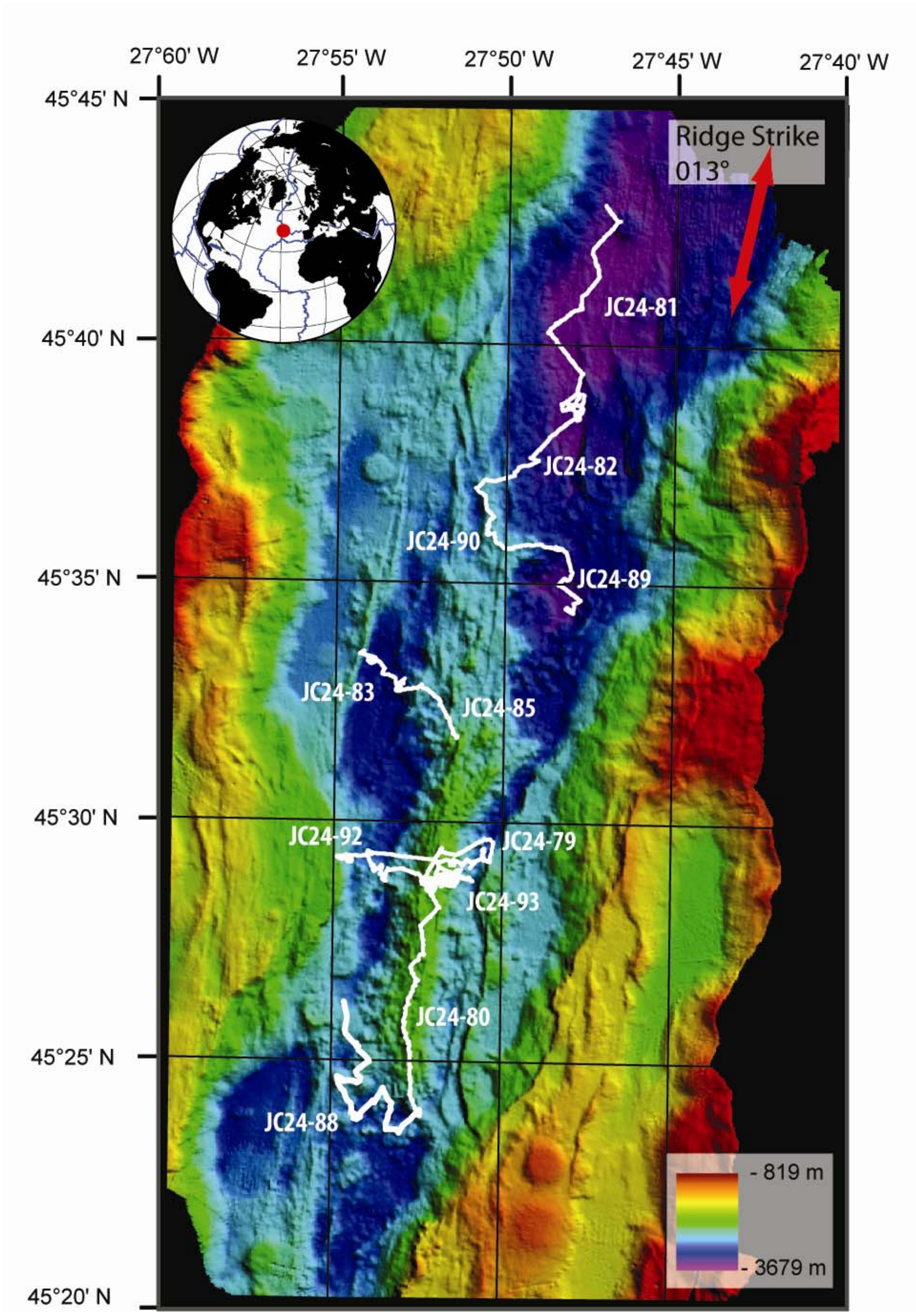

Figure 2.1: EM120 bathymetry for the ridge segment at 45˚30 N on the Mid-Atlantic Ridge. Video dive tracks are shown in white, with their dive numbers.

Figure 2.2: Lithology along the dive track for each dive shown. In each figure, the first panel shows 20 m contoured maps (thicker contours at 100m intervals), the second panel shows the corresponding TOBI sidescan sonar imagery, and the third panel shows a cross section, with distance along track shown as a horizontal coordinate, in metres . Letters correspond to dive descriptions in the chapter. The sidescan sonar is south looking for every dive. Letters correspond to dive descriptions in the chapter. The dives in the JC24-91 high-resolution study area are shown, on the high-resolution bathymetry in figure 2.2xii. Digital versions of each map (at 1:10,000 scale) are included in appendix 9.5.

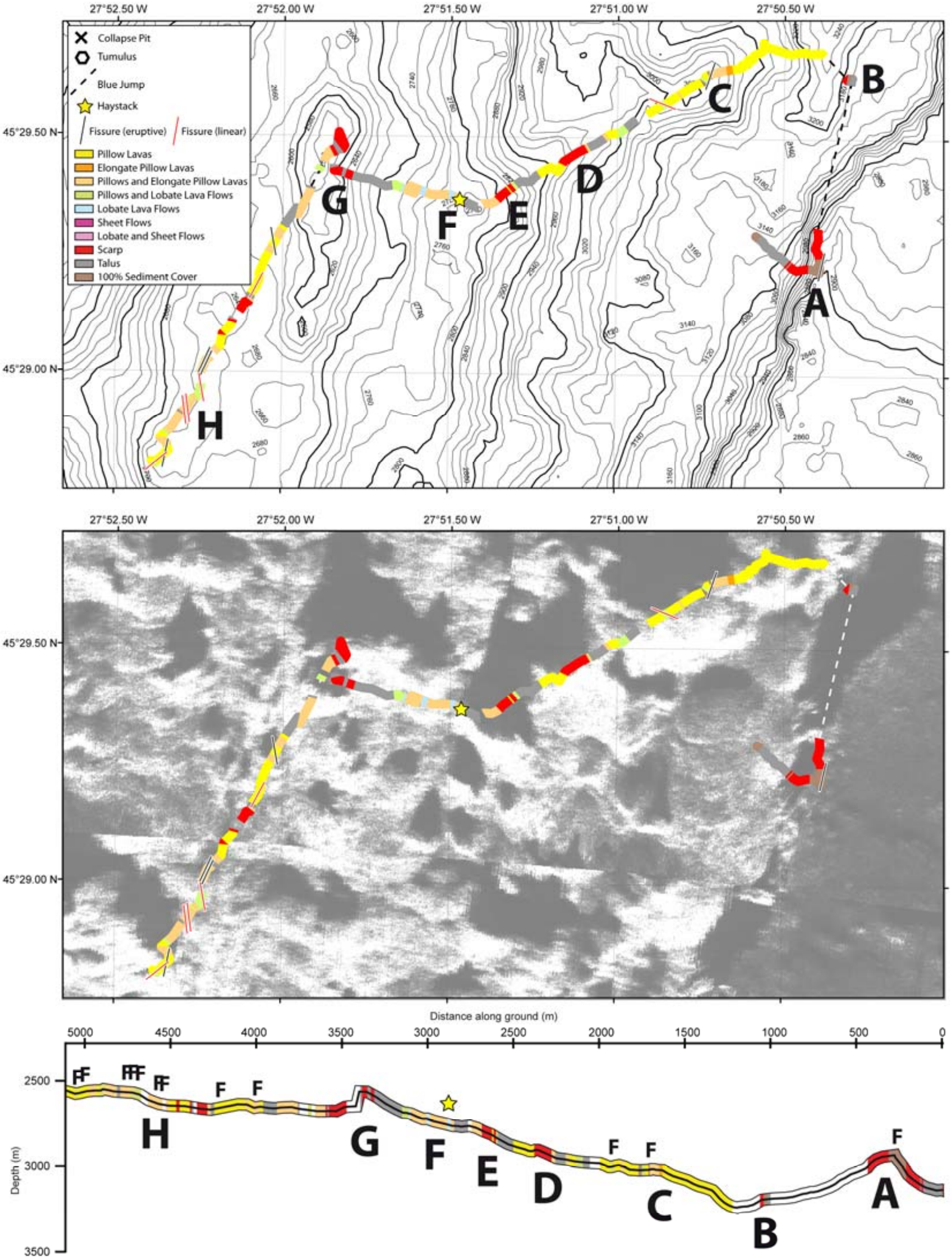

Figure 2.2i: Dive JC24-79 (see also 2.2xii)

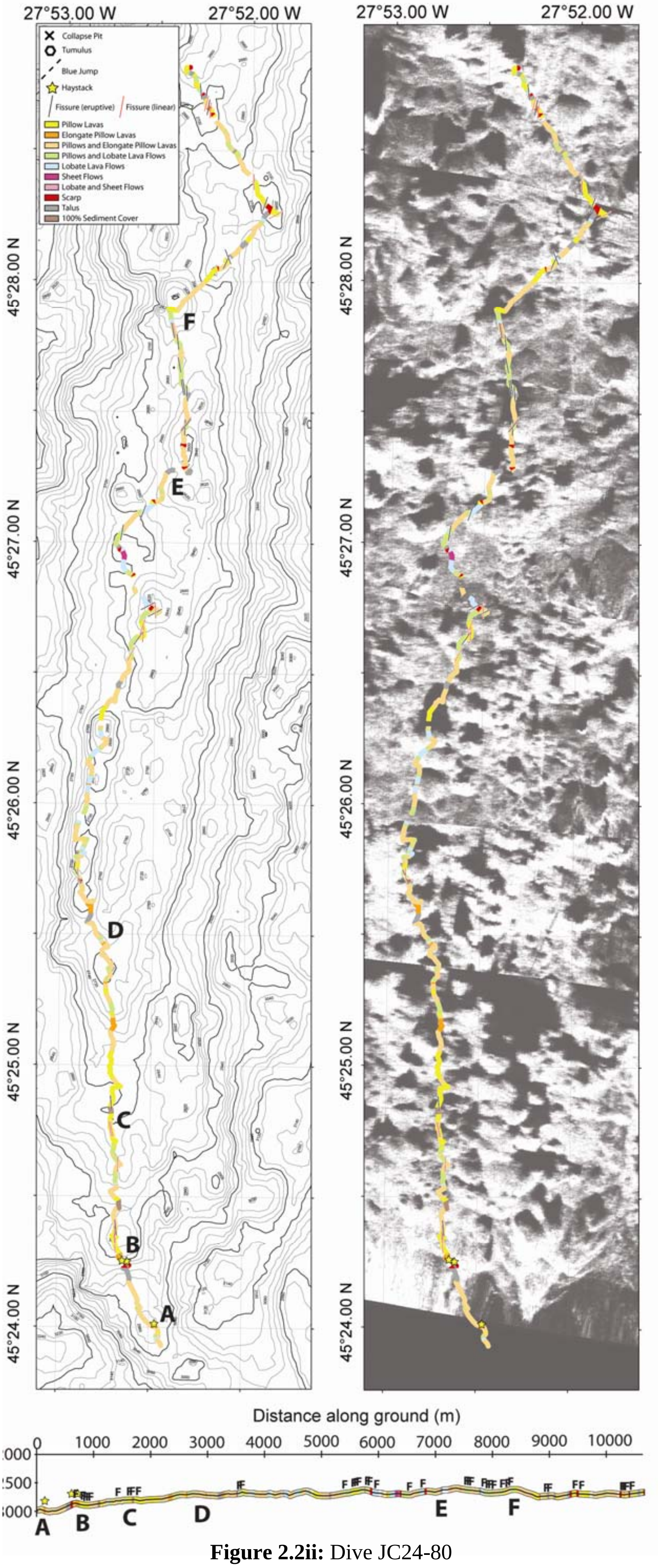

Figure 2.2ii: Dive JC24-80

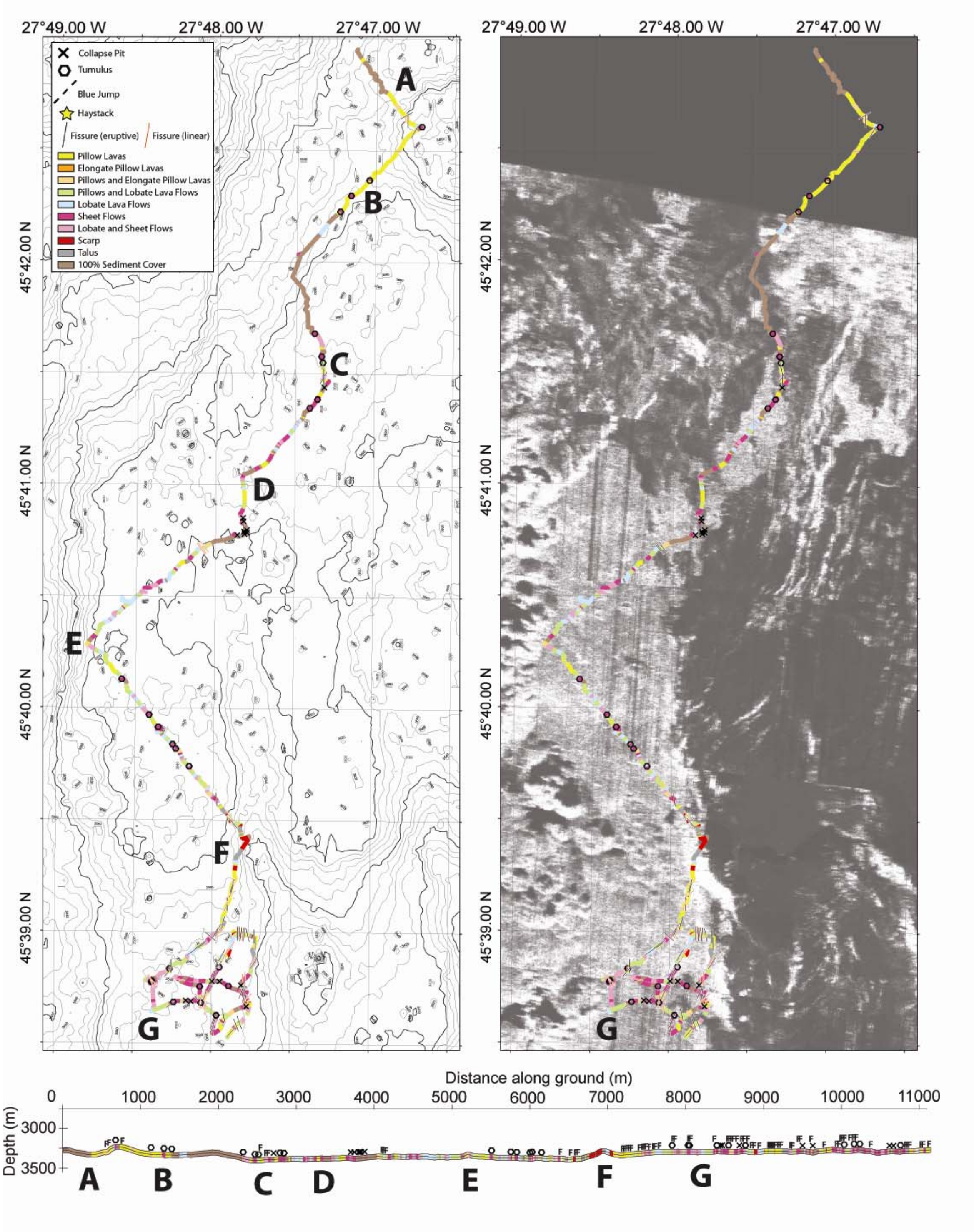

Figure 2.2iii: Dive JC24-81

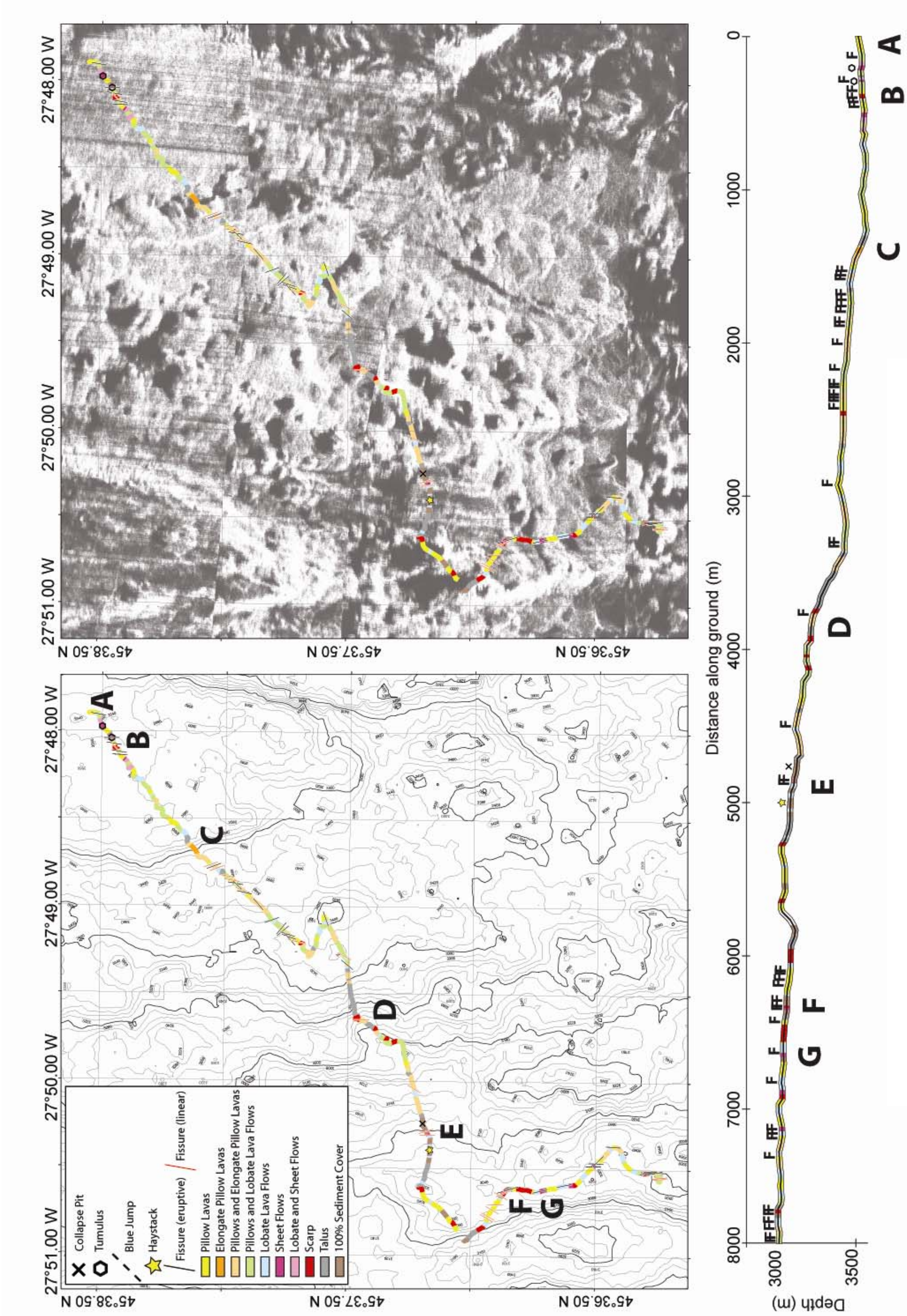

Figure 2.2iv: Dive JC24-82

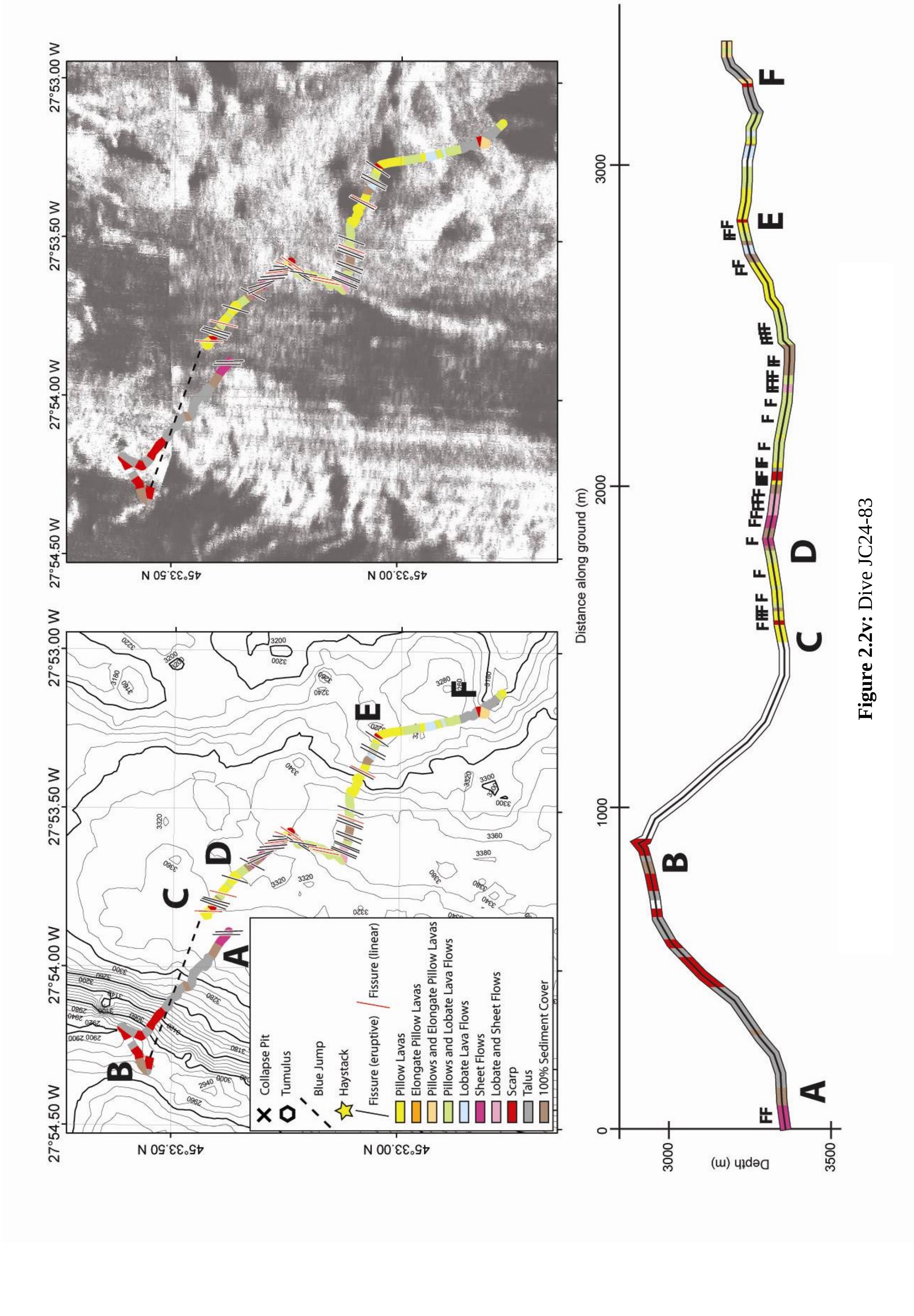

Figure 2.2v: Dive JC24-83

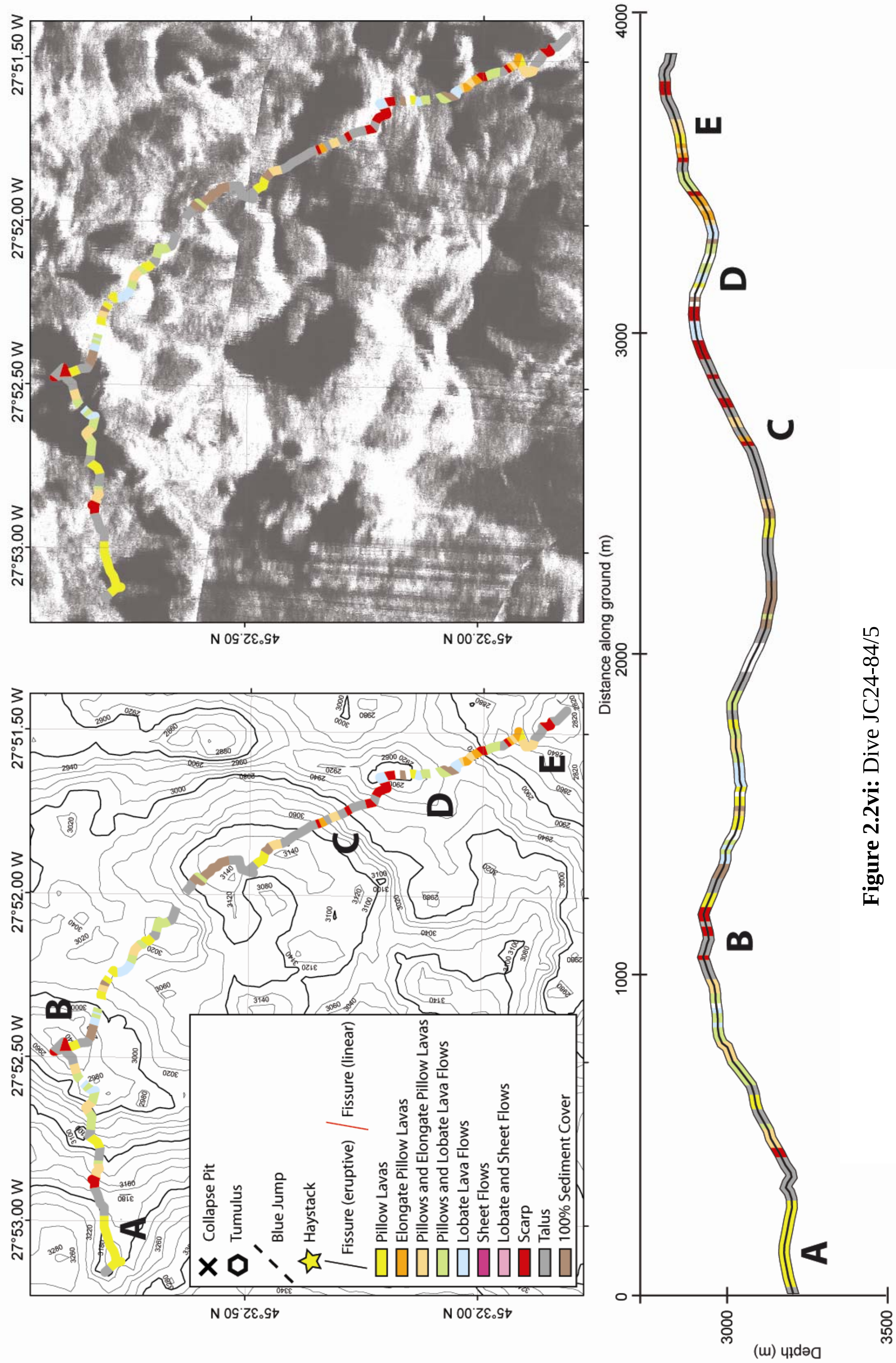

Figure 2.2vi: Dive JC24-84/5

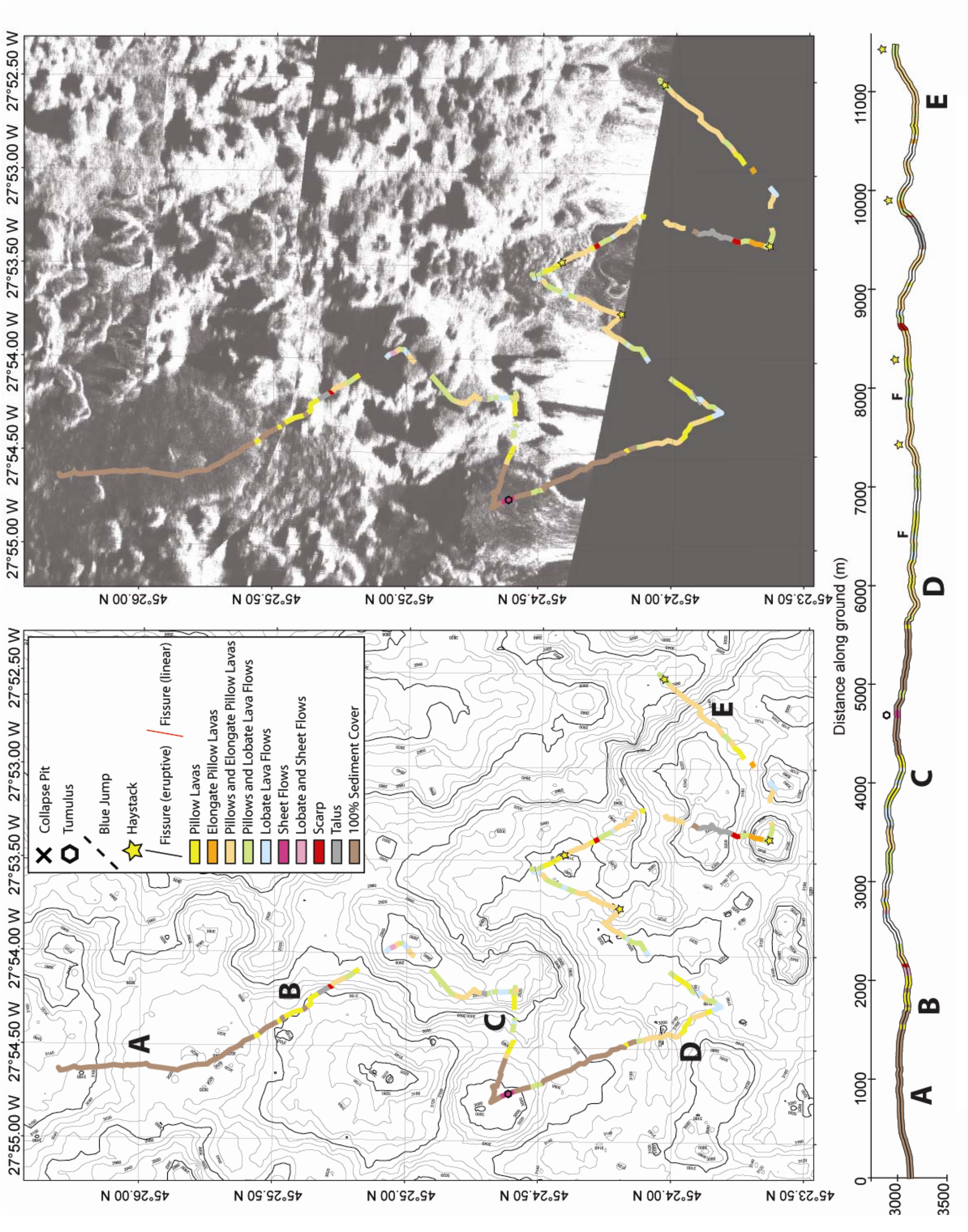

Figure 2.2vii: Dive JC24-88

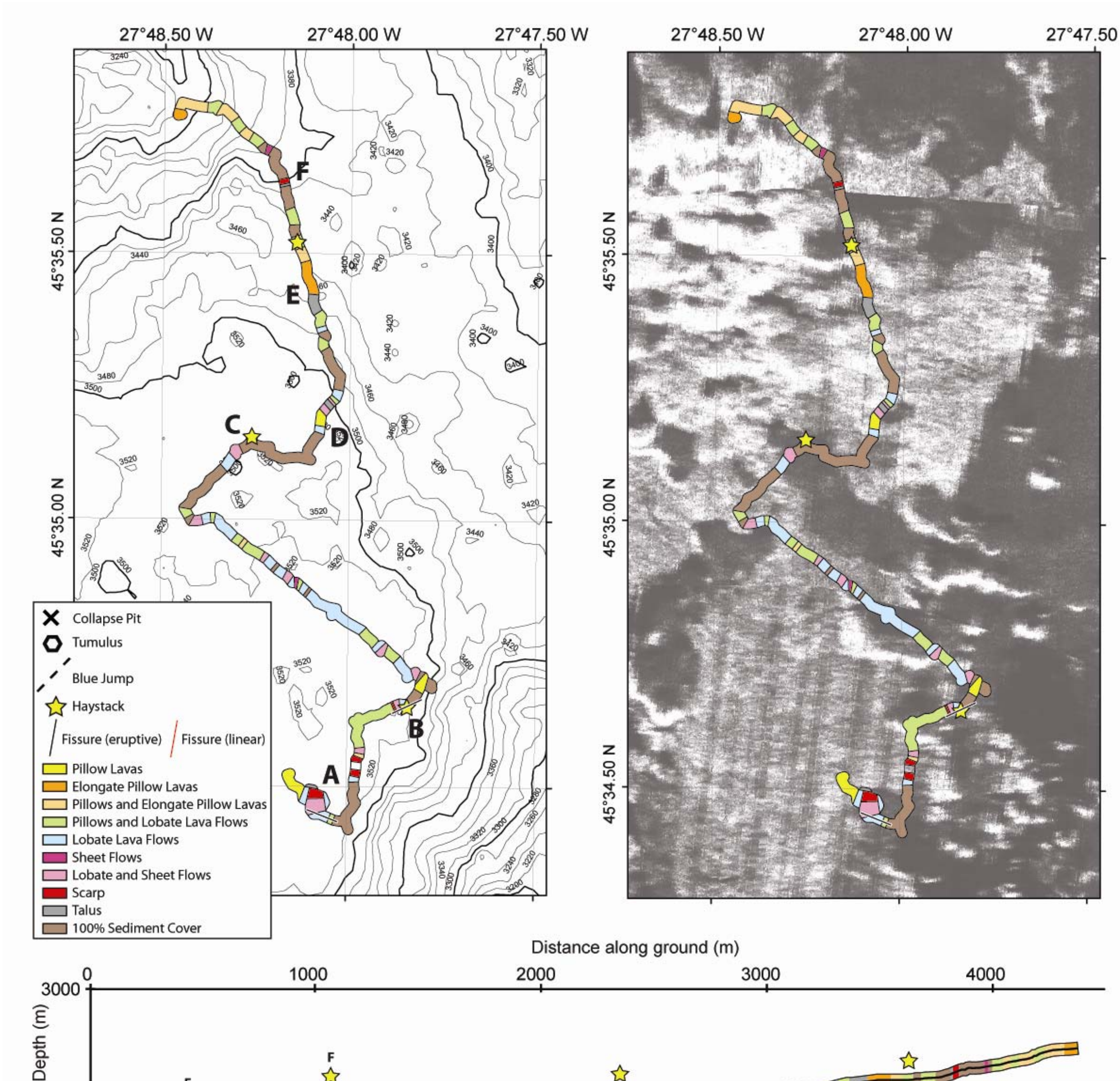

Figure 2.2viii: Dive JC24-89

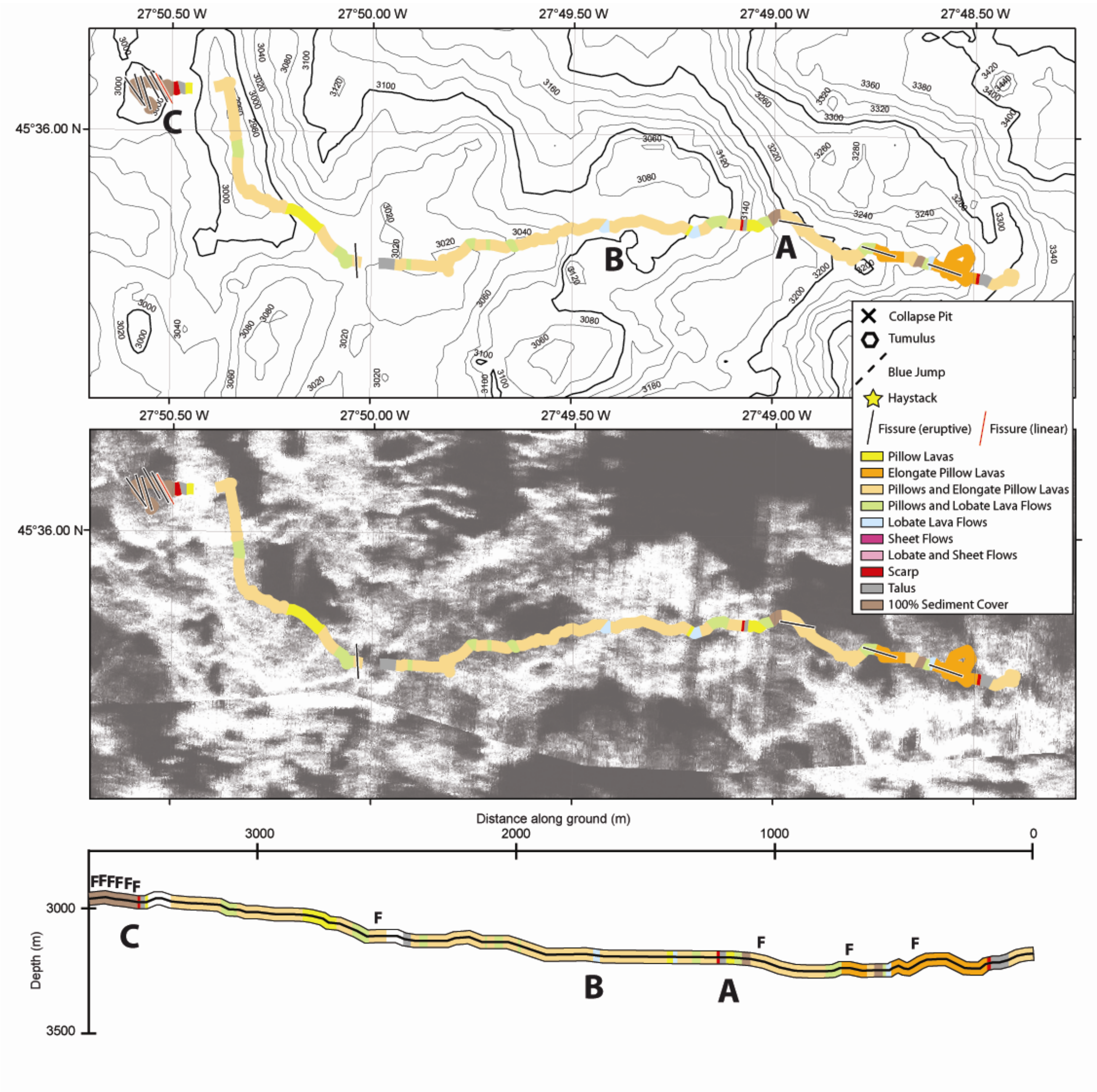

Figure 2.2ix: Dive JC24-90

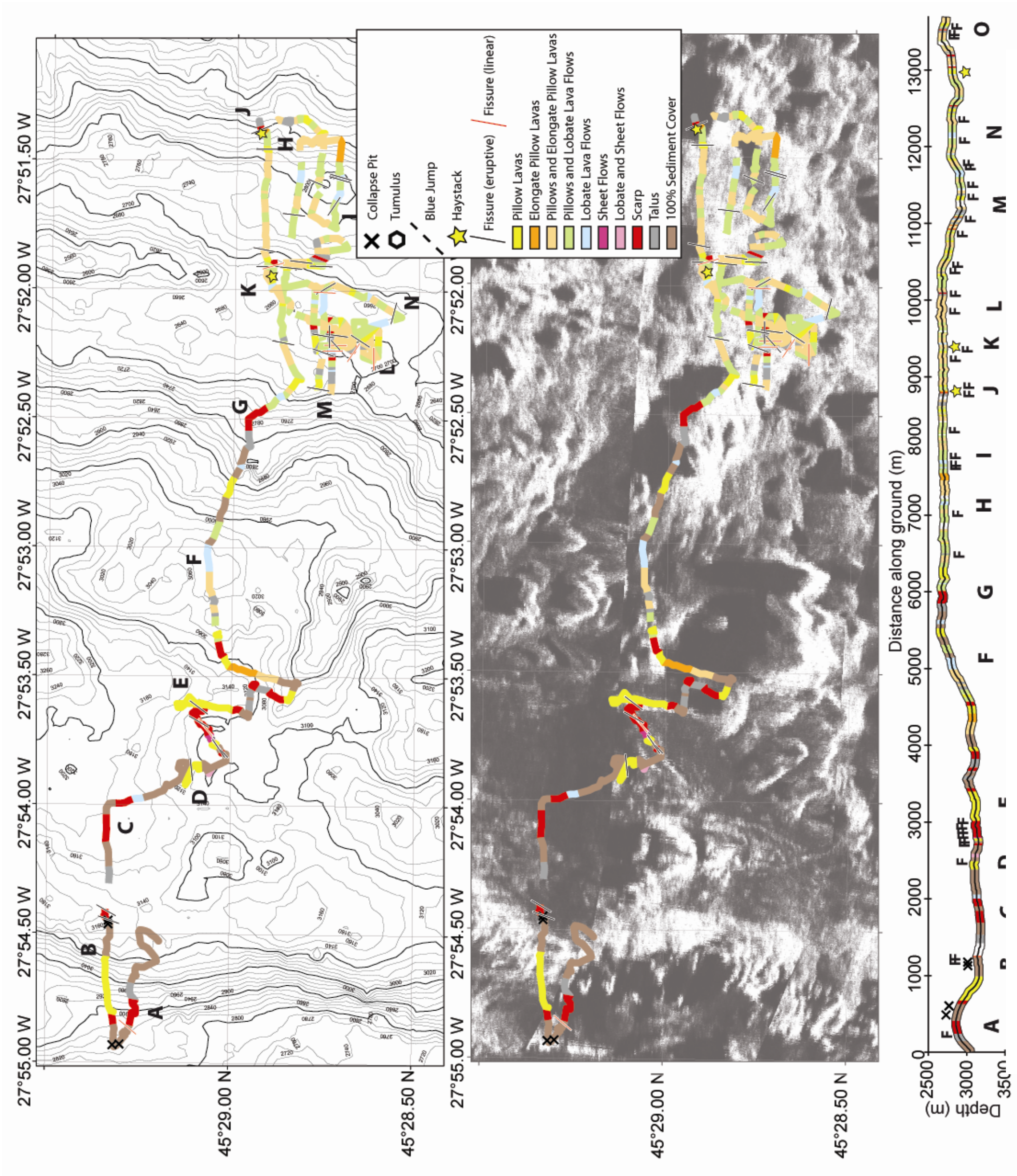

Figure 2.2x: Dive JC24-92 (see also 2.2xii for larger scale version of the second half of the dive)

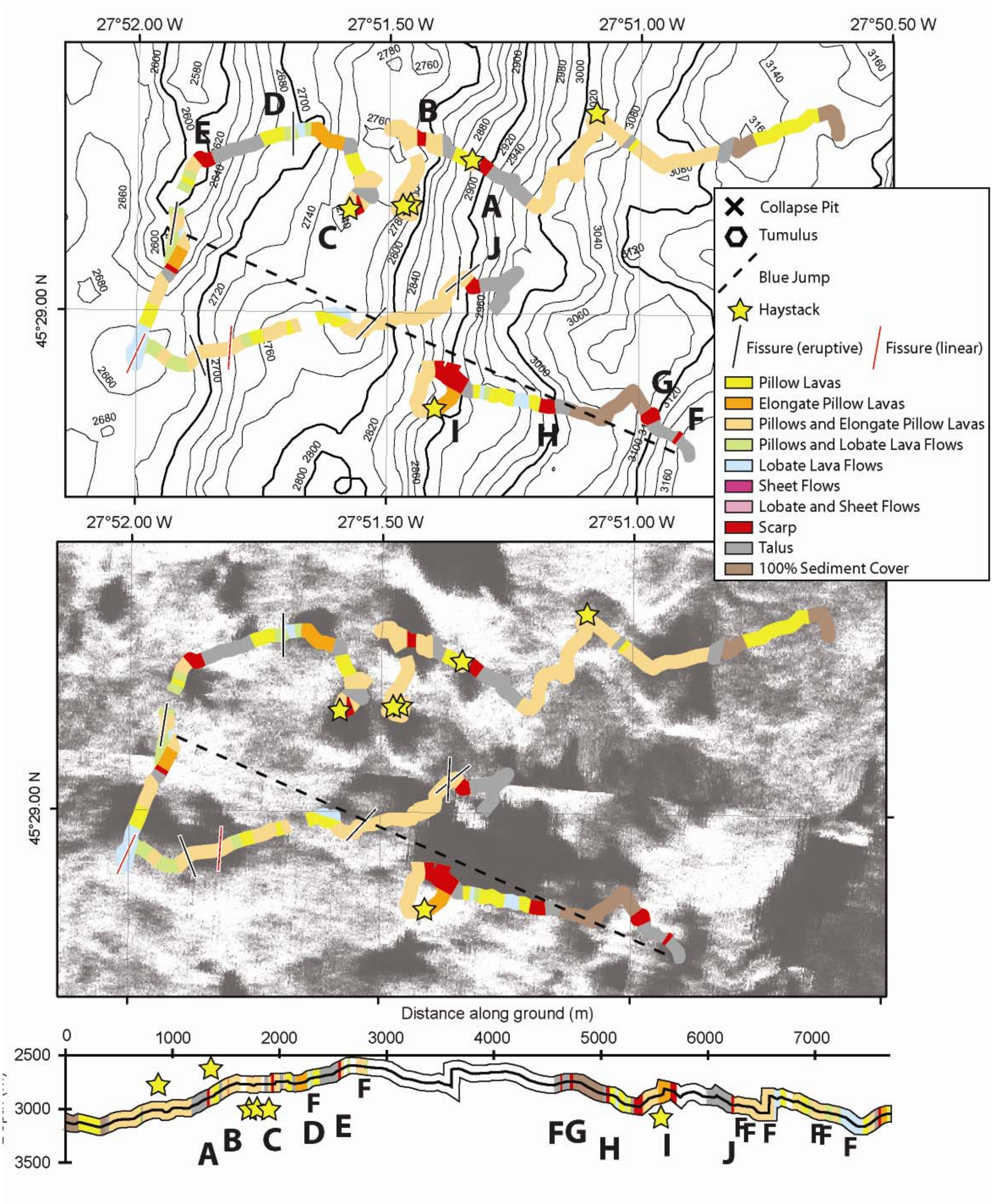

Figure 2.2xi: Dive JC24-93 (see also 2.2xii)

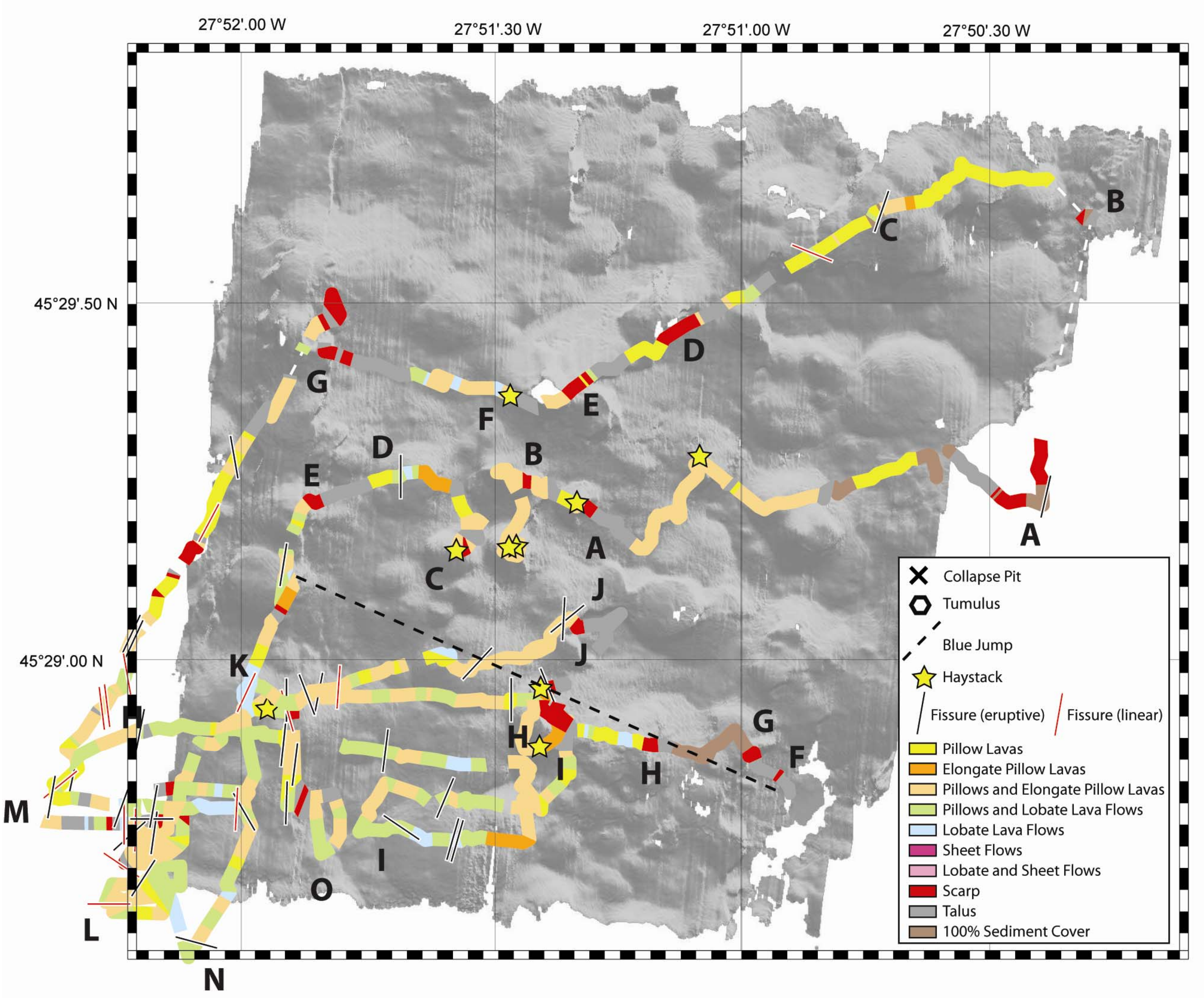

Figure 2.2xii: Relevant sections of dives JC24-79, JC24-92 and JC24-93 on SM2000 high-resolution bathymetry.

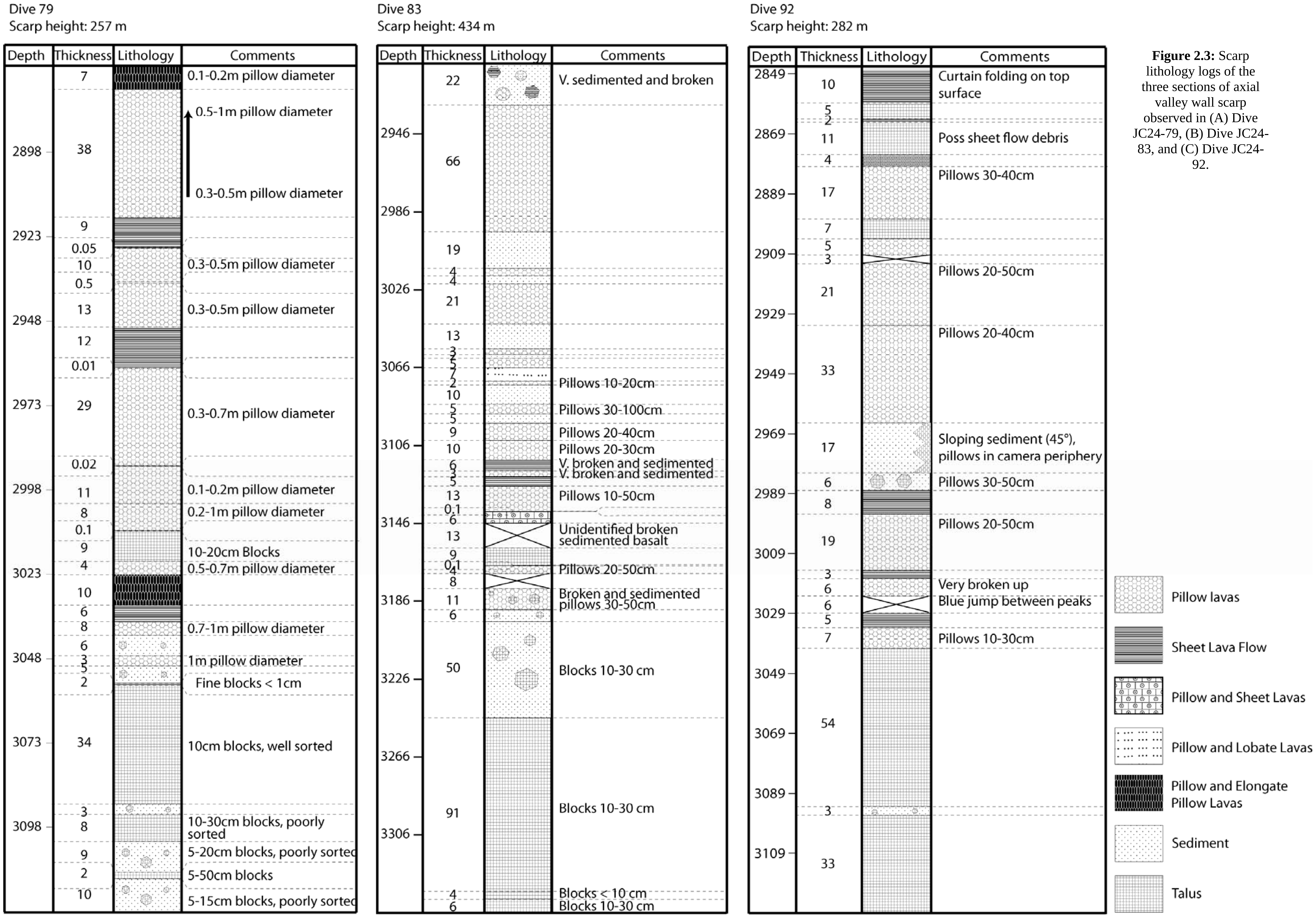

Figure 2.3: Scarp lithology logs of the three sections of axial valley wall scarp observed in (A) Dive JC24-79, (B) Dive JC24-83, and (C) Dive JC24-92.

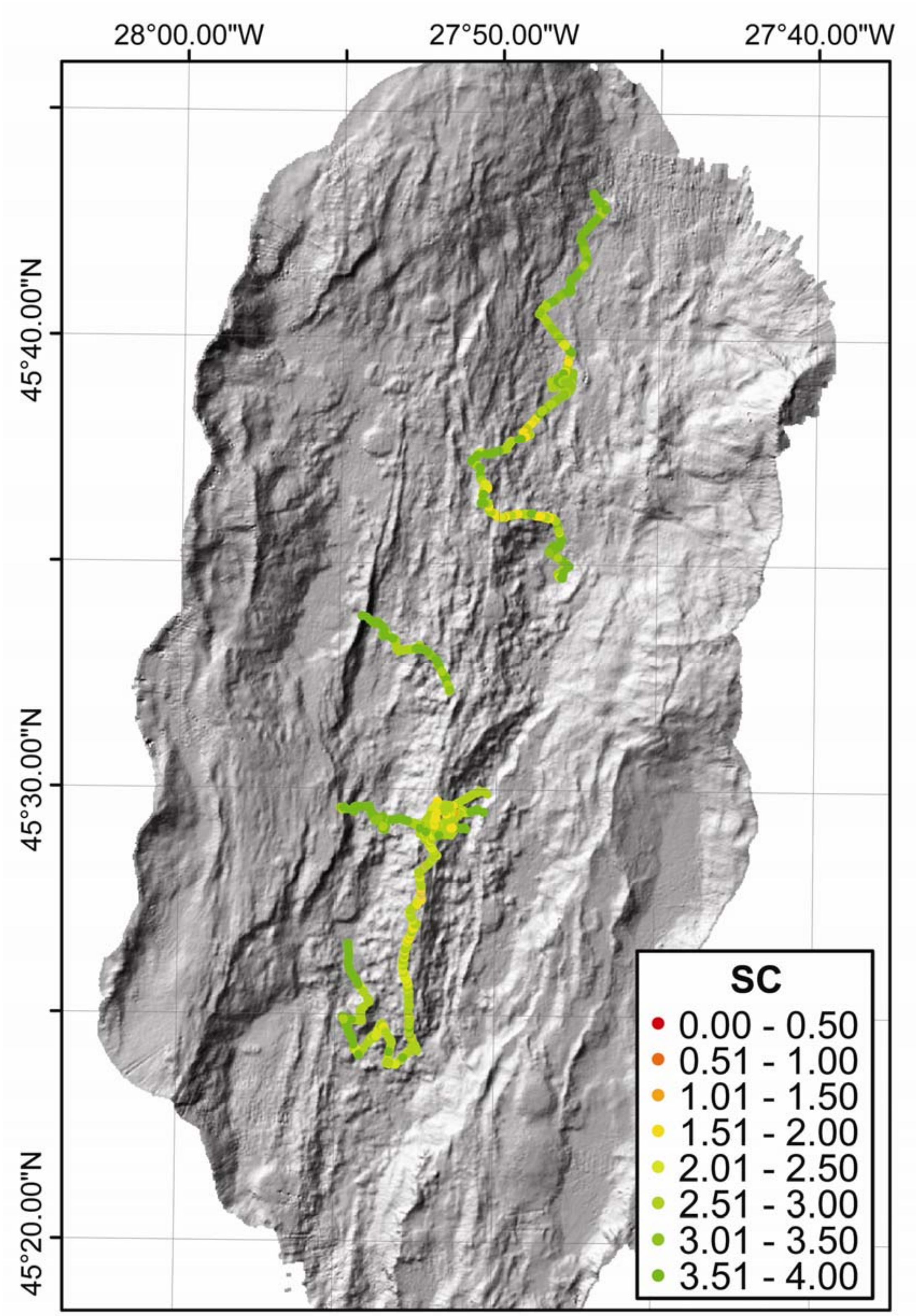

Figure 2.4: Sediment age classifications and sediment cover map for the dives. No lavas of sediment age 0 were observed. Sediment cover ages were recorded every minute and every point along the dive tracks represents one observation.

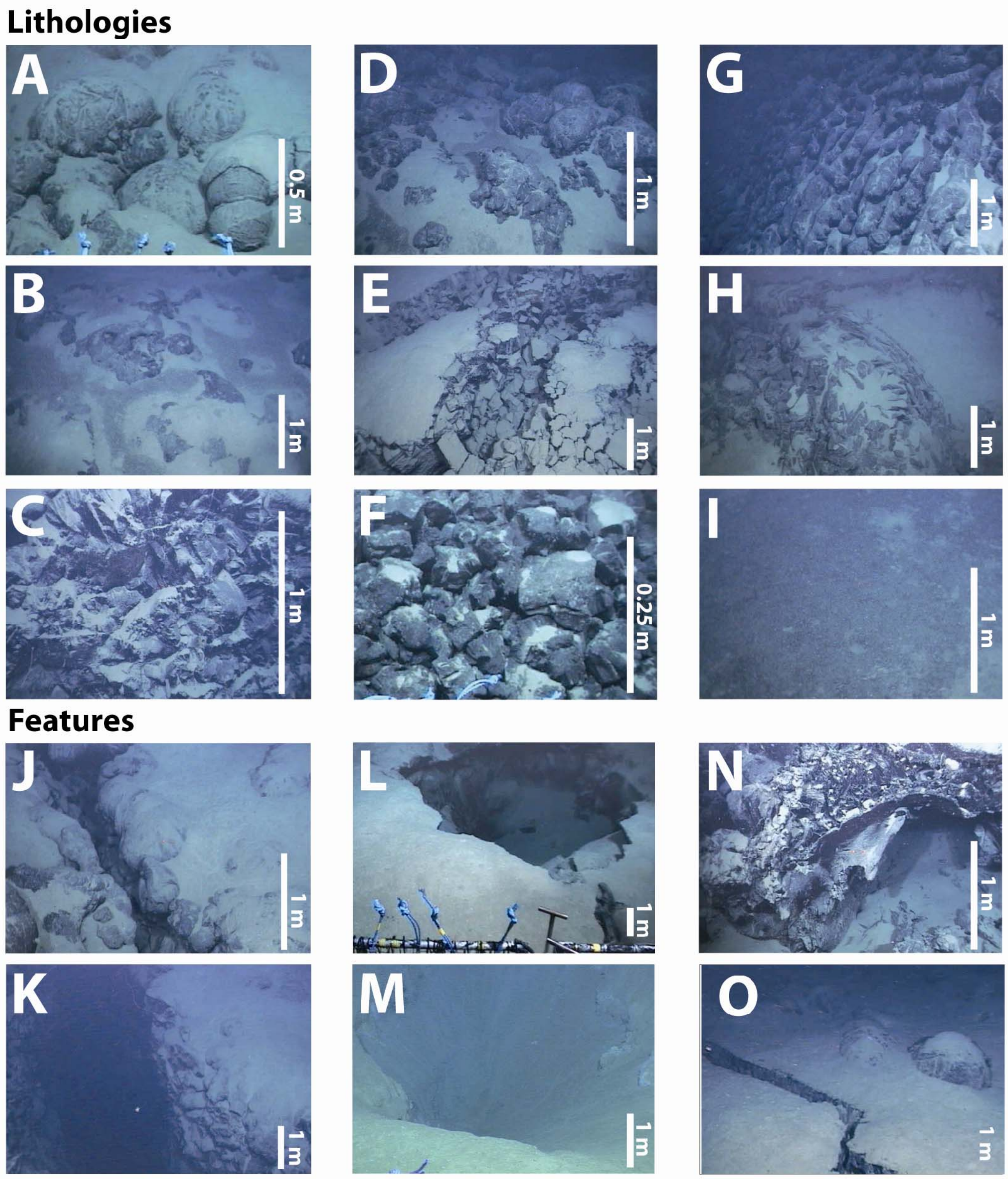

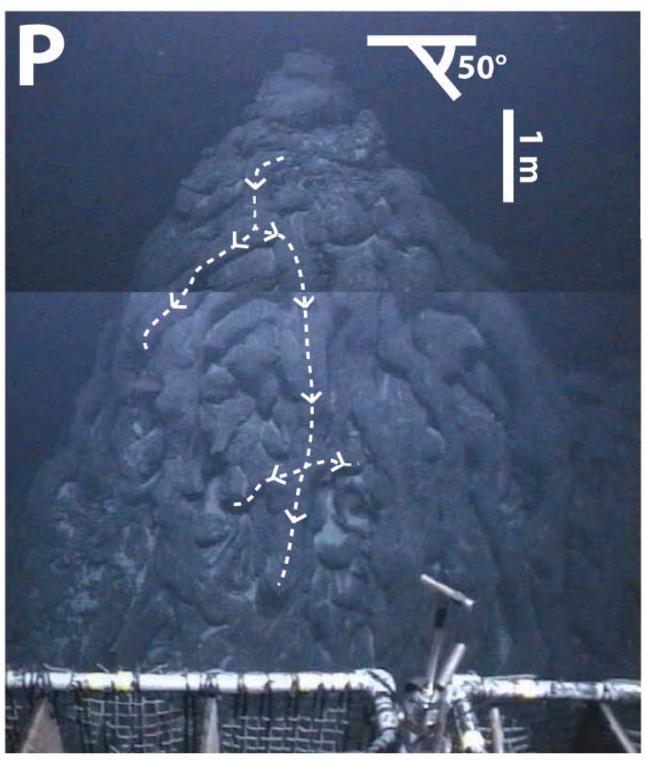

Figure 2.5: Typical lava morphologies and features observed on the sampling dives. (A) Pillow lavas (dive JC24-82); (B) Lobate lava flows (dive JC24-82); (C) Broken lavas in a fault scarp wall (dive JC24-81); (D) pillow lavas (dive JC24-90); (E) Broken sheet flow (dive JC24-83); (F) Talus deposit at the base of a fault scarp (dive JC24-80); (G) Elongate pillow lavas (dive JC24-88); (H) Textured sheet flow surface (dive JC24-82); (I) 100% sediment cover (dive JC24-82) (J); eruptive fissure (dive JC24-81); (K) Non-eruptive crack on the seafloor (dive JC24-81); (L) Trapdoor (dive JC24-89); (M) Collapse pit (dive JC24-81); (N) Lava tube (dive JC24-89); (O) Sheet flow lavas (seen in fissure) with associated pillow lavas visible through the thin sediment layer covering their surface (dive JC24-81); (P) Haystack (dashed lines show the length of a single pillow) (dive JC24-92)

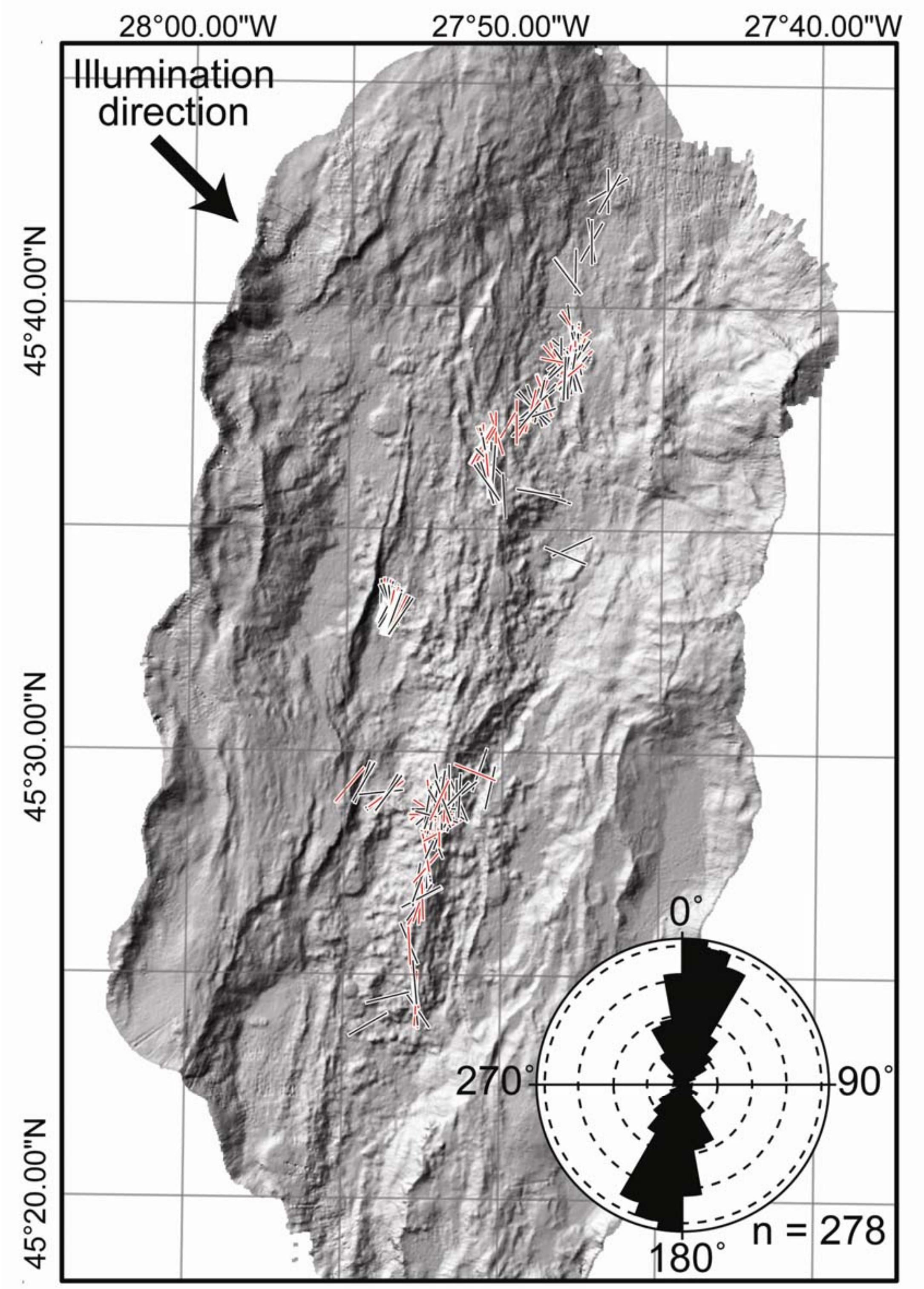

Figure 2.6: Fissure orientations for all dives. Purely eruptive fissures are shown in black, while those which have also been opened tectonically (which are wider than 1m) are shown in red. 70% of the 277 fissures observed and measured lie within 025˚ of the ridge strike. Dashed lines on rose diagram are divisions of 2.5 n.

	Pillow	Lobate	Sheet	Elongate Pillow	Pillow & Lobate	Lobate & Sheet	Pillow & Elongate
All Dives	20	13	6	4	26	4	27
79	51	2	0	26	9	0	37
80	23	10	0	4	15	0	47
81	10	13	23	0	34	14	6
82	23	19	5	2	20	6	24
83	32	6	9	0	42	8	3
85	33	17	0	7	20	0	24
88	20	14	1	2	24	2	39
89	6	30	2	5	33	10	14
90	10	3	0	13	10	0	64
92	15	9	2	3	32	2	37
93	15	9	1	7	10	0	58

Table 2.1: Measured dive length of each observed lava lithology as a percentage of total cumulative dive length for all dives together and for individual dives. Areas of scarp, talus or sediment cover, and sections of dive where the seafloor was not observed, were omitted from the measurements.

	Pillow	Lobate	Sheet	Elongate Pillow	Pillow & Lobate	Lobate & Sheet	Pillow & Elongate
Hummocky	24	12	0.5	5	23	0.3	36
Flat Seafloor	12	15	20	0	33	16	4

Table 2.2: Lithology as a percentage of total observed lithology on hummocky vs. flat-seafloor. Areas of scarp, talus or sediment cover, and sections of dive where the seafloor was not observed, were omitted from the measurements.

3 Eruption volumes, hummock dimensions and spatial statistics

Chapter 3: Eruption volumes, hummock dimensions and spatial statistics

3.1 Rationale

In order to model AVR construction it is important to understand the morphology and distribution of the volcanic units that build them. While we know AVRs are built of volcanic hummocks (Smith and Cann, 1990), we do not know how many of these edifices are involved. We do not know the dimensions or volumes of most of these features (although estimates have been made e.g. Magde and Smith (1995)), nor how many are produced by a volcanic eruption. We have observed different lava morphologies at hummock summits and interpreted them as a result of differing effusion rates, but do not know if effusion rate controls the dimensions of a hummock. These questions take on additional importance given that AVRs are the most likely sites for the production of most of the upper oceanic crust (above the sheeted dyke layer) at slow-spreading mid-ocean ridges and therefore hummocks are likely to be not only the building blocks of AVRs, but also of most of the extrusive section of the oceanic crust.

Statistical analysis of the dimensions and distributions of volcanic hummocks are made possible in this area by the comprehensive TOBI sidescan sonar coverage in N – S insonification directions and additional less detailed coverage in E – W insonification directions over an entire spreading segment. This study will address the questions of how volcanic units are distributed spatially, how they are related to one another and what the upper oceanic crust is made of (as set out in section 1.2.2). Additionally, if specific statistical distributions of features are associated with different stages of an AVR life cycle then we can use them to examine the Parson et al. (1993) model of AVR development.

All work on this chapter was done by I Yeo, hence there is no work division section. Data can be found in appendices 9.6, 9.7 and 9.8.

3.2 Introduction

In the past it has been difficult to obtain information on the accurate dimensions of mid-ocean ridge hummocks because they are too small (typically < 50 -100 m tall) to be imaged well by ship-based bathymetry systems, as sidescan sonar does not record bathymetry. They were defined by Smith and Cann (1993) as round, or almost round, volcanic edifices, 50 – 500 m in diameter and less than 50 m high with an average density of ~ 80 – 190 per 1000 km^2 (Smith and Cann, 1990; Smith and Cann, 1992). Hummocks play an important part in oceanic crustal construction, as axial volcanic ridges appear to be constructed predominantly of such edifices (Smith and Cann, 1990; Smith and Cann, 1992). Estimates of hummock dimensions have been attempted (Magde and Smith, 1995; Smith and Cann, 1990), however such studies typically focus on the larger seamounts visible in EM120 and therefore may overestimate typical dimensions. Population statistics developed by Jordan et al. (1983) are useful for comparing seamount populations in different locations or of different ages. They recognised that seamounts are typically exponentially distributed in size, and this distribution can be described by:

$$v(R) = v_o e^{-\alpha R}$$

Where v_o is the total expected number of seamounts per unit area and α^{-1} is the characteristic height used to define the population.

Distribution statistics are commonly used to investigate volcanism where direct measurements are more difficult. As the spatial distribution of volcanoes is controlled by the magma supply, where detailed topographic information is not available this distribution can be used to identify sites of high and low magma flux to the surface, and can provide information on how lavas are spatially distributed. High densities of volcanic edifices and hydrothermal activity can be used to pinpoint the location of magma chambers (e.g. Haymon et al. (1991)) and on a larger scale, to distinguish between time periods of high and low magmatism (e.g. Wessel and Lyons (1997)).

Distribution statistics are also commonly used in planetary research, where again detailed topographic information and subsurface data is not available. Density analyses, which measure the distance between every volcanic cone and all the others in the dataset, are commonly used in planetary studies to assess how clustered volcanic edifices or vents are, and to identify zones of high magmatism (e.g. Baloga et al. (2007)) or areas where volcanic edifices appear to be distinct from one another (e.g. Bleacher et al., (2009)).

Further information on volcanic feeder systems or the local stress regimes can be gleaned from other statistical analyses of point datasets, such as alignment of volcanic features. We know there are aligned features at mid-ocean ridges because they have been observed (Bryan et al., 1994) and mapped Searle et al. (2010). A commonly used tool to investigate the orientation and strength of alignment is the standard deviational ellipse (SDE), which creates an ellipse for a point dataset centred on the mean centre of all points and elongated according to the distances of the points from this mean centre, meaning that the stronger the alignment the larger the length to width ratio in that direction will be (Wong and Lee, 2005).

In this chapter, detailed point files are created using the sidescan sonar imagery for every volcanic hummock on the AVR and also for every hummock (outside the AVR) covered by the survey. Hummock heights and diameters are measured in the areas of high-resolution bathymetry to produce estimates of typical hummock volumes. Lineaments of hummocks are identified and the number of hummocks along these lineations and their volumes are used to produce minimum estimates of typical eruption volumes per hummock and of entire eruptions. Density maps are used to investigate hummock distribution on the 45˚N AVR and SDE analyses are used to look at hummock alignment. Both these statistical analysis techniques are used to investigate AVR life cycles.

3.3 Methodology

3.3.1 Hummocks and dimensions

Volcanic edifices were picked from the TOBI sidescan sonar north and south insonified datasets (as those were the best navigated with the most comprehensive coverage); this should minimise the problem of acoustic shadowing as almost all hummocks should be shown in one or other dataset. Hummocks were picked using both insonification directions, however each was only represented once in the final dataset. Hummocks were picked in ArcGIS 9.1 as both a pointfile, where a point was assigned to each hummock summit, and a shapefile where every hummock is represented by a circle representing the basal contour. Diameters of hummocks were calculated using the "easy calculate 5.0" toolbox (written by Ianko Tchoukanski at ESRI) operating on the ArcGIS platform.

In the high-resolution areas, heights were measured from the base (or the average height of the basal contour where they lay on a slope) to the highest point on the edifice. Volumes were estimated by approximating hummocks to a cone using the equation:

$$v = \frac{1}{3}\pi\ r^2 h\,.$$

Volume as a spherical cap was calculated using the equation:

$$v = \frac{\pi h}{6}\left(3r^2 + h^2\right)$$

Where h is the height and r is the radius of the basal circle. As most edifices are more conical in shape the cone estimates were used for subsequent calculations. AVR volume was calculated using 3D analyst in ArcGIS 9.1.

The statistical population analysis was done, following Magde and Smith (1995) and Raffell (2010, unpublished), by binning diameter data into 20 m bins and plotting the natural log of the cumulative frequency against the diameter. Diameters < 100 m were excluded as these deviated from the pattern, suggesting under sampling. Diameters > 640 m were all flat-topped seamounts and were also excluded. Errors were calculated using the methodology set forward in Lyons (1991) and used in Raffell (2010).

Summit morphology was assigned from ROV video observations of hummocks (figure 3.7).

3.3.2 Density

Hummock density (figures 3.8 and 3.9) was calculated using the ArcGIS Spatial Analysis point density tool using the hummock summit point files as described above. Densities are calculated for each pixel by counting the number of edifices within a user defined radius of the pixel. Density maps were produced for a number of different radii: 1000 m, 600 m and 200 m. Radii larger than 1000 m did not show any detail, while radii smaller than 200 m were too small to produce meaningful maps, given the spacing of the hummocks. Density maps were all plotted with a pixel size of 50 m.

3.3.3 Alignment

Lineaments were picked from hillshade images of the EM120 ship based bathymetry illuminated from four different angles to remove bias. These maps were then combined to produce a single map of lineaments. Lineaments were picked from the EM120 where they were observed in more than one illumination direction, where they were clear in both the hillshade maps and the sidescan sonar surveys, or where combined surveys gave a better indication of their shape and length. Azimuths of these lineaments were calculated using the "easy calculate 5.0" toolbox operating on the ArcGIS platform. Hummocks along each lineament were picked from the TOBI sidescan sonar imagery and the hummock shapefiles.

Standard deviational ellipses (SDEs) were produced using the ArcGIS Spatial Statistics Directional Distribution (Standard Deviational Ellipse) tool. The ArcGIS tool calculates the ellipse by averaging the coordinates of every point to get the mean centre, thus the central point coordinate will be (0, 0) and the transformed ones will have positive and negative values relative to their position from the centre. As explained in Mitchell (2005) the ellipse is given as:

$$SDE_x = \sqrt{\frac{\sum_{i=1}^{n}(x_i - \overline{X})^2}{n}}$$

$$SDEy = \sqrt{\frac{\sum_{i=1}^{n}(y_i - \overline{Y})^2}{n}}$$

(where $\overline{X}$ and $\overline{Y}$ represent the mean centre for the features, and *n* is equal to the total number of features).

The ellipse is then rotated using:

$$\tan\theta = \frac{A+B}{C}$$

$$A = \left(\sum_{i=1}^{n} \tilde{x}_i^2 - \sum_{i=1}^{n} \tilde{y}_i^2 \right)$$

$$B = \sqrt{\left(\sum_{i=1}^{n} \tilde{x}_i^2 - \sum_{i=1}^{n} \tilde{y}_i^2 \right)^2 + 4\left(\sum_{i=1}^{n} \tilde{x}_i \tilde{y}_i \right)^2}$$

$$C = 2\sum_{i=1}^{n} \tilde{x}_i \tilde{y}_i$$

(where $\tilde{x}_i$ and $\tilde{y}_i$ are the deviations of the *xy*-coordinates from the mean centre).

The standard deviations for the *x*-axis and *y*-axis are:

$$\sigma_x = \sqrt{\frac{\sum_{i=1}^{n}(\tilde{x}_i \cos\theta - \tilde{y}_i \sin\theta)^2}{n}}$$

$$\sigma_y = \sqrt{\frac{\sum_{i=1}^{n}(\tilde{x}_i \sin\theta - \tilde{y}_i \cos\theta)^2}{n}}$$

The SDE for the whole pointfile was produced using a circular dataset around the mean centre of the data so as to avoid any bias from the shape of the surveyed area on alignment. This SDE was used to show the orientation and strength of alignment of the whole AVR dataset. Further circular datasets were used in the north and south, within the bounds of the AVR in order to look for the strength of alignments along different sections of the AVR.

3.4 Observations

3.4.1 Number, density and size of edifices

In the area covered by the TOBI surveys 4,463 individual volcanoes are clearly imaged. The base of the AVR can be roughly defined by the 3220 m depth contour (figure 3.1), except where the base of the AVR meets the axial valley wall or off axis features where it can be approximated by eye, however this contour omits some areas of lower level hummocky terrain (shown by dashed green line in figure 3.1) which probably also forms part of the AVR. These areas roughly respond to the outlines in Searle et al. (2010), with the solid green line roughly outlining the 'recent hummocky volcanoes' and the dashed line corresponding to the Searle et al. (2010) 'older hummocky volcanoes'. Using just the 3220 m contour, ~1,850 edifices lie on the AVR (41 % of all volcanoes), or 2,800 (63 %) if we include lower level hummocky areas included in the pale green dashed contour (figure 3.1).

Of all the volcanic edifices picked, 19 are flat-topped seamounts and 4,444 are volcanic hummocks, meaning that hummocks account for 99.5 % of the volcanic edifices observed. The entire area covered by TOBI is 732 km^2 giving an average density of 6 hummocks per km^2. The turns in the TOBI are much harder to pick volcanic edifices from though and therefore this probably represents a minimum value. If we define the AVR using the 3220 m contour then it has an area of 83.5 km^2, giving it a hummock density of ~ 22 hummocks per km^2. Away from the AVR hummocks are increasingly likely to buried or masked by sediment.

The average diameter of all the volcanic edifices covered by the survey is 147 m and the mode is 124 m. The smallest measured diameter was 23 m and the largest non flat-topped edifice had a diameter of 639 m, although this edifice was probably a composite pile of more than one hummock, and most have diameters less than ~ 450 m (figure 3.2). Nineteen flat topped-seamounts are observed, ranging from 445 m to 2,302 m in diameter.

An exponential distribution of hummock diameters > 100 m is observed (figure 3.3). The equation for the line is given as y = -0.0171x + 10.109, giving a characteristic diameter of 58.5 $\pm$ 0.5 m and v_o 24563 +2112/-1945 edifices per unit area.

3.4.2 High-resolution study areas

3.4.2.1 Hummock height and diameter

The TOBI sidescan sonar data provides no useable information on edifice height, however we also have the two areas of high-resolution bathymetry (figure 3.4) collected with the ROV Isis (see section 2.3.3) which provide us with ~ 1 m horizontal and vertical resolution maps of two hummocky areas on the AVR, which contained 75 and 78 hummocks respectively. Hummock heights were measured from the base to the peak, and relative to the average depth of the basal circle where they lay on sloping terrain, giving hummock heights of between 5 and 146 m with an average height of 35 m (figure 3.5).

In the southernmost high-resolution study area (figure 3.4) hummocks are slightly larger than in the northern area (figure 3.5) with average diameters of 142 m and heights of 39 m in the southern area) and diameters of 117 m and heights of 33 m in the northern area. The hummocks here were also harder to pick as the area is cut by a number of normal faults and a large number of the hummocks appear to have undergone collapse and mass wasting (Yeo et al., 2012). This will be discussed further in chapter 4.

There is a general relationship between tall edifices and large basal diameters (figure 3.5) but there is a large amount of scatter and height to diameter ratios range from approximately 1:15 to almost 1:1. Ratios do not increase or decrease with changing diameter, although the tallest edifice observed (146 m) does correlate with the largest diameter (327 m).

3.4.2.2 Hummock volume

Assuming hummocks are roughly cone shaped edifices with a circular base (at an average depth on sloped terrain) means the volume can be easily approximated (ignoring any faulting or slumping). Hummock volumes (when calculated as a cone) ranged from 1,400 m^3 to 4,000,000 m^3 with an average volume of 290,000 m^3. Volumes were also calculated as a spherical cap, which may be a closer approximation to some of the rarer, flatter and larger seamounts. These volumes were of the same order of magnitude as those calculated using the cone method, and were typically around 70 % larger than the volumes calculated using the cone method and were larger for hummocks > 500,000 m, ranging from 2,400 m^3 to 7,700,000 m^3 with an average volume of 520,000 m^3. The distribution of volumes calculated using both methods is shown in figure 3.6 (truncated at 2,400,000 m^3, seven exceed this, the largest is ~7,800,000 m^3). As most hummocks appear conical, the volumes calculated for a conical edifice will be used for the rest of the calculations, this may be a slight underestimate for some hummocks.

Hummocks in the southernmost high-resolution study area (figure 1.25; dive 91) are marginally larger than those in the northern one (figure 1.25; dive 87) with average hummock volumes of 366,000 m^3 in the south and 224,000 m^3 in the north.

3.4.2.3 Hummock shape and summit morphology

In area 1 we carried out 3 video and sampling dives with the ROV Isis over the imaged hummocky terrain. In order to asses whether there is a relationship between edifice dimensions and effusion rates, we compared the dimension of hummocks where summit lava morphology was observed. The summit morphology should minimise any effects associated with cooling with distance from the vent and give us the best estimation of lava effusion rate during, or at least at the end of, the eruption.

The dives covered the summits of 24 different hummocks in the southern high-resolution bathymetry area. As discussed in section 2.3.5.1, hummock summits tend to be characterised by either pillow or lobate lava flows and both these types were observed in area 1. Of the 24 imaged by Isis, 10 had lobate summits and 14 had pillowed summits. The lobate hummocks on average had larger diameters but smaller heights (average diameter of 204 m (σ 52 m) and height of 51 m (σ 34 m) as opposed to 170 m (σ 53 m) and 67 m (σ 34 m) for the pillowed hummocks) (figure 3.7). With the exception of one hummock, there is a fairly clear separation between the pillowed hummocks and the lobate ones, with all the lobate hummocks bar one having heights less than 60 m.

3.4.3 Clustering

3.4.3.1 Large Scale Clustering

Density maps were produced at three different scales (figure 3.8), with densities per square kilometre being calculated for each pixel by measuring the density of hummocks within circles (of three different radii) of the pixel. The largest scale (figure 3.8 C) shows a broad high (of 32 hummocks in a 1000 m radius) within the axial valley and bounded by the wall faults, although other smaller highs, with similar densities to the central high can also be seen outside the axial valley, particularly to the north of the current AVR. The intermediate scale (figure 3.8 B) shows a similar pattern to the large scale map, with the highest hummock densities predominantly lying on the AVR and additionally in a few discrete areas off axis. This map also shows that the AVR does not have uniform densities of hummocks on its surface though, with areas of high and low density distributed patchily along it rather than along the crest or near the centre. The smallest scale density map (figure 3.8 A) shows that density is not very uniform along the AVR, with a number of small areas of high and low density distributed randomly along the AVR, with the largest high density areas towards the centre (in a N – S sense) of the AVR. The high density hummock areas that lie off the AVR on top of the axial valley wall faults also show similar clustering.

3.4.3.2 Clustering on the AVR

Similar density maps were produced for the hummocks sitting within the bounds of the AVR, as defined by the 3220 m depth contour, to investigate the detail of the clustering on the AVR and ignore patchy hummocky areas around it. The maps are shown at two scales (figure 3.9) with radii of 250 m and 400 m. Both scales show a patchy distribution of higher and lower density areas which do not appear to correlate with either the top or flanks of the AVR. Higher densities are slightly more common on the northern more faulted ends of the AVR in both maps (figure 3.9).

3.4.4 Volcano Alignments

3.4.4.1 Lineaments

A number of lineaments formed of rows of hummocks can be identified on the surface of the AVR (figure 3.10). Lineaments were picked on the AVR from four different illuminations of the EM120 bathymetry (figure 3.10) and the results were combined to produce a single set of 84 lineaments (figure 3.11). The lineaments varied in length from 0.5 to 3.8 km, with an average length of 1.4 km. Of these lineaments 37 (44 %) lie within 20˚ of the AVR strike (at 013˚). There is no relationship between length of lineament and orientation.

Five lineaments can be attributed to fault traces and the rest to hummock alignments. These hummocky lineaments comprise between 3 and 18 hummocks each, with an average of 8 hummocks. These hummocky ridges are 1.4 km long on average, and are thought to be the result of a single eruption point focusing along a fissure (Head et al., 1996; Wylie et al., 1999), and the ridge parallel alignments are typical of the linear, fissure-fed eruptions of multiple hummocks described by Smith and Cann (1999). The majority of alignments (54 %) occur orthogonal to the ridge axis and are aligned down the steepest sections of the AVR flank, suggesting they are gravity controlled (Searle et al., 2010), however in both axis parallel and axis-orthogonal cases a single eruption builds a number of hummocks.

3.4.4.2 Standard Deviational Ellipse

Standard deviational ellipses (see 3.3.3) were produced for circular datasets with a diameter of 10 km centred on: a) the mean centre of the point file dataset b) the northern end of the AVR, and c) the southern end of the AVR (figure 3.12). The SDE for the mean centre of all the data had an alignment of 009˚ and a ratio between the major and minor axis of 1.54 (table 3.1). The SDE for the southern dataset had an alignment of 019˚ and a similar ratio between the major and minor axes of 1.52. In the northern area the ellipse was aligned 001˚ and had a lower major to minor axis ratio of 1.23.

3.5 Discussion

3.5.1 Dimensions and Density

3.5.1.1 Population statistics

The calculated population statistics for the 45˚N seamounts give a characteristic diameter of 58.5 $\pm$ 0.5 m and ν_o of 24,563 +2112/-1945. The density is obtained by scaling ν_o for the TOBI area (736 km^2) up to a value per 10^3 km, giving a total expected number of seamounts of 33,556 per 10^3 km. This value is much higher than those measured by Magde and Smith (1995) of 160 $\pm$ 10 per 10^3 km on axis or 310 $\pm$ 20 per 10^3 km off axis for the Reykjanes Ridge, of 200 $\pm$ 10 per 10^3 km on the Mid-Atlantic Ridge, and of their maximum measured density of 400 $\pm$ 30 per 10^3 km. Other Mid-Atlantic Ridge estimates of 200 per 10^3 km (Smith et al., 1995) and 310 per 10^3 km (Smith and Cann, 1990) are also significantly lower than my measured estimate. The same is true for Cochran (2008), who predicts a density of 275 $\pm$ 6 per 10^3 km This discrepancy suggests that previous studies done with lower resolution data have significantly under sampled seamounts at the smaller end of the scale. Figure 3.3b shows the frequency distribution of diameter data from 45˚N against the exponential relationship from Cochran (2008). This plot clearly demonstrates that the smaller seamounts (those < 200 m in diameter) are not accounted for by the Cochran (2008) curve, and therefore these smaller seamounts are hugely under represented in the Cochran (2008) study, and presumably in the other studies cited.

As demonstrated in figure 3.5, at no measured diameter (up to 350 m) are hummocks always > 50m in height, and therefore it is conceivable that many hummocks would simply have been too low lying to be imaged by the lower resolution data used in these examples. Our study also appears to under represent seamounts at the larger end of the scale, although this is partly deliberate as we wished to analyse only the hummock population and therefore omitted any flat-tops larger than 640 m. However, the main discrepancy is probably due to the fact that this survey was conducted on hummocks, which cannot be detected in lower resolution studies, and therefore in comparing our numbers with those from older surveys we are comparing different things. A number of hummocks clustered together may appear as a single seamount, additionally hummocks partially buried by others will not have a full circular basal contour and would have been omitted from the Magde and Smith (1995) study. As hummocks are the fundamental building blocks of AVRs and the fact that lower resolution studies cannot image them makes volcano density estimates based on such data almost meaningless.

The characteristic diameter of 58.5 ± 0.5 m is comparable to those observed by Cochran at the Mid-Atlantic Ridge (39.8 ± 0.8 m for the axial valley and 42.1 ± 1.6 m for the whole surveyed area) and slightly larger than those observed on the ultra-slow spreading Gakkel Ridge (Western Volcanic Zone (82˚57'N – 83˚45'N): 26.9 ± 3.5 m, Western Volcanic Zone (83˚45'N – 84˚33'N): 31.4 ± 3.5 m, Eastern volcanic zone: 22.9 ± 0.8 m). This suggests that hummock dimensions are similar on most segments and, in general, slightly larger than those at ultra-slow spreading ridges. A typical hummock of diameter 58.5 m would typically have a height between ~ 10 – 30 m (chapter 3). This is lower than the characteristic height estimates of Magde and Smith (1995), which are 68 ± 2 m at the Reykjanes Ridge and 58 ± 2 m at the Mid-Atlantic Ridge.

3.5.1.2 Overall density of hummocks

The hummock densities measured in this study are much higher than have been measured before. Smith and Cann (1990) measured average seamount densities from surface multibeam contoured at 20 m (which from their description sound analogous to our hummocks) of 80 per 1,000 km^2 for seamounts over 50 m in height on the Mid-Atlantic Ridge between 24 and 30˚N. The TOBI sidescan is capable of imaging features over ~10 m in height (LeBas and Huvenne, 2008). I measured a density of approximately 6 hummocks per km^2, equivalent to 6,000 hummocks per 1,000 km^2. However in order to be comparable with the Smith and Cann figure, we should only count edifices > 50 m in height. The resolution of the EM120 (~50 m horizontal and vertical) is not high enough to image many of the hummocks individually, however in the high-resolution bathymetry areas 33 of the 153 hummocks imaged were > 50 m in height, equivalent to ~ 20% of all the hummocks imaged. Therefore, if we assume these areas are representative of hummocky terrain as a whole, then it is likely that around 20 % of the hummocks imaged in the TOBI study will have heights > 50 m. This equates to an approximate density of 1,200 hummocks with heights > 50 m per 1000 km^2, still 15 times the Smith and Cann (1990) estimate.

It could be argued that as both these study areas lie on the AVR they are not representative of hummocks off axis, which may be partially buried by sediment or tectonically degraded reducing their height.

However 41% of all the hummocks imaged lay on the AVR, and therefore if we assume that only hummocks on the AVR have heights > 50 m (which is unlikely) we are still left with an approximate density of 492 hummocks > 50 m in height per 1,000 km^2, which is still 6 times larger than the Smith and Cann (1990) estimate. It therefore seems fair to say that the prevalence of these edifices has, until now, been vastly underestimated on ridge segments containing AVRs. This is supported by the Magde and Smith (1995) observation that small seamounts are probably underrepresented in these studies, as they are unable to measure small volcanoes.

3.5.1.3 Density distribution

The highest observed densities were, as expected, on the AVR (figure 3.8). However other high density areas, with densities comparable to those observed on the AVR, could be observed off axis, particularly north and south of the main AVR outside the median valley. These areas were typically less than 2 – 3 km across, but displayed very similar character to the AVR in the sidescan sonar maps, suggesting the terrain here is very similar to that on the AVR and was probably produced there.

The fact that these small areas still show clear hummocky character is interesting. If it is simply typical hummocky terrain then it should be buried or flattened by the processes that are burying or flattening such terrain almost everywhere else on the ridge. If this is the case then these areas might have the same density of hummocks as the AVR, but the lower sections of hummocks would be buried meaning they would appear to have smaller heights and diameters than unburied hummocks. Murton et al. (2012, in prep) suggest that hummocky terrain is buried by sheeted flows prior to being faulted out of the axial valley (discussed further in chapter 7), reducing the roughness of the terrain. If this is correct then these areas of high density hummocks could just represent the highest sections of an AVR, which had too high a relief to be buried by the sheet flows. The same could also be true if hummocky terrain is being buried by sediment, although sediment draping might smooth the hummocks out more, given them a less sharp change in gradient at their bases. If either of these scenarios is correct then the high density areas identified in this study should correspond to higher roughnesses (as determined by Murton et al. (2012, in prep). Their roughness map was produced by making a 5x5 (450 m by 450 m) high pass filter of the EM120 bathymetry and comparing it to a 3x3 standard deviation filter to distinguish the high frequency hummocky terrain. This does appear to be the case (figure 3.13), suggesting that while these hummocks have the same density as those on the AVR, they have a much lower relief, and must have either been tectonically degraded and flattened, or partially buried by lava flows or sediment.

The AVR itself is not characterised by uniform densities either along or across axis (figure 3.9). At both 250 m and 400 m scales, density variations can be observed within the bounds of the AVR. On both scales there are large variations in density within a few hundreds of meters. Densities on the AVR range from 61 hummocks within a 250 m radius to < 5 in the same radius. High density areas do not show alignments at either scale, and instead seem to form irregular-shaped or sub-rounded high density areas. At both scales the higher density areas are most commonly located on the northern more tectonised end of the AVR. These density highs may correspond with zones of melt supply, or may be a function of different sizes of edifice – i.e. lower density areas may have a few large edifices while high density areas may have many small ones. As the pointfile used to produce these maps was produced using north and south insonified datasets acoustic shadowing should not affect the results.

Figure 3.14 shows the same hummock map as shown in figure 3.1, but with the hummocks colour coded according to their diameters (categories were assigned using so-called 'natural breaks' calculated in ArcGIS 9.1 as this picked out the flat topped seamounts clearly and also displayed the variations in the dimensions of the smaller hummocks). The largest diameter category (shown in red) picks out most of the flat-topped seamounts and demonstrates clearly that they are mostly found off axis. The other 4 categories almost entirely pick out the hummocks. North of ~ 45˚35.00 N there are fewer hummocks in the larger yellow (796 – 2009 m diameter) and orange (540 – 795 m diameter) categories than to the south, a similar number of hummocks in the green category (383 – 539 m diameter) and many more in the smallest diameter blue category (< 382 m diameter). This supports the idea suggested above that these higher density areas do correspond to larger numbers of smaller hummocks. This could be a result of lower effusion rates in these areas causing vents to solidify sooner than those with faster effusion, and therefore build more, smaller hummocks. Alternatively strain may be accommodated through more frequent, smaller eruptions.

The hummocks forming the off-axis patches have smaller diameters (falling mostly in the < 120 m and 121 – 171 m diameter categories) than is typical on the AVR. This again suggests that if they were formed at an AVR, the most likely location for their construction, then they have either undergone tectonic degradation or partial burial. Tectonic degradation is less likely to uniformly reduce an edifice's diameter, typically taking the form of sector collapse (see chapter 4) and therefore partial burial, which is exposing only the upper portions of edifices, seems the most likely mechanism responsible for reducing both their height and diameter while not effecting their spatial density.

It should also be noted that on the AVR, the presence of a flat-topped seamount reduces the measured density value (e.g. the flat-top at 45˚34'N, 27˚50'W), as seamounts have diameters comparable to the radii used to calculate density and only count as a single edifice. There are very few flat-topped seamounts on the AVR however so most of the observed low density areas are assumed to be accurate.

3.5.2 Hummock dimensions in the northern and southern high-resolution study areas

The southern high-resolution study area (figure 3.4) is located on the AVR flank, on one of its more robust looking sections. In the EM120 bathymetry few faults appear to cut the area and the AVR crest in this section is one of the highest along the AVR. In contrast the northern high-resolution study area (figure 3.4) forms an almost complete transect across the more faulted and tectonised northern half of the AVR, taking in a faulted flat-topped seamount.

The southern area contains 75 hummocks and the northern area contains 78, equivalent to 17 and 16 hummocks per km^2, respectively. There is no noticeable difference between the dimensions of the hummocks in the two areas (figure 3.5) and neither area displays a characteristic height to diameter ratio, or any relationship between the two, other than a loose relationship between taller hummocks having slightly larger diameters. This is not surprising as these hummocks are formed predominantly of pillow lavas which are capable of building almost vertically upwards and therefore there is no need to build a wide base before building upwards.

A 1:10 height to diameter ratio is common for flat-topped volcanoes (Magde and Smith, 1995; Smith et al., 1995); however, figure 3.5 also demonstrates that larger edifices do not trend towards any such height to diameter ratio. It has been suggested that flat-topped seamounts are first formed as pointed cones or hummocks and then grow upwards until they reach a magmastatic limit (controlled by the magmastatic head and volatile content) (Lawson, 1996; Magde and Smith, 1995; Smith et al., 1995). If this were the case here, we might expect to see the largest hummocks beginning to trend towards a 1:10 height:diameter ratio, which is not observed. On the other hand as our largest hummock diameter in this area is 327 m and our smallest flat-top diameter is 445 m, it is possible that the hummocks covered in these areas (with the obvious exception of the flat-topped seamount in the northern area) simply did not grow large enough to reach their magmastatic limit. However, if there is continuous growth from one to the other then it is strange that there is such a gap in the distribution.

3.5.3 Eruption volumes and durations

3.5.3.1 Building hummocks

If the effusion rate and volume of an eruption can be estimated, it should be possible to put constraints on the duration of eruptions. It is generally agreed that lava morphology is controlled by effusion rate (Bonatti and Harrison, 1988; Fundis et al., 2010), and wax analogue experiments can provide approximate estimates of effusion rate (Gregg and Fink, 1995). Such experiments suggest that lavas with a viscosity of 100 Pa s (Dietrich et al., 1980), produce pillowed flows at low effusion rates (<1 m^3 s^{-1}), progressing to lobate (1 – 100 m^3 s^{-1}) and sheet flows ($>$ 100 m^3 s^{-1}) (Gregg and Fink, 1995; Gregg and Smith, 2003). While these experiments were conducted on 10° slopes, lower than the average slope in our study area, gravitational forces are not expected to exert control on morphology until slopes exceed 25° (Gregg and Smith, 2003), and do not dominate until 40° (Gregg and Fink, 1995), which is appropriate for 97% of observed hummocks.

It is possible to estimate hummock growth rates in the southern high-resolution study area using lava morphologies from summits (to minimise the effects of cooling away from the lava source). Twenty-four hummocks were imaged by Isis, ten of which have lobate morphology. All are $< 2.2 \times 10^6$ m^3 and would have formed in 0.1 - 25 days (using the upper limit of 100 m^3 s^{-1} and lower limit of 1 m^3 s^{-1}). Fourteen hummocks had pillowed morphology; the largest of these, with a volume of 4.1×10^6 m^3, would have taken > 47 days of constant effusion to form, assuming an upper effusion rate limit of 1 m^3 s^{-1} (Griffiths and Fink, 1992). The remaining pillowed hummocks have volumes < 1×10^6 m^3, and would have formed in > 11 days at constant effusion.

No discernible sediment intercalations are seen in the collapsed cross sections of any hummocks, though we know our methods could detect them since sediment layers were seen in dives on the median valley wall faults. With a regional sedimentation rate ~ 5 cm/ky (Keen and Manchester, 1970) we can thus rule out periods of quiescence on the thousand-year time scale. While continuous hummock effusion on the scale of days to years is difficult to prove, a single eruption origin seems likely. If we make the reasonable assumption that an average sized hummock conduit is no more than 20m wide (I show it cannot be > 40 m in section 2.3.6.4), it would cool in ~13 yr or less (Turcotte and Schubert, 1982), so repeat eruptions would have to occur on this timescale if they are to exploit earlier thermally weakened zones. I expect this to be a large overestimate as it is likely that the hummocks are being fed by dykes. Dykes have been observed to be only a few metres wide (Qin and Buck, 2007) and therefore conduits are unlikely to be wider than this. Additionally, the pillowed hummocks are likely to be fed through a network of pillow lavas and elongate pillows and these conduits are also likely to be less than a few meters. Thus I suggest hummocks are monogenetic. It is possible the same fissure may erupt repeatedly, although I see no evidence of this.

3.5.3.2 Fissure eruptions

From this study I identify 79 volcanic lineaments, built of an average of 8 hummocks each. Searle et al., (2010) identify fewer (but longer) lineaments, which have an average of 12 hummocks along them (measured from their lineaments on the TOBI). This difference is predominantly due to connecting orthogonal lineaments with ridge parallel counterparts (i.e. the lateral spurs which run off the AVR), which, as we expect eruption to occur along ridge parallel fissures parallel to the local stress regime (Fujita and Sleep, 1978) and then feed these orthogonal spurs, is probably the most realistic way to represent them. In the following sections estimates for eruptions consisting of 8 and of 12 hummocks are given. Even this number of 12 may be an underestimate if not all the hummocks created by an eruption lie along the strike of a lineament.

If we assume that all the hummocks on a lineament are produced by the same eruption (8 – 12 hummocks per eruption) and we know the average volume of a hummock (292,000 m^3) then it is possible to estimate the volume of the eruptive products for a single eruption as being between 2,336,000 m^3 and 3,504,000 m^3. This is similar to eruption volumes on the fast-spreading East Pacific Rise (3.6×10^6 – 5.8×10^6 m^3 (Gregg et al., 1996)), and differs from the suggestion that eruption volumes should be significantly larger at slow-spreading ridges (Perfit and Chadwick, 1998; Sinton et al., 2002; Soule et al., 2007).

The volume of the AVR (using the 3220 m contour) can be calculated to be ~16 km^3, assuming a flat base, and therefore would require ~55,000 hummocks or 4,500 – 7,000 average sized eruptions to build it.

The AVR sits within an axial valley 6 km wide at its centre, representing 286 ka at the full spreading rate of 2.1 cm yr^{-1}; the maximum possible AVR age. This yields a minimum magma flux to the seafloor of 5.6×10^4 m^3 yr^{-1} (given by dividing the volume of the AVR by the age of the axial valley) sufficient to produce one average volume hummock every 5 yr. If AVR lineaments comprise an average of 8 – 12 hummocks, then assuming each lineament represents a single fissure eruption (Smith and Cann, 1999) and assuming the whole AVR is built only by such eruptions there would be approximately one eruption every 40 – 60 yr.

Alternatively eruption duration can be estimated using the volume of hummocks and the eruption rates typical for the observed proportions of lava lithologies observed at their summits. Assuming the AVR is built entirely of average-sized (2.92×10^5 m^3) hummocks, it would contain ~55,000 hummocks. Of the twenty-four hummocks where we can be certain the summit morphology was imaged by ROV *Isis*, ten have lobate morphology and 14 are pillowed. This ratio of 42% lobate and 58% pillowed hummocks and the effusion rates estimated by Gregg and Fink (1995), can be used to estimate the time required to build the whole AVR. Using the estimate of 55,000 hummocks the entire AVR could be built in only 300 yr, or less if hummocks are erupted in groups (lineaments). This is much lower than other published estimates (e.g., Searle et al., 2010) and implies lower eruption rates and/or large eruptive pauses.

3.5.4 AVR life cycles

The AVR life cycle described by Parson et al. (1993) is characterised by distinct phases of focused eruptive activity and non-volcanic tectonic extension (figure 3.15). These different phases should be characterised by different degrees of alignment and patterns of cluster. The adolescent and mature phases (figure 3.15 b, c) should be characterised by a strong density maximum (on a large scale) centred on the AVR. You would not expect to see many areas of high density hummocks off the AVR, nor many areas of low density on the AVR as a result of faulting. During these stages you would also expect most of the hummocks to be erupted on the AVR and therefore a strong degree of ridge parallel alignment. During the young and old stages (figure 3.15 a, d) hummocky volcanism is likely to be more spread out across the valley floor, either as a result of eruption of a number of small hummocky ridges which have yet to coalesce (i.e. a new proto-AVR) or could form a much smaller hummocky ridge, or of old hummocky terrain being broken into slivers by normal faulting as extension is progressively accommodated tectonically. In these scenarios high density hummocks would form elongate, ridge parallel lenses, separated by areas of low density representing flat seafloor between new ridges, or faults. Additionally, if the AVR is being broken up tectonically one would expect to see a reduction in the strength of any ridge parallel alignment, as the faults would spread the hummocky terrain out perpendicular to the ridge axis.

Alternatively, if the AVR is steady-state (as described by Murton et al. (2012, in prep)) then different degrees of faulting and eruption frequency could cause different patterns of cluster. In a typical steady-state AVR situation high densities would be focussed on the AVR with low densities on the sheet flows that surround it, burying the hummocky terrain.

At 45˚N there is no simple pattern of high and low density across the axial valley, and the northern end appears more tectonically degraded than the southern end. In the EM120 bathymetry a number of faults, both inward and outward facing, can be identified cutting the AVR. Additionally the northern end forms a wider, lower relief (predominantly less than 200 m above the 3220 m contour) high than the southern half of the AVR, which in contrast forms a single, narrow, taller (usually > 600 m above the 3220 m contour) topographic high. This is reflected in the statistics, with the southern area producing a narrower high density area than the northern half, which covers a much wider area (figure 3.7 B, C). The hummocks are also more strongly aligned in the southern half of the AVR (figure 3.12), with an SDE ellipse minor:major axis ratio of 1:1.52, as opposed to 1:1.23 in the north. In fact the two ends of the AVR appear to be in different stages of the Parson et al. (1993) life cycle model – the southern end looks more like the adolescent or mature stage (figure 3.15), with a robust central AVR, cut by a few small faults, while the northern section bears a closer resemblance to the old stage (figure 3.15) with a lower relief cut by many faults and spread out laterally.

This difference in hummock distribution on the same AVR argues against a simple model of AVR life cycles. We know that melt supply is episodic to slow-spreading ridges (Detrick et al., 1990) and it follows that it is the availability of melt supply to the AVR that governs which life cycle stage it will be in at any one time. If melt is readily available then all extension will be accommodated through dyke intrusion and there will be little tectonism associated with the ridge. This appears to be the case for the southern section, and is supported by evidence that the most recent volcanic eruptions have occurred at its southern end (see section 2.3.5.4). On the other hand, where little melt is available more of the extension will be accommodated through normal faulting and fissuring, and the AVR will move into the "old" stage. This appears to be the case for the northern end of the AVR, which has been spread out laterally by a number of faults (faults are mapped in Searle et al. (2010)), and is supported by the observed heavier sedimentation in the north (see section 2.3.5.6). All this evidence suggests that the northern end of the AVR is older, meaning it has not experienced volcanism as recently as the southern end and the mode of extension appears to have switched from dyke injection to faulting.

If this hypothesis is correct then it means that a single AVR may be in one, or several, life stages at the same time, depending on how continuous the melt supply is. If melt supply to the entire ridge drops then the whole AVR may be tectonically dismembered, however it would also be possible for sections, or even the entire AVR to be rejuvenated if melt supply increased again.

3.6 Conclusions

The AVR at 45˚N is composed of hummocky terrain, and between 1,850 and 2,800 hummocks are found on the surface of the AVR, depending on how its limits are defined. Nineteen flat-topped seamounts were observed of which only two lie on the AVR. The hummocks have diameters between 23 m and 639 m, although the largest edifices are probably composite edifices formed of several hummocks. Hummocks have a characteristic diameter of 58.4 m $\pm$ 0.5 m, which is similar to other Mid-Atlantic Ridge studies. Hummocks are formed by pillow or lobate lava flows, and it is possible that the lobate hummocks have slightly lower relief, although we do not have enough evidence to prove or disprove this theory. There is no strong correlation between hummock heights and hummock diameters, and we see no evidence here of hummocks building into flat-topped seamounts (moving towards the 1:10 height:diameter ratio measured elsewhere). Although as almost all of the hummocks for which we have height data are smaller than the flat-topped seamounts it is possible none of them are large enough to make the transition. There is no real difference in dimensions between the hummocks in the northern and southern high-resolution areas, although those in the north appear more tectonised.

Both the observed hummock density of ~ 6,000 hummocks per 1,000 km^2, and the characteristic hummock density of 33,556 per 10^3 km are much larger than estimates of seamount density in the past, probably because smaller seamounts could not be detected by these lower resolution studies, and because the “seamounts” identified in multibeam data comprise only the largest hummocks, and clusters of hummocks which can only be resolved individually in sidescan sonar. The highest hummock density in the survey is on the AVR, although small patches of similarly high density hummocky terrain are observed off axis, mostly to the north of the AVR. The fact these areas have a similar density to the AVR suggests they may have been formed there, however they have smaller heights and diameters, suggesting that something has acted to reduce their relief – probably burial by sediment or other lava flows. They may have formed some of the highest sections of an old AVR (now rifted off-axis), which placed them above most of the lava flows/sediment which buried the rest of the hummocky terrain around them.

The AVR is not characterised by uniform hummock densities. Higher density patches are observed, which may correlate to sources of melt, although this cannot be proved (further geochemical work being carried out at NOC Southampton may help to answer this question in the future). Higher hummock densities are observed on the north end of the AVR, although the hummocks here typically have smaller diameters and lower reliefs than those in the south. This may mean that this end underwent more intense eruption than the south before being broken up and the relief reduced by burial from sediment or other lava flows (this is discussed further in chapter 7), or that the eruption volumes here were similar to the south but produced more, smaller hummocks.

The average volume of a volcanic hummock is 292,000 m^3. Hummocks form a number of ridge parallel and orthogonal lineaments, which are on average between 8 and 12 hummocks long. Those that lie ridge parallel are probably produced by ridge parallel fissure eruptions, while the orthogonal flows lie down the steeper ridge flanks and are probably supplied by gravity driven lava tubes (Searle et al., 2010; Smith and Cann, 1999). Single eruptions of 8 – 12 hummocks will typically have volumes between 2,336,000 m^3 and 3,504,000 m^3, similar to eruption volumes on the fast spreading East Pacific Rise. The volume of the AVR is ~16 km^3, meaning it requires ~55,000 average volume hummocks or ~7,000 average volume eruptions to build it. Using the maximum estimated effusion rates for the observed lava lithologies the AVR could be built in as little as 300 years of continuous eruption, implying lower effusion rates and/or large eruptive pauses.

The whole AVR cannot be characterised statistically by a single stage in the Parson et al. (1993) life cycle model. Instead, at 45˚N, the north and south of AVR appear to be in different stages. As the life cycle stage is dependent on melt supply this implies that there is currently, or has recently been, more melt supply to the southern half of the AVR than the northern half, resulting in extension in the south predominantly by dyke intrusions and in the north by normal faulting. If the life cycle stage relies on melt supply, and melt supply to the AVR is episodic, it follows that the same AVR can all be in one stage or in several and that even once it enters the old stage, renewed supply of melt can cause rejuvenation of a tectonised AVR.

3.7 References

Baloga, S.M., Glaze, L.S., and Bruno, B.C., 2007, Nearest-neighbor analysis of small features on Mars: Applications to tumuli and rootless cones: J. Geophys. Res., v. 112, p. E03002.

Bleacher, J.E., Glaze, L.S., Greeley, R., Hauber, E., Baloga, S.M., Sakimoto, S.E.H., Williams, D.A., and Glotch, T.D., 2009, Spatial and alignment analyses for a field of small volcanic vents south of Pavonis Mons and implications for the Tharsis province, Mars: Journal of Volcanology and Geothermal Research, v. 185, p. 96-102.

Bonatti, E., and Harrison, C.G.A., 1988, Eruption styles of basalts in oceanic spreading ridges and seamounts - Effect of magma temperature and viscosity Journal of Geophysical Research-Solid Earth and Planets, v. 93, p. 2967-2980.

Bryan, W.B., Humphris, S.E., Thompson, G., and Casey, J.F., 1994, Comparitive volcanology of small acial eruptive centres in the MARK area Journal of Geophysical Research-Solid Earth, v. 99, p. 2973-2984.

Cochran, J.R., 2008, Seamount volcanism along the Gakkel Ridge, Arctic Ocean: Geophysical Journal International, v. 174, p. 1153-1173.

Detrick, R.S., Mutter, J.C., Buhl, P., and Kim, II, 1990, No evidence from multichannel reflection data for a crustal magma chamber in the MARK area in the Mid-Atlantic Ridge Nature, v. 347, p. 61-64.

Dietrich, G.K., Krauss, K.W., and Siedler, G., 1980, General Oceanograpy: New York, John Wiley, 625 p.

Fujita, K., and Sleep, N.H., 1978, Membrane stresses near mid-ocean ridge-transform intersetions Tectonophysics, v. 50, p. 207-221.

Fundis, A.T., Soule, S.A., Fornari, D.J., and Perfit, M.R., 2010, Paving the seafloor: Volcanic emplacement processes during the 2005-2006 eruptions at the fast spreading East Pacific Rise, 9 degrees 50 ' N: Geochemistry Geophysics Geosystems, v. 11.

Gregg, T.K.P., and Fink, J.H., 1995, Quantification of submarine lava-flow morphology through analog experiments Geology, v. 23, p. 73-76.

Gregg, T.K.P., Fornari, D.J., Perfit, M.R., Haymon, R.M., and Fink, J.H., 1996, Rapid emplacement of a mid-ocean ridge lava flow on the East Pacific Rise at 9 degrees 46'-51'N: Earth and Planetary Science Letters, v. 144, p. E1-E7.

Gregg, T.K.P., and Smith, D.K., 2003, Volcanic investigations of the Puna Ridge, Hawai'i: relations of lava flow morphologies and underlying slopes: Journal of Volcanology and Geothermal Research, v. 126, p. 63-77.

Griffiths, R.W., and Fink, J.H., 1992, Solidification and morpholoy of submarine lavas - A dependence on extrusion rate Journal of Geophysical Research-Solid Earth, v. 97, p. 19729-19737.

Haymon, R.M., Fornari, D.J., Edwards, M.H., Carbotte, S., Wright, D., and Macdonald, K.C., 1991, Hydrothermal vent distribution along the East Pacific Rise crest (9°09′–54′N) and its relationship to magmatic and tectonic processes on fast-spreading mid-ocean ridges: Earth and Planetary Science Letters, v. 104, p. 513-534.

Head, J.W., Wilson, L., and Smith, D.K., 1996, Mid-ocean ridge eruptive vent morphology and substructure: Evidence for dike widths, eruption rates, and evolution of eruptions and axial volcanic ridges: Journal of Geophysical Research-Solid Earth, v. 101, p. 28265-28280.

Jordan, T.H., Menard, H.W., and Smith, D.K., 1983, Density and Size Distribution of Seamounts in the Eastern Pacific Inferred From Wide-Beam Sounding Data: J. Geophys. Res., v. 88, p. 10508-10518.

Keen, M.J., and Manchester, K.S., 1970, The Mid-Atlantic Ridge near 45ºN. X. Sediment distribution and thickness from seismic reflection profiling: Canadian Journal of Earth Sciences, v. 7, p. 735-747.

Lawson, N.K., 1996, Crustal Accretion Near Ridge-Transform Intersections: Kane Fracture Zone, Mid-Atlantic Ridge: Durham, University of Durham.

LeBas, T.P., and Huvenne, V.A.I., 2008, Acquisition and processing of backscatter data for habitat mapping – Comparison of multibeam and sidescan systems: Applied Acoustics.

Magde, L.S., and Smith, D.K., 1995, Seamount volcanism at the Reykjanes Ridge - Relationship to the Iceland hot-spot Journal of Geophysical Research-Solid Earth, v. 100, p. 8449-8468.

Mitchell, A., 2005, The ESRI Guide to GIS Analysis, ESRI Press.

Parson, L.M., 1993, Sidescan sonar and swath bathymetry investigation of the Reykjanes Ridge, southwest of Iceland, R/V Maurice Ewing EW9008 Cruise Report (unpublished).

Parson, L.M., Murton, B.J., Searle, R.C., Booth, D., Evans, J., Field, P., Keeton, J., Laughton, A., McAllister, E., Millard, N., Redbourne, L., Rouse, I., Shor, A., Smith, D., Spencer, S., Summerhayes, C., and Walker, C., 1993, En-echelon axial volcanic ridges at the Reykjanes Ridge- A life-cycle of volcanism and tectonics Earth and Planetary Science Letters, v. 117, p. 73-87.

Perfit, M.R., and Chadwick, W., 1998, Magmatism an Mid-Ocean Ridges: Constraints from Volcanological and Geochemical Investigations, *in* Buck, R., ed., Faulting and Magmatism at Mid-Ocean Ridges, Americal Geophysical Union.

Qin, R., and Buck, W.R., 2007, Why metre-wide dikes at oceanic spreading centres?:: Earth and Planetary Science Letters, v. 265.

Raffell, D.K., 2010, unpublished, A Statistical Investigation into Seamount populations at the Southwest Indian

Ridge and Mid-Atlantic Ridge.: Durham university dissertation project.

Searle, R.C., Murton, B.J., Achenbach, K., LeBas, T., Tivey, M., Yeo, I., Cormier, M.H., Carlut, J., Ferreira, P., Mallows, C., Morris, K., Schroth, N., van Calsteren, P., and Waters, C., 2010, Structure and development of an axial volcanic ridge: Mid-Atlantic Ridge, 45°N: Earth and Planetary Science Letters, v. 299, p. 228-241.

Sinton, J., Bergmanis, E., Rubin, K., Batiza, R., Gregg, T.K.P., Gronvold, K., Macdonald, K.C., and White, S.M., 2002, Volcanic eruptions on mid-ocean ridges: New evidence from the superfast spreading East Pacific Rise, 17 degrees-19 degrees S: Journal of Geophysical Research-Solid Earth, v. 107.

Smith, D.K., and Cann, J.R., 1990, Hundreds of small volcanoes on the median valley floor of the Mid-Atlantic Ridge at 24-30[deg] N: Nature, v. 348, p. 152-155.

—, 1992, The role of seamount volcanism in crustal construction and the Mid-Atlantic Ridge (24-degrees-30-degrees-N) Journal of Geophysical Research-Solid Earth, v. 97, p. 1645-1658.

—, 1999, Constructing the upper crust of the Mid-Atlantic Ridge: A reinterpretation based on the Puna Ridge, Kilauea Volcano: Journal of Geophysical Research-Solid Earth, v. 104, p. 25379-25399.

Smith, D.K., Humphris, S.E., and Bryan, W.B., 1995, A comparison of volcanic edifices at the Reykjanes Ridge and the Mid-Atlantic Ridge at 24-degrees-30degrees-N Journal of Geophysical Research-Solid Earth, v. 100, p. 22485-22498.

Soule, S.A., Fornari, D.J., Perfit, M.R., and Rubin, K.H., 2007, New insights into mid-ocean ridge volcanic processes from the 2005-2006 eruption of the East Pacific Rise, 9 degrees 46 ' N-9 degrees 56 ' N: Geology, v. 35, p. 1079-1082.

Turcotte, D.L., and Schubert, G., 1982, Geodynamics applications of continuum physics to geological problems: New York, Wiley.

Wessel, P., and Lyons, S., 1997, Distribution of large Pacific seamounts from Geosat/ERS-1: Implications for the history of intraplate volcanism: J. Geophys. Res., v. 102, p. 22459-22475.

Wong, D.W.S., and Lee, J., 2005, Statistical Analysis of Geographic Information: with ArcView GIS and ArcGIS New York, Wiley.

Wylie, J.J., Helfrich, K.R., Dade, B., Lister, J.R., and Salzig, J.F., 1999, Flow localization in fissure eruptions: Bulletin of Volcanology, v. 60, p. 432-440.

Yeo, I., Searle, R.C., Achenbach, K.L., Le Bas, T.P., and Murton, B.J., 2012, Eruptive hummocks: Building blocks of the upper ocean crust: Geology, v. 40, p. 91-94.

3.8 Figures

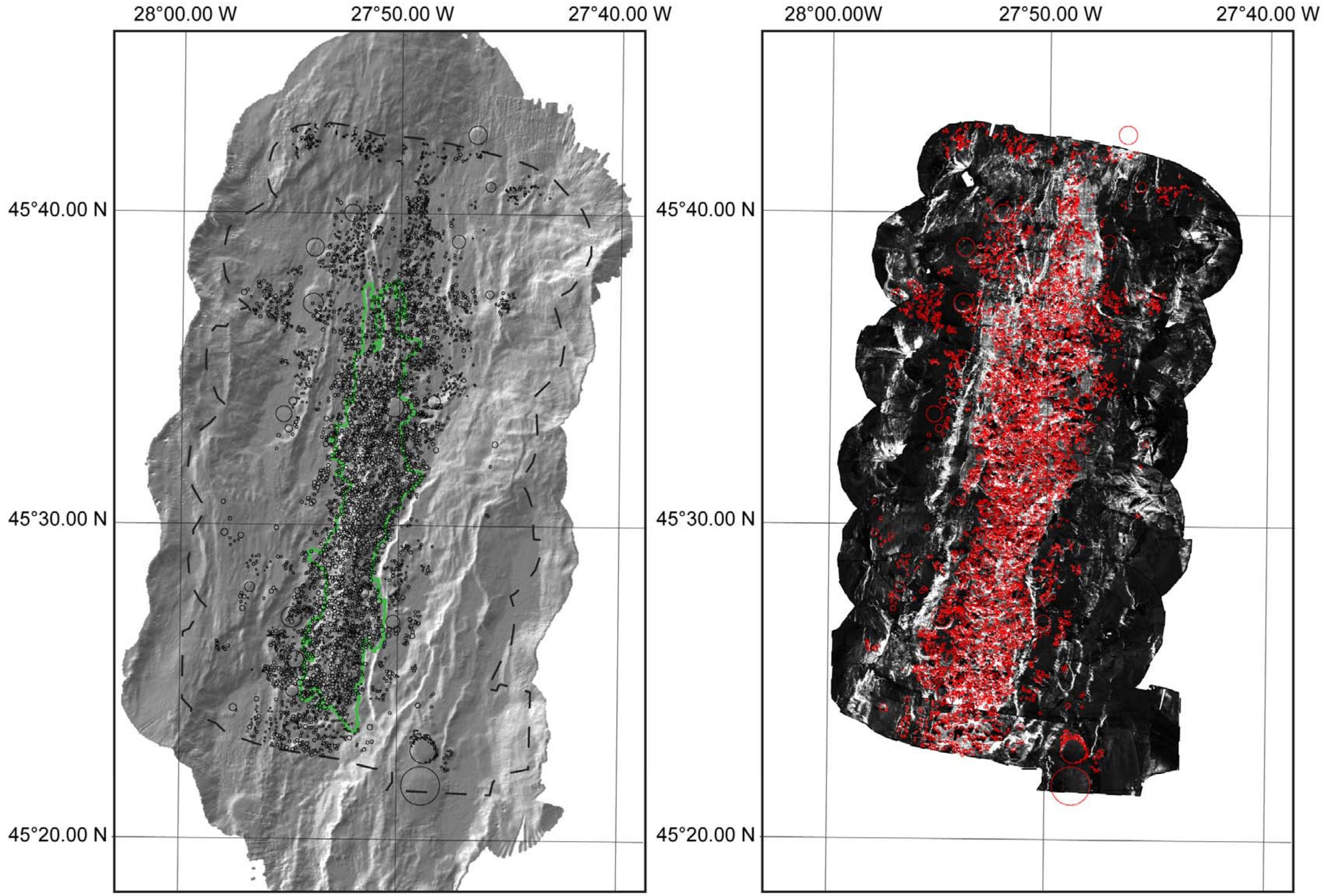

Figure 3.1: All picked hummocks on hill shaded bathymetry (left hand panel) and on TOBI sidescan sonar (right hand panel). The TOBI extent is shown by the dashed black line and the extent of the AVR, as picked from the 3220 m depth contour is shown in green. The further hummocky areas below the 3220 contour is shown by the paler green dashed line. The sidescan sonar shows the north insonified dataset on top of the south insonified one (only visible in the southernmost swath set to show full extent of TOBI coverage); both datasets were used to pick data.

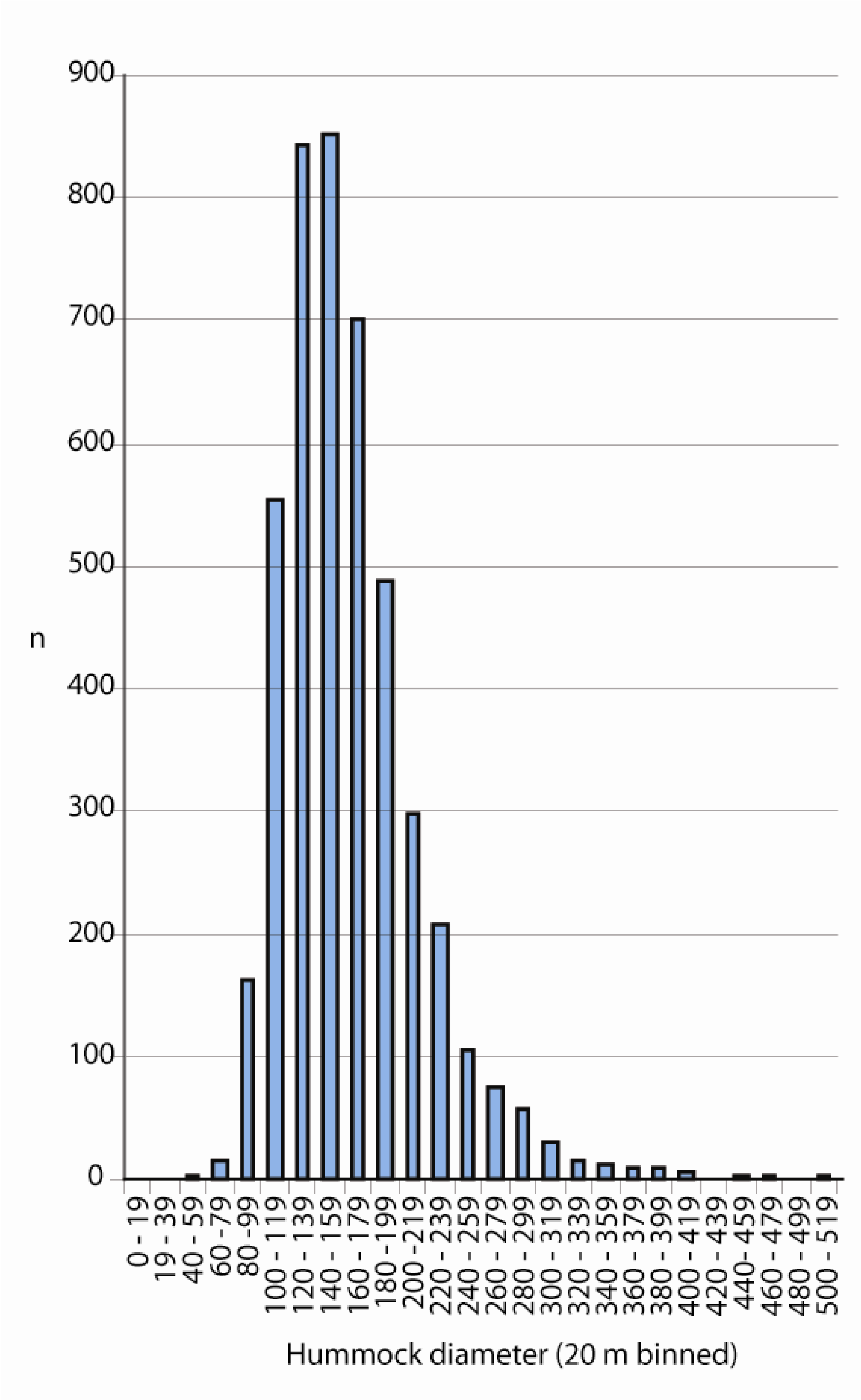

Figure 3.2: Binned (20 m bins) diameters for all edifices identified from TOBI sidescan sonar. All edifices > 640 m in diameter were flat-topped seamounts so are not shown.

A

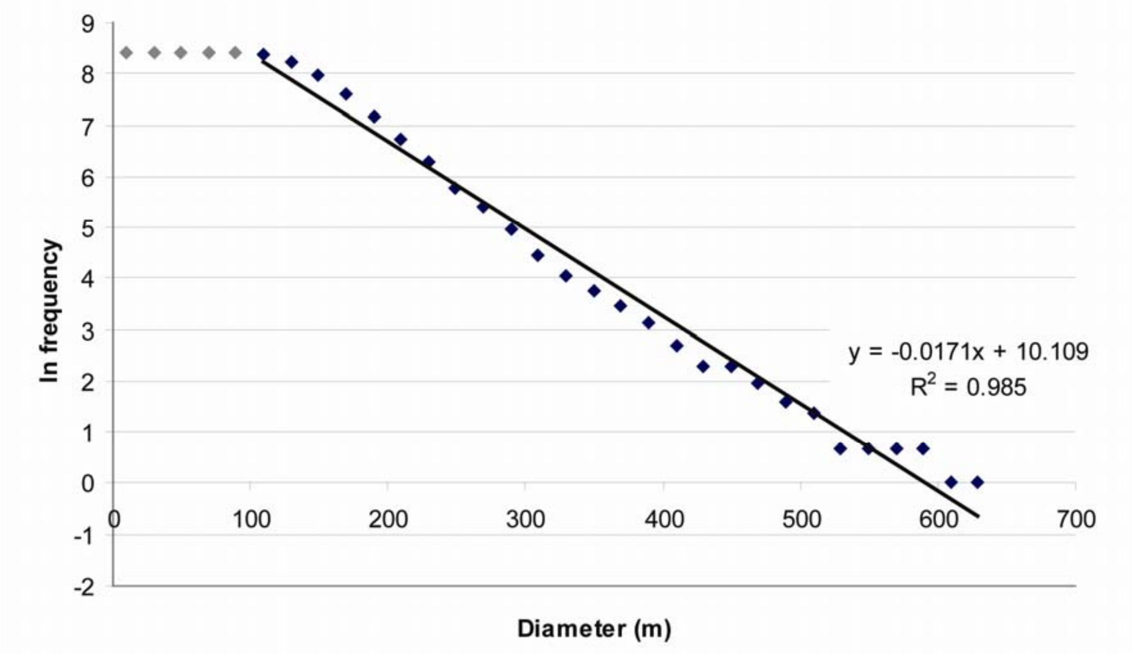

B

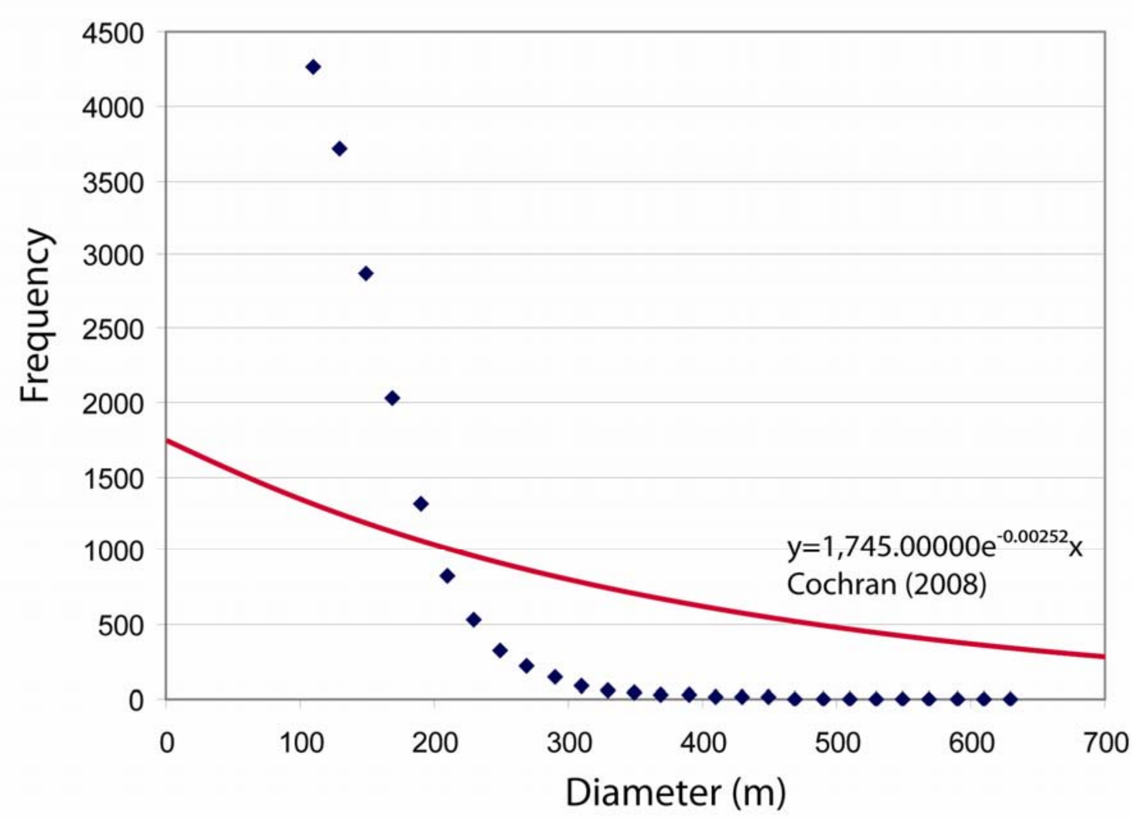

Figure 3.3: A) Natural log of cumulative frequency plotted against diameter for the measured hummocks at 45˚N. A linear trend line was fitted. The equation of the line is shown on the graph. Hummocks smaller than 100m in diameter (shown in grey) deviate from the line and are excluded from the dataset used to produce the trend line (shown in blue). B) Our data distribution for 45˚N (blue points) against the adapted exponential model (red line) from Cochran (2008) in Raffell (2010).

Figure 3.4

Southern High-Resolution Area

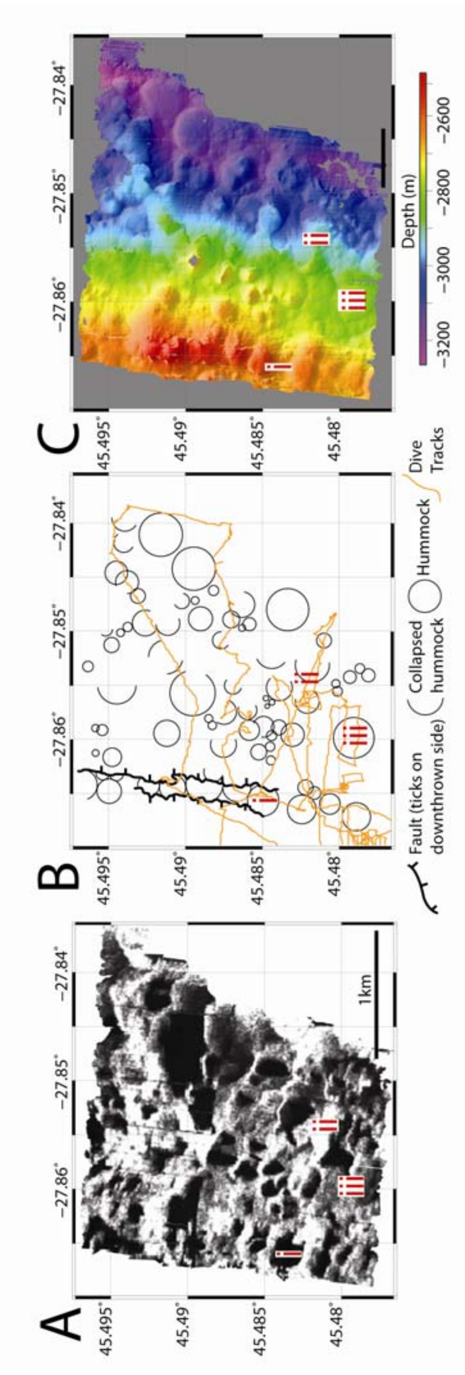

Data from the southern high-resolution bathymetry study area. (A) TOBI sidescan sonar mosaic of two south-looking images, joined near 45.49°N, the northern one overlapping the nadir of the southern. High backscatter is represented by light tones. (C) Corresponding area of high-resolution SM2000 bathymetry. (B) Interpretation (only hummocks robust in both the sidescan sonar and SM2000 bathymetry are included). Three hummocks , identified by roman numerals i to iii, are illustrated in all three datasets. The high-resolution bathymetry allows for the identification of features such as faults hummock-limited collapses that are unresolved by TOBI.

Northern High-Resolution Area

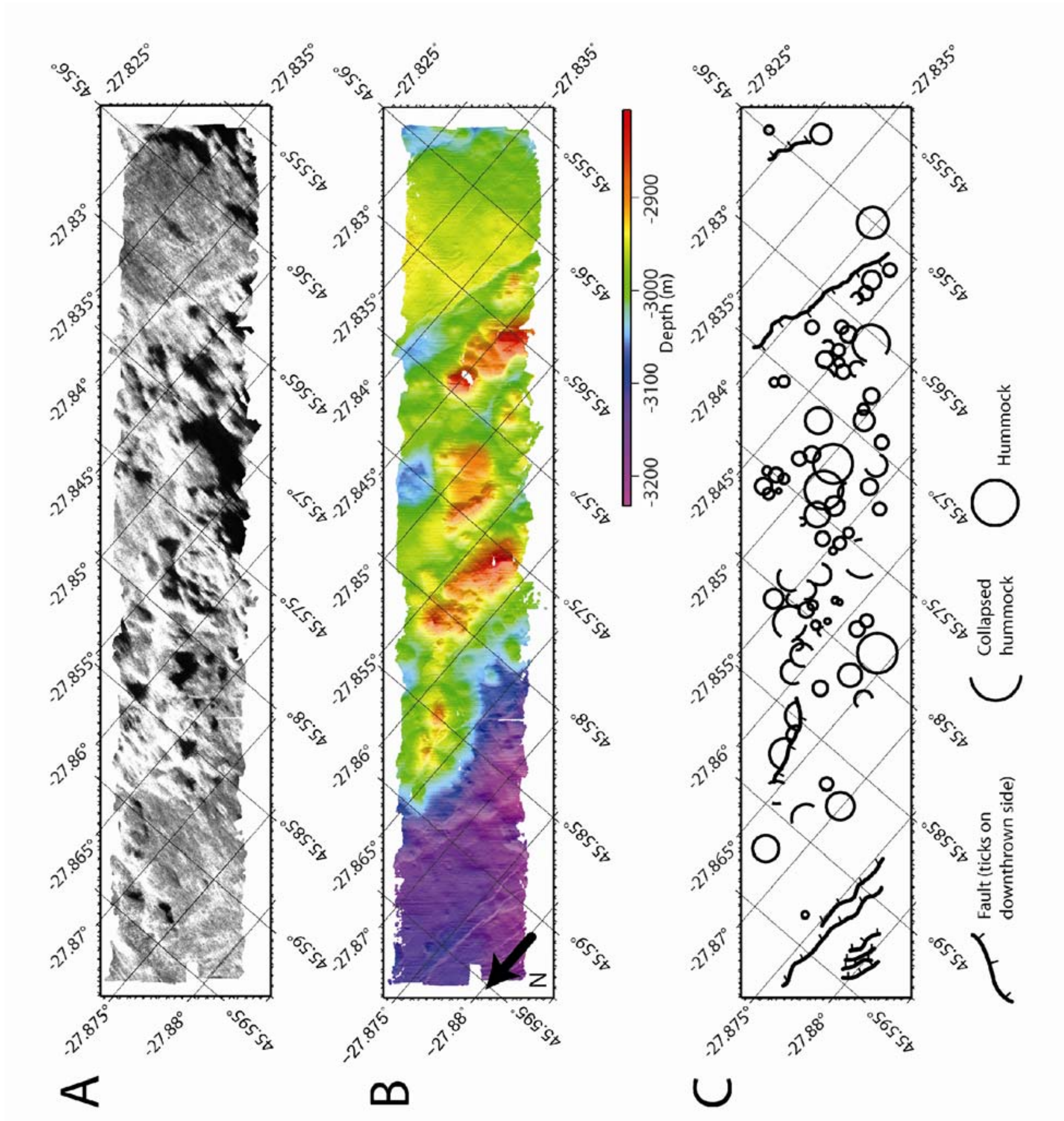

Data from the northern high-resolution bathymetry study area. (A) TOBI sidescan sonar mosaic in which high backscatter is represented by light tones (insonified from N). (B) Corresponding area of high-resolution SM2000 bathymetry. (C) Interpretation (only hummocks robust in both the sidescan sonar and SM2000 bathymetry are included).

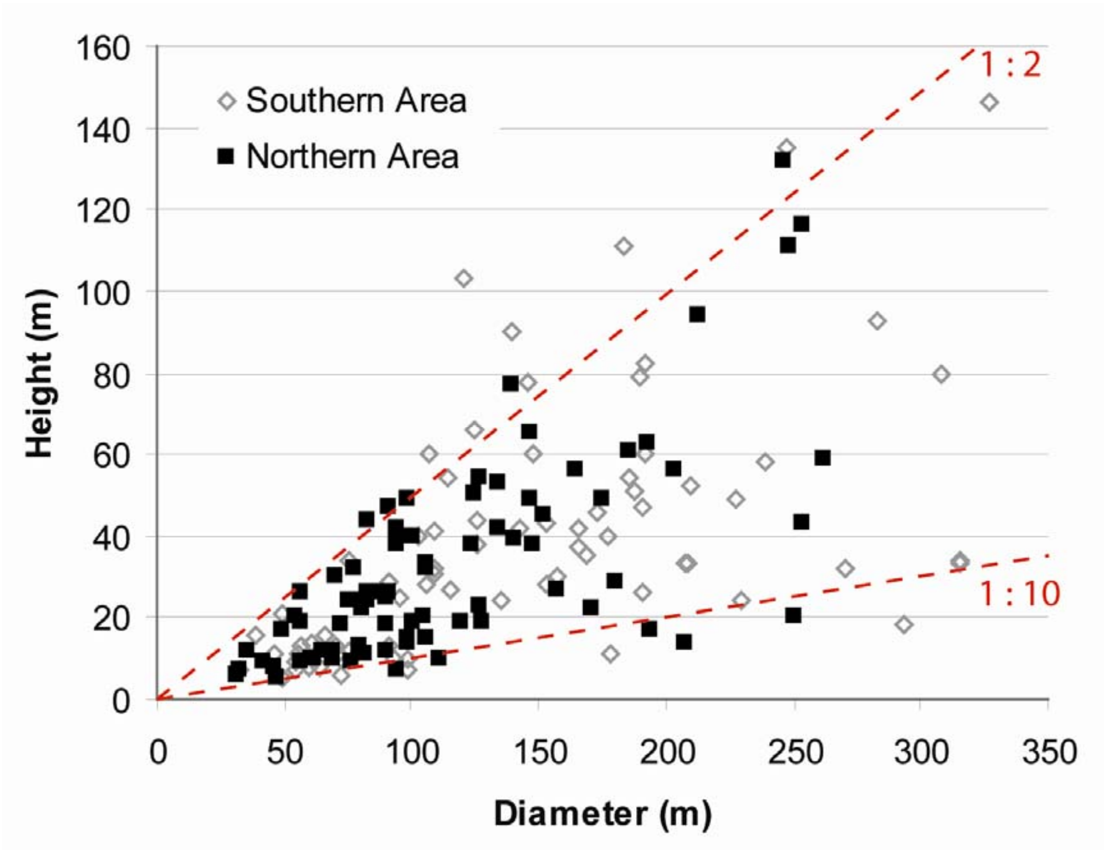

Figure 3.5: Height plotted against diameter for the 153 hummocks identified in the two high-resolution areas of ROV bathymetry.

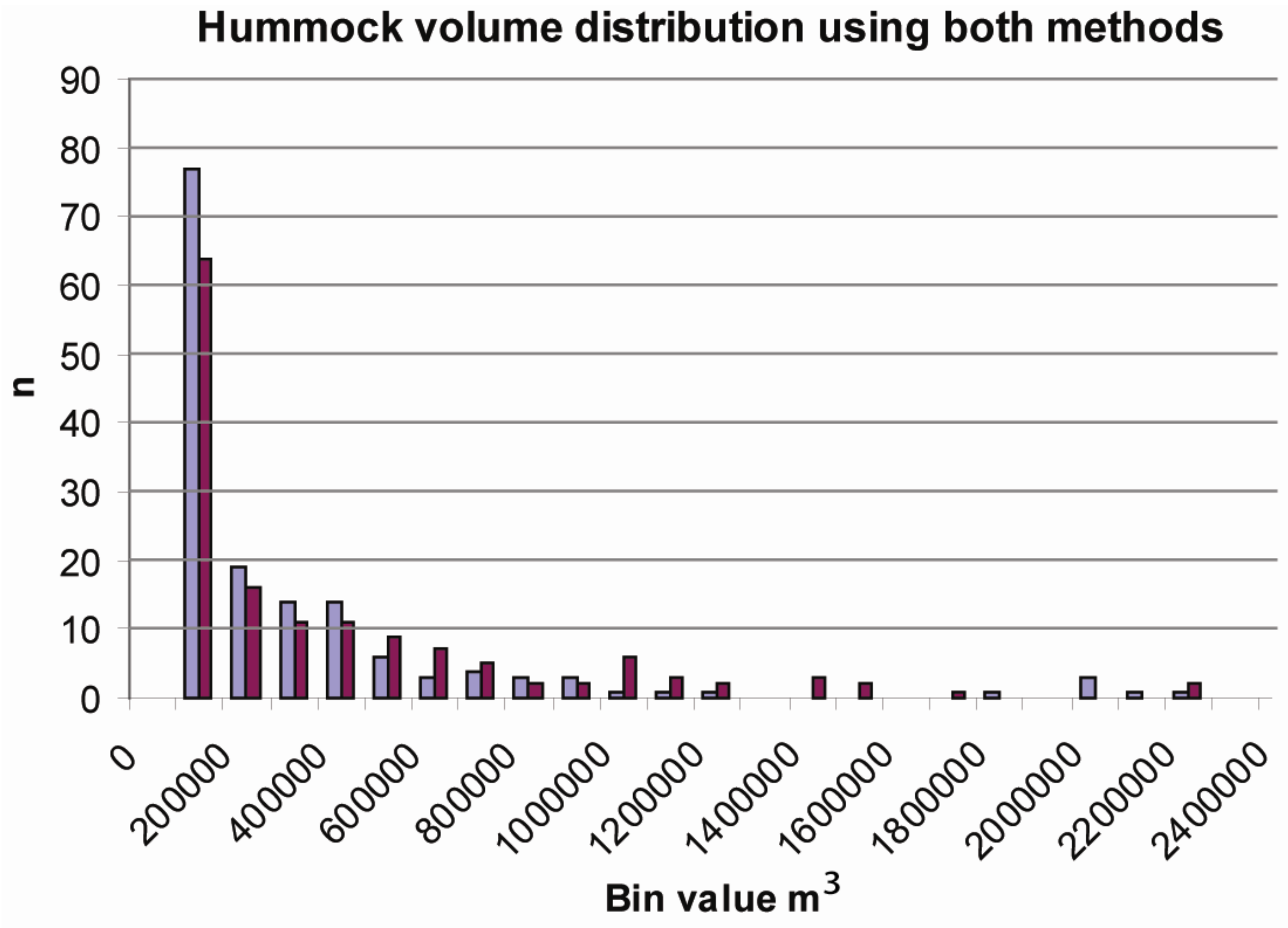

Figure 3.6: Histogram of hummock volumes calculated using the cone shape approximation (lilac) and the spherical cap shape approximation (maroon). Data is binned into 100,000 m^3 bins.

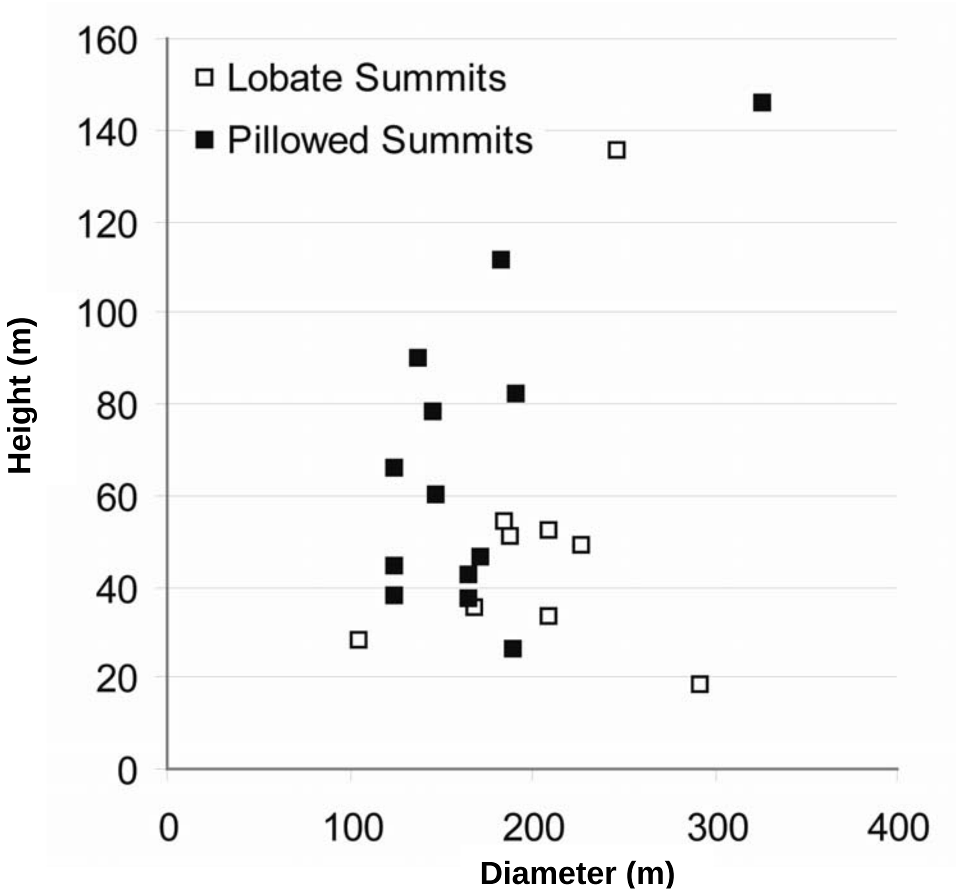

Figure 3.7: Height plotted against diameter for the 10 lobate and 14 pillow summit hummocks observed on ROV dives in high-resolution bathymetry area 1.

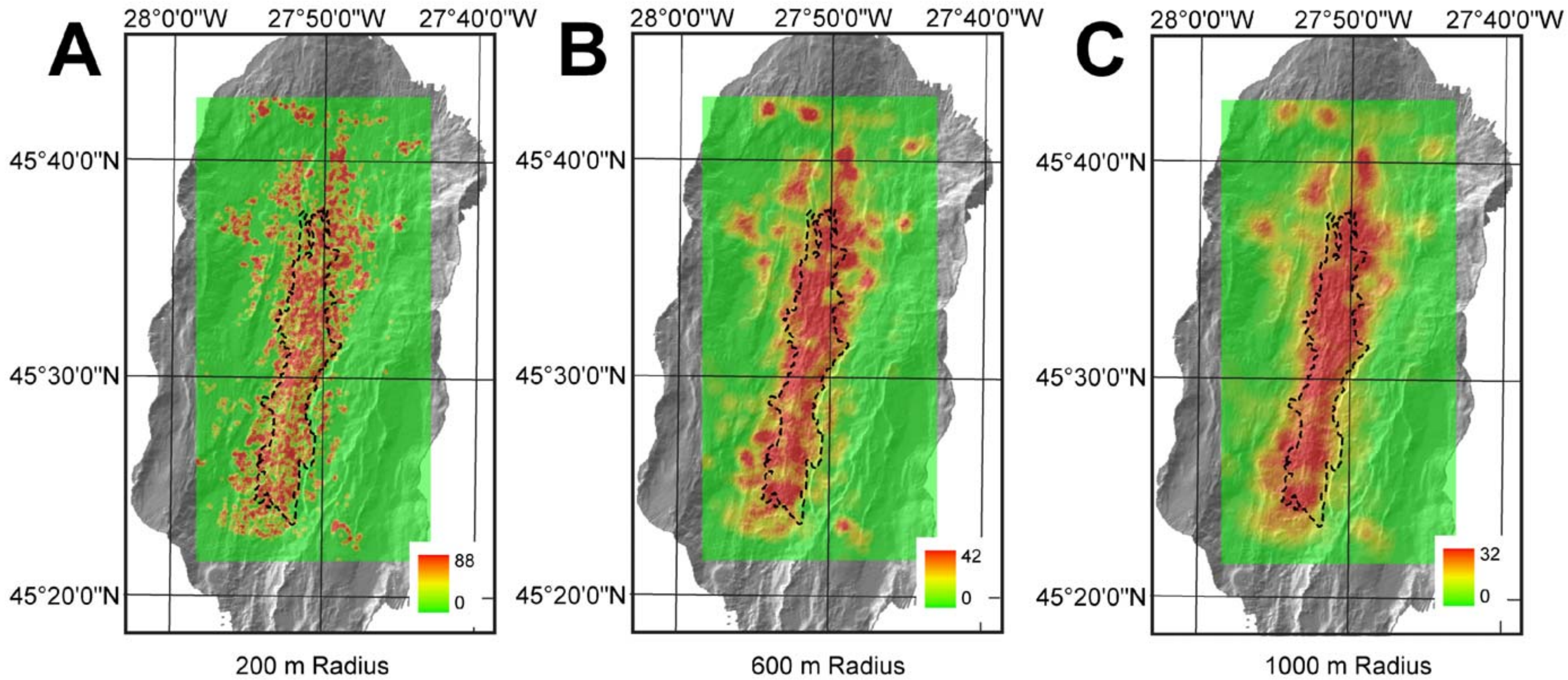

Figure 3.8: Number of hummocks per 1km^2. Densities were calculated per pixel, for all identified hummocks from the TOBI sidescan sonar, at three different radii of circle around the pixel (200 m (A), 600 m (B) and 1,000 m (C) radii). The scale colours each pixel dependant on how many other hummocks lie within the circular radius at each scale. Higher densities will have larger numbers of hummocks within the 1 km circle than lower density areas. At the smallest scale (A) a number of discrete clustered areas can be identified, while a more general pattern can be identified at the intermediate scale (B). At the largest scale (C) the density map shows that the highest density of volcanic hummocks lies within the two bounding axial valley wall faults, however smaller patches of high density hummocks can also be identified off axis at all three scales, with densities equivalent to those observed on the ridge axis. Dashed lines show the 3220 m AVR outline contour.

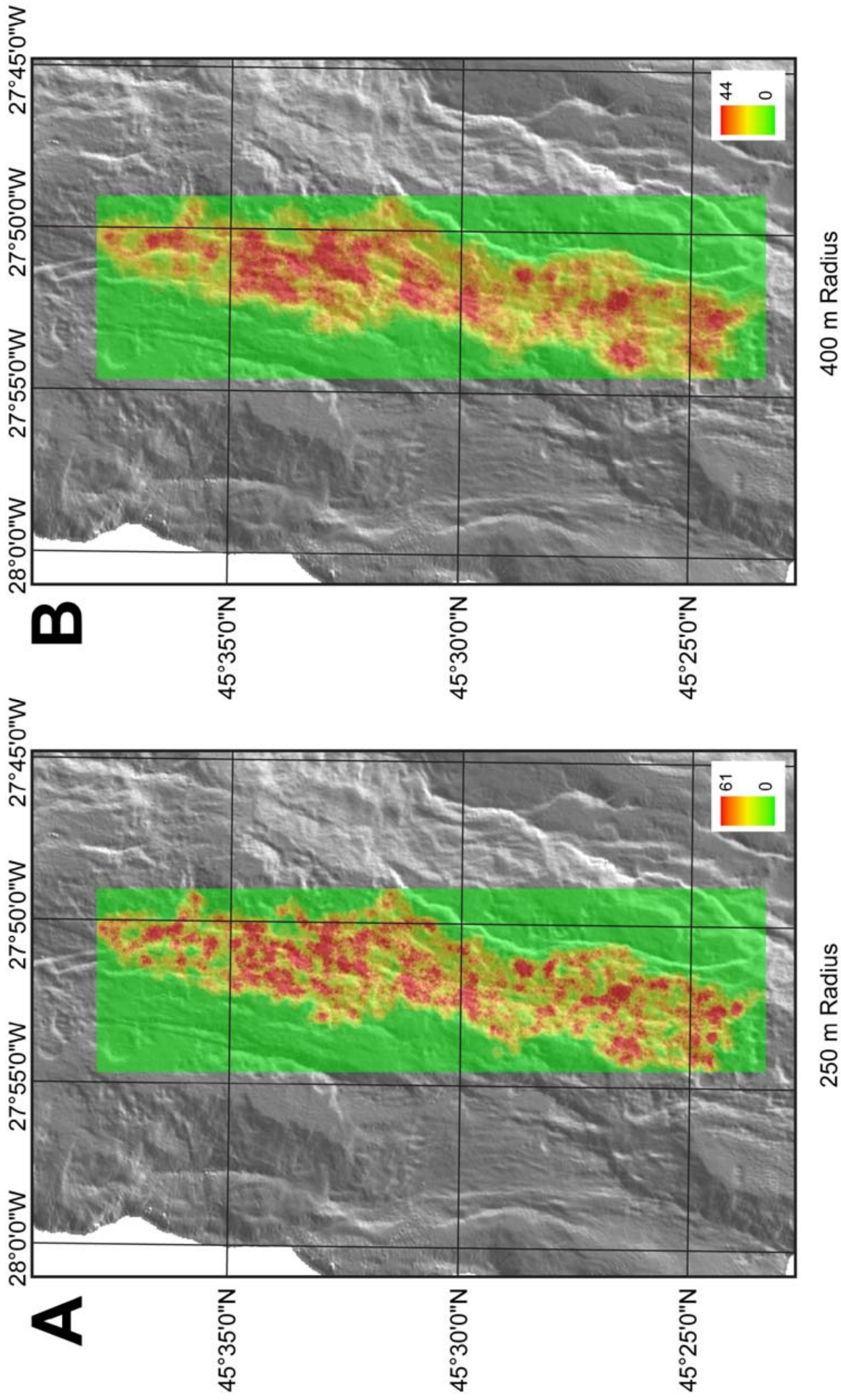

Figure 3.9: Density of all identified hummocks on the AVR at two different scales (250 m (A) and 400 m (B). Both maps show hummock density is not uniform all over the AVR with higher and lower density patches. At both scales these patches appear to be fairly randomly distributed across the AVR, with slightly higher densities in the northern more faulted area.

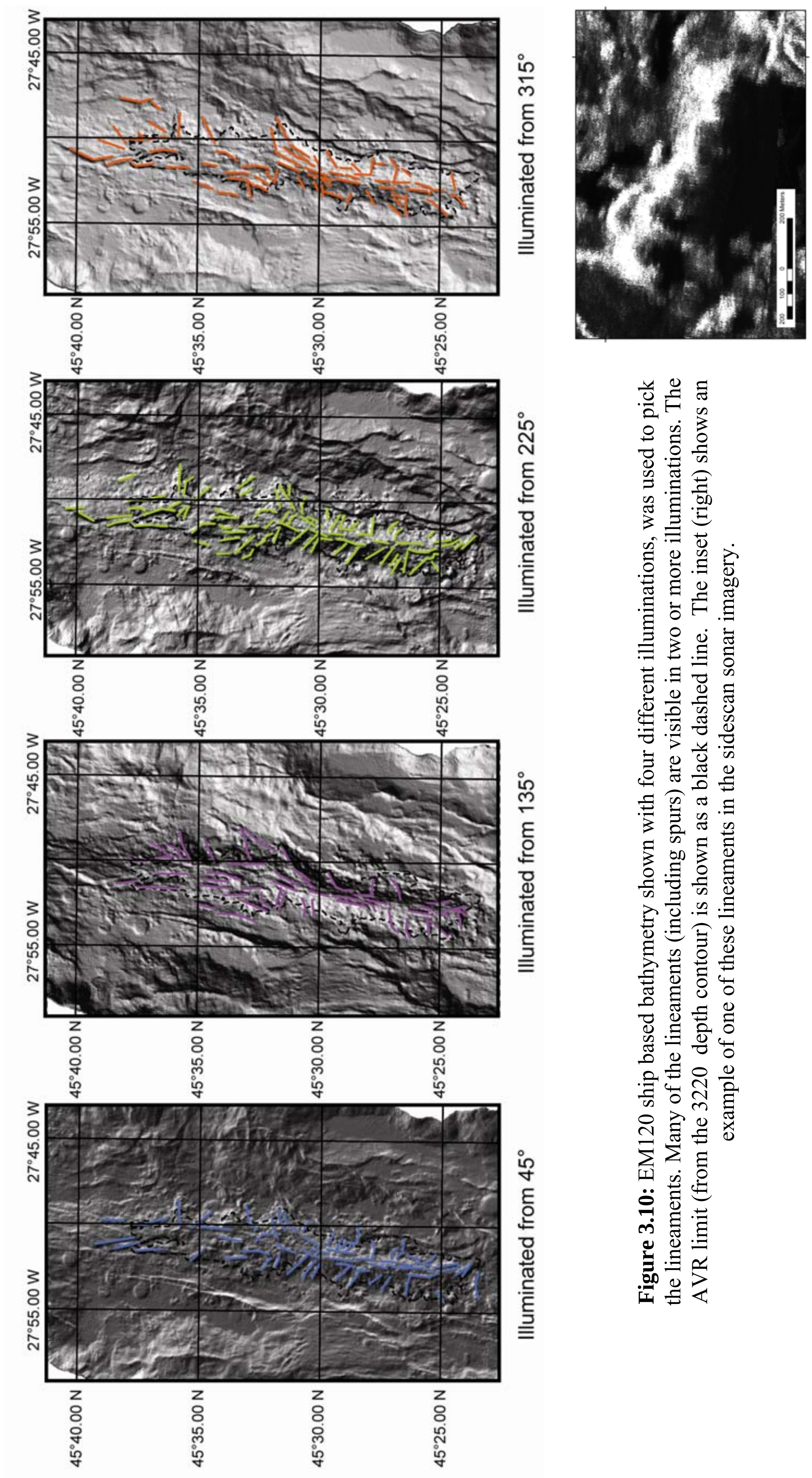

Figure 3.10: EM120 ship based bathymetry shown with four different illuminations, was used to pick the lineaments. Many of the lineaments (including spurs) are visible in two or more illuminations. The AVR limit (from the 3220 depth contour) is shown as a black dashed line. The inset (right) shows an example of one of these lineaments in the sidescan sonar imagery.

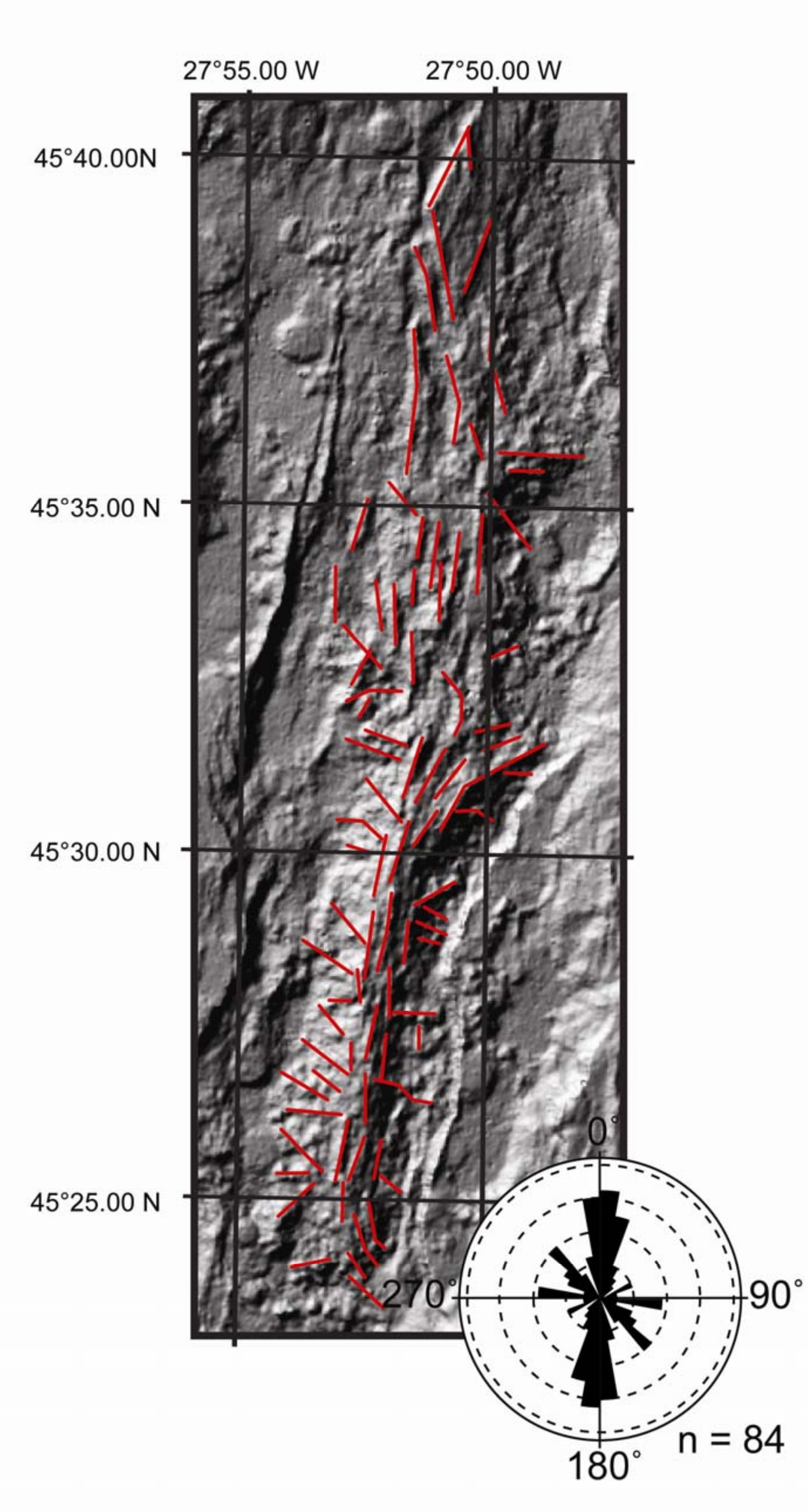

Figure 3.11: Amalgamated map of the 84 lineaments (red) picked from the EM120 bathymetry of the AVR and (inset) rose diagram of lineament azimuths (10˚ bins). Dashed lines represent divisions of 4 n.

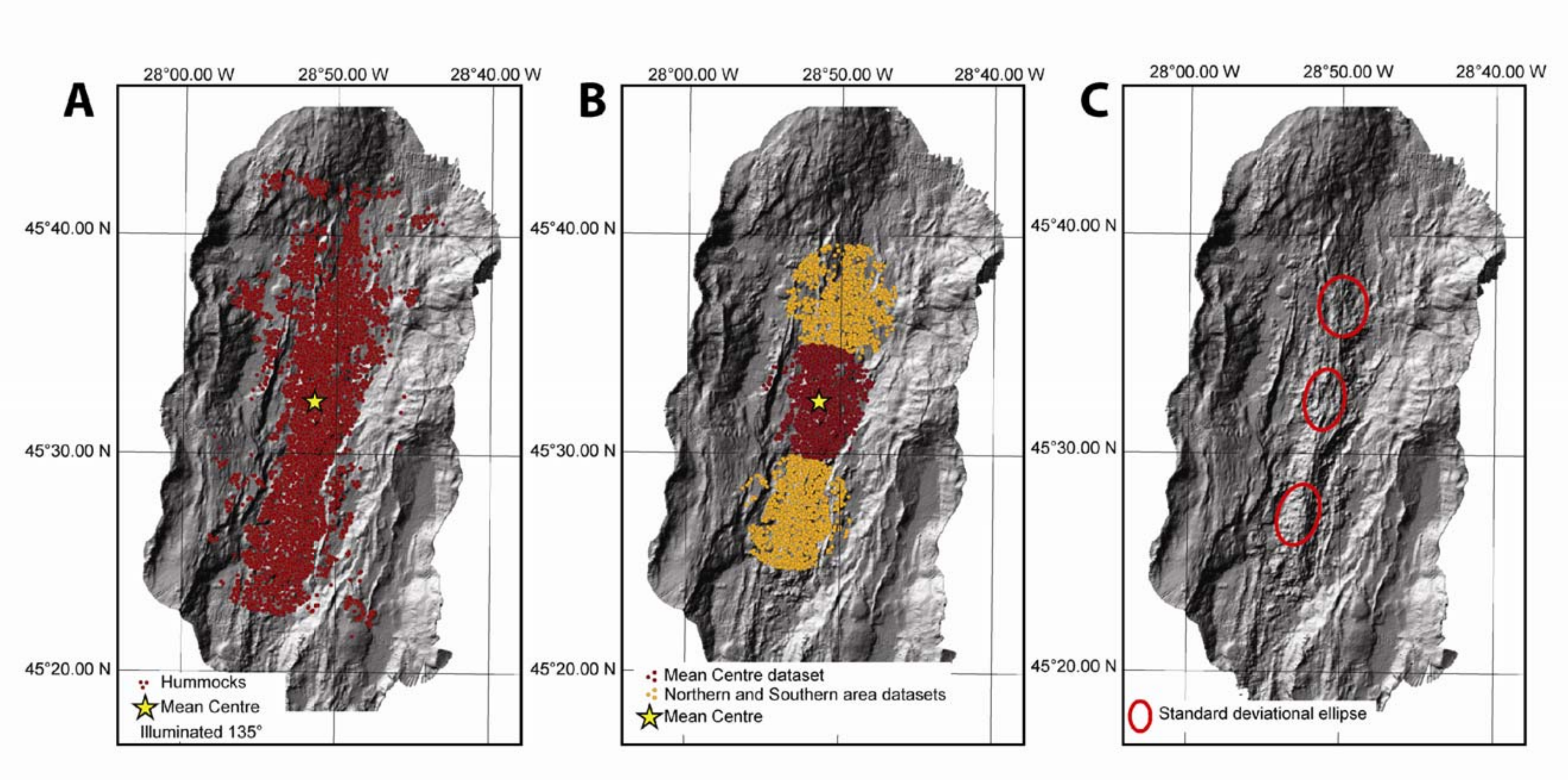

Figure 3.12: Analysis by Standard Deviation Ellipses. A) the entire point file dataset, with a point at every hummock. The mean centre of the dataset is shown by the star. B) The three 10 km diameter circular datasets used to look at strength and orientation of alignment at either end for the whole AVR. C) The standard deviational ellipses produced for each dataset shown in B. The orientation of the ellipse reflects the orientation of alignment, while the larger the length to width ratio, the stronger this alignment is. The AVR is aligned at approximately 013˚, the southern area has a stronger alignment, closer to that of the ridge, than the northern area which is less strongly aligned.

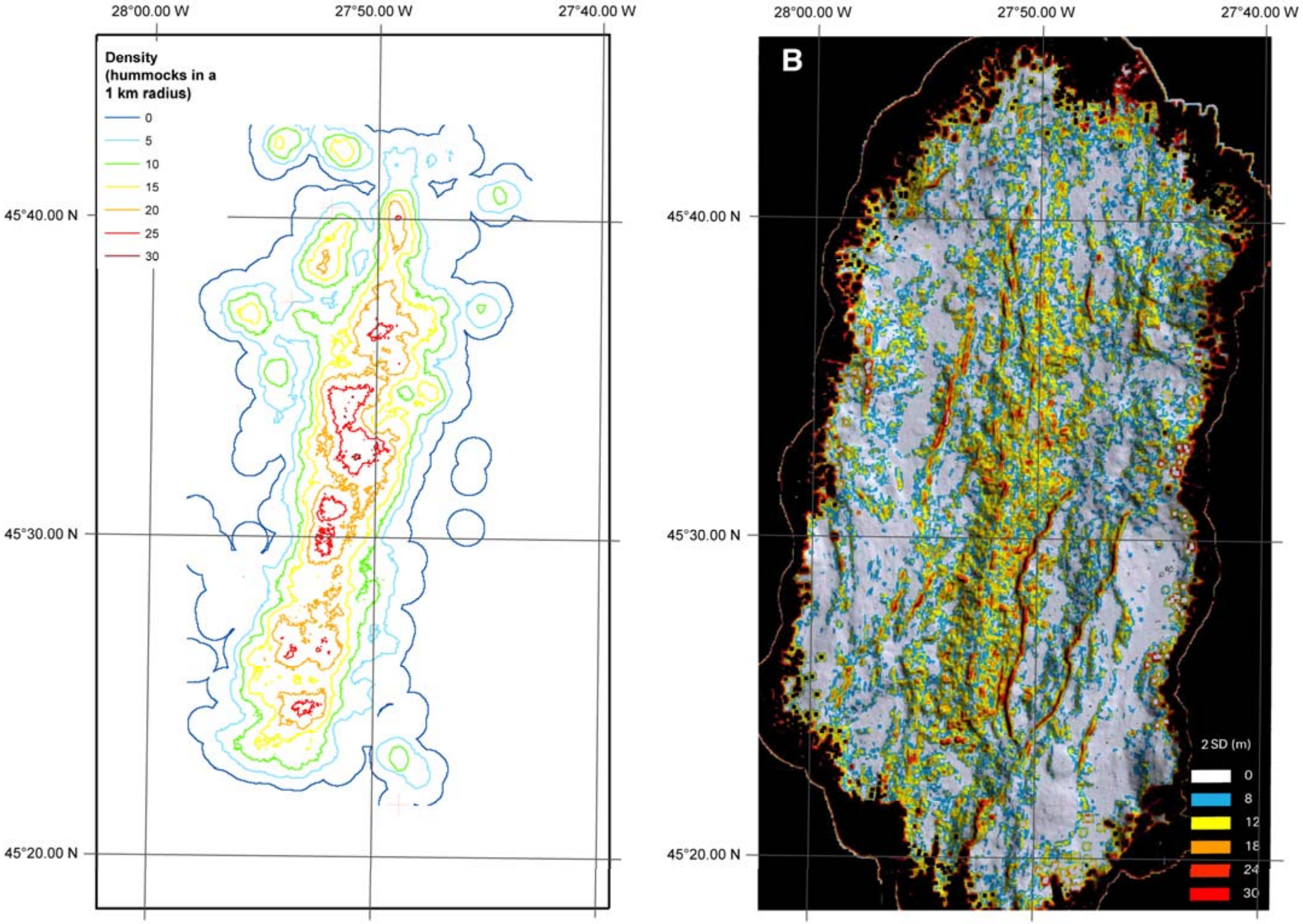

Figure 3.13: Left hand panel shows contours of hummock densities as a number of hummocks in a 1 km radius. The right hand panel shows the seafloor roughness map of the same area from Murton et al. (2012, in press). The roughness map is produced by comparing a 3x 3 standard deviation filter with a 5 x 5 pass filter. Colours represent the roughness, with red representing the highest difference between the two filters and white representing the lowest roughness, where there is no difference between the two grids.

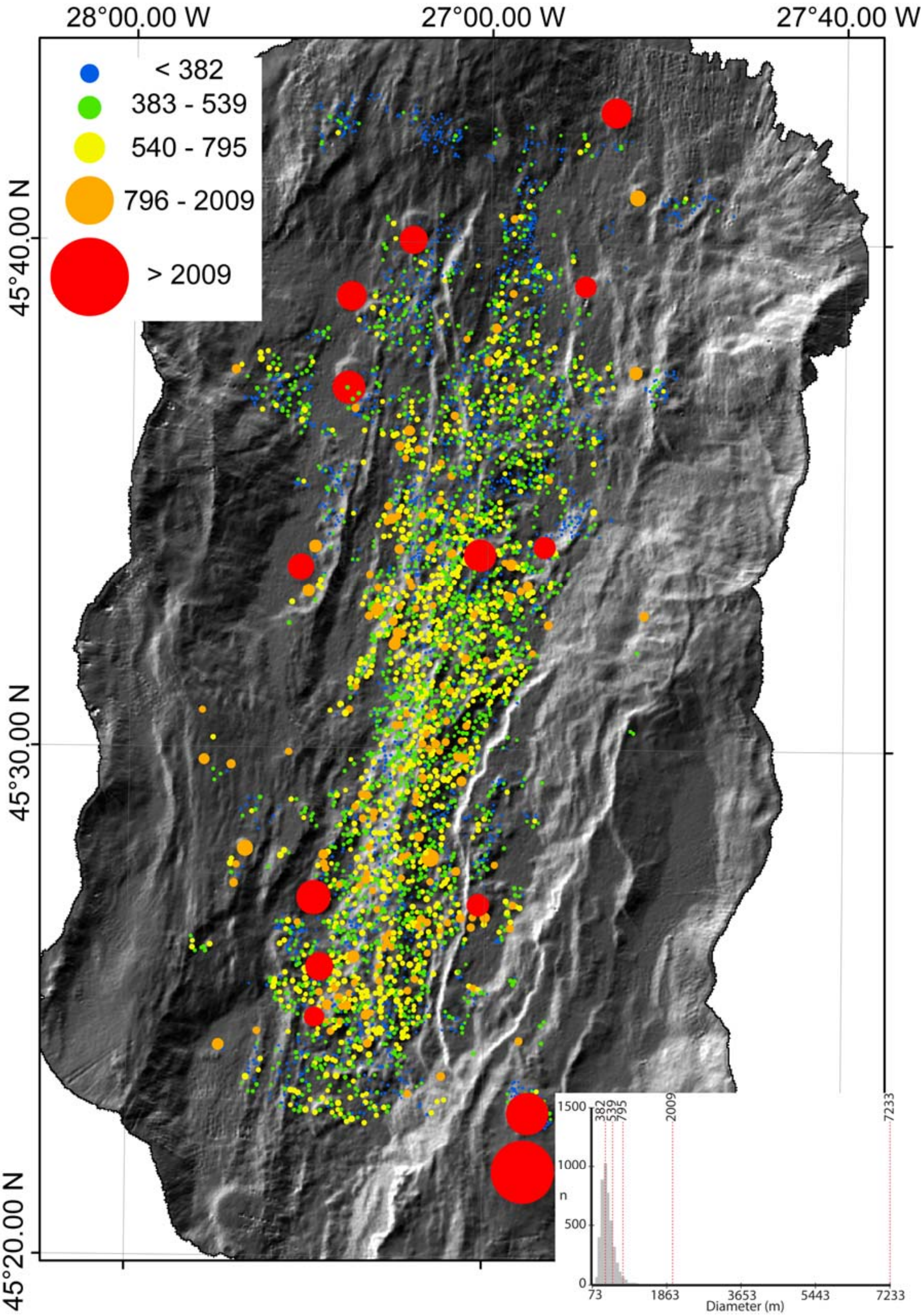

Figure 3.14: All AVR hummocks coloured according to diameter. Categories are 'natural breaks' (as calculated in ArcGIS 9.1). The inset graph shows the distribution of 'natural breaks'.

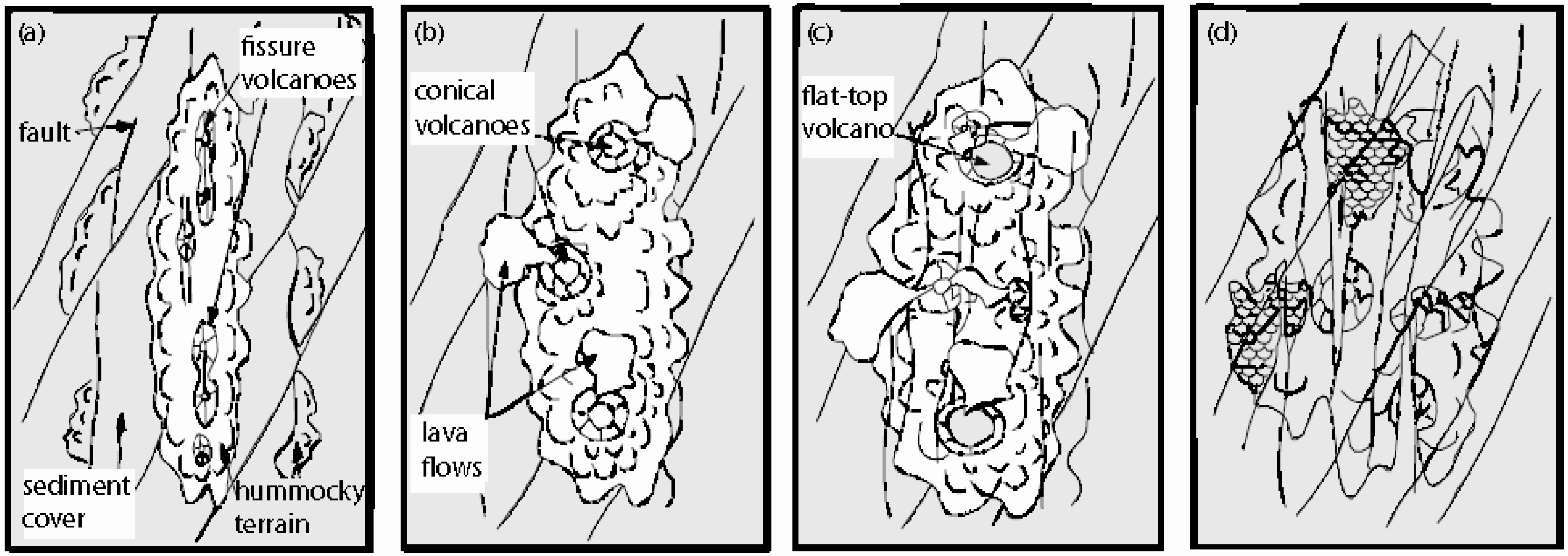

Figure 3.15: The AVR life cycle model from Parson et al. (1993). The first stage (a) is the young stage and shows the overprinting of a previously tectonised terrain by new volcanics erupted from fissures, this magmatic outpouring becomes more focussed as the eruption continues producing the seamounts appearing in the adolescent stage (b). As the high magmatic flux wanes the AVR is cut by faults and broken up as shown in the mature stage (c) and old stage (d).

Table 3.1

	Orientation (°)	Length Major Axis (m)	Length Minor Axis (m)	Ratio (minor: major)
Mean Centre	9	2590	1678	1:1.54
North AVR	1	2521	2053	1:1.23
South AVR	19	2638	1730	1:1.52

Table 3.1: Orientations (clockwise from North) and length of minor and major axes of standard deviational ellipses produced using circular point data sets at the mean centre of the data and datasets in the North and South of the AVR. Ratios are of minor:major axis, the larger the ratio the more elongated the ellipse and the stronger the degree of alignment.

Chapter 4: Collapse Structures

4.1 Rationale

In section 2.3.5.4 I noted that a number of scarps could be recognised from the video dive data and the high resolution bathymetric data. Many of these scarps appeared to be associated with regional faulting trends, but just as many did not line up with regional faulting or display any disturbance of the seafloor away from the hummock, as one would expect if they were fault scarps. These scarps are very common and are thus clearly an important feature on AVRs. As hummocks are the fundamental building blocks of AVRs, and therefore probably the upper oceanic crust, any process which degrades a large number of them is important for crustal structure. Additionally, these collapse features produce large talus deposits, which have distinctly different geophysical properties to lava flows and therefore it is important we recognise their contribution to the upper oceanic crustal layer and the effect this may have on measurements of this layer.

In this chapter I concentrate on these hummocky collapses. These were partially described in the attached paper (appendices 9.1) Yeo et al. (2012) and other features of the hummocks are covered in chapters 2 and 3.

4.2 Introduction

Landslide structures have been well documented on many large submarine basaltic edifices (Holcomb and Searle, 1991; Masson, 1996; Mitchell, 2003) and include landslides – fast moving granular rock flows, and slumps – slow moving, relatively intact, bodies of material (Moore et al., 1989; Varnes, 1978). They can be a major destructive process of ocean volcanoes (Hampton et al., 1996). They have never before been recognised on small (< 50 m high) edifices, probably because until now we have not had high enough resolution bathymetric data to detect them. Additionally, the scarps they produce are indistinguishable from fault scarps in video or photographic data meaning that camera tows and submersible studies would be unable to identify them.

Landslides on larger volcanic edifices are characterised by steep scarps and are associated with large slide deposits of broken, redeposited volcanic material, which may account for 10 – 20% of the total edifice volume (Holcomb and Searle, 1991). Landslides on Hawaiian volcanoes have been observed at many different stages throughout eruptive and dormancy cycles, suggesting that landsliding is a very common process and occurs throughout most of a volcano's life (Hampton et al., 1996). Mechanisms proposed for larger scale collapses include over-steepening of the flanks (Hampton et al., 1996), building on unstable material, physical cracking by dyking (Elsworth and Voight, 1996; Mitchell, 2003), building on old landslide deposits (Holcomb and Searle, 1991; Keeper, 1984) and triggering by earthquakes (Hampton et al., 1996; Keeper, 1984).

Over-steepening of flanks has been suggested as a cause for landsliding of carbonate and siliclastic sediments on slopes > 600 m high (Schlager and Camber, 1986). In these cases growth of reef communities steepened the slopes until they became gravitationally unstable. Presumably the same processes can operate on volcanic edifices if the edifice is oversteepened by continuing eruption (Hampton et al., 1996). Similarly for sub aerial landslides there is a relationship between flank slope and edifice height, which separates stable from unstable edifices (Schmidt and Montgomery, 1995).

Dyke-intrusion triggered landslides are predicted to occur as a result of increased fluid pore pressures associated with dyke intrusion (Elsworth and Voight, 1996). In a potential fracture plane, the addition of these increased pore pressures can dramatically reduce cohesion and frictional resistance to sliding. This may result in shallow or deep seated failures, which differ only in the dip of the failure surface. This process is possibly observed where landsliding is associated with the onset of volcanic rifting, (Mitchell, 2003), although not all volcanic landslides are found at rift zones.

Earthquakes are also major causes of subaerial and submarine landslides (Hampton et al., 1996; Keeper, 1984). In a study of 40 earthquakes Keeper et al. (1984) found that steep slopes, overhangs, slopes underlain by unconsolidated material and weakly cemented material are all particularly susceptible to landsliding caused by earthquake shaking, and the greater the magnitude of the earthquake the larger the landslides that are typically triggered. Earthquakes below magnitude 4 were not found to cause land sliding, however earthquakes with magnitudes greater than magnitude 4 have been recorded on the Mid-Atlantic Ridge (Francis, 1968). In all cases, volcanoes which are unbuttressed by other edifices are probably the most susceptible to flank failure (Holcomb and Searle, 1991)

A survey of small Mid-Atlantic ridge seamounts (Mitchell, 2003) found only 2 of 44 seamounts to show evidence of large scale collapse (although a number display evidence of smaller scale gullying and small scale failures). However, like all of these studies, Mitchel1 (2003) deal with larger edifices than the volcanic hummocks identified in this study. As a result both this, and the studies described above, is not directly comparable with this study; however, they may provide insights into collapse processes.

4.3 Work Division

This chapter forms part of the paper in appendix 9.1 (other sections are found in chapters 2 and 3). All mapping, calculations and writing were done by I. Yeo while discussion and support were provided by the co-authors. The high-resolution Isis bathymetry maps used here were processed, renavigated and plotted by K L Achenbach. EM120 bathymetry and TOBI Sidescan Sonar was processed by T P LeBas. Further development of the importance of talus in seismic layer 2A was encouraged by the editor and reviewers, who are acknowledged in the paper.

4.4 Study (modified from paper: Eruptive hummocks: building blocks of the upper oceanic crust (Appendix 9.1)

I. A. Yeo[1], R. C. Searle[1], K. L. Achenbach[1], T. P. LeBas[2] and B. J. Murton[2]

[1] *Department of Earth Sciences, Durham University, South Road, Durham, DH1 3LE*

[2] *National Oceanography Centre, Southampton, European Way, Southampton, SO14 3ZH*

4.4.1 Methodology

Microbathymetry and seafloor video were acquired using the ROV Isis (German et al., 2003), operated by the National Oceanography Centre, Southampton, UK. Processing and renavigation of the bathymetry was done by K. L. Achenbach in Matlab. Analysis and mapping were carried out by I Yeo using ArcGIS 9.1, Arc Scene 9.1 and Adobe Illustrator.

The two microbathymetry sites were chosen to cover hummocky terrain on the AVR in the magmatically robust appearing south and more tectonically degraded north, as described in section 3.5.4 and 1.3.1.3 (figure 1.25) and Searle et al. (2010). The southern high-resolution study area (Area 1, figure 4.1) lies on the eastern flank of the magmatically robust southern part of the AVR (Searle et al., 2010). It covers ~5 km^2 from the AVR crest to its base at the eastern axial valley wall. The northern high-resolution study area (Area 2, figure 4.1) provides an almost complete (~5.7 km) oblique transect across the lower-lying, probably older AVR, north of 45°32N. This bathymetry was acquired using the ROV Isis operating a Simrad SM2000 bathymetry system flying 100 m above the seafloor, yielding bathymetry with a horizontal and vertical resolution of ~1 – 2 m. Area 1 also had > 17 km of continuous near-bottom visual observations from three dives carried out with Isis while carrying video and high-resolution still cameras.

The collapses were identified from these high-resolution microbathymetry areas. Hummocks were classified as ‘collapsed’ if they were cut by a visible vertical or near vertical scarp, and as ‘unconnected with regional faulting’ if the scarp did not extend beyond the basal contour and did not disturb the surrounding seafloor. Collapse strikes were measured using the Easy Calculate toolbox (written by Ianko Tchoukanski at ESRI) operating on an Arc 9.1 platform. Collapse normals were measured at 90° to collapse scarp strike in the down slope direction in which the collapse occurred.

Volumes of collapses were calculated as section of the volume of the entire cone for sector collapses (collapses that occur as a segment of the cone from the centre) and by integration for segment collapses (collapses that occur along a cord of the basal circle) (figure 4.2).

4.4.2 Observations

Both the high-resolution areas display typical hummocky terrain. However, the southern area is cut by only two clear faults, whilst the northern is cut by at least 8 (figure 4.1). Both areas may contain further faulting, possibly buried by constructional lava flows, but faults are only picked where the scarp could be seen clearly in the high-resolution bathymetry and sidescan sonar data, and where the trace could be accurately picked from these datasets.

More than a third (29) of the hummocks in the southern high-resolution area and more than a quarter (24) of those in the northern high-resolution bathymetry area have suffered collapse (figure 4.1ii). Two types of collapse were observed (figure 4.2), those that occur as a segment of the cone from the centre, from here on called segment collapses, and those which collapse along a chord of the base, from here on called sector collapses (figure 4.2). There was no geographical separation of these two types, no difference in the heights/volumes of hummocks which had undergone each type, nor did they appear to be constructed differently.

No clear relationship exists between height or diameter of an edifice and its likelihood of collapsing (figure 4.3), although all edifices taller than 80 m have collapsed. Two prominent alignments in the strikes of collapse normals can be observed at ~095° and 275° (figure 4.3), approximately normal to the strike of the ridge axis.

4.4.3 Discussion

4.4.3.1 Causes of collapse

There is no evidence in our data that steeper flanks increase the likelihood of collapse as collapses occur at all slope gradients (Figure 4.3 A). I also discount the idea that cones collapse as a result of building on unstable material, since this would lead to the total collapse of some edifices, not purely flank collapse as we observe. I therefore address other potential collapse mechanisms.

The first consideration is whether many of these edifices are unstable and naturally prone to collapse. For subaerial landslides, the relationship between flank slope and edifice height clearly separates stable from unstable edifices (figure 4.4), with edifices over a certain threshold (dependant on material and cohesion) far more likely to collapse than those below it (Schmidt and Montgomery, 1995). Figure 4.5 shows a plot of the same parameters for the hummocks in our high-resolution study areas. The graph shows that above heights of ~ 80 m and gradients of ~ 50° most of the edifices collapse, and this boundary is represented quite well by the superimposed curves A and B taken from sub-aerial stability thresholds (Schmidt and Montgomery, 1995). However below this threshold we also see a large number of collapses (60% lie below the lowest curve) which have dimensions indistinguishable from uncollapsed hummocks. As the Schmidt and Montgomery (1995) curves were plotted for sedimentary units and as hummocks are built of interconnected pillow lavas, the curves are unlikely to be the same; however no curve could be plotted which would separate these smaller collapsed edifices from their uncollapsed counterparts. Therefore, while it appears that there may be a threshold value above which all hummocks are prone to collapse, this is not the control on collapse initiation as collapses are occurring on edifices below this threshold.

The second possibility is that collapses are structurally controlled. Figure 4.3 B and C show two prominent alignments in the strikes of collapse scars (i.e. at 90° to the plotted normals), at about 005° and 040°. The first is close to the regional strike of the ridge axis (013°), while the second is the trend of several oblique spurs running off the AVR, which we attribute to rotation of stresses associated with dextral non-transform offsets affecting the segment (Searle et al., 2010). This similarity in orientation suggests that the underlying tectonic stresses play a part in causing flank collapse. However there are collapses that do not occur parallel to the ridge strike or the oblique spurs. Therefore these collapses are unlikely to have been caused by tectonic stress.

This also applies for cracking due to dyke intrusion as dykes are intruded predominantly parallel to the normal faulting regime (i.e. perpendicular to σ_3) and therefore cannot be responsible for all the collapse directions observed. Additionally, the dykes intruding the area are probably much longer than the length of a single hummock, and therefore we would expect to see multiple hummocks with aligned collapses, which is not observed.

In fact it seems that most of the hummocks are simply collapsing normal to the local steepest seafloor gradient, which is typically (but not always) ridge parallel. This relationship suggests that the hummocks are weak structures and collapses are simply gravity driven. It is not possible to measure the underlying slope as it has been buried by talus deposits, however there may be a maximum seafloor gradient, above which any edifice built on it will collapse. Collapsing hummocks within volcanic alignments may also be buttressed by flanking edifices, allowing them to collapse only on their free edges (Hammond, 1997; Holcomb and Searle, 1991), which are, for the most part, parallel to the AVR axis.

4.4.3.2 Timing of collapses

The smallest numbers of collapse scarps were observed in the areas with the youngest volcanism (see section 2.3.4.), suggesting that collapses are not occurring as the edifices are being built. However, as this area is slightly south of the AVR it is possible that the seafloor gradients here are not as great as those observed on the AVR and therefore it could simply be a case of fewer edifices lying on slopes steeper than the ‘collapse gradient’.

None of the talus deposits imaged showed particularly heavy sedimentation; however sediment collecting on a talus slope would be very easily disturbed by slips or ground tremors, and have very different surface characteristics to that settling on in-situ lavas. Therefore it is only possible to use sediment cover to estimate the relative ages of talus in the same deposit and not to estimate when the deposits were produced relative to the in-situ lava, or talus forming other deposits.

The talus deposits associated with the hummock collapses also differ from those observed next to the axial valley walls as an entire collapse talus deposit is typically characterised by similar degrees of sediment cover (e.g. figure 4.6 B). The fault scarps appear to have produced a number of different talus deposits that lie on top of each other and may be related to different tectonic events or to mass wasting of an overstep slope through time (figure 4.6 A). These different deposits can be distinguished by different amounts of sediment cover as shown in figure 4.6 A, which appears to show talus with at least three distinct amounts of sediment cover, relating to at least three different deposits.

4.4.3.3 Seismic Layer 2A

Flank collapse is clearly very common and a fundamental process in the development of the hummocky terrain that eventually forms the upper oceanic crust. In this study area around a third of hummocks have collapsed, with each collapsed hummock losing ~40% of its volume. Thus ~12% of all lavas erupted as hummocks (essentially 12% of the AVR) end up as talus. The porosity of pillow lava systems is 0.3%–11.3% (Goldberg et al., 2008; Johnson and Christensen, 1997) with a mean of 3.4% (Johnson and Christensen, 1997) for intact basalts and ~20% for fractured basalts (Goldberg et al., 2008). Talus deposits have much greater porosities, perhaps upwards of 40% (Freeze and Cherry, 1979). Thus a young buried talus flow could significantly increase the effective porosity in the crust. The addition of 12% of such material could increase the average upper crustal porosity by 3.4% – 4.8% compared to unfractured pillowed crust and by 2.4% compared to fractured pillowed crust. Wilkens et al. (1991) show that an increase in porosity by ~3% can reduce seismic velocity by >0.5 km/s, so this could make a substantial contribution to velocity reduction in upper oceanic crust.

Goldberg and Sun (1997) note that drill logs from slow-spread crust show higher porosity than those from intermediate-spread crust, yet layer 2A velocities at most spreading rates lie between 2 and 5 km/s (Barclay and Wilcock, 2004; Grevemeyer et al., 1998; Hussenoeder et al., 2002a; Hussenoeder et al., 2002b; Jacobs et al., 2007) and show no consistent pattern of lower values (associated with higher porosities) at slow-spreading ridges. However, fast-spreading ridges have more drained sheet flows and lava tubes, both of which are major contributors to porosity. Therefore the fact that porosities are not noticeably lower in slow-spreading crust does not necessarily mean that talus is not incorporated, and in fact the large talus component being added to the crust may be the dominant mechanism for lowering the effective porosity of the upper oceanic-crust at slow spreading ridges.

4.4.4 Conclusions

Up to a third of AVR hummocks, the main building blocks of AVRs, have collapsed. The hummocks typically lose 40% of their material, meaning that if this effect is ubiquitous across the AVR, then 12% of all hummock forming erupted material is being converted to talus. Two types of collapses are observed, those occurring from the centre of the hummock and those which collapse along a chord of the base. There is no obvious spatial or dimensional control on which type occurs. Some collapses are related to regional faulting and are clearly caused by faults, but the majority are not connected to any obvious fault scarp.

Collapse appears to be gravity controlled and occurs predominantly down the gradient of local seafloor, which is predominantly ridge parallel, or oblique on the spurs. It is possible there is a maximum underlying seafloor gradient above which edifices become unstable, but this cannot be measured here. Few collapses occur with normals parallel to the ridge strike, possibly because edifices are being buttressed by other hummocks in this orientation. Collapse deposits appear to be formed by a single flank failure event and probably occur after the eruption has ended. In contrast, talus deposits from major fault scarps appear to form in several stages. This is not very surprising as mid-ocean ridge earthquakes are very small, typically less than magnitude 4. Such small earthquakes are usually only associated with ~ 1 m of slip or less, so a single fault may slip hundreds of times.

The talus deposits produced by edifice collapse may be a significant cause of reduced upper-oceanic-crust seismic velocity at slow-spreading ridges, where lower average eruption rates inhibit the formation of macroscopic pore spaces characteristic of faster spreading ridges.

4.5 References

Barclay, A.H., and Wilcock, W.S.D., 2004, Upper crustal seismic velocity structure and microearthquake depths at the Endeavour Segment, Juan de Fuca Ridge: Geochemistry Geophysics Geosystems, v. 5.

Elsworth, D., and Voight, B., 1996, Evaluation of volcano flank instability triggered by dyke intrusion: Geological Society, London, Special Publications, v. 110, p. 45-53.

Francis, T.J.G., 1968, The detailed seismicity of Mid-Oceanic ridges: Earth and Planetary Science Letters, v. 4, p. 39-46.

Freeze, R.A., and Cherry, J.A., 1979, Groundwater, Prentice Hall, Inc.

German, C., Tyler, P., and Griffiths, G., 2003, The maiden voyage of UK ROV "Isis": Ocean Challenge, v. 12, p. 16-18.

Goldberg, D., and Sun, Y.F., 1997, Attenuation differences in layer 2A in intermediate- and slow-spreading oceanic crust: Earth and Planetary Science Letters, v. 150, p. 221-231.

Goldberg, D.S., Takahashi, T., and Slagle, A.L., 2008, Carbon dioxide sequestration in deep-sea basalt: Proceedings of the National Academy of Sciences of the United States of America, v. 105, p. 9920-9925.

Grevemeyer, I., Weigel, W., and Jennrich, C., 1998, Structure and ageing of oceanic crust at 14 degrees S on the East Pacific Rise: Geophysical Journal International, v. 135, p. 573-584.

Hammond, S.R., 1997, Offset caldera and crater collapse on Juan de Fuca ridge-flank volcanoes Bulletin of Volcanology, v. 58, p. 617-627.

Hampton, M.A., Lee, H.J., and Locat, J., 1996, Submarine landslides: Rev. Geophys., v. 34, p. 33-59.

Holcomb, R.T., and Searle, R.C., 1991, Large Landslides from Oceanic Volcanoes: Marine Geotechnology, v. 10, p. 19-32.

Hussenoeder, S.A., Detrick, R.S., Kent, G.M., Schouten, H., and Harding, A.J., 2002a, Fine-scale seismic structure of young upper crust at 17 degrees 20 ' S on the fast spreading East Pacific Rise: Journal of Geophysical Research-Solid Earth, v. 107.

Hussenoeder, S.A., Kent, G.M., and Detrick, R.S., 2002b, Upper crustal seismic structure of the slow spreading Mid-Atlantic Ridge, 35 degrees N: Constraints on volcanic emplacement processes: Journal of Geophysical Research-Solid Earth, v. 107.

Jacobs, A.M., Harding, A.J., and Kent, G.M., 2007, Axial crustal structure of the Lau back-arc basin from velocity modeling of multichannel seismic data: Earth and Planetary Science Letters, v. 259, p. 239-255.

Johnson, J.E., and Christensen, N.I., 1997, Seismic Properties of layer 2 basalts: Geophysical Journal International, v. 128, p. 285-300.

Keeper, D.K., 1984, Landslides caused by earthquakes: Geological Society of America Bulletin, v. 95, p. 406-421.

Masson, D.G., 1996, Catastrophic collapse of the volcanic island of Hierro 15 ka ago and the history of landslides in the Canary Islands: Geology, v. 24, p. 231-234.

Mitchell, N.C., 2003, Susceptibility of mid-ocean ridge volcanic islands and seamounts to large-scale landsliding: Journal of Geophysical Research-Solid Earth, v. 108, p. 34.

Moore, J.G., Clague, D.A., Holcomb, R.T., Lipman, P.W., Normark, W.R., and Torresan, M.E., 1989, Prodigious Submarine Landslides on the Hawaiian Ridge: J. Geophys. Res., v. 94, p. 17465-17484.

Schlager, W., and Camber, O., 1986, Submarine slope angles, drowning unconformities, and self-erosion of limestone escarpments: Geology, v. 14, p. 762-765.

Schmidt, K.M., and Montgomery, D.R., 1995, Limits to Relief: Science, v. 270, p. 617-620.

Searle, R.C., Murton, B.J., Achenbach, K., LeBas, T., Tivey, M., Yeo, I., Cormier, M.H., Carlut, J., Ferreira, P., Mallows, C., Morris, K., Schroth, N., van Calsteren, P., and Waters, C., 2010, Structure and development of an axial volcanic ridge: Mid-Atlantic Ridge, 45°N: Earth and Planetary Science Letters, v. 299, p. 228-241.

Varnes, D.J., 1978, Slope movement types and processes: Landslides : Analysis and Control, p. 11-33.

Wilkens, R.H., Fryer, G.J., and Karsten, J., 1991, Evolution of porosity and seismic structure of upper oceanic-crust - importance of aspect ratios Journal of Geophysical Research-Solid Earth, v. 96, p. 17981-17995.

4.6 Figures

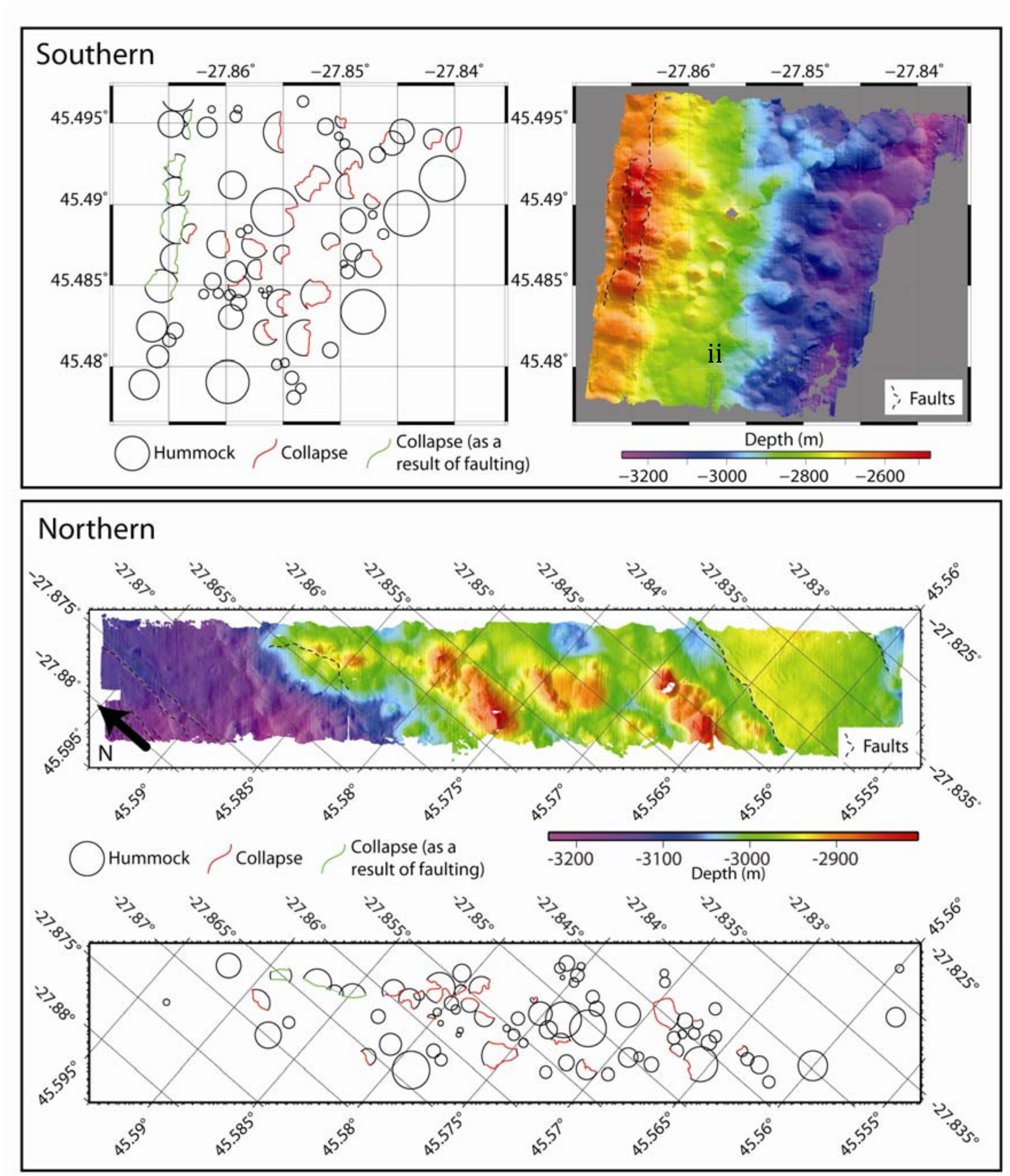

Figure 4.1: Northern (Area 2) and southern (Area 1) high-resolution study areas showing the Isis SM2000 bathymetry and hummock location interpretation. Collapse scarps are shown by a red (unconnected to regional faulting trends) or green (clearly connected to regional faulting trends) line. Collapses were only mapped as related to regional faulting where a scarp could clearly be observed extending away from the collapse on either side, however the ridges in the northern area are probably separated by less clear faulting and therefore more collapses here may be related to regional faulting than are mapped. Faults are shown on the bathymetry by black dashed lines.

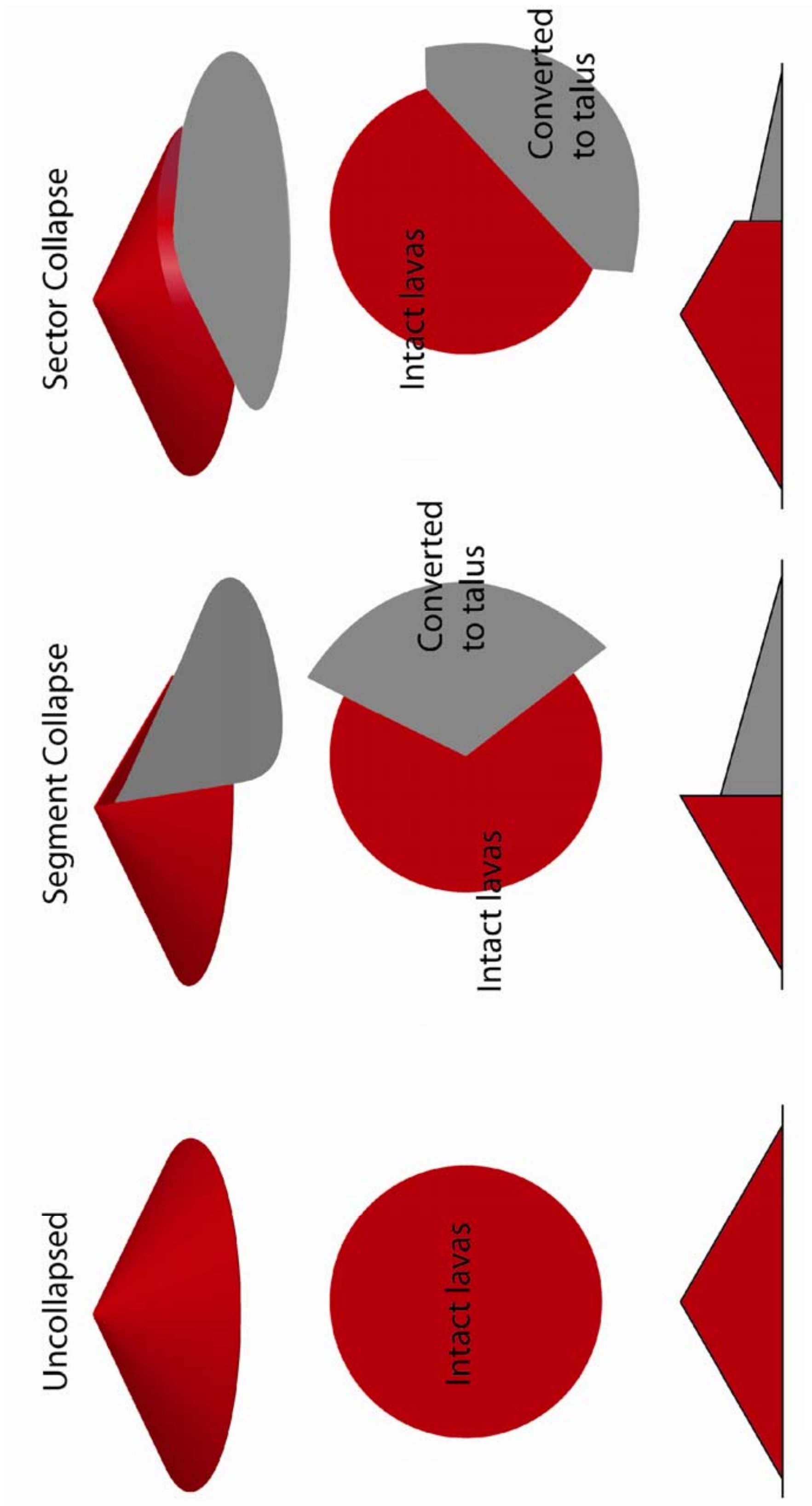

Figure 4.2: Different styles of collapse observed in the high-resolution study areas in 3D, map view and cross section.

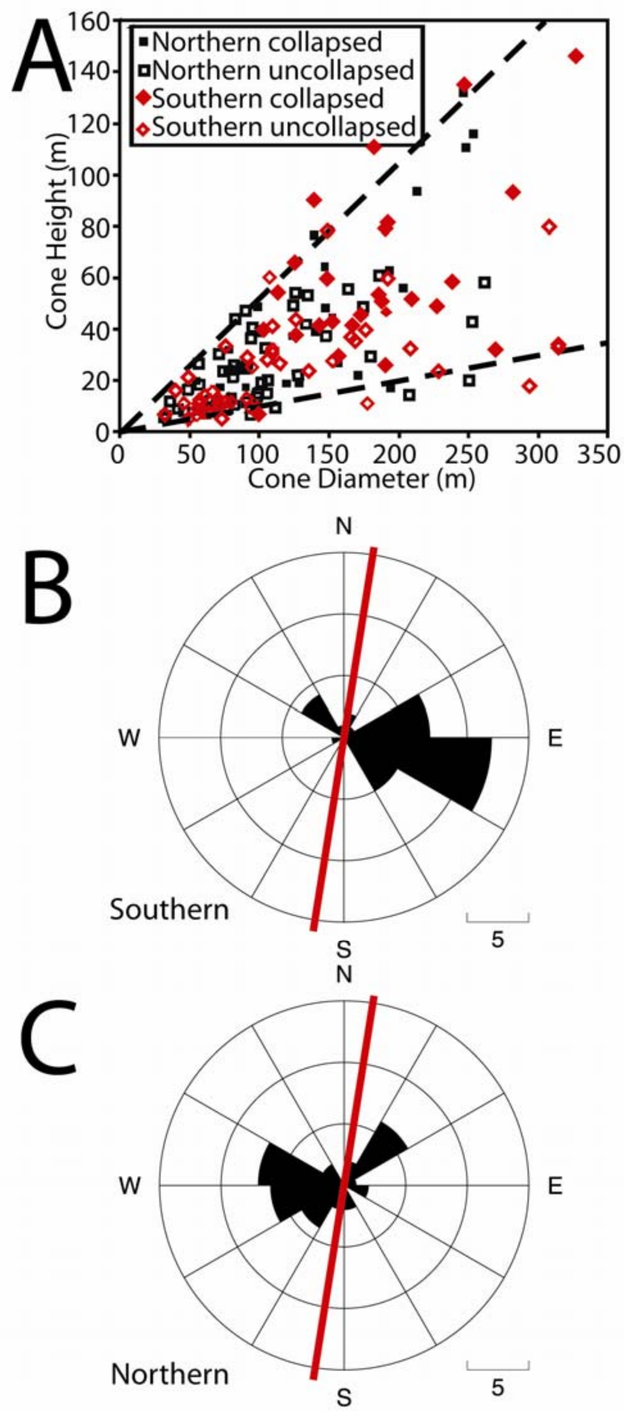

Figure 4.3: Height:diameter for hummocks identified in southern (red diamonds) and northern (black squares) high-resolution bathymetry areas. Collapsed hummocks are shown by filled symbols, uncollapsed hummocks by open symbols. Lower dashed line indicates 1:10 height:diameter ratio of flat-topped seamounts; upper dashed line brackets the data with an upper height:diameter ratio of 1:2. B: Orientations of collapse directions for the 24 collapsed hummocks in the southern area. Collapse direction vectors are normal to the scarp orientation. C: Orientations of collapse directions for the 29 collapsed hummocks in the northern area.

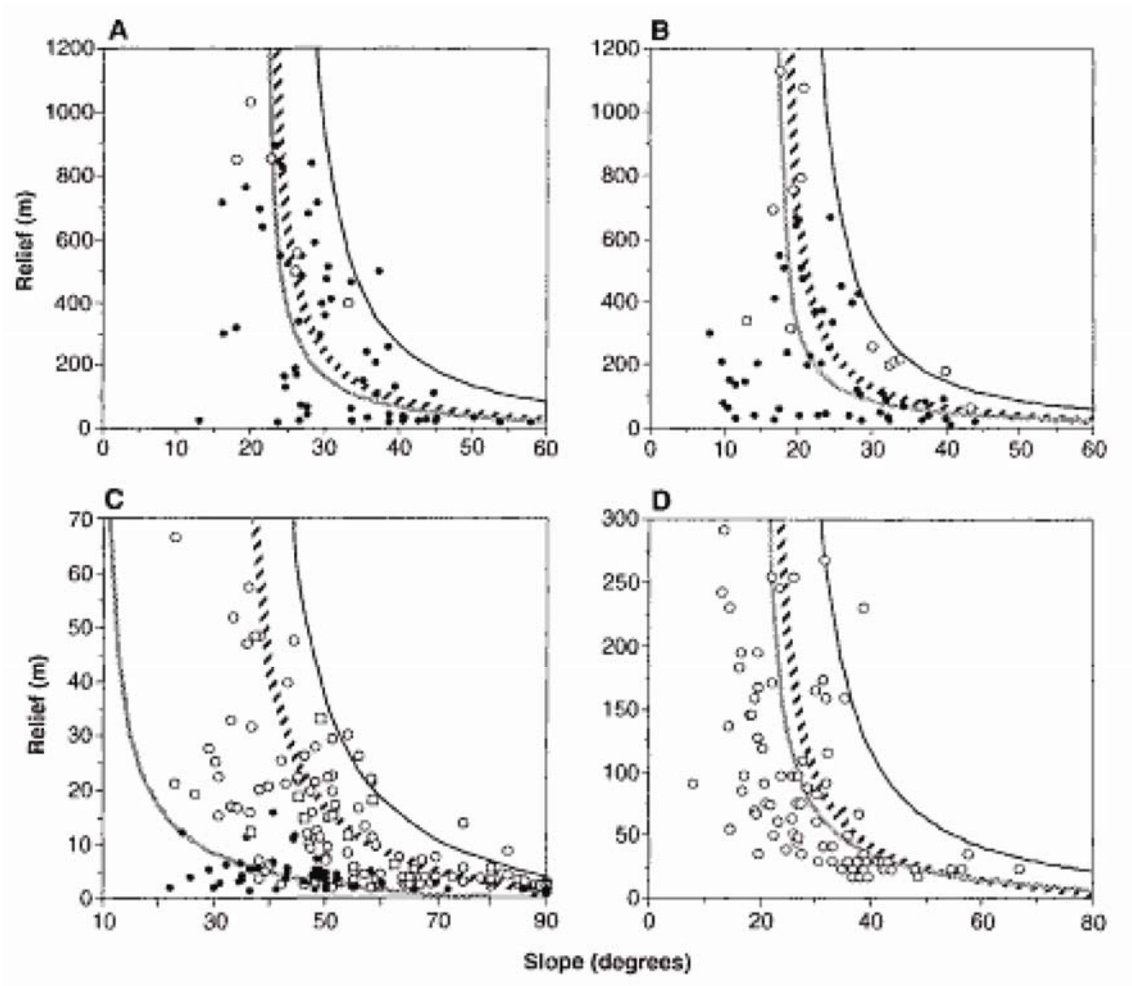

Figure 4.4: Gradient vs. relief for stable hill slopes (solid black circles), for landslide sites (open circles) and for reconstructed landslide site (open squares) for a number of different (all sedimentary) sub aerial locations (A – D) from Schmidt and Montgomery (1995). Unstable edifices (collapsed) are separated from stable ones (uncollapsed) by the black curves which change under different conditions. The solid black curve represents dry conditions, the thick hatched curve represents saturated conditions, and the grey curve represents failure under horizontal seismic accelerations of 0.6g.

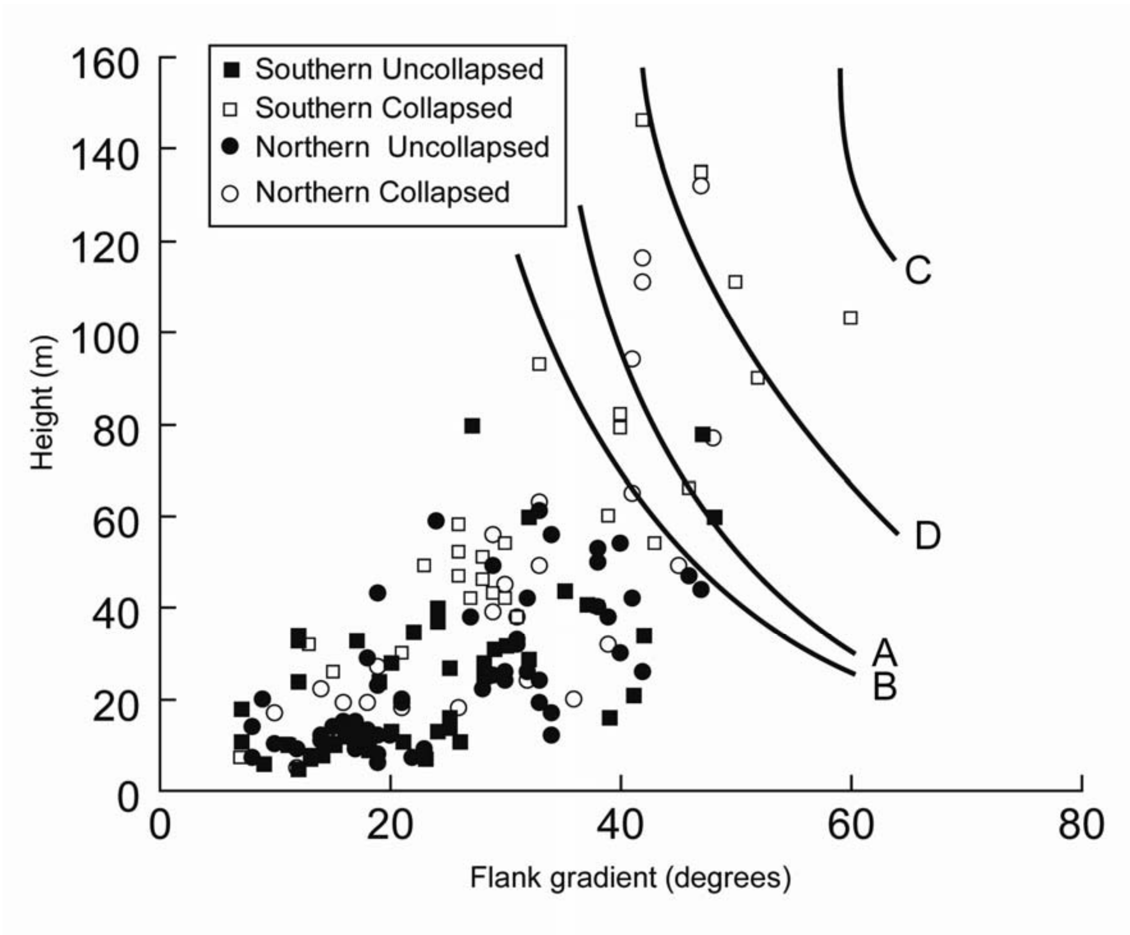

Figure 4.5: Gradient vs. relief for the hummocks in the high-resolution study areas. Collapsed hummocks are shown in empty symbols and uncollapsed edifices are shown by solid symbols. The saturated curves from Schmidt and Montgomery (1995) are superimposed on the data labelled A – D (these were for different locations).

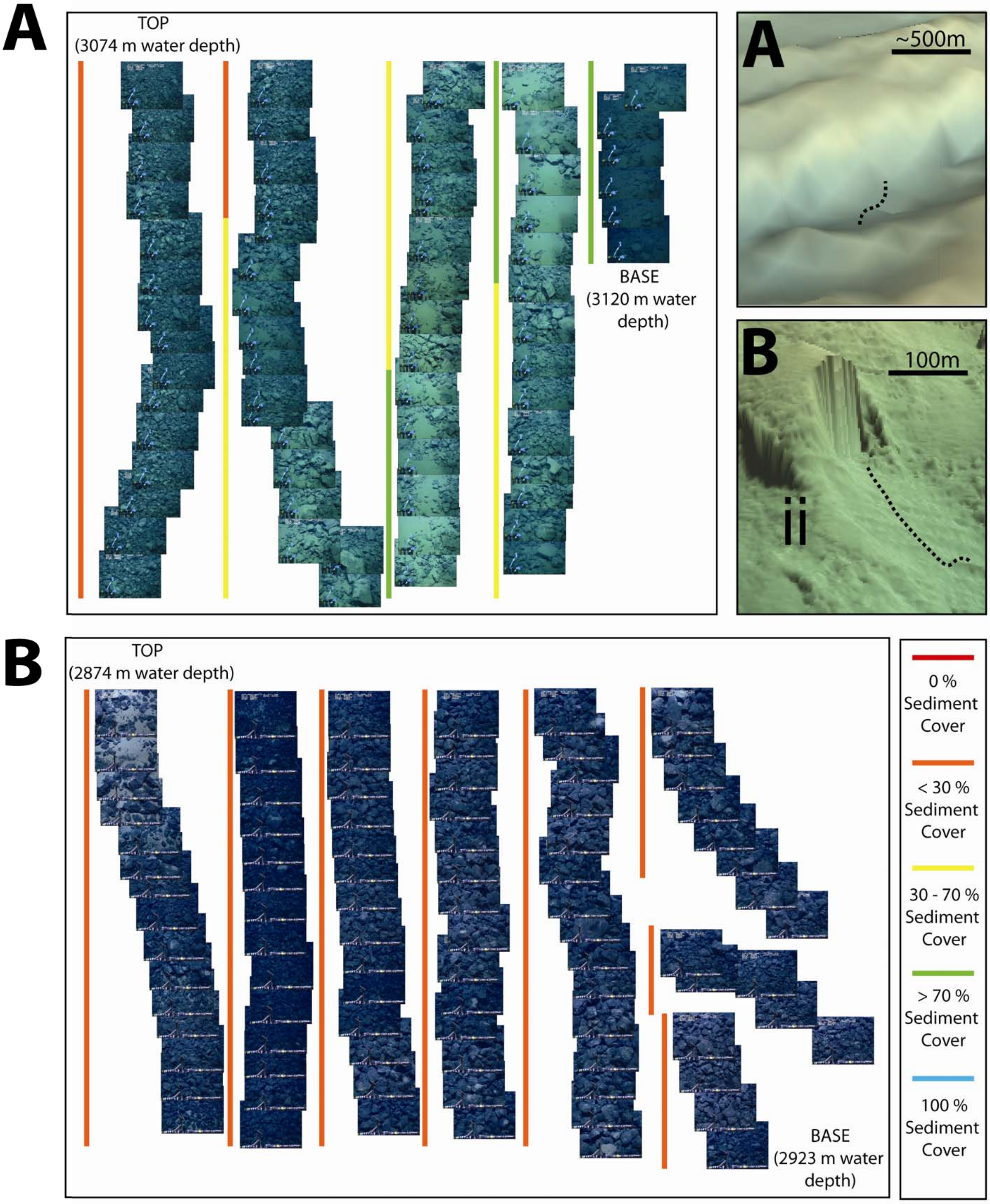

Figure 4.6: Photo logs (matched by eye with no perspective correction) from base to top (captured at approximately 10 second intervals) of talus deposits for (A) the axial valley wall (dive JC24-79) and (B) the talus deposit associated with the collapsed cone (ii) (figure 4.1; figure 3.3). The Isis dive tracks corresponding to the photo logs are shown by dashed lines in the panels on the right hand side. Roman numerals correspond with those in the paper (figure 3.3; appendix 9.1). Sediment cover percentages are estimated and colour coded. No totally unsedimented or 100 % sediment deposit sections were seen in these locations. There appear to be at least three different sediment deposits (shown by different coloured bars) associated with the axial valley wall fault (suggesting multiple different talus producing collapse events), while similar sediment cover on the entire deposit at the collapsed hummock suggests there is only one talus flow or several that occurred very close to each other in time.

5 Volcanism on the intermediate-spreading rate Juan de Fuca and Gorda Ridges

Chapter 5: Volcanism on the intermediate-spreading rate Juan de Fuca and Gorda Ridges

5.1 Rationale

Volcanic eruption at many intermediate-spreading ridges produce edifices termed *pillow mounds*. The term pillow mounds has been used to cover both individual small pillowed volcanoes as well as agglomerations of these edifices to form larger features. Individual pillow mounds appear superficially like volcanic hummocks on the Mid-Atlantic Ridge, while agglomerations of such features look like hummocky seamounts and ridges; this similarity has not yet been examined in any detail. I spent a summer internship at the Monterey Bay Aquarium Research Institute (MBARI) where I was able to work with high-resolution bathymetric AUV datasets. The AUV bathymetry over 3 three intermediate-spreading areas revealed pillow mound volcanoes (figure 5.1) making direct comparison of pillow mounds with hummocks and hummocky seamounts/ridges possible. The fact that all three of these ridge segments have experienced volcanic eruptions in the last 30 years makes it possible to very accurately map the eruption boundaries. This makes estimating their volumes, and the comparison of these volumes with eruption volumes at the MAR possible. Additionally, as two of the eruptions were detected acoustically, eruption rates can be calculated and compared with those estimated at 45˚N. Finally, during the mapping it was noticed that the intermediate-spreading rate eruptions were very spatially discontinuous; this is an interesting observation and may be relevant to eruptions at slow-spreading ridges.

5.2 Work division

Processing of the AUV bathymetry was done by D W Caress and J B Paduan at MBARI. Mapping and first order volume estimates were carried out by I Yeo at MBARI. After additional geochemical analyses and bathymetry became available from a second cruise, secondary flow outlines were produced by I Yeo and D Clague. Second order volume estimates (modelled underlying surface) were carried out by J. F. Martin at MBARI. All dyke discontinuity work and writing was done by I Yeo. The paper which follows was written by I Yeo.

5.3 Paper: New Insights into Diking Processes from High-Resolution Bathymetry of Historic Pillow Ridges on the Juan de Fuca and Gorda Ridges

I. A. Yeo[1], D. A. Clague[2], J. B. Paduan[2], D. W. Caress[2] and J. F. Martin

[1] *Department of Earth Sciences, Durham University, South Road, Durham, DH1 3LE*

[2] *Monterey Bay Aquarium Research Institute, 7700 Sandholdt Road, Moss Landing, CA 95039, USA*

For submission to *Geochemistry, Geophysics, Geosystems*

5.3.1 Introduction

Volcanic eruptions on mid-ocean ridges normally take the form of fissure eruptions (commonly producing a row of volcanic edifices) (Smith and Cann, 1990), which occur where a dyke connects a magma chamber with the seafloor. These eruptions, likened to the fire fountain style eruptions common on Iceland and Hawaii, initially supply lava along their entire length, but later focus down to several and eventually a single point source. This flow focusing is a result of heat exchange between the magma and the walls of the dyke. Cooling of certain sections of the flow within the dyke creates temperature gradients, resulting in variations in the cross sectional resistance to flow (Wylie et al., 1998). The magma within the dyke solidifies at different rates depending on numerous parameters, including the initial geometry of the fissure, mechanical effects, volatile exsolution and heterogeneities in the rock the fissure is propagating through. This solidification creates physical changes in the fissure dimensions that may control the duration of the eruption and the location in which the eruption will be most long lived (Wylie et al., 1998). Sections of the dyke solidifying while other sections remain open creates a flow focusing effect, in which the magma flow is concentrated down to a number of short sections of fissure, which behave like point sources.

Flow focusing is thought to be responsible for hummocky style eruptions along a fissure (Smith and Cann, 1992), suggesting that fissures on the seafloor initially erupt along their entire length and then focus down to a few point sources that build discrete volcanic mounds as an eruption progresses. These mounds are called hummocks at slow-spreading mid-ocean ridges, and *pillow mounds* at intermediate-spreading ridges, and are one of the most common efeatures observed at these spreading rates (Smith and Cann, 1990; Yeo et al., 2012). They are characterised by pillow lava flows, which form one or many cone or dome-shaped mounds, several hundred metres in diameter and tens of metres high. At intermediate-spreading ridges the term ‘pillow mound’ has been used to describe both single pillowed mounds as well as several pillow mounds which have coalesced together to form one larger edifice. In this study we will distinguish between small hummock-like pillow mounds and these groups of coalesced mounds by calling the first pillow mounds and the latter composite mounds.

The recent eruptions at North Gorda, CoAxial and North Cleft were first described from early bathymetric and sidescan sonar studies and identified as discontinuous pillow ridges (Chadwick et al., 1998; Embley et al., 1991; Embley et al., 2000; Smith et al., 1994a). Recently developed methods of Autonomous Underwater Vehicle (AUV) high-resolution bathymetry collection (Caress et al., 2008; Clague et al., 2010) make it possible to image them in high-resolution, shedding light on how dykes propagate both laterally and vertically, and potentially allowing their volumes and eruption rates to be more accurately calculated.

The North Gorda segment of the Gorda Ridge and the CoAxial and North Cleft segments, of the Juan de Fuca Ridge, are all intermediate-rate spreading-centres, with total spreading rates of 5.5 cm/yr, 5.5 cm/yr and 6cm/yr respectively (Chadwick et al., 1998; Embley et al., 2000; Embley et al., 1991). All these ridges display morphological characteristics of both slow-spreading and fast-spreading mid-ocean ridges, however the North Gorda ridge in particular bears many similarities to the slow-spreading Mid-Atlantic ridge, and is characterised by a deep, wide axial valley, bounded by large-throw axial valley wall faults. These ridge segments were selected for our high-resolution AUV surveys specifically because each had at least one known historic eruption that was mapped soon after the eruptions (using ship-based bathymetry, camera tows, sidescan sonars, visual observations and sampling using submersibles), as described below. This prior mapping is critical to this study in that it allows us to accurately identify which mounds formed during the historic eruptions and which mounds predate them.

Eruptions occurred in 1996 on the North Gorda Ridge (Chadwick et al., 1998), in 1993 and between 1982 and 1991 on the CoAxial Ridge (Chadwick and Embley, 1994), and in 1986 on the North Cleft Ridge (Embley et al., 1991; Smith et al., 1994b). These eruptions were mapped soon after their emplacement by comparison of pre- and post- eruption Seabeam data sets (Chadwick and Embley, 1994; Chadwick et al., 1998; Embley et al., 1991; Embley et al., 2000) and this initial mapping means the bounds of these lava flows were already fairly well constrained. In addition, two of these eruptions were detected acoustically, giving an indication of eruption duration (Fox and Dziak, 1998). The large amount of information already available for these sites did not include complete high-resolution bathymetry nor bathymetry with resolution adequate to describe these eruptions in enough detail to investigate how they were fed. Our new 1-m resolution data of these flows are utilized to better understand their feeding mechanisms and the lateral and vertical propagation of dykes at mid-ocean ridges.

In this paper we combine high-resolution bathymetric mapping and ROV studies to fully describe the mechanism by which these eruptions are fed, and to attempt to make accurate estimates of their volumes and eruption rates, and compare these findings to the Mid-Atlantic Ridge at 45°N.

5.3.2 Materials and methods

High resolution bathymetry was collected with the MBARI autonomous underwater vehicle (AUV) *D. Allan B* during cruises on the R/V *Zephyr* in 2009. Bathymetric data were collected using a 200 KHz multibeam sonar (Caress et al., 2008) and processed using MB System (Caress and Chayes, 1996) yielding bathymetric maps with ~1 m resolution. The full data processing routine is explained in detail in Clague et al. (2010) and includes a final step of co-locating the high-resolution grids to the best ship-based multibeam data available, giving location accuracy on the order of 20 m.

Video was recorded on high resolution video cameras mounted on the MBARI remotely operated vehicles (ROVs) *Tiburon* (on Panasonic 3- chip pan and tilt colour cameras recording to Digital BetacamTM) and *Doc Ricketts* (using a ROS PT-25 pan and tilt HDTV) operated from the R/V *Western Flyer* on cruises in 2005 and 2009. The video was used to identify lava flow boundaries crossed by the dives, as well as flow superposition.

Lava flow extents were identified using high resolution bathymetry (predominantly from the degree of fissuring), video data and published bulk geochemistry for samples from the area plus additional major element geochemistry analysed at MBARI (Davis and Clague, 1987). Lava flow volumes were calculated using the high resolution datasets for each of the ridge segments (gridded at either 1m or 1.5m) with lava flow shapefiles created in ArcGIS 9.2. First order lava flow volumes were calculated in ArcView 3.2 using two extensions within ArcView to tilt the underlying seafloor (written at MBARI by Gerry Hatcher and described in Clague et al. (2000) and Faichney et al., (2010)) and volumes were calculated by subtracting this surface from the AUV bathymetry. Second order, more accurate volumes were then calculated by interpolating a new base surface using natural neighbour based on depth extracted from the bounding outline of the pillow ridges (see appendix 9.9). Differences that could result from the interpolation process were compared by creating a planar surface using trend interpolation, calculated from the same bounding outline depths.

5.3.3 Observations

All four historic eruptions (North Gorda 1996, CoAxial 1993 and 1982-1991 and North Cleft 1986) were mapped in the new high resolution bathymetry (figure 5.2). All four eruptions took the form of pillow mound eruptions, which commonly coalesced to form composite mounds. Eruptions produced 2 - 17 single or composite mounds. The 1996 North Gorda eruption mounds extend for 2.44 km on a bearing of ~ 015˚, the 1993 CoAxial flow for 2.49 km on a bearing of ~ 020˚, the 1982 – 1991 CoAxial flow for 1.62 km on a bearing of ~ 020˚, and the North Cleft 1986 eruption for 15.5 km on a bearing of ~ 017˚

The composite pillow mounds formed during the 1996 North Gorda and 1986 North Cleft eruptions take the form of a number of discrete mounds, not connected to each other and between which no new lava flows are observed. At CoAxial the flows appear to be more connected, although small gaps between composite mounds are observed in the 1993 flow. Composite mounds at North Gorda and CoAxial show no fissuring between them (figure 5.2 A and B). Fissuring might be expected if the fissure eruption met the seafloor along the entire length of the dyke trace and erupted or if the top of the dyke lay close to the seafloor. Some fissuring is observed between composite mounds at North Cleft (figure 5.2 C), however it is unclear if these fissures are related to the 1986 eruption as they do not line up with the locations of fissures which built the mounds. The spacing and length of composite mounds is random, with gaps ranging from 0.1 – 34 % of the total dyke length (10 – 1319 m).

Eruption volumes calculated using the first order method range from 0.017 km^3 to 0.258 km^3 (Table 5.1). Volume estimates calculated using the interpolated surfaces were all lower than the first order estimates, with the three eruptions and North Gorda and CoAxial between 0.007 and 0.02 km^3, and a North Cleft volume of 0.048 km^3. Very little variation was observed with grids of different size (1.5 m and 1 m) or using the trend surface (all values were within 10 % of each other).

Those eruptions with discrete composite mounds consisted of one or two large elongate composite mounds, composed of a number of pillow mounds, and further smaller composite mounds or individual pillow mounds (table 5.2). Larger mounds are typically located towards one end of the fissure, although this is less obvious at North Gorda. These larger mounds were found to contain between 58 % and 75 % of the total volume of the eruption.

The pillow mounds covered by video dives on both the North Gorda and CoAxial ridge segments were composed almost entirely of pillow lavas and elongate pillow lavas (> 90%). They ranged from 5 – 95 m in height (average 23 m) and from 33 – 420 m in diameter (average 138 m). Dimensions were also slightly different between the three ridges, with average heights of 18 m at North Cleft, 27 m at CoAxial and 33 m at North Gorda, and average diameters of 154 m at North Cleft, 133 m at CoAxial and 96 m at North Gorda. These pillow mounds have similar dimensions to the hummocks at 45˚N (figure 5.3), although the three ridges show a distinct separation with highest height: diameter ratios (i.e. the flattest edifices) at North Cleft, and the lowest (i.e. the pointiest edifices) at North Gorda. The hummocks at CoAxial sit roughly between the two. All three sets of ridge hummocks lie within the envelope of height: diameter ratios observed at 45˚N.

The 1996 North Gorda and the 1993 CoAxial eruptions were detected by the U.S. Navy's SOSUS (SOund SUrveillance System (Fox and Dziak, 1998)) network. In both cases, acoustic data above the background was identified for a period of time at a location that corresponds with each eruption. Duration of seismicity gives an indication of how long the eruption lasted. We can therefore use the newly calculated eruption volume and the duration of this seismicity to estimate an average eruption rate for these two eruptions. The 1996 North Gorda eruption was detected acoustically for 523 hours (21.8 days) (Fox and Dziak, 1998). The total erupted volume of 0.007 km^3 (7,000,000m^3) yields an average eruption rate of 320,000m^3 per day or 13,000m^3 per hour $\pm$ 60 %. The 1993 CoAxial eruption was detected acoustically for 453 hours (18.9 days) (Schreiner et al., 1995) and has a volume of 0.008km^3 (8,000,000m^3). This equates to an average eruption rate of 420,000m^3 per day, or 18,000m^3 per hour $\pm$ 60 %.

5.3.4 Discussion

5.3.4.1 Discontinuous eruption

This is the first time discontinuous eruptions have been documented at the North Gorda and CoAxial segments. The mounds are not connected, with no fresh volcanics between them and at North Gorda no fissuring, which would be indicative of a dyke at shallow depth below the surface.

That dyke eruptions quickly localize into a number of point sources is well documented for subaerial fissure eruptions, particularly in Iceland and Hawaii (Decker et al., 1987; Wylie and Lister, 1995) yet has not been observed commonly on mid-ocean ridges. During subaerial examples, the eruption initiates with extrusion of lava along large lengths of the fissure and quickly localizes (often in as little as a few hours) to effusion from a number of point sources which may further localize through time to just one or two erupting vents.

In the eruptions studied, we observe examples of both regularly spaced and irregularly spaced point focusing. In each of the mapped examples one or two of the composite mounds were larger and took the form of a typical fissure type eruption, consisting of a number of pillow mounds aligned along a possible fissure. These pillow mounds each appear to be fed by a central conduit (hence their circular shape) and the spacing of the vents appears to be fairly constant. These large composite mounds contain 58 – 75 % of all erupted material, suggesting that they were fed by a well established and constant source along the length of mound.

On a large scale, the spacing of eruptive centers along the fissure appears to be more random, with the distances between composite mounds equal to 0.1 - 34% of the total dyke length. From the high resolution bathymetry there is no evidence of coeval extrusive volcanics between the mapped volcanic mounds. Video footage from the ROV dives also shows that there are no young lavas between the mounds at North Gorda and North Cleft. This suggests flow localization is occurring before the fissure even reaches the surface, possibly at substantial depths given the lack of fissures observed between eruption sites on the North Gorda ridge. This effect, known as ‘dyke fingering’ has been recognised for igneous intrusions occurring under high confining pressure on land (Rubin, 1993), and in analogue models (Helfrich, 1995) but has not been documented for seafloor eruptions, predominantly because no data has existed until recently with a high enough resolution to confidently identify individual composite mounds.

The width and geometry of a dyke is unlikely to remain the same over several kilometers. Thus, the magma flow upwards along the dyke is unlikely to be constant, with narrower portions of the dyke losing heat faster to the walls. This increases the viscosity of the rising magma to a greater extent than in the wider sections, creating conditions which could allow solidification in some areas and an irregular point focusing effect. In addition, as shown by Qin and Buck (2007), the thickness of mid-ocean ridge dykes rarely exceeds 1.5m as the low melt supply limits the width of dykes. A low melt supply to an irregular dyke would increase the likelihood of high viscosity and solidification in thinner areas, especially if the rate of flow through the dyke is decreasing (Delaney and Pollard, 1982). If this is the case it would be the original variations in dyke thickness combined with the variations in melt supply rate which dictated the areas of point fissure focusing at depth, creating a number of dyke fingers at irregular intervals, much like those observed at these ridges.

The existence of larger elongate composite mounds suggests that some dykes are wide enough to develop a stable flow to the surface along 25 - 45% of their length. The much larger volume of these mounds also indicates that the fissure may have erupted for longer or that they had higher eruption rates. This suggests that as the eruption continues the smaller dyke fingers, which originally reached the surface and fed the smaller composite mounds, also solidify leading to further point focusing to just one or two robust dyke fingers with a magma flux great enough for them to remain active for extended periods.

5.3.4.2 Validity of interpolating a base surface

The calculated eruption volumes depend on an estimate of the shape of the seafloor pre eruption. This is difficult as pillow mound seafloor is, by its nature, extremely irregular. Several different methods were used to estimate the shape of the seafloor: firstly by estimating a flat surface based on the height of three points, roughly equally spaced on areas of fairly flat seafloor around the eruption contour, secondly by interpolating a flat surface with a trend based on the height all around the basal contour, and thirdly by interpolating a natural neighbour surface beneath the flow. Additionally J Martin carried out the trend analyses and natural neighbour analyses for lava flows at another eruption site (Axial Seamount, Martin (2012, pers. comm.)) where pre- and post-eruption bathymetry was available.

The interpolated natural neighbour and flat trend volume calculations were very similar (within 10 % of each other) however both methods underestimated the actual volume of the Axial Seamount eruption by 30 – 60 % (table 5.3). This could be reduced by calculating a different surface using the first order ‘three point method', and deliberately picking the lowest bathymetry points near the boundary, however such a method is obviously highly inaccurate and subjective.

The differences between the actual and calculated volume may be a result of lava filling in topographical lows first, and then growing upwards. In such a scenario, the eruption will fill in all the low areas and therefore the entire bounding outline will be at a shallower depth than the pre-eruption surface. In this case estimating an accurate pre-eruption surface would be impossible. Secondly, although we did not observe an eruption where this was the case, it is conceivable than an eruption could totally bury smaller, pre-existing edifices, and therefore attempts to estimate the pre-eruption surface from the depths of the outline would lead to an overestimation of the eruption volume.

While calculating an accurate volume is likely to be impossible without before and after bathymetric surveying (such as at Axial Seamount), an error of 30 – 60% still provides a useful estimation of the volume of an eruption and will allow for the identification of any significant differences in eruption volume. In this scenario we expect the most accurate estimate to be produced using the interpolation method based on the heights around the entire boundary, as this is able at least to recreate some hummocky type topography around the boundary.

5.3.4.3 Flow volumes and comparison to previous volume estimates

The new high resolution bathymetric maps for these three areas has made it possible to accurately identify flow boundaries on the seafloor. North Cleft 1986 had previously been mapped as individual composite mounds, rather than a continuous flow (Chadwick and Embley, 1994), but North Gorda 1996, like the two historic CoAxial flows, was previously mapped as a single erupted ridge (Chadwick et al., 1998). Chadwick and Embley (1994) identified 13 individual pillowed mounds and we refine the mapping of these mounds, and identify an additional 5 composite mounds, bringing the total number of eruptive mounds to 17 (figure 5.2 C). Some of these mounds such as mounds 1 and 4 (Chadwick and Embley, 1994) were originally mapped as one mound but the high resolution bathymetry reveals they are actually separated by older, fissured seafloor.

Given our 30 – 60 % typical underestimation on our volume estimates, the estimates for the 1996 North Gorda eruption, the 1993 CoAxial eruption and the 1986 North Cleft eruption, are well within error of those estimated from Seabeam comparisons (Chadwick and Embley, 1994; Chadwick et al., 1998; Embley et al., 2000). However, the estimate for the 1982 – 1991 CoAxial eruption volume is ~ 250 % the Seabeam estimate, while the first order estimate was nearly 500 %. The fact that the calculated volumes are typically an underestimation suggests that the Seabeam estimate for this eruption is probably too small.

5.3.4.4 Eruption rates

The 1996 North Gorda and the 1993 CoAxial eruptions were detected by the U.S. Navy's SOSUS (SOund SUrveillance System (Fox and Dziak, 1998)) network. Dividing their volumes by these periods of activity yield average eruption rates of 320,000 m^3 per day or 13,000 m^3 per hour $\pm$ 60 % for North Gorda, and 420,000 m^3 per day, or 18,000 m^3 per hour $\pm$ 60 % for North Cleft.

As a comparison, during the Pu´u ´Ō´ō eruption of Kīlauea in 1983, the most active phases of fissure eruption were expelling lava at rates of between 80,000 - 1,760,000m^3/hr (Garcia et al., 1992). The fissure at Pu´u ´Ō´ō was 7.5 km long, discontinuous, and the majority of these lavas were extruded from localized vents along the fissure, much like those observed at North Gorda and CoAxial. The fissures at North Gorda and CoAxial are shorter than the Pu´u ´Ō´ō fissure at 2.4km and 2.5km respectively. In order to compare them properly an extrusion value per kilometer of fissure was calculated (table 5.1). The eruption rates per kilometer on the North Gorda (5,000 m^3/hr/km fissure) and CoAxial (7,000 m^3/hr/km fissure) eruptions are both lower than the lowest observed eruptions at Pu´u ´Ō´ō (11,000 m^3/hr/km fissure), although with 60 % error may fall into the very lower ranges of those observed at Pu´u ´Ō´ō.

Additionally, these values are an average and it is likely that the effusion rate was not constant. Therefore effusion rates may well have exceeded average eruption rates, probably at the beginning of the eruption when magmastatic pressure is likely to have been highest. Therefore, I conclude typical eruption rates for submarine eruptions on these two ridges are slightly lower than the effusion rates observed for Hawaiian fissure eruptions, but could have effusion rates comparable to the lowest observed at Pu´u ´Ō´ō during the early stages of an eruption.

5.3.4.5 Eruption off strike

Not all the material associated with each eruption was erupted along the strike of the dyke. Dyke thicknesses are unlikely to exceed 1.5 m (Qin and Buck, 2007) and the average pillow mound has a diameter of 138 m, yet the composite mounds were regularly > 300 m wide. Therefore not all the pillow mounds produced by the same eruption were fed directly from the dyke. In the three study areas examined in this study, the average distance off strike of the centre of furthest pillow mound (the predicted location of its feeder vent) was 150 m, suggesting that melt is regularly transported more than 100 m away from the dyke to feed pillow mounds.

5.3.4.6 Comparison to the Mid-Atlantic Ridge

Pillow mounds

Both the observations of lava morphology (> 90% pillow lavas) and the dimensions of the pillow mounds at all three ridges suggest that they are comparable to the hummocks observed at 45˚N (figure 5.3), although the fisures at all the intermediate-spreading rate ridges studies are longer than those at 45˚N, with lengths of 1.7 km, 2.4 km, 2.5 km and 15.5 km, compared to an average length of 1.4 km at 45˚N (see section 3.5.3.2). The elongate composite mounds they typically form appear very similar to the hummocky ridges observed at 45˚N, and are probably formed by the same process – by extrusion of lavas from a point focussed fissure eruption. In this situation, the degree of flatness corresponds to the run out of the lavas, which is a function of effusion rate, viscosity and to some extent slope, although the surrounding seafloor at these three ridges appears to be relatively flat (Gregg and Fink, 1995; Gregg and Fink, 2000; Griffiths and Fink, 1992). Such rheological or eruption dynamic differences may be due to the slightly faster spreading rate at the North Cleft segment (6 cm/yr rather than 5.5 cm/yr) and if we had video coverage of these eruptions we might expect to see them more characterised by lobate lava flows than pillowed ones. Additionally, a large area just south of the 1987 eruption at North Cleft is covered entirely by sheet flows, unlike the other two ridges where such extensive sheet flows are not observed, suggesting North Cleft is characterised by higher effusion rate, larger run out eruptions than the other two. The hummocks at 45˚N mostly lie at the steeper end of the spectrum (figure 5.3), with > 60 % of height: diameter ratios lower than 1:5 as opposed to < 25 % of the North Cleft hummocks, making them more typically like those at North Gorda. However all height: diameter ratios for pillow mounds at all three ridges lie within the envelope of those observed at 45˚N, and therefore both higher and lower run out length eruptions must have occurred.

The observation that eruptions can also occur away from the dyke trace is probably also relevant for the Mid-Atlantic Ridge, as the same thing may well happen in the linear hummocky eruptions observed on and around the AVR. In this case, the volumes of eruptions based on the hummocks on a lineation may be a substantial underestimation. There is no way to constrain this using the data collected for our area, however a detailed geochemical study could help to identify which hummocks belong to which eruption and quantify the extent to which lavas can erupt away from a dyke.

Eruption volumes and rates

The estimated average eruption volume at 45˚N is ~ 3,500,000 m^3 (see 3.5.3.2), compared to 7,000,000 – 48,000,000 m^3 at the studied intermediate-spreading rate ridges. This makes the studied eruptions 2 – 14 times bigger than a typical 45˚N eruption. However, this averaged 45˚N volume does not take account of any hummocks which do not lie directly on the strike of the dyke, and therefore volumes probably do overlap the lower range of intermediate ridge volumes.

Average eruption rates for the pillow mound forming eruptions were 5,000 – 7,000 m^3/hr/km of fissure. The pillow mounds are very similar to the hummocks, both in morphology and dimensions. As lava morphology is predominantly a function of effusion rate (Gregg and Fink, 1995; Griffiths and Fink, 1992), these similarities suggest that eruption rates of Mid-Atlantic Ridge hummock forming eruptions are probably similar. In this case, given an average linear hummock length of 1.4 km (see 3.5.3.2) the total eruption rate of the eruption would be 7,000 – 9,800 m^3/hr, meaning an average volume eruption would take 350 -500 hours. Given that the AVR requires 4,500 – 7,000 average sized eruptions to build it, this would take between 180 and 400 years of continuous eruption to build the AVR (assuming that only one fissure was active at a time). These estimations are in agreement with those based on specific lava morphology effusion rates (determined from analogue experiments) and lava proportions discussed in section 3.5.3.2. However again, these estimates do not take account of any hummocks produced away from the dyke, and therefore these times represent a minimum.

5.3.5 Conclusions

Eruptions at intermediate-spreading rate ridges typically take the form of pillow mound eruptions, which commonly coalesce together to form composite mounds. These mounds have similar dimensions and are probably formed in a similar way to hummocks at slow-spreading mid-ocean ridges. A number of small, discrete composite mounds (similar to hummocky ridges and seamounts on slow-spreading ridges) can be formed during a single eruption, with no erupted products or fissuring between them. This suggests that feeder dykes may point focus before reaching the seafloor.

Estimated flow volumes for the four historic eruptions range from 0.007 – 0.048 km^3, however estimating flow volumes based on a post-eruption surface is difficult as it is impossible to accurately estimate the shape of the pre-eruption seafloor, therefore these estimates have an error of ~ $\pm$ 60 %. Despite these errors we are able to conclude that eruption volumes at intermediate-spreading rate ridges are of the order of 10^6 to 10^7 cubic metres of lava. These volumes are between 2 and 14 times those for the Mid-Atlantic ridge, suggesting eruptions at intermediate spreading rates are slightly larger than those at slow-spreading ridges.

Estimated average eruption eruption rates are 5,000 m^3/hr/km fissure at North Gorda and 7,000 m^3/hr/km fissure at CoAxial. These eruption rates are both lower than the 11,000 m^3/hr/km fissure lowest effusion rate observed for the 1983 Pu´u ´Ō´ō eruption on Hawaii, but are subject to the same $\pm$ 60 % error as the volumes which, combined with the fact they are average estimates and therefore rates at the start of an eruption are probably higher, could place them within the lower bounds of the observed Hawaiian fissure eruption effusion rates. Applying these eruption rates to slow-spreading ridge eruptions gives similar eruption durations to those observed at intermediate rate ridges, Pillow mounds may be fed more than 150 m away from the dyke. Such ‘off dyke’ pillow mounds may be formed relatively early in an eruption and later partially buried by more long lived pillow mound eruptions closer to the dyke trace. This is probably also the case at the Mid-Atlantic Ridge, meaning estimates of eruption volumes based purely on hummocks which lie on the strike of a dyke are likely to be too low.

5.5 References

Caress, D.W., and Chayes, D.N., 1996, Improved processing of Hydrosweep DS multibeam data on the R/V Maurice Ewing: Marine Geophysical Researches, v. 18, p. 631-650.

Caress, D.W., Thomas, H., Kirkwood, W.J., McEwen, R., Henthorn, R., Clague, D.A., Paull, C.K., and Paduan, J., 2008, High-Resolution Multibeam, Sidescan, and Subbottom Surveys Using the MBARI AUV: Marine Habitat Mapping Technology for Alaska.

Chadwick, W.W., and Embley, R.W., 1994, Lava flows from a mid-1980s submarine eruption on the Cleft Segment, Juan de Fuca Ridge Journal of Geophysical Research-Solid Earth, v. 99, p. 4761-4776.

Chadwick, W.W., Embley, R.W., and Shank, T.M., 1998, The 1996 Gorda Ridge eruption: geologic mapping, sidescan sonar, and SeaBeam comparison results: Deep-Sea Research Part Ii-Topical Studies in Oceanography, v. 45, p. 2547-2569.

Clague, D., Lundsten, L., Hein, J., Paduan, J., and Davis, A., 2010, Spotlight 6: Davidson Seamount: Oceanography, v. 23, p. 126-127.

Clague, D.A., Moore, J.G., and Reynolds, J.R., 2000, Formation of submarine flat-topped volcanic cones in Hawai'i: Bulletin of Volcanology, v. 62, p. 214-233.

Davis, A.S., and Clague, D.A., 1987, Geochemistry, mineralogy, and petrogenesis of basalt from the Gorda Ridge Journal of Geophysical Research-Solid Earth and Planets, v. 92, p. 10467-10483.

Decker, R.W., Wright, T.L., and Stauffer, P.H., 1987, Volacism in Hawaii, USGS.

Delaney, P.T., and Pollard, D.D., 1982, Solidification of basaltic magma during flow in a dyke American Journal of Science, v. 282, p. 856-885.

Embley, R.W., Chadwick, W., Perfit, M.R., and Baker, E.T., 1991, Geology of the Northern Cleft Segment, Juan de Fuca Ridge - Recent lava flows, sea-floor spreading, and the formation of megaplumes Geology, v. 19, p. 771-775.

Embley, R.W., Chadwick, W.W., Perfit, M.R., Smith, M.C., and Delaney, J.R., 2000, Recent eruptions on the CoAxial segment of the Juan de Fuca Ridge: Implications for mid-ocean ridge accretion processes: Journal of Geophysical Research-Solid Earth, v. 105, p. 16501-16525.

Faichney, I.D.E., Webster, J.M., Clague, D.A., Paduan, J.B., and Fullagar, P.D., 2010, Unraveling the tilting history of the submerged reefs surrounding Oahu and the Maui-Nui Complex, Hawaii: Geochemistry Geophysics Geosystems, v. 11.

Fox, C.G., and Dziak, R.P., 1998, Hydroacoustic detection of volcanic activity on the Gorda Ridge, February-March 1996: Deep-Sea Research Part Ii-Topical Studies in Oceanography, v. 45, p. 2513-2530.

Garcia, M.O., Rhodes, J.M., Wolfe, E.W., Ulrich, G.E., and Ho, R.A., 1992, Petrology of lavas from episodes 2-47 of the Pu´u ´Ō´ō Eruption of Kīlauea Volcano, Hawaii - Evaluation of magmatic processes Bulletin of Volcanology, v. 55, p. 1-16.

Gregg, T.K.P., and Fink, J.H., 1995, Quantification of submarine lava-flow morphology through analog experiments Geology, v. 23, p. 73-76.

—, 2000, A laboratory investigation into the effects of slope on lava flow morphology: Journal of Volcanology and Geothermal Research, v. 96, p. 145-159.

Griffiths, R.W., and Fink, J.H., 1992, Solidification and morpholoy of submarine lavas - A dependence on extrusion rate Journal of Geophysical Research-Solid Earth, v. 97, p. 19729-19737.

Helfrich, K.R., 1995, Thermo-viscous fingering of flow in a thin gap: a model of magma flow in dikes and fissures: Journal of Fluid Mechanics, v. 305, p. 219-238.

Qin, R., and Buck, W.R., 2007, Why metre-wide dikes at oceanic spreading centres?: Earth and Planetary Science Letters, v. 265.

Rubin, A.M., 1993, Tensile Fracture of Rock at High Confining Pressure: Implications for Dike Propagation: J. Geophys. Res., v. 98, p. 15919-15935.

Schreiner, A.E., Fox, C.G., and Dziak, R.P., 1995, Spectra and magnitudes of T-waves from the 1993 earthquake swarm on the Juan-de-Fuca Ridge Geophysical Research Letters, v. 22, p. 139-142.

Smith, D.K., and Cann, J.R., 1990, Hundreds of small volcanoes on the median valley floor of the Mid-Atlantic Ridge at 24-30[deg] N: Nature, v. 348, p. 152-155.

—, 1992, The role of seamount volcanism in crustal construction and the Mid-Atlantic Ridge (24-degrees-30-degrees-N) Journal of Geophysical Research-Solid Earth, v. 97, p. 1645-1658.

Smith, M.C., Perfit, M.R., and Jonasson, I.R., 1994a, Petrology and geochemistry of basalts from the southern Juan-de-Fuca Ridge - controls on the spatial and temporal evolution of mid-ocean ridge basalt Journal of Geophysical Research-Solid Earth, v. 99, p. 4787-4812.

—, 1994b, Petrology and geochemistry of basalts from the southern Juan de Fuca Ridge: Controls on the spatial and temporal evolution of mid-ocean ridge basalt: J. Geophys. Res., v. 99, p. 4787-4812.

Wylie, J.J., Helfrich, K.R., Dade, B., Lister, J.R., and Salzig, J.F., 1999, Flow localization in fissure eruptions: Bulletin of Volcanology, v. 60, p. 432-440.

Wylie, J.J., and Lister, J.R., 1995, The effects of temperature-dependent viscosity on flow in a cooled channel with application to basaltic fissure eruptions: Journal of Fluid Mechanics, v. 305, p. 239-261.

Yeo, I., Searle, R.C., Achenbach, K.L., Le Bas, T.P., and Murton, B.J., 2012, Eruptive hummocks: Building blocks of the upper ocean crust: Geology, v. 40, p. 91-94.

5.6 Figures

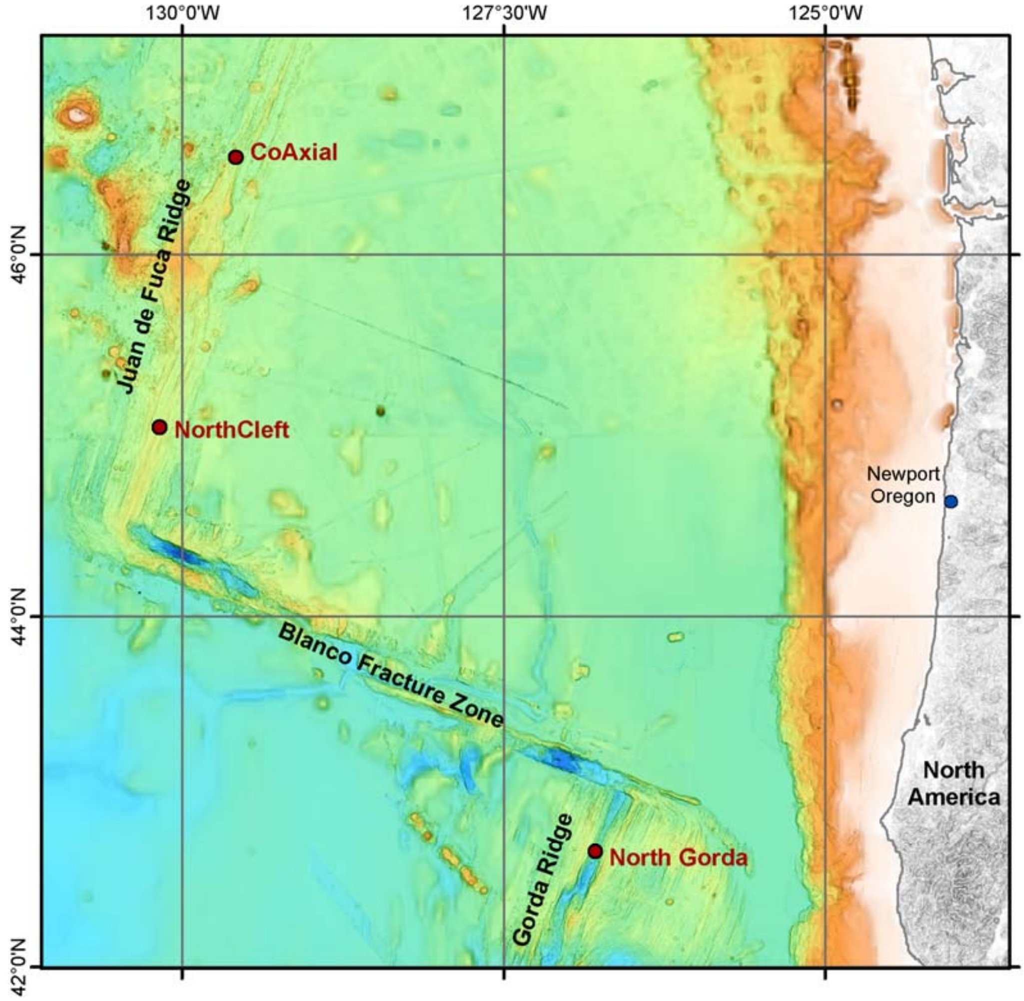

Figure 5.1: Location map of the study sites, ridges and transforms off the west coast of the USA and relationship to land.

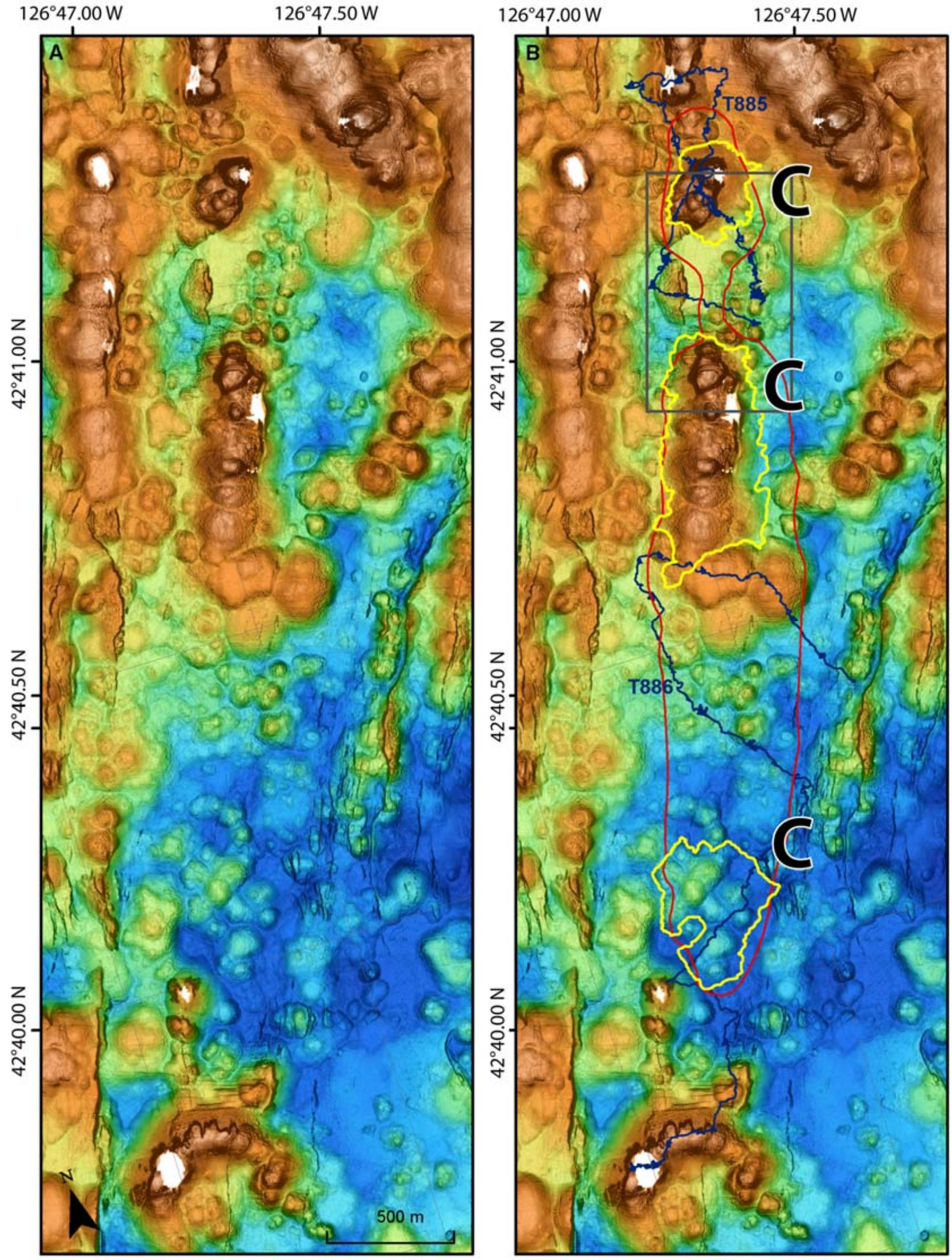

Figure 5.2 A: (A) AUV bathymetry (gridded at 1m) of the North Gorda ridge segment in the area of the 1996 eruption. (B) Shows the same bathymetry but with the dive tracks (blue lines), the Chadwick et al. (1998) possible eruption bounds from seabeam bathymetry (red line), and our new flow bound interpretation based on the high-resolution AUV bathymetry and dive footage (yellow line). Note the lack of fissuring between the three composite mounds. 'C' denotes composite mounds and 'P' denotes an individual pillow mound.

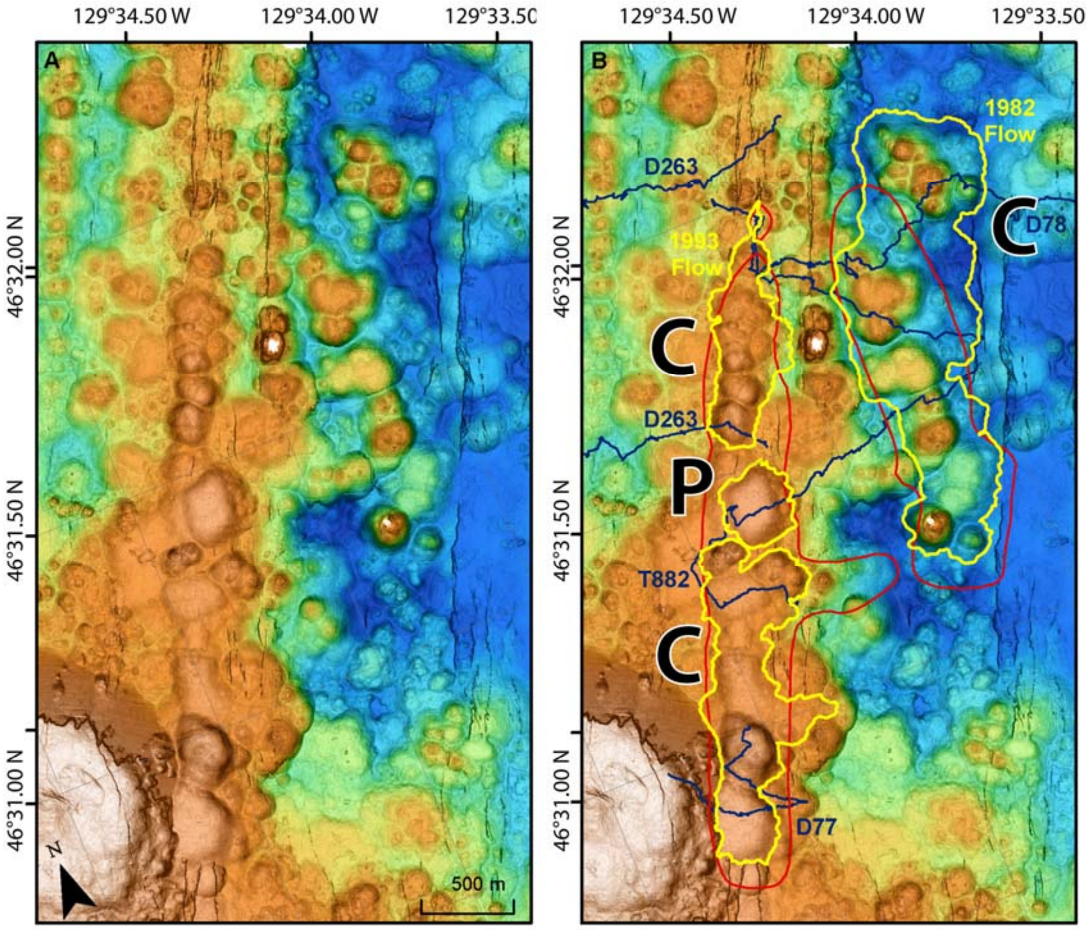

Figure 5.2 B: (A) Shows AUV bathymetry (gridded at 1m) of the CoAxial ridge segment in the area of the 1993 and the 1982-1991 eruptions. (B) Shows the same bathymetry but with the dive tracks (blue lines), Embley et al. (2000) possible eruption bounds from seabeam bathymetry (red line) and our new flow bound interpretation based on the high-resolution AUV bathymetry and dive footage (yellow line). Note the burial of proximal pillow mounds by the taller central ones. 'C' denotes composite mounds and 'P' denotes an individual pillow mound.

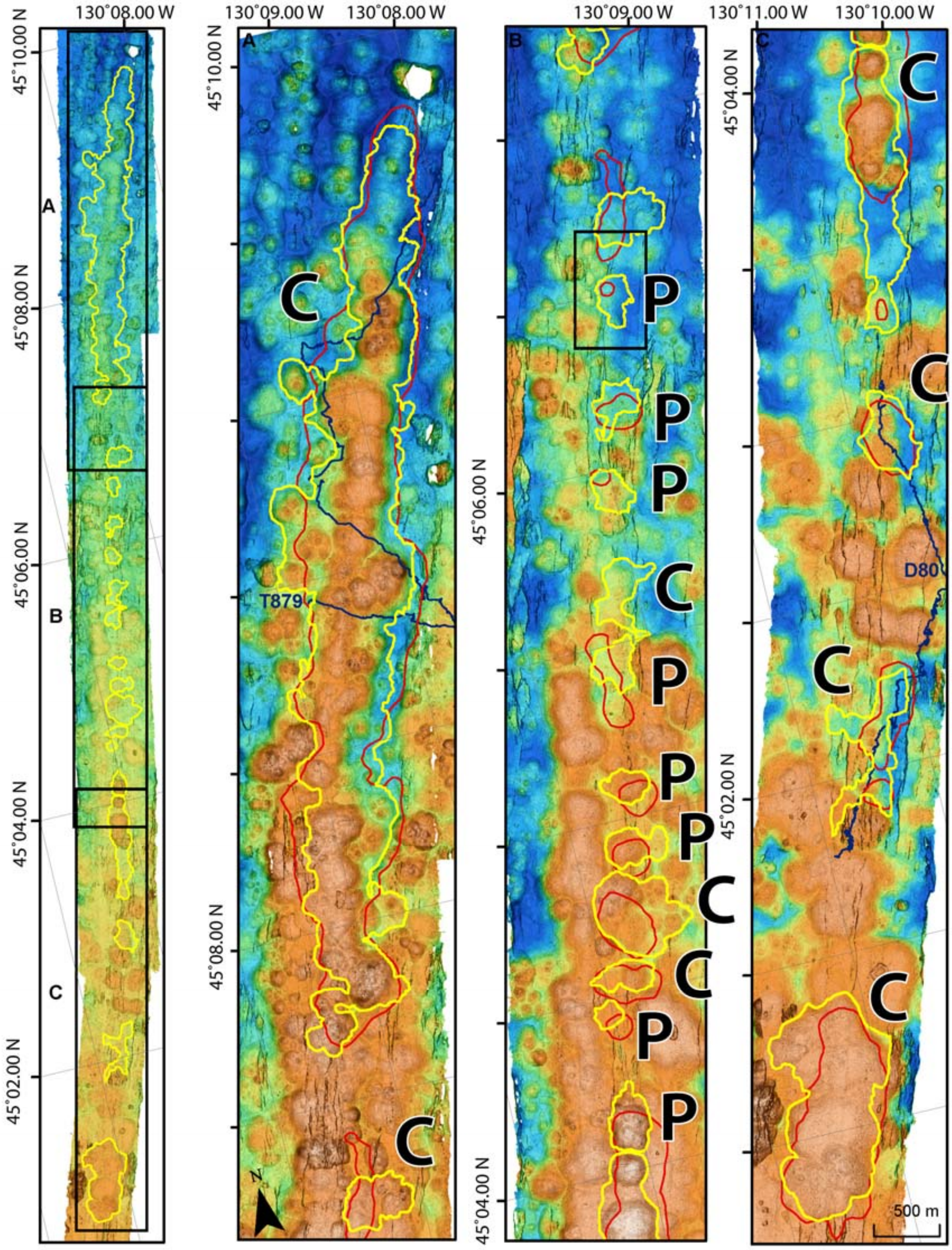

Figure 5.2 C: Left hand panel shows AUV bathymetry (gridded at 1m) of the North Cleft ridge segment in the area of the 1986 eruption. The right hand 3 panels show the same bathymetry at a larger scale with the dive tracks (blue lines), the Chadwick and Embley (1994) possible eruption bounds from seabeam bathymetry (red line) and our new flow bound interpretation based on the high-resolution AUV bathymetry and dive footage (yellow line). ‘C’ denotes composite mounds and ‘P’ denotes an individual pillow mound.

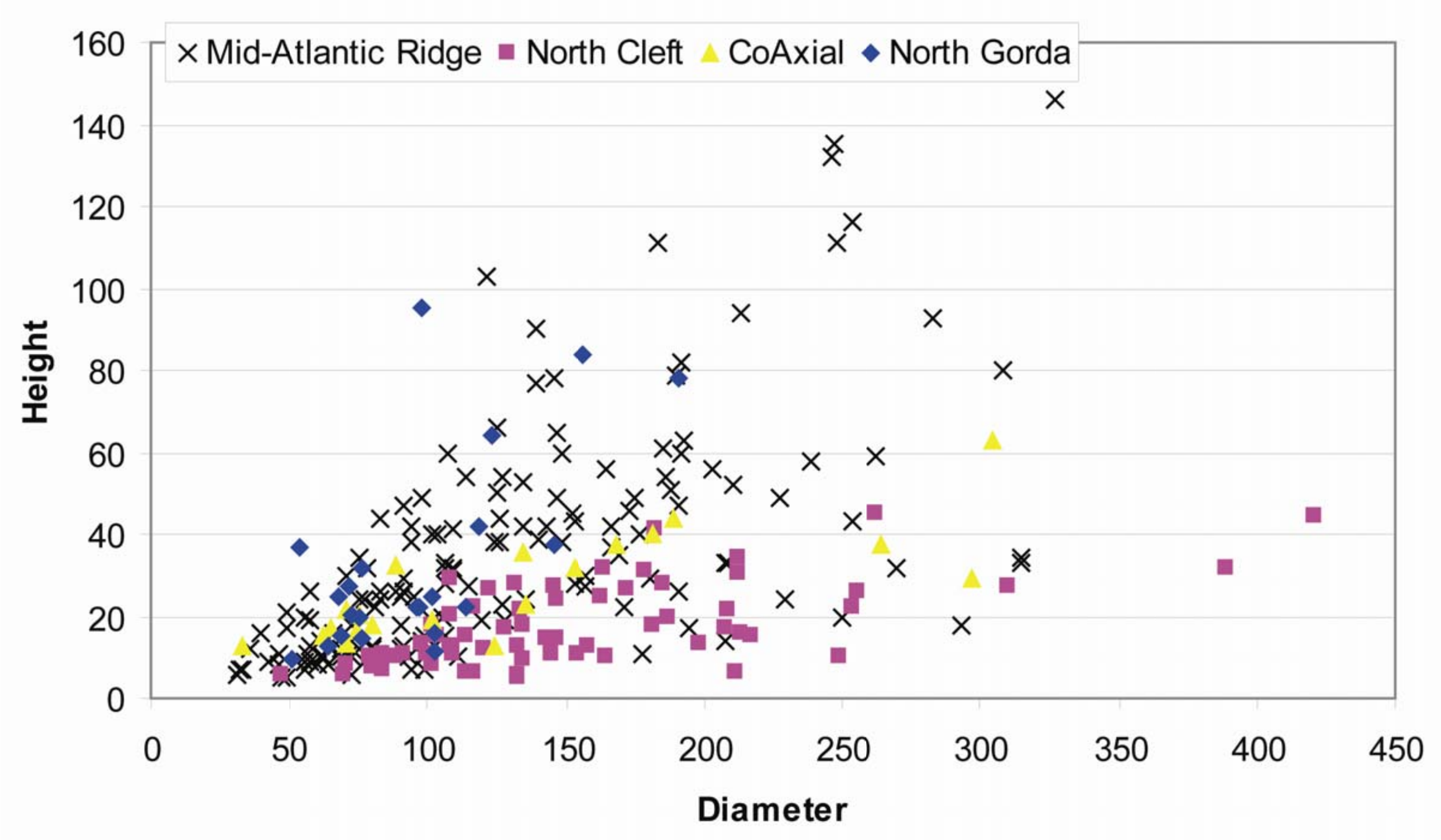

Figure 5.3: Height plotted against diameter for pillow mounds at North Gorda, CoAxial and North Cleft and for hummocks measured at the Mid-Atlantic Ridge at 45°N (chapter 3). The hummocks observed at all three intermediate-spreading rate ridges lie within the envelope of those at 45°N, although appear to be steeper at North Gorda and flattest at North Cleft, possibly correlating to effusion rates.

Eruption	Previous volume (km^3) (Chadwick et al., 1996)	First order volume estimate (km^3)	Interpolated volume (km^3)	New (interp) volume as % published	Duration (hrs) (Fox and Dziak, 1998)	Effusion rate (m^3/hr)	Effusion rate per km fissure ($m^3/hr/km$)
1996 North Gorda	0.018	0.017	0.007	39 %	523	13,000	5,000 ± 60 %
1993 CoAxial	0.0087	0.057	0.008	92 %	453	18,000	7,000 ± 60 %
1982-1991 CoAxial	0.0078	0.052	0.019	244 %	—	—	—
1986 North Cleft	0.055	0.258	0.048	87 %	—	—	—
Puu Oo 1983	—	—	—	—	—	80,000 - 1,760,000	11,000 - 235,000

Table 5.1: Published values for flow volumes at North Gorda, CoAxial and North Cleft compared to the volume values from this study and as a percentage of each other. Effusion rates for these ridges plus the published values for the Puu O'o eruption in 1983 on Kilauea, Hawaii from Carcia et al., (1992).

North Gorda

Mound (from north)	Volume (m^3)	% Total Volume
1	2,900,000	17
2	11,700,000	68
3	2,500,000	15

CoAxial

Mound (from north)	Volume (m^3)	% Total Volume
1	13,800,000	25
2	4,700,000	8
3	38,000,000	67

North Cleft

Mound (from north)	Volume (m^3)	% Total Volume
1	176,600,000	68
2	2,200,000	1
3	600,000	0
4	700,000	0
5	500,000	0
6	1,800,000	1
7	1,200,000	0
8	800,000	0
9	900,000	0
10	2,800,000	1
11	4,200,000	2
12	300,000	0
13	1,600,000	1
14	24,800,000	10
15	2,700,000	1
16	6,300,000	2
17	30,400,000	12

Table 5.2: Individual mound volumes for each eruption calculated using the first order 'three pint method'. Mounds are numbered from the north (i.e. northernmost mound is 1, then 2, then 3 working southward). Volumes are also given as a percentage of the total eruption volume calculated using the same method.

Axial	Volume with Interp Surface km^3	Volume Two Bathy grids km^3	Published values	% diff btwn interp and 2bathy	% diff btwn 2bathy and published
North	0.0109	0.0254	0.0257	43.01	99.02
N1	0.0021	0.0042		50.78	
N2	0.0007	0.0021		33.50	
South	0.0281	0.0643	0.066	43.62	97.49
S1	0.0033	0.0056	0.00547	58.76	102.45
Total (North + South)	0.0390	0.0898	0.099	43.45	90.70

Table 5.3: Comparison of volumes calculated from pre and post eruption bathymetry from Axial seamount with values created using the interpolated surface method (Marten; 2012, pers comm.). The interpolation method consistently underestimates the volume of the eruption by 30 – 60 %.

Discussion 6

Chapter 6: Discussion

6.1 Introduction and rationale

Most of the questions set forward in section 1.2.1 have been addressed in the previous chapters; however the two largest questions, "What is oceanic crust made of?" and "Are AVRs steady state or cyclic features?" have not yet ben discussed. These questions are central to this thesis and require evidence to be drawn from two or more of the previous chapters. This chapter aims to address these two main questions and discuss them with reference to other studies.

6.2 Building blocks of oceanic crust

6.1.1 Building blocks of an AVR

Three volcanic morphologies are observed in the axial valley and on the AVR; hummocks, flat-seafloor and flat-topped seamounts. These morphologies are easily recognisable from the sidescan sonar imagery and have been described and used in many studies of mid-ocean ridges.

Visually the hummocks are by far the most common lithology observed in the surveyed area. Hummocky terrain (i.e. clustered volcanic hummocks) comprises 99.5% of the material observed on the surface of the AVR, with a single flat-topped seamount being the only other volcanic edifice observed on the AVR. These hummocks are commonly collapsing and converting approximately 12 % of hummock-forming lavas to talus deposits (see section 4.4.3.3). As hummocks are the main building blocks of AVRs and

AVRs are the main site of upper oceanic crustal construction, then these talus deposits must also form part of oceanic crust. The remaining 88% is likely to be roughly equivalent to the percentages of lava morphology observed on dives over areas of mapped hummocky terrain: 35 % Pillows and elongate pillows, 23 % pillow lavas, 5 % elongate pillows, 23% pillow and lobate flows, 12% lobate flows and < 1% sheet flows. Therefore the AVR is likely to be constructed of 56% pillow lavas (pillows and elongate pillows), 20% pillow and lobate flows, 12% talus, 11% lobate flows and < 1% sheet flows.

As we do not know the mode or location of formation of the flat-topped seamounts we are currently unable to predict their contribution to the upper oceanic crustal section, however they cover very little of the seafloor by area and therefore their addition should not change any of the findings from this section (6.1.) significantly. We can however say that, like the hummocks, they are characterised by pillow lavas on their steep flanks and higher effusion rate lobate and sheet flow lavas on their flat summits.

6.1.2 Flat areas outside the inner axial valley floor

While it is clear that the AVR is built almost entirely of hummocks, volcanic lithology can only be mapped easily over 70% of the TOBI surveyed area. The other 30% comprises dark looking, smooth, flat terrain (slopes < 5˚), most of which is found on the axial valley flanks (figures 6.1 and 6.2). This terrain looks very smooth, unlike the hummocky volcanic terrain observed on the AVR, although patches of hummocky terrain are observed in and around these flatter areas. These patches have a similar density of hummocks and the hummocks have similar shapes to the hummocky terrain observed at the AVR but appear older (darker looking in the sidescan sonar), suggesting that they were formed in the inner floor, rather than in situ (figure 6.3). The hummocks here also have a similar density, but on average smaller diameters than those on the AVR, suggesting that they have been partially buried. Hummocky terrain covers ~ 60 % of the inner floor by area, but covers < 10 % of the survey area outside the axial valley. This difference in seafloor relief is anomalous (Murton et al. 2012, in prep) and suggests that either styles of crustal extension or eruption have changed through time or that a large proportion of the hummocky terrain has been flattened or buried. If the style of eruption (and crustal extension) has changed, more hummocks would have been produced in the last ~ 286 ka period than the previous ~ 550 ka, this means magma supply to the segment must have been different in the past than it is currently, supporting the Parson et al. (1993) theory of cyclic AVR evolution.

The following sections consider various explanations for the flat areas.

6.1.2.1 Changing eruption style

If magma supply was more voluminous in the past then we should expect to see larger volume, higher effusion rate eruptions, more likely to produce sheet and lobate lava flows, as is observed at settings with large, robust melt supplies like the East Pacific Rise (e.g. Sinton et al. (2002)). While such flat flows would be much more easily buried by sediment to produce the large, flat plains observed in the sidescan sonar, this style of volcanism is not commonly observed occurring alone on slow-spreading ridge segments (Ballard and Moore, 1977; Bonatti and Harrison, 1988; Brown and Karson, 1987; Johnson and Vogt, 1973; Magde and Smith, 1995; Ramberg and Van Andel, 1977; Schilling et al., 1983; Smith and Cann, 1990; Smith and Cann, 1992, 1993; Smith et al., 1995) and most slow-spreading ridge segments (89 % between 24˚N and 30˚N (Smith and Cann, 1992)) display an AVR. There are some exceptions, for example the Tadpole Ridge at 25˚N is surrounded by low lying flat seafloor, comprising mainly pillow lavas, which probably lie on top of higher effusion rate morphologies (Cann and Smith, 2005). However, these examples are rare and could simply be the result of a period of anomalously high effusion rate eruptions which totally bury the pre-existing topography for a short period.

At 45˚N there is at least 6 km either side of the inner floor which does not display an AVR, suggesting that during this time then only around a third of crustal extension would have occurred while an AVR is present. If this is the case, then AVRs should only be active on a third of ridge segments. This is not compatible with the Smith and Cann (1992) observations, nor the rarity of slow-spreading ridges displaying purely sheet and lobate flow volcanism.

Additionally, as discussed in chapter 5, even at faster spreading rates (associated with increased numbers of sheet flow eruptions) eruptions do not typically occur entirely as sheet flows, but as a combination of sheet flows and pillow mounds. As pillow mounds have similar dimensions to the hummocks at 45˚N (chapter 6) we would still expect to observe hummocky type terrain in the flat areas. This is not the case.

Given this evidence it seems unlikely that even if a large magma batch was supplied to the ridge, that it would produce purely sheet flow style eruptions, nor that extension by this mechanism should be occurring more than 11 % of the time (as AVRs are observed on most ridge segments). Therefore increased magma supply and higher effusion rate sheet flow style eruptions are unlikely to be the only cause of the large flat, sedimented areas.

6.1.2.2 Tectonic degradation

Another possibility is that, as in the model proposed by Parson et al. (1993), these areas may be composed of hummocky terrain, which has been flattened and degraded by extension through normal faulting. In this scenario, one might expect to see normal faults closer spaced, or with greater throws than those present when an AVR is accommodating extension. However, the flat areas are not associated with any increase in the number or throw of observed faults picked from the EM120 profiles and TOBI sidescan sonar (figure 6.2). Additionally, in the northern area of the AVR, where we see an increase in faulting and the throws of faults on the AVR, the terrain is reduced in height, but not flattened, with a number of scarps and hummocky areas still clearly visible.

6.1.2.3 Flattening by collapse

As discussed in chapter 4, collapse of volcanic hummocks is a very important process on the AVR and converts 12 % of the erupted material to talus deposits. A collapse of a total edifice would be capable of reducing the overall relief substantially; meaning less sediment or lava flows would be required to bury hummocky terrain. However, collapse of a sector or segment of a cone may reduce its volume, but unless it includes the highest point, not its height, and the relief of the hummocky terrain will remain unchanged. We see no evidence of whole edifice collapse, and only one collapsed hummock surveyed appeared to have lost its highest point. Additionally, we do not see increased collapse volumes with distance from the AVR, or between the apparently younger southern and older northern areas, suggesting that this process does not continue as an edifice ages. It therefore seems unlikely that edifice collapse accounts for substantial changes in the relief of hummocky terrain.

6.1.2.4 Burial by sediment

There is some evidence of the fault blocks having tilted backwards, as a number of the fault scarps display shallow dips (< 30˚) (figure 6.1), which is typical of flexural unloading observed at mid-ocean ridges (MacLeod et al., 2009), and are lower than those typically observed closer to the ridge axis or on the AVR, which we observe to regularly slope > 60˚, and which appear > 45˚ in the profiles in figure 6.2. It should be noted that the EM120 bathymetry effectively averages slopes over the 50 m beam footprint, and we know this is occurring because Isis observations of the inner valley wall faults showed that in places they were near vertical. Despite this a number of the fault slopes do appear to be less steep off axis.

If back tilting of fault blocks is occurring, it will produce basins which will fill with sediment, burying any underlying detail and producing large, flat, sedimented plains. However, not all the flat areas appear to be fault bounded, and in some cases large flat areas are bounded by relatively small, widely spaced faults, which would be unlikely to produce the required rotation – in one location the flat area is a horst, bounded to the east and west by small outward facing normal faults, suggesting that in this case at least, the flat area is not a sediment pond (figure 6.2; profile 4, at approx. 4000 m along the profile). Other large flat areas are found next to normal faults with scarps dipping > 30˚. Additionally, if block rotation and sediment basin filling was the cause we might expect to see an increase in the width of these areas with distance from the axis, which is not observed. Finally, in some small areas within the smooth terrains, dark looking (old) hummocks can be observed (figure 6.3). These do not decrease in diameter away from the scarp, as might be expected if they sat on a tilted fault block (e.g. figure 6.4).

The observation of hummocky terrain off-axis does suggest that the underlying fault block is composed of volcanic hummocks, and that they have been buried by something. Given a regional sedimentation rate of ~ 5 cm/ka (Keen and Manchester, 1970), it is possible to calculate the approximate sediment thickness across the AVR (figure 6.5). This estimate of ~ 5 cm/ka is important if we are to know whether sediment accumulation is capable of burying hummocky terrain, although the fact it agrees with a second nearby estimate of ~ 6.5 cm/ka (Site 410 Shipboard Scientific Party, 1978) suggests that it is probably quite reliable. There are numerous assumptions and inaccuracies associated with predicting sediment accumulation including: different deposition, slopes and redistribution and ponding of sediment (Mitchell, 1995). However, even taking these into account, averaged sediment accumulation over a long period of time can be approximated using the sedimentation rate. The average height of a hummock is 35 m, so at a distance of ~ 7.5 km off axis the sediment thickness is enough to bury any hummocks smaller than this. However, this is only the average value and therefore we might expect to still see the tops of some of the larger hummocks, still visible through the sediment cover. The closest flat areas to the AVR lie < 3 km off axis, where sediment cover should be only 13.5 m thick; however many of these areas do not show any evidence of partially buried or unburied hummocks. Conversely, some flat areas further off axis do occasionally show evidence of old hummocks in localised patches although, as the TOBI survey only extends ~ 9 km off axis, we cannot say whether flat areas outside this also display hummocky texture in the flat sedimented terrains. Escartin et al. (1999) surveyed much further off axis (up to 30 km on either side of the ridge) at 29˚N. Their sidescan sonar surveys show the same flat planar areas continuing off axis, again with occasional localised patches of more hummocky terrain, which appear to get less common further from the axis.

This difference in the surface characteristics of the seafloor can also be quantified by looking at relief (Murton et al., 2012, under review). Here the surface roughness is calculated passing the EM120 multibeam bathymetry through a 5 x 5 pixel (450 m by 450 m) high pass filter. A 3 x 3 pixel standard deviation filter is then used to distinguish the high frequency hummocky terrain. They find that the AVR has a typical peak to trough amplitude of 62 m for hummocky terrain, very different from the peak to trough amplitude off axis of 16 m. This difference requires burial of ~ 46 m of topography, even more than discussed above.

It is therefore clear that sediment cover is not sufficient to bury hummocky terrain near to the axis, and therefore cannot be solely responsible for reducing relief in these areas.

6.1.2.5 Burial by other lava flows

The alternative appears to be that the hummocky terrain is being buried by other lava flows. Burial of hummocky terrain by higher effusion rate proximal sheet flows is proposed by Murton et al. (2012). In this scenario the hummocky terrain is spread away from the ridge axis and buried in the outer portions of the inner floor by sheet flows (figure 6.6). These sheet flows produce flat plains with little relief, which are easily buried by sediment. The average height of a hummock is 35 m and therefore to bury hummocky terrain the sheet flows would need to be at least this thick (less a small amount for sediment accumulation) and should be observed in cross sections exposed by the axial valley wall scarps beneath flat areas outside the inner floor.

Isis dived three valley wall sections, two of which correspond to fairly flat planar areas (figure 6.7) on top of the scarps (dives JC24-83 and JC24-92). In the logs of these sections (chapter 2, figure 2.6) both display mostly pillow lavas in their sections (supporting the idea that most of the crust is built of hummocks), but neither expose pillow lavas at the tops of their sections as we would expect if they were being produced on the AVR. Dive JC24-83 is very sedimented and broken in the uppermost 22 m of the section and no lithology can be identified. While it is possible that this 22 m could be composed of sheet flows, below 22 m clear pillow horizons are exposed and therefore the sheet lavas cannot be more than 22 m thick, if they are there at all. Sheet flows are exposed at the top of the scarp covered by JC24-92 and may be up to 30 m thick, although exposure is again not continuous, with horizons of very broken up material where lithology cannot be distinguished. Therefore even at the maximum possible thicknesses these observed sheet lava flows are only capable of burying ~ 50 % of the hummocks and therefore are not capable by themselves of producing the totally flat plains observed. The flat area associated with the JC24-92 scarp lies 3.9 km off axis and therefore with 5 cm/ka sediment accumulation (Keen and Manchester, 1970) the top should be covered with ~ 18 m of sediment. This gives a combined thickness of 48 m, capable of burying 76 % of the hummocky terrain, which is still not enough to produce a totally flat plain. To cover 90 % of hummocks a total thickness of 66 m is required which, with 30 m of sheet flows, requires a sediment depth of 36 m and would be reached at ~ 8 km off axis. It therefore seems that even a combination of burial by lava flows and sedimentation is not thick enough to bury the hummocky terrain to produce flat plains, although sediment could be locally thicker if there were areas of slumping. Such slumps are common on mid-ocean ridges (Mitchell, 1995), however are localised features and should not produce the uniform flat terrain observed off axis. Further low relief pillow flows (such as those suggested to fill in terrain in chapter 6) or thicker sheet flows not observed in our sections of the inner floor wall may also contribute. Additionally, back tilting of fault blocks may also help to reduce the vertical relief of the hummocks to some extent. I therefore suggest that a combination of flat lying lava flows, pillow lava infilling and sediment accumulation are responsible for flattening the terrain off axis.

6.1.2.6 Burial by eruption off axis

It is additionally possible that further eruptions may have occurred off axis, as have been observed on some of the inner faulted plateaus at 13˚N on the Mid-Atlantic Ridge (MacLeod et al., 2009). We see no evidence of younger brightly backscattering volcanic material on these plateaus at 45˚N, nor any evidence of new lavas or overtopping of the fault scarps by lava in the ROV visual observations (although we only observed the top of these fault scarps in a few places). It is therefore impossible to discount such eruptions as a potential burial mechanism, but if such a process is occurring at 45˚N the backscatter would suggest that such eruptions are older than almost all the erupted material in the inner valley.

6.1.3 Sediment between lava flows

Sediment is accumulating all the time on the ridge and therefore if we have large hiatuses between eruptive episodes we would expect to find sediment beds between the lava flows. If these sediment beds are common and thicker than a few cm then they should be observable in the sections of oceanic crust exposed by the axial valley walls. Additionally, if volcanism is cyclic, then we might expect to see thick sediment deposits lying underneath the base of each AVR cycle, as sediment will have accumulated in the inner floor during the tectonic extension period.

Only one small sediment bed is observed in the three axial valley wall sections (Dive JC24-79). It is less than 20 cm thick and extends laterally for only a few metres. Sediment intercalations are not really observed at all, and are certainly no thicker than 5 cm (a thickness that could certainly be resolved from our video data). Additionally, we do not see any thick, laterally continuous beds which could represent long periods of tectonic thinning. It is possible our faults do not cut such areas, or do not have large enough throws to expose the base of an older AVR, as we only observe 450 m of vertical section and the AVR at 45˚N reaches a height of 700 m. Our observations do not show evidence of significant eruptive pauses in the top 450 m, suggesting that substantial quantities of pillow lavas (450 m is equivalent to the combined heights of 13 average hummocks as described in chapter 3 and therefore may expose the sections of more than 13 separate eruptions).

From these observations I suggest sediment beds are very rare; both as thin beds between individual eruptions, and as thicker, laterally continuous sediment beds between different eruptive cycles. These observations suggest that sediment beds are not an important building block of the upper oceanic crustal layer, and that it is most likely composed almost entirely of magmatic products.

6.1.4 Likely structure of upper oceanic crust at slow-spreading rates

The lack of sediment beds observed in the sections exposed by the axial valley fault scarps suggests that locally sediment does not form a major part of the upper oceanic crust, other than collecting on top of lavas as they are transported off axis. Therefore the upper oceanic crust must be built predominantly of erupted basaltic lavas in a variety of forms. The ridge axis, with its AVR, is the location of the most voluminous volcanism. As ~ 90 % of slow-spreading segments contain an axial volcanic ridge (Smith and Cann, 1992), this suggests that the main mode of volcanism at mid-ocean ridges produces an AVR. AVRs themselves are built predominantly of volcanic hummocks, which cover 99.5 % of the AVR surface. Hummocks are constructed mainly of pillow and elongate pillow lavas (60 – 80%), with some lobate lava flows (< 20 %). The common flank collapses of these volcanic hummocks convert around 12 % of material erupted on the AVR to rubble. These talus deposits are a small, but potentially important contributor to upper oceanic crust, as they have much higher porosities and therefore different geophysical properties to unbroken basaltic lavas.

The fact that the AVR is by far (volumetrically) the largest construction in the inner floor suggests that it is the main locus of volcanism and therefore most of the building blocks of the upper oceanic crust are the volcanic hummocks of which it is built. However, the AVR itself is flanked by large, flat areas. Where these were dived upon they were found to consist of 20 % sheet flows, 16% lobate flows and a further 16% sheet and lobate flows together. Lobate and pillow flows accounted for 33 % and pillow and elongate pillow lavas 15 %. The low relief of the sheet and lobate flow lavas mean that they were probably under represented by the visual observations and probably occur across much more than 50 % of these flat areas. The lava flows will also form sections of oceanic crust and may contribute to the burial and smoothing of hummocky terrain to produce the numerous flat, sedimented plains observed off axis. Estimating the proportion of the crust these lava flows account for is difficult. The thickest observed sheet flows in this study were 30 m, although in order to bury all the hummocky terrain they may be > 50 m in places. We expect the approximate thickness for the extrusive layer to be 500 – 1000 m (Karson, 1998), which agrees with the 434 m of extrusive volcanics exposed in the tallest single fault scarp observed in this study (these scarps do not expose the base of the extrusive section so it must be at least 434 m thick), and fits with models of the structure of the oceanic crust at 45˚N (Fowler and Keen, 1979). If these values are correct then sheet flows would account for ~ 3 – 10 % of the upper oceanic extrusive layer. This estimate excludes any sheet flows which are not at the top of the sections, although we expect these to be rare (figure 6.8).

If we use these rough estimates of the proportions of flat-seafloor (10%) and hummocky terrain (90%), it is possible to approximate the relative proportion of each lava morphology in the extrusive crustal section using the proportions of lava observed on each terrain from the video dives. Using this method I suggest the extrusive layer of the upper oceanic crust here is composed of approximately: 52 % pillow and elongate pillow lavas, 21 % pillow and lobate lava flows, 11 % lobate lava flows, 11 % talus, 3% sheet flows and 2% lobate and sheet flows. These percentages are only estimates and assume that there are no interstitial sheet flows between the pillow lavas, and that the modes of volcanism currently operating on the AVR are the same for all crustal production. Where hummocky terrain is observed outside the inner valley floor it cannot have been completely buried by flat lying lava flows and therefore the crustal section here will contain a lower percentage of higher effusion rate lithologies like sheet and lobate lava flows. Sediment will accumulate on the top surface of the extrusives and will thicken by around one metre with every 200 - 300 m off axis.

6.1.5 Comparison with other studies

These estimated proportions are broadly similar and compatible with suggested crustal structure from other studies. Direct seafloor observation and results of crustal drilling in the FAMOUS area as presented by Atwater (1979), suggests that typical volcanic crustal sections probably comprise 10 – 15 % thin sheet flow units, with the rest being composed of 10 – 20 m thick flows of bulbous pillow and elongate pillows with flow front rubble and sediments. Atwater (1979) also describes the existence of ‘massive units’ within volcanoes; however, we see no evidence for such units in the cross sections of collapsed volcanoes at 45˚N. These proportions are very similar to the estimate of 5 – 15 % sheet flows given in section 6.1.4. Based on the observation that hummocks are the main erupted morphology, and the observation that hummocks are probably monogenetic, I would argue that single lava flows are unlikely to be uniformly 10 – 20 m thick. Instead a single hummock forming eruption occurring along a fissure may have a thickness of 0 m (i.e. it does not even reach the surface) in places and may reach thicknesses greater than 100 m at the hummock summits.

The Atwater (1979) study is also one of the few papers that mention rubble in the crustal section. In this paper it is attributed to flow front rubble and fault gouge, however the common collapses and associated talus flows are almost certainly a large contributor to these talus deposits. This fact is supported by the fact they are found predominantly associated with the pillow lavas, which themselves form the hummocky terrain. Fault gouge rubble should be found in both the pillowed sections and the massive flows, which is not observed. We did not commonly observe flow front rubble at 45˚N, although as described by Ballard and Moore (1977), much of it may lie underneath the flow. Such flow front rubble has been observed elsewhere (Clague, pers comm.) and so it may be being formed to some extent at 45˚N, although is not observed in the inner floor wall fault scarps. This means that the percentage of oceanic crust comprised by talus may be slightly higher than the estimated 11 %, although the talus will be slightly different in nature, comprising whole or half pillow lumps (Atwater, 1979), and therefore the porosity could potentially be similar to the pillow lava flows themselves.

Bryan and Thompson (1979) present evidence for the stratigraphy of seismic layer 2 from DSDP drill sites 332 (Famous area - 33.5˚W 36.8˚N), 334 (Famous area - 34.4˚W 37.1˚N), 395 (off-axis MAR – 46.1˚W 22.8˚N) and 417/418 (off axis - approx 72˚W, 24.5˚N). They find an extrusive layer > 500 m thick which contains very little dyke or plutonic material, and little sediment within the extrusive volcanics. Rocks collected from the drill hole show the crustal section to be mostly composed of pillow basalts with some rare massive sheet flow units. These observations agree with the predictions made in section 6.1.4 from observed seafloor lithology, however Bryan and Thompson (1979) do not estimate the relative proportions of high or low effusion rate lithologies. Their observation of few sediment intercalations also agrees with the observations of the axial valley wall faults at 45˚N, which expose very little sediment, supporting the suggestion that there is unlikely to be much sediment in the upper oceanic crust (section 6.1.4). More detailed studies of older crust from holes 417 and 418 (Salisbury et al., 1979) found the crustal section to be composed of 90 % pillow basalts, <1 % limestone, 5 % smectite and 5 % open cracks. These porosity measurements are not comparable to 45˚N due to the age of the crust being studied (~ 100 my (Richardson et al., 1980)), however the observation of 90 % pillow lavas is again consistent with our observations.

Perfit and Chadwick (1998) use the relative proportions of sheet or lava flows to characterise different spreading rates (Perfit and Chadwick, 1998; figure 6.9). They show a dominance of sheet flows is associated with fast-spreading mid-ocean ridges while higher percentage of pillow lavas are found at slow-spreading ridges. The data is based on the lateral extents of each flow, mostly identified from sidescan sonar and bathymetric data, rather than seafloor observation. This means that really the graph shows proportions of flat vs. hummocky seafloor, although as shown in chapter 2, hummocky seafloor is composed mostly of pillow lavas whereas flat seafloor is typically characterised by higher effusion rate morphologies. The graph also does not take account of lobate lava flows. This is a problem when trying to plot our estimated crustal lava proportions on the same graph, as lobate lava flows are found in both hummocky and flat terrain. Additionally, this study (chapter 4) has identified a large talus component being produced by the hummocky terrain, which is also not accounted for by Perfit and Chadwick (1998). In order to compare our results they are plotted twice. The red arrow (figure 6.9) represents the actual percentages of high vs low effusion rate lithologies (i.e. pillows + elongate pillows + pillows and lobate flows, against lobate flows + sheet flows as given in 6.1.4) and hence has a range of 11 %, which represents the unaccounted for talus component. The red box (figure 6.9) shows the percentage of these two categories of the total, minus the percentage accounted for by talus. The data from 45˚N plots close to the two slow/ultraslow-spreading ridges on figure 6.9, and within the range suggested for the MAR at 37˚N. It has a slightly higher percentage of sheet flows than the 37˚N segment, although this could partly be due to including all observations of purely lobate lava flows in the 'sheet flow' category (many are associated with hummocky terrain). This supports the theory that high effusion rate lava lithologies are more common on fast-spreading ridges than slow ones.

The predicted percentages for normal slow-spread oceanic crust from these studies and at 45˚N differ somewhat to those suggested for Iceland (Palmason et al., 1979). On Iceland the increased volume of melt being supplied to the rift as a result of the hotspot has created a much thicker extrusive volcanic layer, often in excess of 1500 m (Palmason, 1971; Palmason et al., 1979). Additionally sheet flows are more common in the crustal section. Some breccias beds are identified, although Palmason et al. (1979) do not speculate on their mode of formation. I therefore conclude that while some of the processes operating are the same, crust produced at hotspots or in areas affected to some degree by a hotspot cannot be considered fully analogous to normal slow-spreading mid-ocean ridge crustal formation.

6.2 AVR life cycles

6.2.1 AVR Models

6.2.1.1 The Parson et al. (1993) model

The Parson et al. (1993) model defines four life stages, through which the AVR continuously evolves. In the model (figure 6.10), the AVR begins as a narrow ridge, comprising a number of aligned, fissure type rows of volcanic hummocks (Head et al., 1996) and small areas of hummocky terrain. Through time the AVR evolves into a broader, magmatically robust ridge with conical seamounts and then into a tall, whale-back shaped ridge with flat-topped seamounts. As the number of volcanic eruptions decreases, more extension is accommodated by faulting and the AVR is dissected by faults and spread laterally. Stage four is characterised by broad, low ridges, cut by many ridge parallel (not necessarily AVR parallel) faults and covered by at least a thin layer of sediment, as there are no new eruptions occurring to resurface it.

In the Parson et al. (1993) paper these life cycle stages are intrinsically connected to the magma supply to the ridge. An AVR is initiated by a batch of magma being supplied to the ridge. In this early stage volcanism may be concentrated on the axis, or form a number of small, parallel ridges. If the batch of magma is large enough, magma supply is maintained for a period of time, in which the AVR increases in height and volume, with most eruptions being fed through linear fissures and erupting as volcanic hummocks along their length. As the magma batch is depleted the volume and frequency of eruptions decreases and more extension is accommodated by faulting. These faults split the AVR up, reducing its height and spreading it out laterally. This tectonic degradation of the AVR will continue until the next batch of magma is supplied to the ridge, resulting in a cyclicity of periods of magmatic and a-magmatic crustal extension. Parson et al. (1993) found very few unfaulted mature AVRs, leading to the conclusion that tectonic dismemberment must occur during, or soon after, the final stages of AVR construction.

They propose that this cyclicity is a result of magma supply focusing on the areas which are undergoing the greatest stresses (those undergoing amagmatic extension). Extension in these areas will produce decompression melting beneath them, resulting in a switch from amagmatic to magmatic extension accommodation as this melt reaches the brittle/ductile transition and is transported to the seafloor through dykes. During magmatic extension less melt is produced beneath the ridge, so as the magma which accumulated during the amagmatic period of extension is depleted, the modes of extension will become increasingly amagmatic and the cycle will begin again. Evidence cited for magmatic cycles includes the observation of sections of apparently old, degraded AVRs off axis (Mendel et al., 2003; Parson et al., 1993) and the existence of overlapping AVRs, as such features cannot spread for any substantial period of time without interacting with each other or developing transform faulting between them (Searle and Laughton, 1981). Apparently similar structures, displaying different degrees of magmatic and tectonic activity, have also been observed on the ultra-slow spreading Southwest Indian Ridge (Mendel et al., 2003). This model, and the Murton et al. model described in section 6.2.1.2, will be discussed and compared in 6.2.2.4.

6.2.1.2 The Murton et al. (2012) model

The model by Murton et al. (2012) is based on the data collected during our study at 45˚N. In this model AVRs are considered to be steady state features, maintained by frequent, small-volume eruptions. These eruptions produce hummocky terrain near the axis of the AVR, which is then transported outwards and down the flanks of the AVR by subsidence and normal faulting. Once off the AVR this hummocky terrain is buried by episodic, large volume eruptions of massive lavas which cover much of the median valley floor, before being faulted out of the inner floor (figure 6.6).

Evidence cited for steady state AVRs includes the almost ubiquitous presence of AVRs on slow-spreading mid-ocean ridges and the difference in ‘roughness’ between the AVR and the seafloor outside the inner valley floor (where high roughness is characteristic of hummocky morphology and low roughness is typical of the smooth, flat terrains produced by sheet and lobate lava flows). Murton et al.

(2012, in prep) also point out that sediment accumulation is not fast enough to bury hummocky terrain (46 m of sediment are required to reduce the roughness of the hummocky terrain to that observed outside the AVR).

6.2.2 AVR cyclicity at 45˚N

6.2.2.1 Faulting

The AVR at 45˚N displays very different characteristics at its northern and southern ends. The southern end forms a tall, narrow, strongly ridge-parallel ridge, while the northern end of the AVR is much lower and wider (although still roughly ridge parallel). The northern end is cut by a number of faults which are visible in the EM120 bathymetry, suggesting they have greater throws than the smaller faults that are in the southern area, which are only visible in the sidescan sonar. The northern area is also characterised by slightly thicker sediment cover (from both visual observations of the seafloor and sidescan sonar brightness) (Searle et al., 2010) and few fresh lava flows are observed.

Both these pieces of evidence suggest that in the northern and southern areas crust is being extended differently; being dominated by dyke injection in the south and tectonism in the north. This is demonstrated by the profiles across the inner floor (figure 6.2), which show several faults, large enough to be picked up by the EM120 bathymetry, extending the northern end of the AVR (profiles 2 and 3). No such faults are visible in the south (profile 4). Profiles 1 – 3 also show that the northern end of the AVR is wider and flatter than the more robust southern end in profile 4.

Additionally, while AVRs are observed on a large percentage of mid-ocean ridges, they often display different degrees of faulting (e.g. Smith and Cann (1992), Mendel (2003)). In cyclic models almost all volcanism occurs during the AVR building volcanic stage, thus during the tectonic phase, the faults will be cutting and extending AVRs. Depending on the lengths of these cycles – estimates range from 20 thousand to 3 million years (Mendel et al., 2003; Peirce et al., 2007; Tucholke and Lin, 1994) – an AVR may still be detectable during part or all of the tectonic phase of the life cycle. Figure 6.11 shows a profile across the faulted northern end of the AVR with the faults picked. The rough horizontal extension accommodated by a fault can be estimated from the fault displacement and is shown by the pale red bars above each fault. On this profile four clear faults are observed, together capable of accommodating ~ 700 m of horizontal extension, equivalent to ~ 30,000 yr of horizontal extension at the regional spreading rate. This clearly demonstrates that if magmatic-tectonic cycles are operating on 20,000 year time scales (Peirce et al., 2007) then the faulting required to accommodate the extension during this period is not enough to degrade the AVR to the extent that it no longer looks like an AVR.

6.2.2.2 Attempts at Dating

In order to assess whether the AVR at 45˚N is a cyclic feature as opposed to steady state it is useful to know how old various lava flows are. This makes it possible to examine whether eruptions are regular through time and if they are occurring near the AVR summit ridge. The Murton et al. (2012) model predicts that the youngest eruptions should be found near to the axis, getting progressively older further from it, whereas the Parson et al. (1993) model predicts that a number of eruptions occur in the same time period and are followed by an eruptive pause. Further evidence for cyclic or steady state AVRs could come from looking at the age of the higher effusion rate sheet flows that surround the AVR. In the Parson et al. (1993) model these flows should be older than the AVR, corresponding to high melt supply as the AVR was initiated. Alternatively, in the Murton et al. (2012) model we would expect them to be of similar age to the AVR, occurring episodically in order to bury subsided hummocky terrain. Dating lava flows can also provide information on where melt is currently being supplied to the AVR and how regularly eruptions occur.

The models also predict different eruption timing. The Murton et al (2012) paper requires regularly spaced (geographically and in time) eruptions, where as the Parson et al. (1993) cyclic model requires most of the eruptions to occur in a short space of time and therefore would all be of a similar age.

Sediment

The mapping section of this study relies heavily on sediment cover to estimate the relative ages of lava flows. This is an imperfect method as sediment cover is very variable and may be affected by ocean currents, earthquakes, slope and lithology. However, despite these limitations if used to compare similar terrains over large areas then it can provide a useful indicator of relative age. As discussed in chapter 2, most of the lava flows on the AVR are covered by a similar range of sediment thickness. This ranges from < 1 cm to 50 cm, which with a sedimentation rate of 5 cm/ka (Keen and Manchester, 1970), suggests that they all erupted within 10,000 yr of each other. This number probably represents a maximum, as the areas with thicker sediment cover tend to be small basins between pillows and hummocks where sediment redistributed by earthquakes or currents is likely to accumulate. This appears to support the Parson et al. (1993) model, in which large volumes of magma are erupted in a short period.

Sediment thicknesses can only be determined for the lavas on the surface of the AVR, so it is possible that the lavas beneath them are much older and it has been resurfaced recently. However, we observe so few sediment beds between pillowed lava flows in the axial valley wall sections that substantial periods of quiescence seem unlikely. This would be compatible with both models if the section is not thick enough to cut the base of an old AVR, however in the Murton et al. (2012) model lavas should be getting progressively older (and sediment cover should get progressively thicker) away from the axis of the AVR, which is not observed.

The sheet flows have very low relief and therefore are very easily buried by sediment; however, when observed in cross section (usually on top of fissures or scarps) this sediment thickness is again between 1 and 50 cm (mostly less than 25 cm). This degree of cover puts them in the same timeframe as the eruptions occurring on the AVR and does not support the Parson et al. (1993) theory that these flat-lying flows were the earliest products of a batch of magma which later went on to build the AVR, unless both the flat lying lava flows and the AVR were erupted within a single < 10 ka period. In this latter scenario the temporal separation between the sheet flows and pillowed flows on the AVR wouldn't be big enough to detect with sediment; however, the sheet flows would still be being erupted first and therefore would be unable to bury the hummocky terrain and another process would be needed to reduce its relief. Observations of the contact relationships around the AVR suggest that the sheet flows are onlapping the hummocky terrain, which does not support the cyclic hypothesis.

Coeval flat-seafloor and hummock-forming eruptions are compatible with the Murton et al. (2012) model, in which these flat-lying lava flows are erupted continually and at the same time as hummock-forming eruptions on the AVR. In this case however we might also expect to see some hummocks onlapping the sheets, which was not observed in the video dives, although the contact relationships were never clearly exposed.

The sediment evidence appears to support the idea that there was a magmatic episode lasting less than 10,000 yr which resurfaced most of the AVR. It also demonstrates that either the flat-lying seafloor and AVR were erupted in a single, short (< 10 ka) period, or that the sheet flows which form the flat-seafloor are coeval with the hummocky terrain.

Palaeointensity dating

The results of the palaeointensity analyses are presented in Searle et al. (2010) (figure 6.12). Magnetic palaeointensity can be converted into virtual axial dipole moments (VADMs) and compared to measure VADM through time. It was assumed that all samples measured were less than 50 ka based on sedimentary cover. Six samples were measured across a transect of the AVR at ~ 45˚30'N. All of the four samples measured from the AVR had ages < 10 ka, while those from the seafloor to the west of the AVR and from the top of the axial valley wall east of the AVR are between 50 and 5 ka.

The number of samples analysed was small, and samples JC24-79-10, JC24-79-11 and JC24-79-13 may well be from the same lava flow as they all lie on the same spur. However, these findings do agree with those from the sediment dating and suggest that not only were most of the lavas erupted in a single 10 ka period, but that they were erupted in the last 10 ka.

Uranium Series

Uranium series dating was carried out by Peter Van Calsteren and Louise Thomas at the Open University, Milton Keynes (Van Calsteren et al., 2012). When $^{230}Th/^{232}Th$ is plotted against $^{238}U/^{232}Th$, the majority of the 12 samples analysed (figure 6.13) plot within error of each other (figure 6.14). The difference between the error bars for the cluster of samples is ~ 10 ka, while the three samples which plot lower ($^{230}Th/^{232}Th < 0.9$) may be $\leq$ 350 ka or displaying signs of alteration (Van Calsteren, pers com.). Nine samples may not be representative of the entire AVR, and most were within a few km of each other, although spaced far enough apart to sample more than a single flow (figure 6.13). Nevertheless, the clustering of samples within the 10 ka age range also supports the sedimentary evidence that most of the AVR has seen eruptive activity in the last 10 ka.

6.2.3 Evidence for AVR cyclicity at other spreading segments

Much of the evidence presented in the previous sections does not support long period AVR life cycles, yet many studies do suggest this hypothesis. It is possible that the AVR at 45˚N is anomalous, and therefore observations here would not be relevant to other segments or mid-ocean ridges in general. In this section (6.2.3) I look at some of the observations from studies which support the cyclicity model to see how their findings compare with those from 45˚N, and whether similar features are observed on ridges elsewhere.

6.2.3.1 Mid-Atlantic Ridge

Of the 18 Mid-Atlantic Ridge spreading segments between 24˚ and 30˚ N (Smith and Cann, 1992), 16 contain an AVR. These AVRs are described as a mix of robust and broken or discontinuous ridges, although no information is given on the degree of faulting that either of the segments without an AVR has undergone (the Smith and Cann study includes Tadpole Ridge (Cann and Smith, 2005) as a segment with an AVR).

While the different degrees of volcanic robustness observed on the AVRs support the theory of life cycles, the fact that AVRs are observed on ~ 90 % of the ridge segments surveyed suggests that an AVR is present for most of the cycle. This suggests that the tectonic degradation stage is considerably shorter than the volcanic construction phases, although it may account for more than 10 %, as we know from the northern end of the AVR at 45˚N that even a moderately tectonised AVR is visible in relatively low resolution bathymetric surveys.

AVRs on the Mid-Atlantic ridge also do not exist along the entire length of a slow-spreading segment but typically occur only in the middle of a segment, away from offsets. This could be a problem for the

Murton et al. (2012, in prep) model, which suggests all volcanic crust is initially produced on an AVR, however hummocky volcanism is observed north and south of the topographic high which forms the AVR in both Smith and Cann (1992) and at 45˚N, and in some places as far as the transform itself (Lawson, 1996). In this case the same processes could be operating off the AVR where hummock forming eruptions still occur, just not frequently enough to build a large topographic high, possibly due to lower melt supply and/or more infrequent dyking events.

6.2.3.2 Southwest Indian Ridge

AVRs have also been observed at the ultra-slow spreading Southwest Indian Ridge (Mendel et al., 2003). Here, like on the Mid-Atlantic Ridge (Smith and Cann, 1992), Mendel et al. (2003) observe a series of AVRs which display different degrees of tectonic deformation. They identify three different types of ridge morphology: Robust AVRs with few faults, partially faulted volcanic constructions, and segments with no intact AVR which are dominated by faults and fissures. Approximately 25 % of their observed ridges do not show a clear AVR. These observations support the theory of sustained periods of tectonism, and their tectonised AVRs appear similar to, although in some places more comprehensively faulted than, the northern end of the AVR at 45˚N. These observations support the theory that sustained periods of tectonism occur.

Mendel et al. (2003) also claim that, in cross section, old AVR flanks can be observed truncated by the large axial valley bounding faults (figure 6.15:Ai, Bi). However, the sections presented in the paper are significantly vertically exaggerated and when this exaggeration is removed (figure 6.15: Aii, Bii), what originally looked like moderately steep, volcanic constructional terrain actually bears far more resemblance to the off axis profiles at 45˚N (figure 6.2). On these recreated profiles few slopes exceed 5˚, much flatter than the 10 – 30˚ slopes typical of AVR flanks in their study (e.g. segment 9 in Mendel et al. (2003) figure 3) and at 45˚N (this study figure 6.1).

These profiles also show similar areas of flat plains, which are morphologically the same as the smooth, flat areas observed off axis at 45˚N. Estimates of sediment accumulation in the southern Indian Ocean are much lower than in the Atlantic (1 – 5 mm / ka (Borole, 1993; Ewing et al., 1969)); therefore at a distance of 60 – 75 km off axis sediment thicknesses would be < 19 m thick. The description of hummocky terrain at the Southwest Indian Ridge does not suggest that hummocks have very different dimensions from those at the Mid-Atlantic Ridge, and therefore it is unlikely that 19 m of sediment would be sufficient to bury them. Smooth lava flows are observed in the Mendel et al. (2003) study, predominantly at the sites of the most robust AVRs, and therefore this is a possible mechanism for reducing the topography of hummocky terrain here as well.

6.2.3.3 Reykjanes Ridge

Many of the models of cyclic AVRs are based on the observation of faulted overlapping AVRs on the Reykjanes ridge (Parson et al., 1993; Peirce et al., 2005; Peirce et al., 2007; Peirce and Sinha, 2008). At the Reykjanes Ridge entire AVRs can be seen rafted off axis. This occurs as the oblique spreading direction of the ridge results in a number of overlapping AVRs. This arrangement is not stable and therefore spreading will flip from one AVR to the adjacent one, and continued spreading on the newly active AVR will raft the outer one off axis (Peirce and Sinha, 2008). Such overlapping AVRs are not typically observed on normal slow-spreading mid-ocean ridges, so there is no such instability to cause the rafting of entire AVRs off axis. These rafting cycles are estimated to have a periodicity of 100 – 350 ky (Peirce and Sinha, 2008).

However, shorter tectonic-magmatic cycles are suggested to operate within these longer period rafting cycles by geophysical studies, which image magma chambers capable of accommodating 20,000 years of extension but which would freeze in much shorter periods (Heinson et al., 2000; MacGregor et al., 1998; Navin et al., 1998; Sinha et al., 1998; Sinha et al., 1997). Such cycles would last 20 – 60 ka and a number would occur on the same AVR before a rafting event occurs (Peirce et al., 2005; Peirce et al., 2007). These cycles are totally independent of the overlapping AVRs and therefore there is no reason that such cycles are not operating on normal mid-ocean ridge segments. It is therefore important to bear in mind that the cycles that could be occurring at 45°N may be much shorter than the long period cycles observed at the Reykjanes Ridge, and those inferred elsewhere which are > 2 my (Tucholke et al., 1997).

6.2.4 Are AVRs cyclic features?

The observation of similar sediment cover across the AVR at 45˚N supports the cyclic model over the steady state model, in which sediment cover should increase with distance from the ridge axis. Sediment cover along with the small amount of palaeomagnetic and uranium-series dating carried out on samples collected from cruise JC24 all point to the AVR having been constructed within a single 10,000 year period. As we only sample the surface of the AVR, it is impossible to know whether the interior of the AVR is the same age, although the observation of no sedimentary beds between pillow lava flows in the axial valley wall scarps supports this.

Despite their having similar sedimentary cover, the differences in spreading character between the northern and southern ends of the AVR at 45˚N (and elsewhere) demonstrate clearly that a single AVR can display characteristics of more than one life cycle stage at a time. At the southern end of the 45°N segment a robust, relatively unfaulted AVR appears to represent primarily magmatic spreading, whereas in the north the AVR is broken by numerous faults accommodating extension, apparently in the absence of recent magmatic intrusion. Therefore it appears that magmatic extension has continued in the south (and possibly moved further south as the youngest lava flows observed lie right at the southern end of the AVR), while the northern end is now experiencing a magma starved period dominated by tectonic extension. Assuming the cyclic model is correct, the whole AVR cannot be older than 286 ka (based on the width of the inner floor and the spreading rate) and therefore this cycling between magmatic and tectonic cycles would have to be occurring on a much shorter time scale than the 1.7 – 2.7 m.y. predicted for the ultra-slow spreading Southwest Indian Ridge segments with robust AVRs (Mendel et al., 2003) and that predicted on the Mid-Atlantic Ridge (from crustal thickness variations) of 2 – 3 million years (Tucholke et al., 1997). Instead, if there are cycles, they appear to be of the order of 2 – 70 ka as proposed by Peirce et al. (2007). It is possible that these shorter cycles are occur during the magmatic period of accretion in a long period life cycles (Peirce et al., 2007), however the near ubiquity of AVRs (faulted or otherwise) on slow-spreading mid-ocean ridges suggests that there are no long periods of time when an AVR is not present.

The steady state model (Murton et al., 2012) does not require any periods of sustained tectonic degradation of an AVR, instead suggesting continuous transport off the AVR by small, outward facing normal faults as new material is erupted near the summit. Yet, we know that major tectonic degradation of AVRs does happen, as faulted AVRs are commonly observed (Mendel et al., 2003; Parson et al., 1993; Smith and Cann, 1992). Some tectonic degradation is not incompatible with the model, but if large magmatic pauses occur and the AVR is destroyed by tectonic activity, then by definition the AVR is not a steady state feature. Shorter periods of tectonic extension, associated with short tectonic-magmatic cycles (Peirce et al., 2007), will not totally destroy the AVR, thus only the observation of robust, unfaulted AVRs on most slow-spreading segments would really be evidence of steady state features, not simply the fact they can be observed in some segments (Murton et al., 2012, in prep).

In order to account for the observation of tectonised sections of AVR, the steady state model must include at least short periods of tectonic extension. However, if in the steady state model of AVR accretion magmatic activity is broken by periods of tectonic degradation, then whether or not the AVR is steady state is simply a matter of how long such periods last. If magmatism stops for long enough that tectonic dismemberment reduces the height of the AVR so much that it is no longer detectable then the AVR is cyclic; if magmatism restarts before the AVR is dismembered to the extent it no longer looks like an AVR, then it is steady state.

In both models the presence and surface appearance of an AVR is intrinsically tied to the presence or lack of melt beneath the ridge. We know that magma chambers at normal slow-spreading mid-ocean ridges (i.e. those not near hot spots) are small and therefore probably transient (Detrick et al., 1990; Sinha et al., 1998; Sinton and Detrick, 1992; Smith and Cann, 1993) and therefore we expect melt supply up and down the ridge to be extremely variable in space and time. It is possible that amagmatic extension initiates a new batch of melt through decompression melting, as presented in Parson et al. (1993), however it is not necessary for a ridge to be totally tectonically degraded before this melt is produced, and the fact we see AVRs on 90% of slow-spreading ridge segments suggests that this is not the case. Additionally, the fact that the ridge at 45°N appears to be displaying different life cycle stages at either end (as defined by the Parson et al. (1993) model) also shows that a single segment does not need to be experiencing similar melt availability along its length.

The fact that at 45°N the northern end of the AVR has clearly undergone amagmatic extension which has reduced its height to < 400 m (souther end is ~ 700 m) above the surrounding seafloor is also not compatible with the steady state scenario. Instead at 45°N the best model seems to lie somewhere between the Parson et al. (1993) and Murton et al. (2012) models.

Based on the data collected from 45°N, it seems that axial volcanic ridges are purely the surface expression of magmatic crustal extension. Magma chambers at slow spreading mid-ocean ridges are small and transient, meaning that the locations and volumes of melts being supplied are likely to be variable. There is no need for these eruptions to be occurring predominantly at the AVR crest, as suggested by Murton et al. (1993) and are probably occurring across the AVR as no systematic increased sedimentation with distance from the axis is observed. This hypothesis is supported by the palaeointensity magnetisation values (figure 6.12) which show also show no systematic increase in age with distance from the axis within the inner floor (although these results must be treated with caution as JC24-79-10, JC24-79-11 and JC24-79-13 all appear to be from the same spur, and therefore probably the same flow, and JC24-93-38 isn't plotted).

The volumes of magma chambers and timescales on which magma is supplied will dictate the surface appearance of an AVR. If melt is supplied fairly frequently to an area, for a long period of time, a robust AVR will be observed, however if melt supply is lower for a sustained period then tectonic processes will degrade an AVR. If melt is again supplied to these tectonically degraded sections, then these areas could be easily rejuvenated. In this scenario AVRs do not have to have a life cycle per se, but are more the product of the balance between magmatic and amagmatic extension. These AVR-forming hummock eruptions must be occurring coevally with sheet-flow-forming eruptions around the AVR, which are probably partially responsible for reducing the height of the hummocky terrain off axis.

6.3 References

Atwater, T., 1979, Constraints from the Famous Area concerning the structure of the oceanic section, in Talwani, M., Harrison, C.G.A., and Hayes, D.E., eds., Deep drilling results in the Atlantic Ocean: Oceanic crust: Maurice Ewing Series: Washington D. C., American Geophysical Union.

Ballard, R.D., and Moore, J.G., 1977, Photographic Atlas of the Mid-Atlantic Ridge Rift Valley: New York, Springer-Verlag, 114 p.

Bonatti, E., and Harrison, C.G.A., 1988, Eruption styles of basalts in oceanic spreading ridges and seamounts - Effect of magma temperature and viscosity Journal of Geophysical Research-Solid Earth and Planets, v. 93, p. 2967-2980.

Borole, D.V., 1993, Late Pleistocene sedimentation: a case study of the central Indian Ocean Basin: Deep Sea Research Part I: Oceanographic Research Papers, v. 40, p. 761-775.

Brown, J.R., and Karson, J.A., 1987, Variations in axial processes on the Mid-Atlantic Ridge: The median valley of the MARK area Marine Geophysical Researches, v. 10, p. 109-138.

Bryan, W.B., and Thompson, G., 1979, Petrologic character of the Atlantic crust from DSDP and IODP drill sites, in Talwani, M., Harrison, C.G.A., and Hayes, D.E., eds., Deep drilling results in the Atlantic Ocean: Ocean Crust: Maurice Ewing Series: Washington, American Geophysical Union, p. 273 - 284.

Cann, J.R., and Smith, D.K., 2005, Evolution of volcanism and faulting in a segment of the Mid-Atlantic Ridge at 25 degrees N: Geochemistry Geophysics Geosystems, v. 6, p. 20.

Detrick, R.S., Mutter, J.C., Buhl, P., and Kim, II, 1990, No evidence from multichannel reflection data for a crustal magma chamber in the MARK area in the Mid-Atlantic Ridge Nature, v. 347, p. 61-64.

Escartín, J., Cowie, P.A., Searle, R.C., Allerton, S., Mitchell, N.C., MacLeod, C.J., and Slootweg, A.P., 1999, Quantifying tectonic strain and magmatic accretion at a slow spreading ridge segment, Mid-Atlantic Ridge, 29°N: J. Geophys. Res., v. 104, p. 10421-10437.

Ewing, M., Eittreim, S., Truchan, M., and Ewing, J.I., 1969, Sediment distribution in the Indian Ocean: Deep Sea Research and Oceanographic Abstracts, v. 16, p. 231-248.

Fowler, C.M.R., and Keen, C.E., 1979, Oceanic crustal structure—Mid-Atlantic Ridge at 45° N: Geophysical Journal of the Royal Astronomical Society, v. 56, p. 219-226.

Head, J.W., Wilson, L., and Smith, D.K., 1996, Mid-ocean ridge eruptive vent morphology and substructure: Evidence for dike widths, eruption rates, and evolution of eruptions and axial volcanic ridges: Journal of Geophysical Research-Solid Earth, v. 101, p. 28265-28280.

Heinson, G., Constable, S., and White, A., 2000, Episodic melt transport at mid-ocean ridges inferred from magnetotelluric sounding: Geophysical Research Letters, v. 27, p. 2317-2320.

Johnson, G.L., and Vogt, P.R., 1973, Mid-Atlantic Ridge from 47 degrees to 51 degrees North Geological Society of America Bulletin, v. 84, p. 3443-3461.

Karson, J.A., 1998, Internal structure of oceanic lithosphere: A perspective from tectonic windows, in Buck, R., Delaney, J.R., Karson, J.A., and Lagabrielle, Y., eds., Faulting and magmatism at mid-ocean ridges: Geophysical Monograph: Washington, American Geophysical Union.

Keen, M.J., and Manchester, K.S., 1970, The Mid-Atlantic Ridge near 45ºN. X. Sediment distribution and thickness from seismic reflection profiling: Canadian Journal of Earth Sciences, v. 7, p. 735-747.

Lawson, N.K., 1996, Crustal Accretion Near Ridge-Transform Intersections: Kane Fracture Zone, Mid-Atlantic Ridge: Durham, University of Durham.

MacGregor, L.M., Constable, S., and Sinha, M.C., 1998, The RAMESSES experiment—III. Controlled-source electromagnetic sounding of the Reykjanes Ridge at 57°45′N: Geophysical Journal International, v. 135, p. 773-789.

MacLeod, C.J., Searle, R.C., Murton, B.J., Casey, J.F., Mallows, C., Unsworth, S.C., Achenbach, K.L., and Harris, M., 2009, Life cycle of oceanic core complexes: Earth and Planetary Science Letters, v. 287, p. 333-344.

Magde, L.S., and Smith, D.K., 1995, Seamount volcanism at the Reykjanes Ridge - Relationship to the Iceland hot-spot Journal of Geophysical Research-Solid Earth, v. 100, p. 8449-8468.

Mendel, V., Sauter, D., Rommevaux-Jestin, C., Patriat, P., Lefebvre, F., and Parson, L.M., 2003, Magmato-tectonic cyclicity at the ultra-slow spreading Southwest Indian Ridge: Evidence from variations of axial volcanic ridge morphology and abyssal hills pattern: Geochemistry Geophysics Geosystems, v. 4.

Mitchell, N.C., 1995, Diffusion transport model for pelagic sediments on the Mid-Atlantic Ridge: J. Geophys. Res., v. 100, p. 19991-20009.

Murton, B.J., Schroth, N., Le Bas, T.P., Van Calsteren, P., Searle, R.C., and Yeo, I., 2012, Formation of oceanic crust at slow spreading ridges by continuous Axial Volcanic Ridge processes: In prep, p. in prep.

Navin, D.A., Peirce, C., and Sinha, M.C., 1998, The RAMESSES experiment—II. Evidence for accumulated melt beneath a slow spreading ridge from wide-angle refraction and multichannel reflection seismic profiles: Geophysical Journal International, v. 135, p. 746-772.

Palmason, G., 1971, Crustal structure of Iceland from explosion seismology: Visindafelag Islendinga.

Palmason, G., Arnorsson, S., Fridleifsson, I.B., Kristmannsdottir, H., Saemundsson, K., Stefansson, V., Steingrimsson, B., and Tomasson, J., 1979, The Iceland Crust: Evidence from drillhole data on structure and processes, in Talwani, M., Harrison, C.G.A., and Hayes, D.E., eds., Deep drilling results in the Atlantic ocean: Ocean Crust: Maurice Ewing Series: Washington, American Geophysical Union, p. 43 - 65.

Parson, L.M., Murton, B.J., Searle, R.C., Booth, D., Evans, J., Field, P., Keeton, J., Laughton, A., McAllister, E., Millard, N., Redbourne, L., Rouse, I., Shor, A., Smith, D., Spencer, S., Summerhayes, C., and Walker, C., 1993, En-echelon axial volcanic ridges at the Reykjanes Ridge- A life-cycle of volcanism and tectonics Earth and Planetary Science Letters, v. 117, p. 73-87.

Peirce, C., Gardiner, A., and Sinha, M., 2005, Temporal and spatial cyclicity of accretion at slow-spreading ridges - evidence from the Reykjanes Ridge: Geophysical Journal International, v. 163, p. 56-U31.

Peirce, C., Sinha, M., Topping, S., and Gill, C., 2007, Morphology and genesis of slow-spreading ridges – seabed scattering and seismic imaging within the oceanic crust: Geophysical Journal International, v. 168, p. 59-89.

Peirce, C., and Sinha, M.C., 2008, Life and death of axial volcanic ridges: Segmentation and crustal accretion at the Reykjanes Ridge: Earth and Planetary Science Letters, v. 274, p. 112-120.

Perfit, M.R., and Chadwick, W., 1998, Magmatism and Mid-Ocean Ridges: Constraints from

Volcanological and Geochemical Investigations, in Buck, R., ed., Faulting and Magmatism at Mid-Ocean Ridges, Americal Geophysical Union.

Ramberg, I.B., and Van Andel, T.H., 1977, Morphology and tectonic evolution of the rift valley at LAT 36°30'N, Mid-Atlantic Ridge Geological Society of America Bulletin, v. 88, p. 577-586.

Richardson, S.H., Hart, S.R., and Staudigel, H., 1980, Vein Mineral Ages of Old Oceanic Crust: J. Geophys. Res., v. 85, p. 7195-7200.

Salisbury, M.H., Stephen, R., Christensen, N.I., Franchet.J, Hamano, Y., Hobart, M., and Johnson, D., 1979, The physical state of the upper levels of cretaceous oceanic crust from the results of logging, laboratory studies and the oblique seismic experiment at DSDP sites 417 and 418, in Talwani, M., Harrison, C.G.A., and Hayes, D.E., eds., Deep drilling results in the Atlantic ocean: Ocean crust: Maurice Ewing Series: Washington, American Geophysical Union, p. 113 - 134.

Schilling, J.G., Zajac, M., Evans, R., Johnston, T., White, W., Devine, J.D., and Kingsley, R., 1983, Petrologic and geochemical variations along the Mid-Atlantic Ridge from 29 degrees N to 73 degrees N: American Journal of Science, v. 283, p. 510-586.

Searle, R.C., and Laughton, A., 1981, Fine-scale sonar study of tectonics and volcanism on the Reykjanes Ridge Oceanologica Acta, v. 4, p. 5.

Searle, R.C., Murton, B.J., Achenbach, K., LeBas, T., Tivey, M., Yeo, I., Cormier, M.H., Carlut, J., Ferreira, P., Mallows, C., Morris, K., Schroth, N., van Calsteren, P., and Waters, C., 2010, Structure and development of an axial volcanic ridge: Mid-Atlantic Ridge, 45°N: Earth and Planetary Science Letters, v. 299, p. 228-241.

Sinha, M.C., Constable, S.C., Peirce, C., White, A., Heinson, G., MacGregor, L.M., and Navin, D.A., 1998, Magmatic processes at slow spreading ridges: implications of the RAMESSES experiment at 57 degrees 45 ' N on the Mid-Atlantic Ridge: Geophysical Journal International, v. 135, p. 731-745.

Sinha, M.C., Navin, D.A., MacGregor, L.M., Constable, S., Peirce, C., White, A., Heinson, G., and Inglis, M.A., 1997, Evidence for accumulated melt beneath the slow-spreading Mid-Atlantic ridge: Philosophical Transactions of the Royal Society of London Series a-Mathematical Physical and Engineering Sciences, v. 355, p. 233-253.

Sinton, J., Bergmanis, E., Rubin, K., Batiza, R., Gregg, T.K.P., Gronvold, K., Macdonald, K.C., and White, S.M., 2002, Volcanic eruptions on mid-ocean ridges: New evidence from the superfast spreading East Pacific Rise, 17 degrees-19 degrees S: Journal of Geophysical Research-Solid Earth, v. 107.

Sinton, J.M., and Detrick, R.S., 1992, Midocean ridge magma chambers Journal of Geophysical Research-Solid Earth, v. 97, p. 197-216.

Site 410 Shipboard Scientific Party, 1978, Site 410, in Luyendyk, B.P., Cann, J.R., Duffield, W.A., Faller, A.M., Kobayashi, K., Poore, R.Z., Roberts, W.P., Sharman, G., Shor, A.N., Steiner, M., Steinmetz, J.C., Varet, J., Vennum, W., Wood, D.A., and Zolotarev, B.P., eds., Initial Reports of the Deep Sea Drilling Project, Volume 49: Washington, National Science Foundation.

Smith, D.K., and Cann, J.R., 1990, Hundreds of small volcanoes on the median valley floor of the Mid-Atlantic Ridge at 24-30[deg] N: Nature, v. 348, p. 152-155.

—, 1992, The role of seamount volcanism in crustal construction and the Mid-Atlantic Ridge (24-degrees-30-degrees-N) Journal of Geophysical Research-Solid Earth, v. 97, p. 1645-1658.

—, 1993, Building the crust at the Mid-Atlantic Ridge Nature, v. 365, p. 707-715.

Smith, D.K., Humphris, S.E., and Bryan, W.B., 1995, A comparison of volcanic edifices at the Reykjanes Ridge and the Mid-Atlantic Ridge at 24-degrees-30degrees-N Journal of Geophysical Research-Solid Earth, v. 100, p. 22485-22498.

Tucholke, B.E., and Lin, J., 1994, A geological model for the structure of ridge segments in slow-spreading ocean crust Journal of Geophysical Research-Solid Earth, v. 99, p. 11937-11958.

Tucholke, B.E., Lin, J., Kleinrock, M.C., Tivey, M.A., Reed, T.B., Goff, J., and Jaroslow, G.E., 1997, Segmentation and crustal structure of the western Mid-Atlantic Ridge flank, 25°25 - 27°10 N and 0 - 29 m.y.: J. Geophys. Res., v. 102, p. 10203-10223.

Van Calsteren, P., Thomas, L., Murton, B.J., and Searle, R.C., 2012, Basalt generation at an axial volcanic ridge: implications for ocean crust composition: In prep.

6.4 Figures

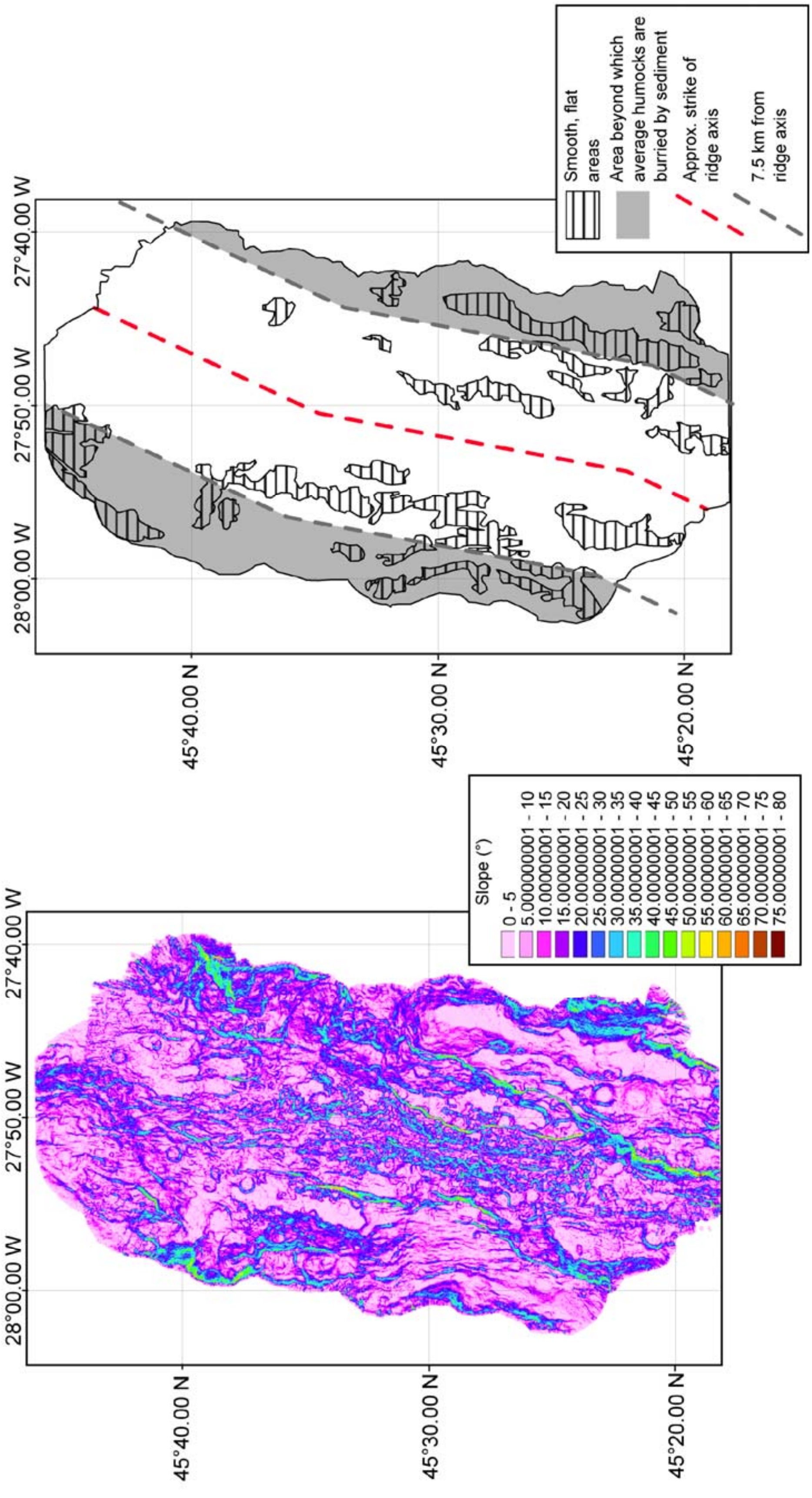

Figure 6.1: Left hand panel shows a slope map of the 45°N spreading segment produced using the EM120 bathymetry. Slope is displayed at 5° intervals. Right hand panel shows the locations of the flat planar areas picked from the slope map and the EM120 and TOBI imagery. The grey area shows the distance off axis at which sediment cover exceeds 35 m (the height of an average hummock).

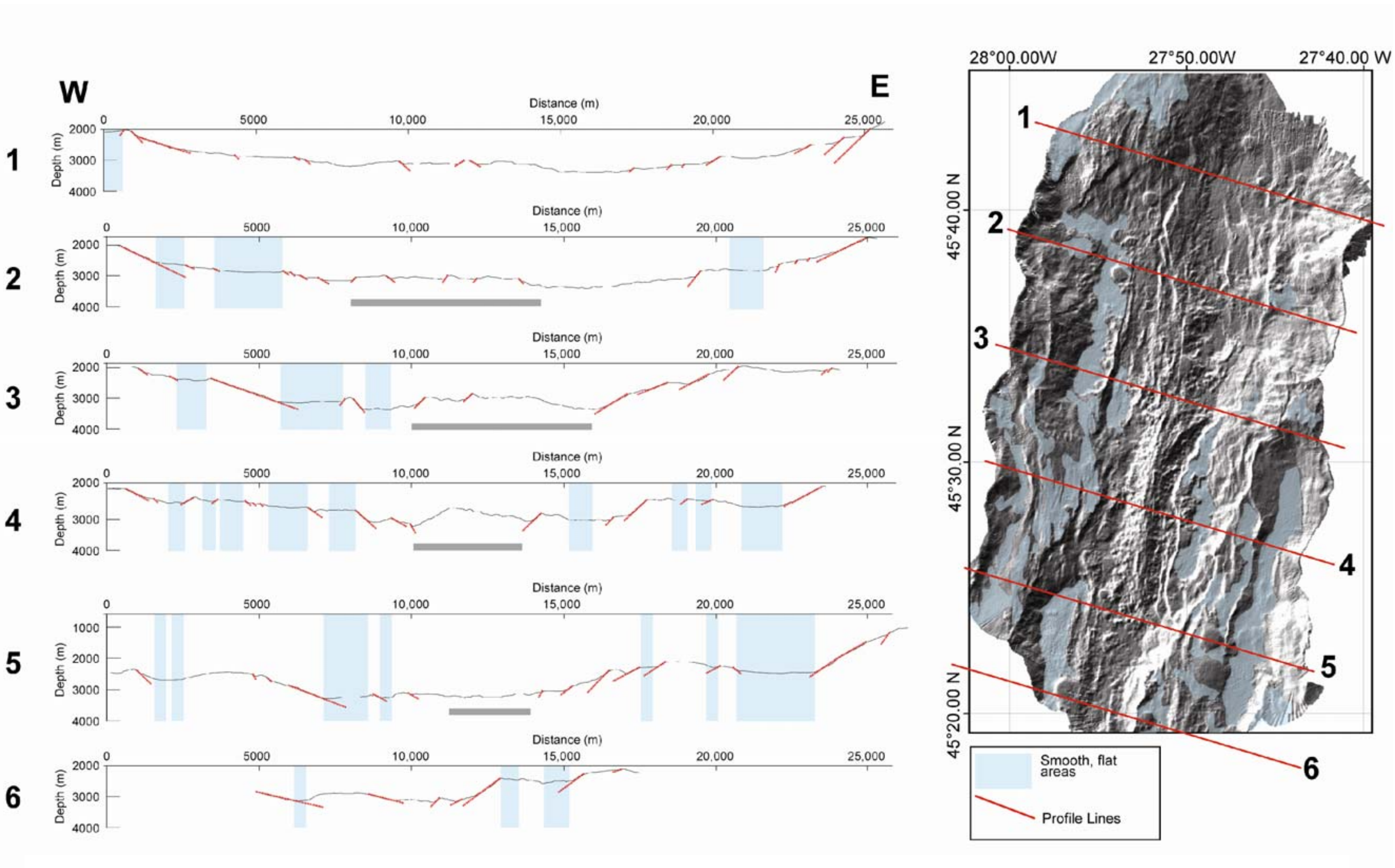

Figure 6.2: Profiles taken across the axial valley floor showing the flat plains and their relationship to regional faulting. Faults are shown by red dashed lines, while the locations of the plains are shown in pale blue. The map shows the plains identified in figure 7.1 on hill shaded EM120 relief of the 45˚N spreading segment .

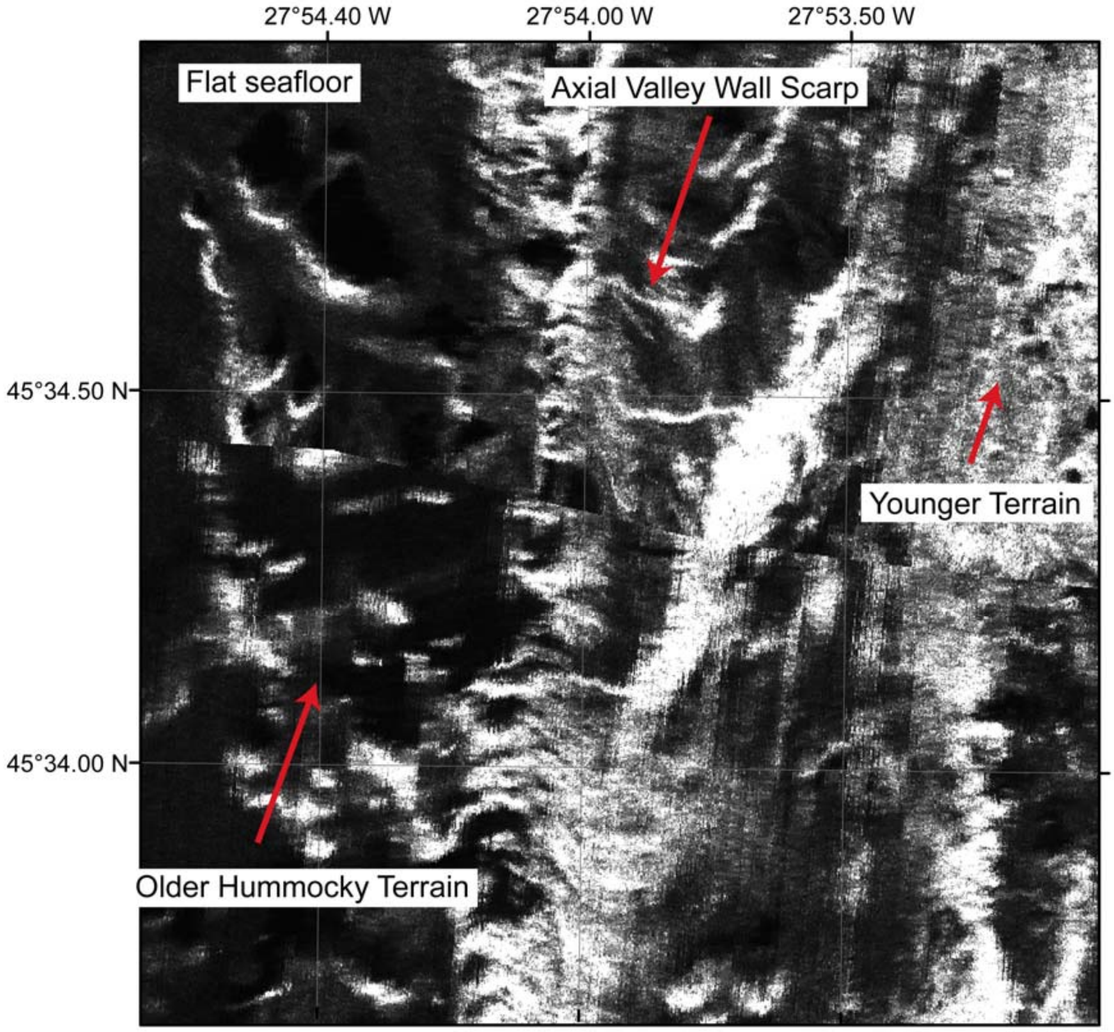

Figure 6.3: Example of younger, more brightly reflecting seafloor inside the axial valley floor, separated from older, darker looking hummocky terrain outside the axial valley.

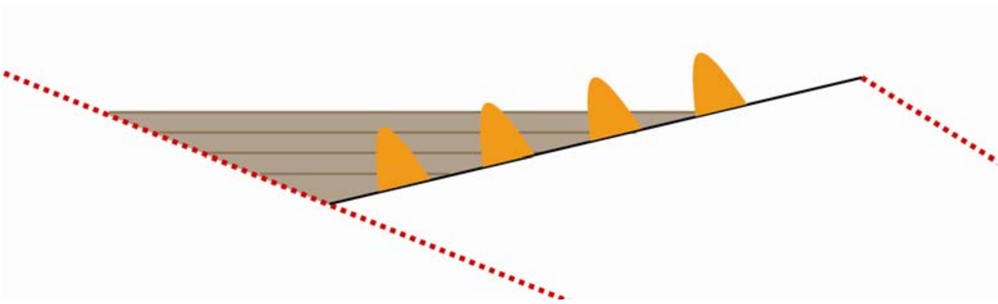

Figure 6.4: Schematic illustration of the effect of fault block rotation on the ability of sediment to bury hummocky morphology.

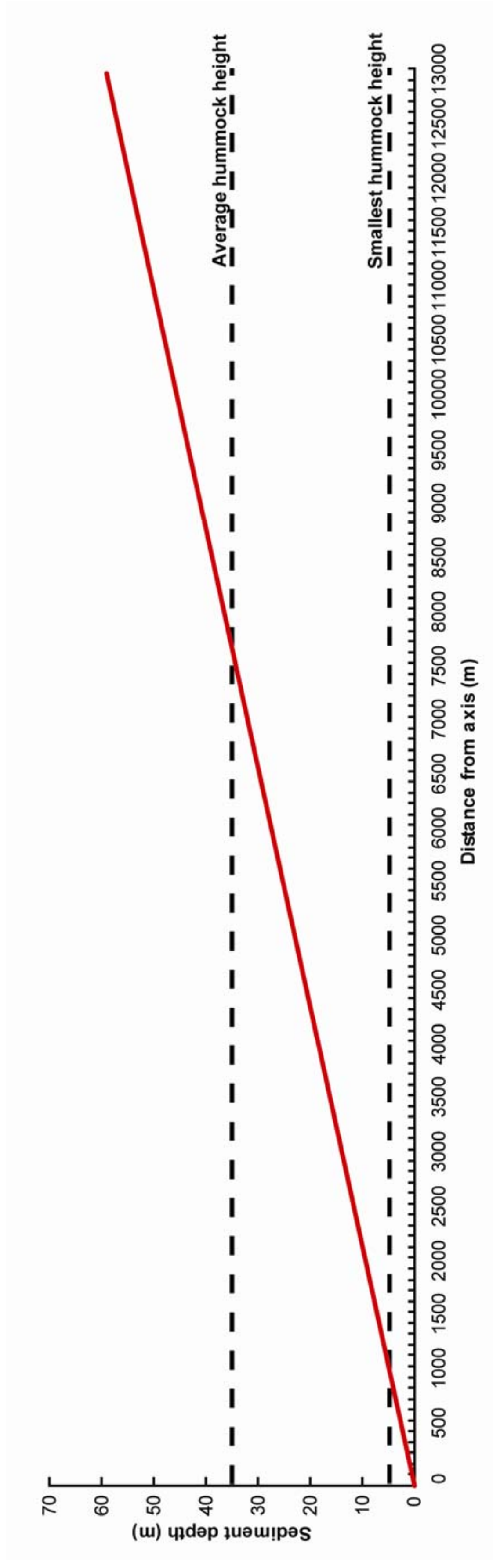

Figure 6.5: Sediment thickness with distance from the axis based on sedimentation rates from Keen and Manchester (1970). The smallest hummocks will be buried within 1 km of the ridge axis, while average sized hummocks can be buried by sediment ~ 7.5 km off axis.

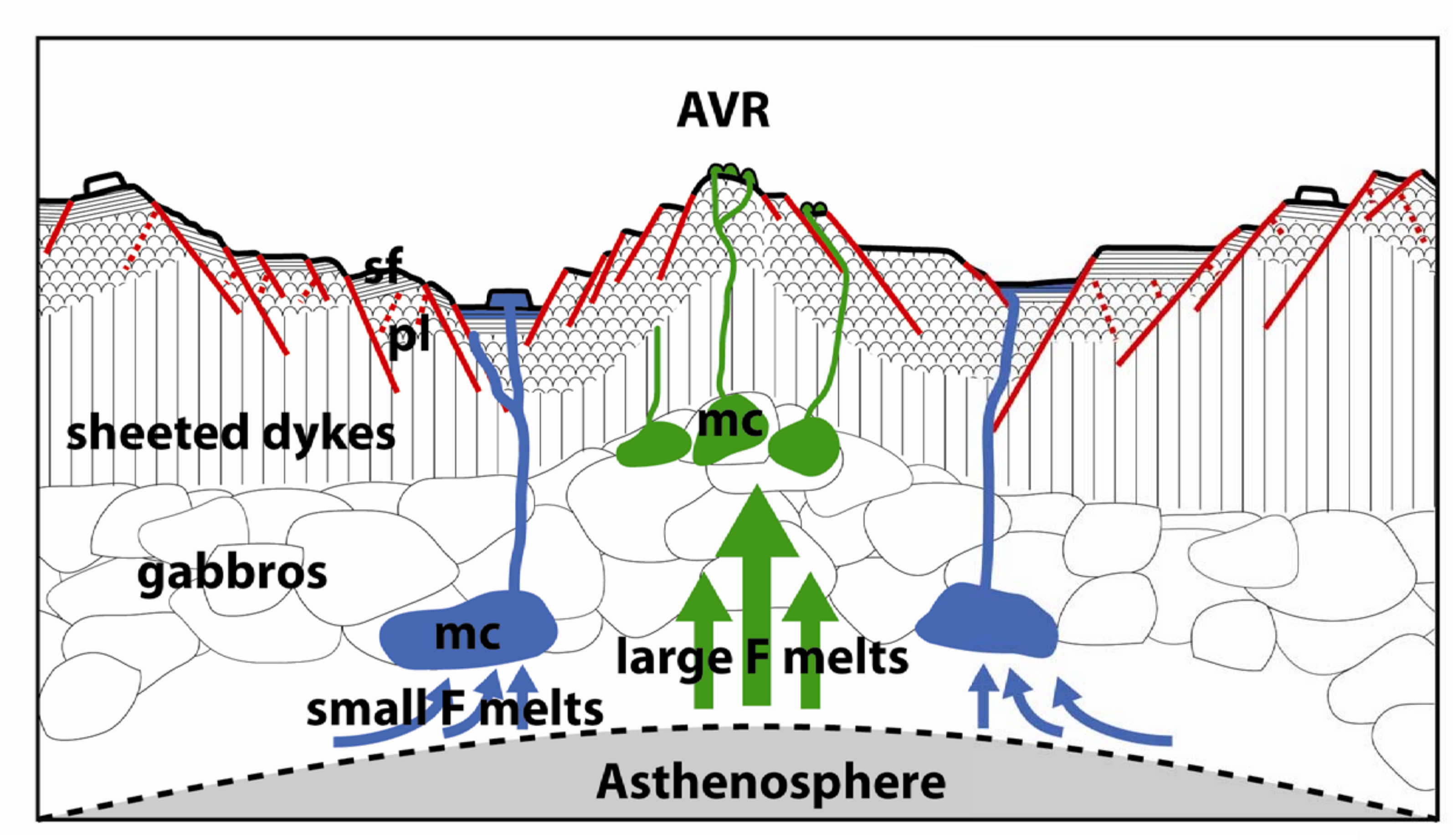

Figure 6.6: The Murton et al. (2012) model of AVR accretion. Field of view is approximately 30 km. In this model, large fraction melts feed numerous small magma chambers ('mc') underneath the AVR, which in turn feed small, hummock forming eruptions near the axis. This hummock material is down-faulted off the AVR by a series of normal faults, and is then buried entirely by sheet flows ('sf'), fed from larger magma chambers containing accumulated small fraction melts. 'pl' = 'pillow lava'). Figure drawn by I Yeo.

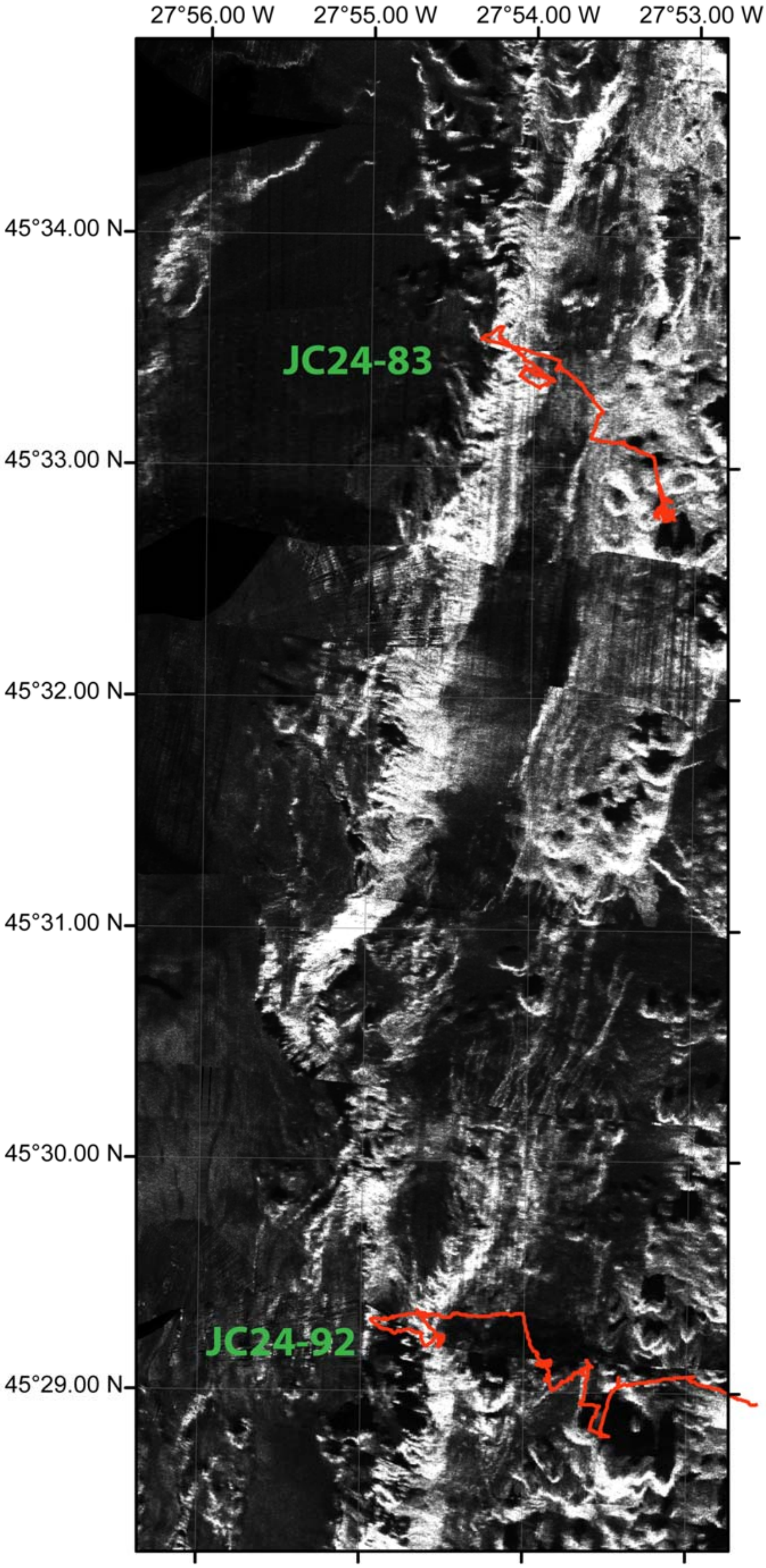

Figure 6.7: Two dives which cover exposed inner valley floor wall scarps beneath areas of relatively flat seafloor.

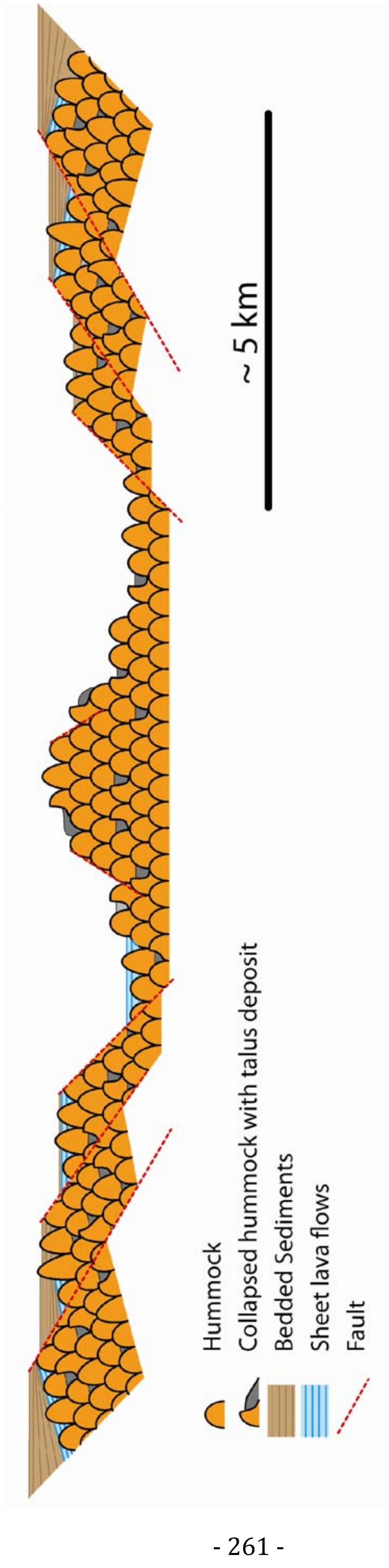

Figure 6.8: Schematic diagram of the volcanic building blocks and structure of the upper oceanic crust. Only the extrusive section is shown and therefore the total vertical scale is between 500 and 1000 m. Feeder dykes are not shown.

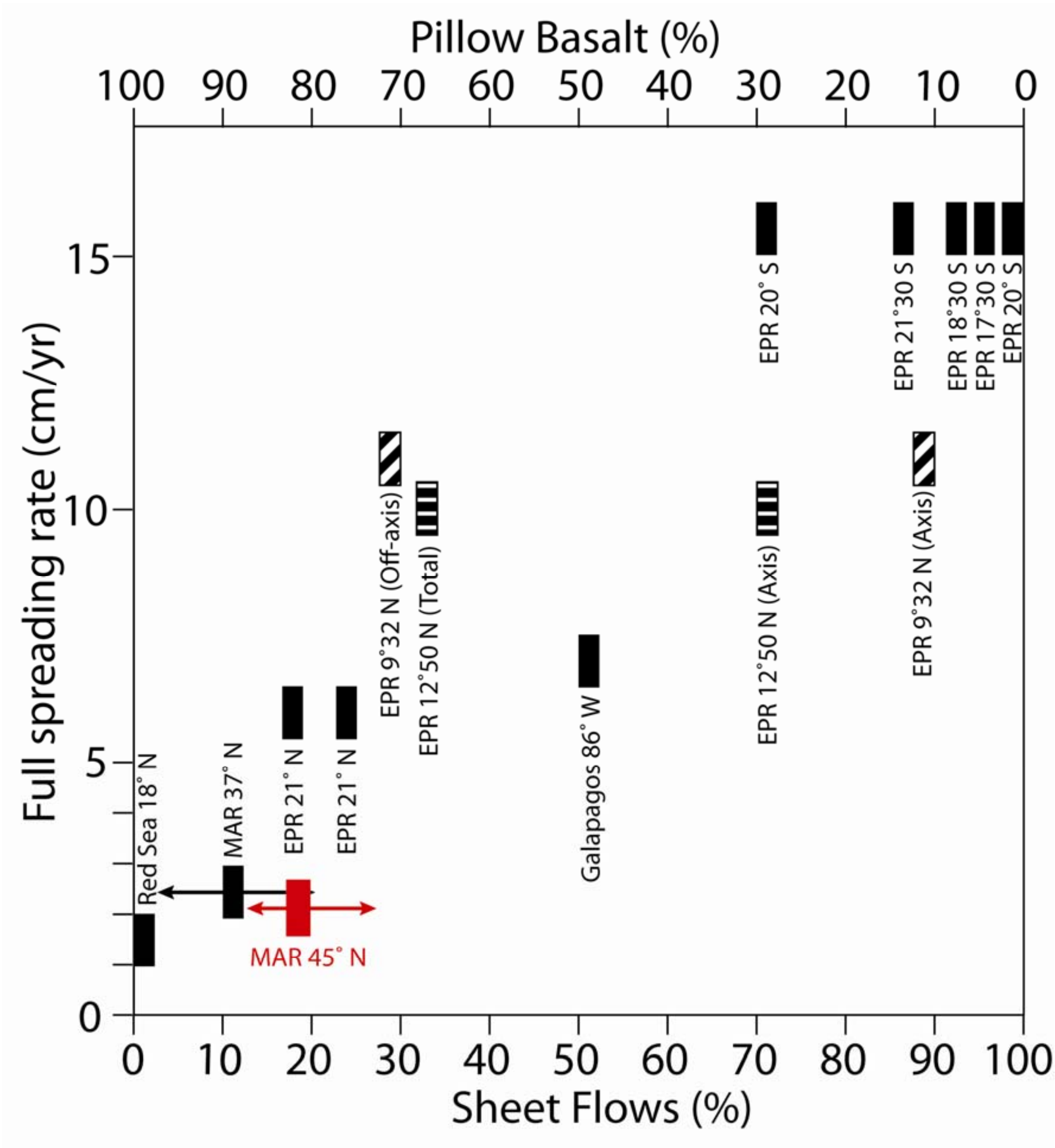

Figure 6.9: Lava morphology percentage against spreading rate for a selection of ultraslow-, slow-, intermediate- and fast-spreading ridges from Perfit & Chadwick (1998). Bars are centred on spreading rate. Percentages are based on areal distributions. Percentages for this study are shown in red. The arrow shows the potential range based on observed values, while the red block shows the relative percentages excluding talus, which is not accounted for in this diagram.

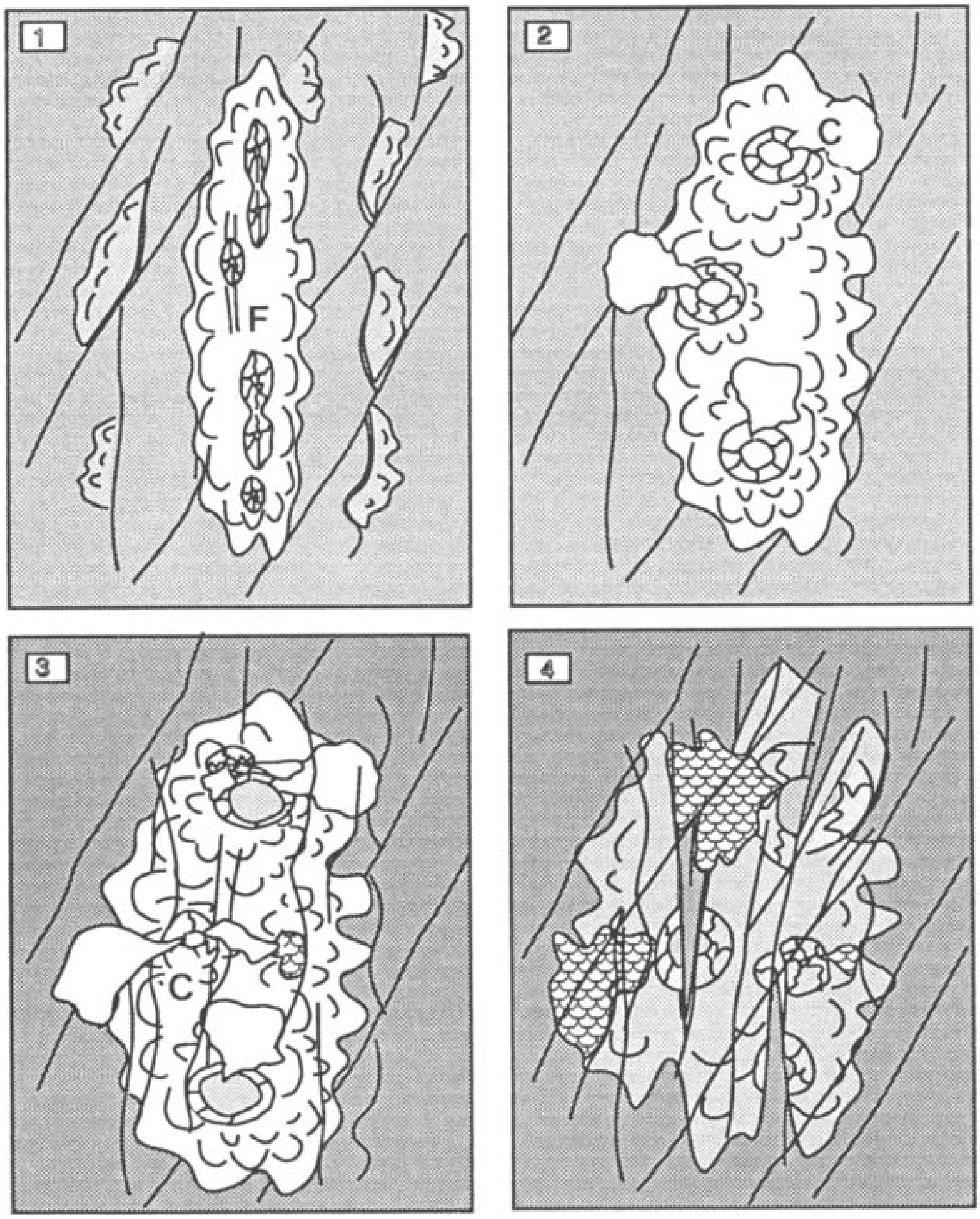

Figure 6.10: From Parson et al. (1993). Schematic cartoon of an axial volcanic ridge at an oblique spreading segment in various stages of its life cycle from young (1), adolescent (2), mature (3) and old (4). Note the change from fissure volcanoes (F) to conical (C) and shield and back to conical types. Also note the initial AVR-parallel faulting, cut by later ridge-parallel faulting as the AVR disintegrates.

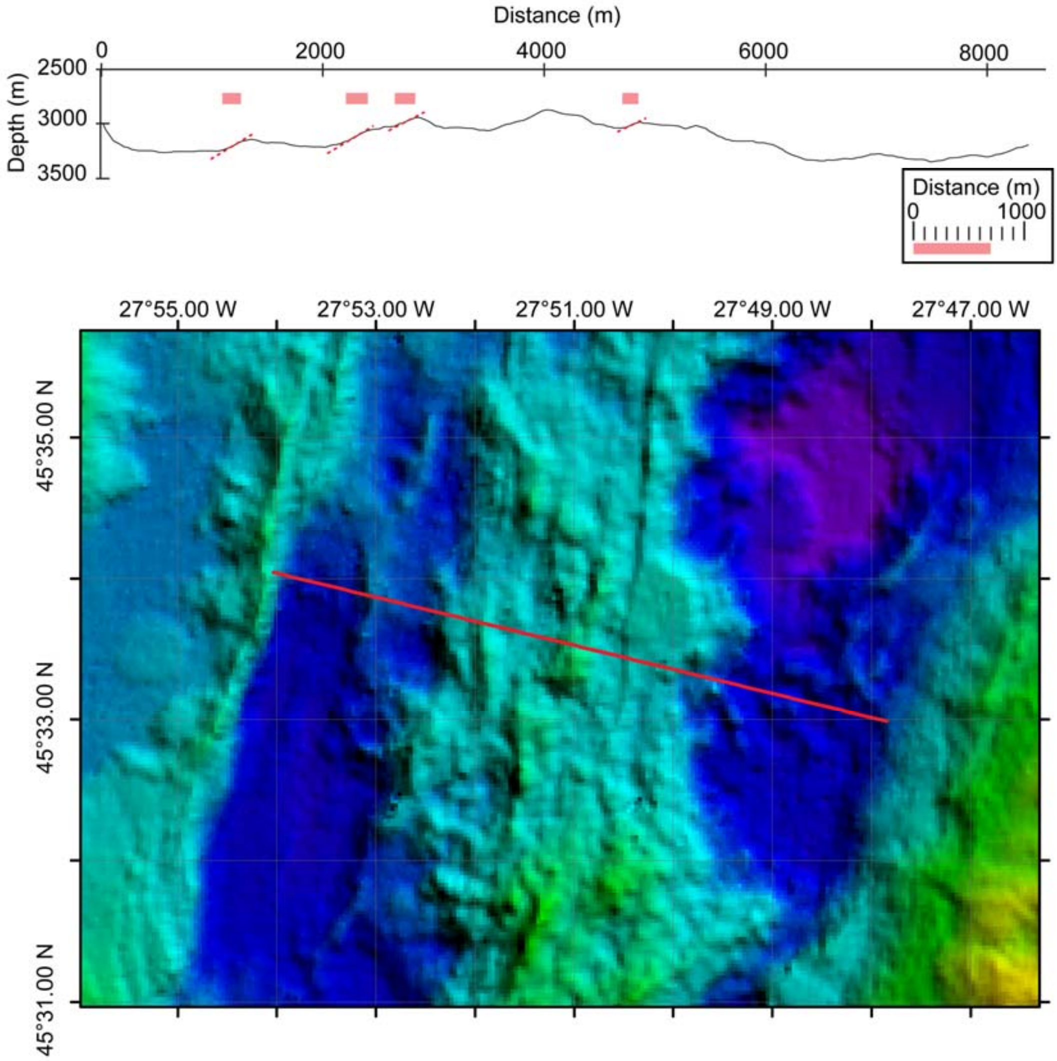

Figure 6.11: Profile across the more tectonically degraded northern end of the AVR. Four faults are shown by dashed red lines and are clear in the bathymetry. The horizontal component of their offset is shown by the pale red bars above each fault. When added together these faults represent a horizontal offset of ~ 700 m.

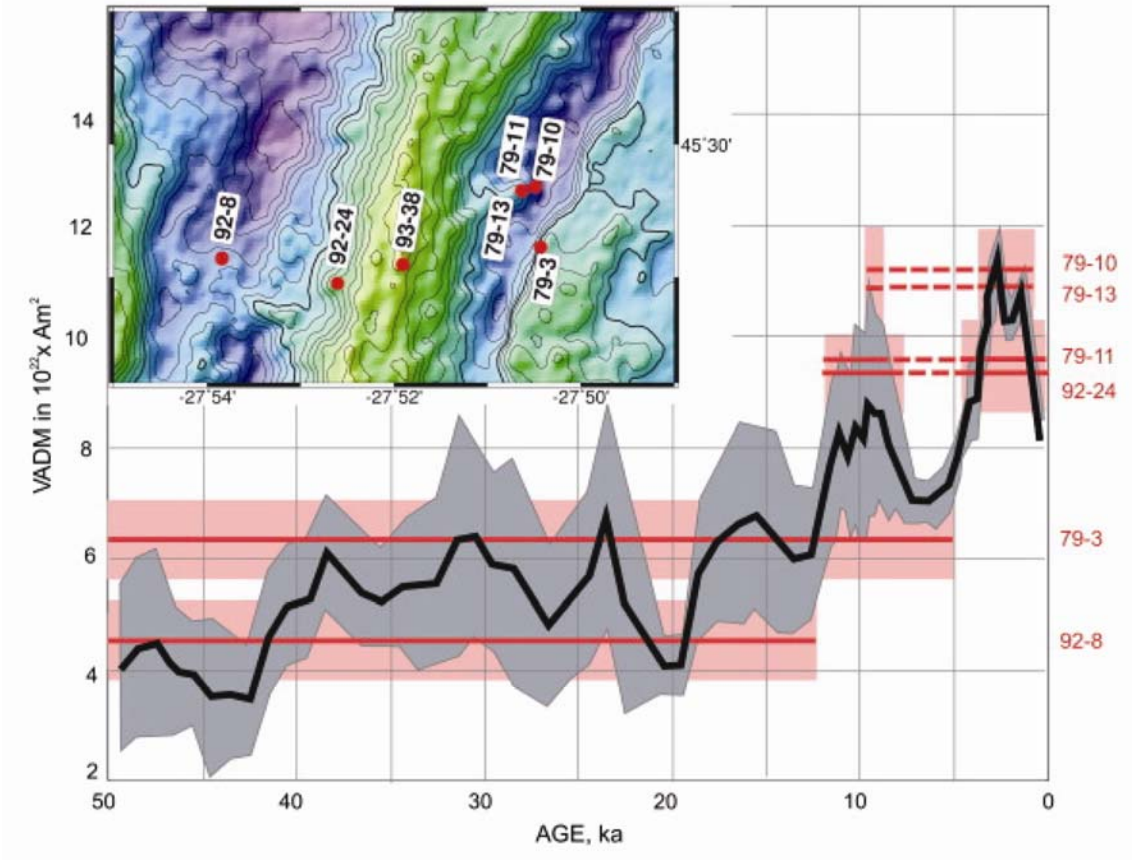

Figure 6.12: From Searle et al. (2010). Plot of magnetic palaeointensity expressed as Virtual Axial Dipole Moment (VADM) against time in thousands of years before present. Black line and grey shaded area: reconstructed variations in the geomagnetic dipole moment over the past 50 kyr from the GEOMAGIA50 database. Horizontal lines indicate measured palaeointensities from this study; red numerals give dive-sample number, with error band (2 s.d.) in pink. Age limits inferred from comparison with the reference curve are shown by solid red lines, with dashed lines indicating other possible age ranges. Inset: bathymetry of the central part of the AVR and adjacent valley floor showing sample locations. Sample 93-38 failed to give a sensible palaeointensity.

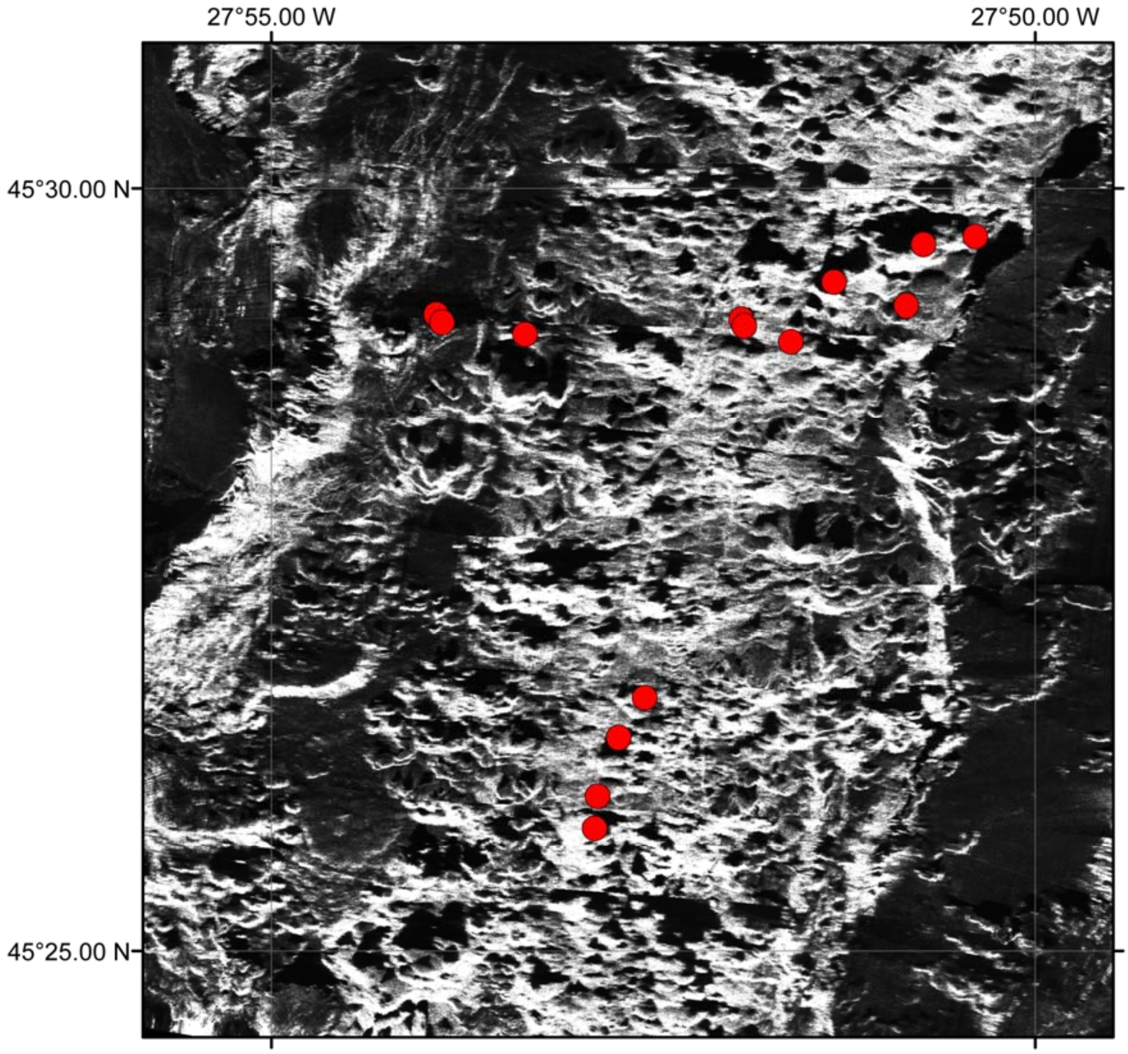

Figure 6.13: Uranium series sample locations on north looking TOBI sidescan sonar.

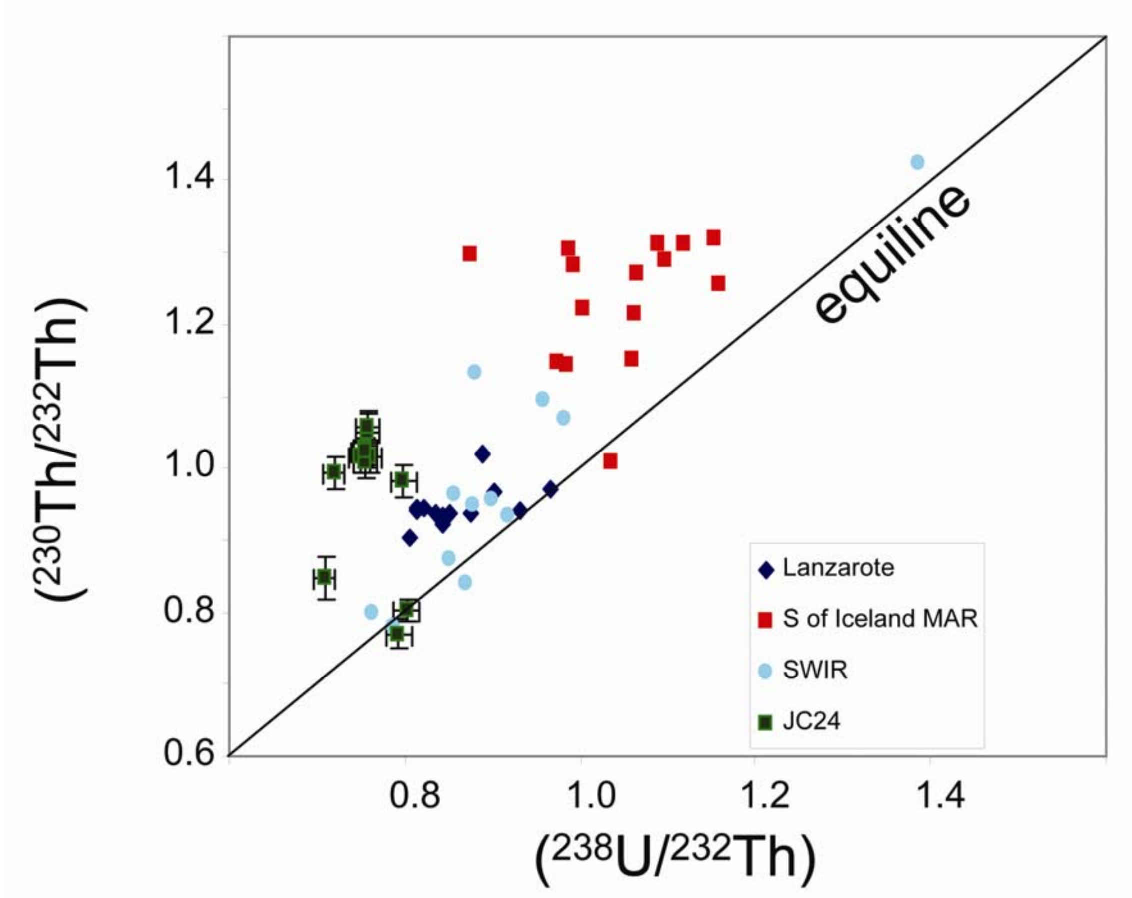

Figure 6.14: From Van Calstreren et al. (2012, in prep). (230Th/232Th) *vs* (238U/232Th) equiline diagram. JC24 data from 45˚N (samples JC24-79- 8, JC 24-79-14, JC24-79-22, JC24-80-16, JC24-80-17, JC24-80-22, JC24-80-23, JC24-92-6, JC24-92-7, JC24-92-21, JC24-93-3, JC24-93-16, JC24-93-31, JC24-93-38) is shown in green.

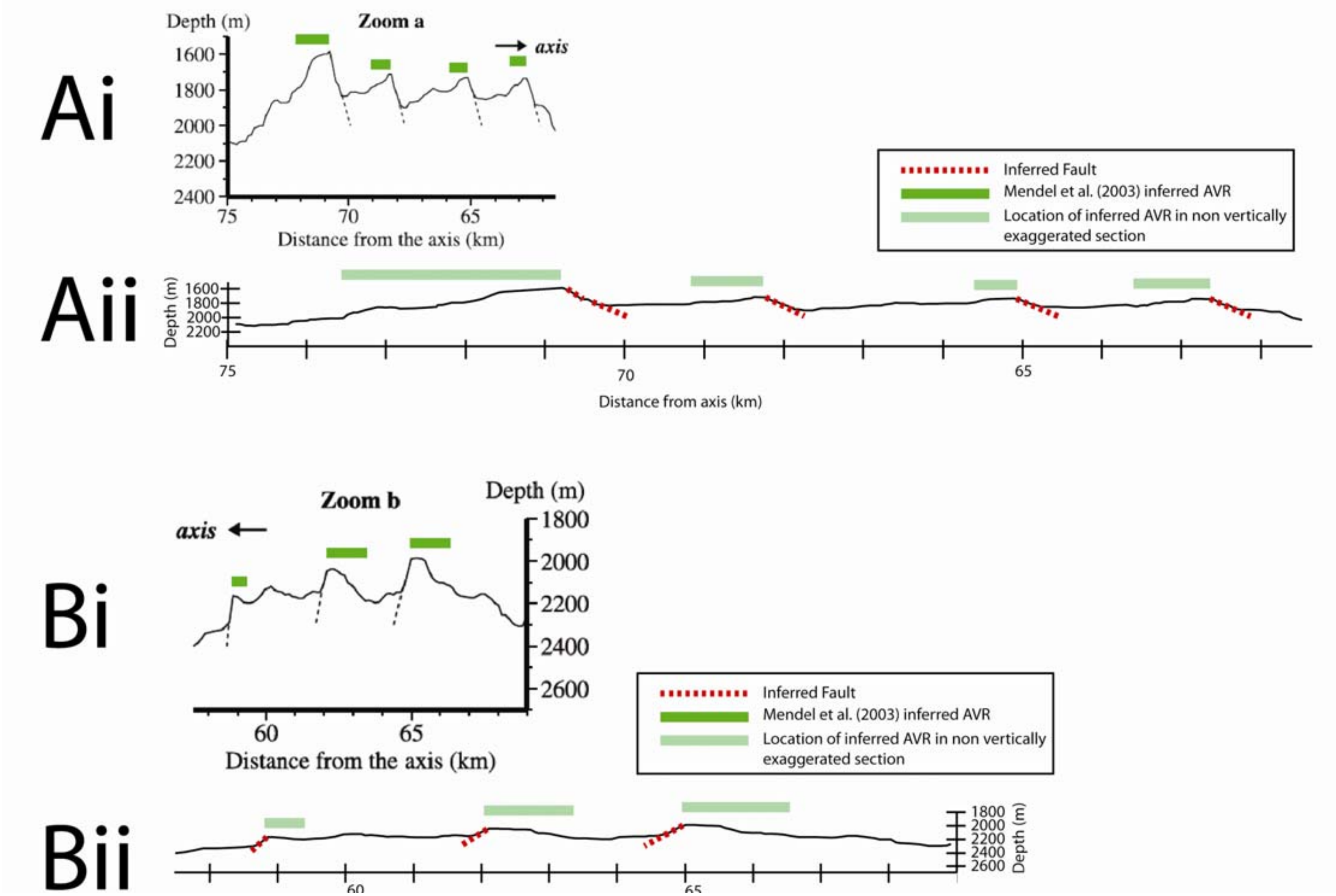

Figure 6.15: Redrawn cross sections from Mendel et al. (2003). Locations of the Mendel et al. (2003) inferred AVR flanks are shown in bright green, corresponding locations on the non-vertically exaggerated sections are shown in pale green. Faults are shown in both by dashed red lines. With no vertical exaggeration these cross sections actually look far more similar to the flat plains observed at 45˚N, with slopes rarely exceeding 5˚ (AVR flanks are typically 10 – 30˚).

7 Conclusions and further work

Chapter 7: Conclusions and further work

The conclusions of this thesis are presented as answers to the questions laid out in chapter 1. This is followed by the future work section in which I suggest ideas for further research based on the work done for this thesis.

7.1 Conclusions

7.1.1 What are the volcanic units at slow-spreading ridge segments? How are they distributed spatially at slow-spreading mid-ocean ridge segments containing an AVR?

Slow-spreading ridge segments are characterised by two distinct seafloor textures: hummocky seafloor and flat seafloor. Hummocky seafloor is composed of many, small (diameters between 23 m and 639 m, heights 5 – 146 m) volcanic hummocks. Hummocks themselves are probably monogenetic edifices fed from a central conduit or network of pillows which gives them their circular shape. Hummocks are predominantly constructed of pillow and elongate pillow lavas, and hummocky terrain is made of: 56% pillow lavas (pillows and elongate pillows), 20% pillow and lobate flows, 12% talus, 11% lobate flows and < 1% sheet flows. The talus component is produced as a result of common, gravitational collapse which affects approximately a third of hummocks, converting around 40 % of the lavas which build them to high porosity rubble. Flat-seafloor is composed of longer run-out, and higher effusion rate, sheet and lobate flows. Flat seafloor is composed of: 33% lobate and pillow flows, 20% sheet flows, 16% lobate flows, 16% sheet and lobate flows and 15% pillow and elongate pillow lavas.

From the evidence at 45˚N we can infer that hummocky seafloor is typically found on AVRs and within the axial valley floor. Small patches of hummocky terrain with similar spatial densities to that on the AVR are observed outside the axial valley, but look older and were probably produced at the axis. Flat seafloor is found mostly around the AVR on the axial valley floor. The largest flow is found to the north of the AVR, approaching the non-transform offset.

7.1.2 What form do volcanic eruptions at AVRs take? How large are they and how long do they last?

Eruptions on the AVR occur predominantly as fissure eruptions, which form mappable lineaments of volcanic hummocks on the AVR surface. Lineaments form both parallel to and oblique to the strike of the AVR. Those that are parallel probably correspond to the underlying fissure, whereas those that are orthagonal form down the steeper AVR flank gradients, suggesting that they are gravity driven. Lineaments are composed of 8 – 12 hummocks.

An average volcanic hummock has a volume of 292,000 m^3 (ranging from 1,400 m^3 to 4,091,000 m^3) and probably forms in periods of hours to months. Lineaments of 8 – 12 hummocks will typically have volumes between 2.3×10^6 m^3 and 3.5×10^6 m^3. Thus ~55,000 average volume hummocks or ~7,000 average volume eruptions are required to build the AVR. Using the maximum estimated effusion rates for the observed lava lithologies the AVR could be built in as little as 300 years of continuous eruption.

These eruption volumes are similar to the Gregg et al. (1996) estimates of 3.6×10^6 m^3 – 5.8×10^6 m^3 for the East Pacific Rise at 9˚46.77 N. They are slightly smaller than the typical volumes at intermediate spreading ridges, which were measured to be 7,000,000 m^3 – 48,000,000 m^3 (chapter 6).

Both the pillow lava flows and the sheet flows around the AVR have similar degrees of sediment cover, suggesting that they were erupted at approximately the same time. There is little variation in the ages of flows on the AVR surface suggesting that most of the lavas observed were erupted over a period of < 10,000 yr.

7.1.3 Are the styles of volcanism similar at faster spreading rates?

The ‘pillow mound’ forming eruptions at intermediate ridges are very similar to the hummock forming eruptions at slow-spreading ridges, with the pillow mounds typically formed of agglomerated hummocks aligned along a fissure.

The volumes of hummock forming eruptions (i.e. the combined volumes of all the hummocks along a fissure) at 45˚N are 5 – 50 % of those observed at the intermediate-spreading Juan de Fuca and Gorda Ridges, although may be larger if not all the hummocks lie on the strike of the fissure or if any non hummock-forming lavas are erupted.

7.1.4 How are eruptions related to each other? Is one section of the AVR more active than the rest? Do flat-topped seamounts begin as hummocks?

Typically 8 – 12 hummocky eruptions occur along a typical fissure eruption at 45°N. All the hummocks in a single fissure eruption are being fed by the same source and would be chemically very similar. Other hummocks which do not lie directly on the strike of the fissure may also be connected to the same eruption, if flow is able to travel laterally. This is hard to identify at 45˚N due to the high hummock density, which makes flows difficult to map, and the low sampling density, which is unlikely to sample more than one or two hummocks from the same flow. However, it is observed for the pillow mound eruptions on the Juan de Fuca and Gorda ridges.

It seems that at 45˚N along-axis melt transport appears restricted to a few kilometres, and does not extend along the whole segment, as the robust magmatism that must be feeding the tall, unfaulted southern end is clearly not reaching the tectonised north. The youngest eruptions are observed at the southern end of the AVR, suggesting this is where melt is currently being supplied.

I see no evidence for large volcanic hummocks approaching the typical 1:10 height:diameter ratio of flat-topped seamounts at either slow or intermediate ridges, and therefore suggest that these edifices are formed by a different process to the hummocks and do not grow from them. Relatively young-looking flat-topped seamounts are observed both on and off the axis, suggesting that they may be formed in either location. Murton et al. (2012) suggest that they may be linked compositionally to sheet flows observed around their bases.

7.1.5 How many melts are combined in each magma chamber? Are isotopic ratios the same as those measured by White and Schilling (1978)?

The geochemical analyses presented in chapter 5 are not reliable enough to distinguish individual batches of melt or indentify the effects of rock wall assimilation. However, the Sr istopic ratios measured for the plagioclase separate crystals are mostly lower than those measured by White and Schilling (1978). This suggests that the higher Sr ratio lavas they collected are not the only ones being erupted at 45˚N.

Within the same sample the plagioclase crystals likely all crystallised from the same batch of melt, rather than being inherited from 2 or more mixing batches. For these few samples this points to a simple model of AVR magma chambers, in which they are formed from a single melt and are not recharged by the addition of further, compositionally different melts once crystallisation has begun. The low Sr ratios observed for whole plagioclases suggest that they have not experienced substantial hydrothermal or seawater alteration.

7.1.6 What is the detailed volcanological structure of slow-spread oceanic crust?

The upper oceanic crust is constructed mostly of hummocky lava flows, which constitute 85 - 95 % of the upper crustal section. The upper ~ 10 % of the extrusive volcanic section is build of higher effusion rate flat lava flows which fill in around hummocky terrain. Using these percentages I suggest the oceanic crust is composed of approximately: 52 % pillow and elongate pillow lavas, 21 % pillow and lobate lava flows, 11 % lobate lava flows, 11 % talus, 3 % sheet flows and 2% lobate and sheet flows.

The addition of high porosity talus as a result of gravitational collapse could be one of the main mechanisms for reducing the averaged seismic velocity of seismic layer 2A at slow-spreading ridges, and is capable of reducing seismic velocity in the layer by more than 0.5 km/s.

The hummocky AVR-forming eruptions have much higher relief than the surrounding seafloor and the seafloor observed outside the axial valley floor. As hummocky volcanism dominates in the axial valley inner floor, such hummocks probably underlie this flatter terrain and are buried by a combination of flat-lying sheet and lobate lava flows and sediment. These higher effusion rate flows are observed around the AVR and must be occurring regularly and coeval with the hummock-forming lava flows on the AVR.

7.1.7 Does the model of AVR development as proposed by Parson et al. (1993) match with observations at 45˚N?

The observations of the axial volcanic ridge at 45˚N do not fit entirely with either the Parson et al. (1993) episodic or the Murton et al. (2012) steady-state model. Instead I suggest that AVRs are the surface expression of robust magmatic crustal extension. Therefore, the volumes of magma chambers and the amount of time that passes between magma batches accumulating beneath the ridge will dictate the surface appearance of an AVR. Where extension is predominantly magmatic it will result in the production of a robust AVR, and where amagmatic extension dominates it will initiate normal faults and degrade any pre-existing AVR. The length of this period of tectonic degradation (and hence the height to which the AVR is reduced) will control whether or not an AVR is present. An AVR need not be totally dismembered before magmatic extension begins again, and this is probably the case as most slow-spreading segments display some sort of AVR.

7.2 Suggestions for further work

There is a lot of information to be gleaned from looking at the major and trace element geochemistry of the samples collected on cruise JC24 and this should be compared with the physical volcanology results discussed in this thesis. This geochemical work is being done by NOC, Southampton. Some of their findings are presented in Murton et al. (2012, in prep), however the results of their work looking at how lava flows are linked and investigating compositional zoning is not yet available and therefore is not discussed here.

7.2.1 Geochemistry to determine feeder systems and hummock connectivity

In order to properly understand how many hummocks are produced by a single volcanic eruption, and therefore how connected the crustal plumbing system is, an extremely detailed sampling and geochemical survey is necessary, ideally associated with high-resolution bathymetry of the area.

Bulk and isotopic geochemistry can be used to identify lavas which belong to specific flows (e.g. Davis et al. (1987); Davis et al. (2008); Taylor et al. (1995)). The southern high-resolution area at 45˚N contains 75 hummocks, of which 23 were sampled on JC24. A further two Isis dive tracks (figure 7.1), of comparable length (< 5.5 km) and sampling density (< 30 samples) to the other dives on hummocky terrain would allow almost every hummock in the area to be sampled. Additional samples could be taken between hummocks where there was available payload available to do so. Such samples would allow us to identify where these lavas between the hummocks came from; whether they are older, compositionally different flows, or non-hummock-building pillowed flows. This sampling program would require less than 4 days of ship time and would provide the first dense geochemical sampling of one or more Mid-

Atlantic Ridge lava flows. Such a survey, combined with high-resolution bathymetric imagery which has already been collected, would allow an individual lava flow to be accurately mapped for the first time. This would make it possible to accurately estimate eruption volumes as well as answer the question of how far off a fissure a volcanic hummock can be formed (possible fissure traces are suggested in figure 7.1). Other geochemical analyses could be used to determine parameters such as degree of fractionation (MgO, Ni, Cr), partial melting (Zr, Nb) and homogeneity of the mantle source (La/Ce, Ba/Th. Zr/Nb, K/Ba, $^{87}Sr/^{86}Sr$). All the above could also be done in the northern high-resolution study area.

Furthermore, more widespread analysis of $^{87}Sr/^{86}Sr$ ratios from whole crystals from all JC24 samples would help to constrain the locations in which E-MORB is being erupted. This could help to answer the question of whether these enriched lavas are being erupted from a different source or are associated with different morphology (i.e. flat seafloor vs. hummocky seafloor), as suggested by Murton et al. (2012, under review). It would also be useful to repeat the isotope and trace element analyses of zoned plagioclase, as explained in chapter 5, without the contamination problem and over a wider range of samples, to attempt to constrain magma chamber processes such as the presence or absence of melt mixing, and the importance of melt wall assimilation.

7.2.2 Flat-topped seamounts

The mode of construction, the location of construction and the timing of formation of flat-topped seamounts is still very poorly understood. From 45˚N we have observed flat-topped seamounts are found both on and off the AVR and inside and outside of the axial valley floor. However, those outside the axial valley floor are not notably more faulted or tectonically degraded as might be expected if they formed at the axis. A focussed sampling and U/Th dating program could help constrain where these structures are being formed, both in relation to each other, and in relation to the other lava morphologies observed.

Additionally phase bathymetry could be extracted from the TOBI data to produce ~ 20 m resolution bathymetry, higher than the EM120 ship-based bathymetry (e.g. (Bralee and Searle, 2001)). This bathymetry could be used to measure the heights of many more hummocks than the 153 imaged by the high-resolution surveys at 45˚N. This would give a much more representative sample of the AVR population.

Furthermore Murton et al. (2012, under review) suggest that the flat-topped seamounts are geochemically similar to the sheet flows and lobate flows around the AVR, but distinct from the hummocks, suggesting they have very different melt sources. Only three seamounts were dived on during cruise JC24, and only a few of the areas of flat seafloor. Further sampling of seamounts and surrounding lava flows would make it possible to constrain this relationship, both geochemically and from their contact relationships. Additionally, high-resolution bathymetric and seafloor observational studies of flat seafloor areas which do not appear to be associated with flat-topped seamounts could help to constrain where they are being fed from by looking at slopes, evidence for dykes, fissuring and flow direction indicators.

7.2.3 Dating of a crustal section

One of the main issues with the 45˚N study of the age of the AVR is that sampling and sediment cover only date the surface of the AVR. This is a fundamental problem as it is difficult to draw conclusions about the age of the interior or base of the AVR without any samples to do so. One way to combat this problem would be to drill a section of fresh volcanic crust on axis, however this would be an extremely expensive solution and recovery of fresh basalt can be low e.g. Marlow et al. (1992) and Batiza et al. (1995).

The axial valley walls provide hundreds of metres of cross section through the upper oceanic crustal section. Through dedicated dives up the axial valley walls and regular sampling on 5 – 10 m intervals, it would be possible to investigate the thickness of flows and contribution of each lithology to the upper oceanic crust in a 200 – 500 m section. Due to the stepped nature of faulting such a large section may not be exposed, however continuous scarps of > 100 m are observed, which would be enough to expose a number of eruptions and give an indication of the time scales on which eruptions occur, and the lengths of periods of quiescence between them. Dating of these samples, through U/Th (or possibly other dating methods e.g $^{40}Ar/^{39}Ar$ (Faure, 1986) on the youngest samples) could help to constrain the periodicity of eruption in the same locations. Such a record would make it possible to distinguish easily between the steady state (where all lavas in a section should be roughly the same age) and the cyclic (where deeper lavas should be older) models and furthermore between steady state and episodic melt supply. Additionally if combined with geochemical analyses, samples could also be used to produce a record of how magma composition, and therefore melt fraction, fractional crystallisation, residence time etc, has changed through time. Further sampling along axis could be used to study variations along axis.

7.3 References

Batiza, R., Allan, J.F., Bach, W., Bostrom, J.G., Brophy, J.G., Fryer, G.J., Goldstein, S.J., Harpp, K., Haymon, R.M., Hekinian, R., Johnston, J.E., Niu, Y.L., and Polyak, B.G., 1995, 1. Petrology, Geochemistry, and Petrogenesis of leg 142 Basalts - Synthesis of Results Proceedings of the Ocean Drilling Programme, v. 142.

Bralee, A.V., and Searle, R.C., 2001, Fault Characteristics and Strain Accommodation at the Ultra Slow Spreading South West Indian Ridge (SWIR). AGU, Fall Meeting: San Francisco, p. #T11A-0850.

Davis, A.S., and Clague, D.A., 1987, Geochemistry, mineralogy, and petrogenesis of basalt from the Gorda Ridge Journal of Geophysical Research-Solid Earth and Planets, v. 92, p. 10467-10483.

Davis, A.S., Clague, D.A., Cousens, B.L., Keaten, R., and Paduan, J.B., 2008, Geochemistry of basalt from the North Gorda segment of the Gorda Ridge: Evolution toward ultraslow spreading ridge lavas due to decreasing magma supply: Geochemistry Geophysics Geosystems, v. 9.

Faure, G., 1986, Principles of Isotope Geology: New York, John Wiley and Sons, 589 p.

Gregg, T.K.P., Fornari, D.J., Perfit, M.R., Haymon, R.M., and Fink, J.H., 1996, Rapid emplacement of a mid-ocean ridge lava flow on the East Pacific Rise at 9 degrees 46'-51'N: Earth and Planetary Science Letters, v. 144, p. E1-E7.

Marlow, M.S., Johnson, L.E., Pearce, J.A., Fryer, P.B., Pickthorn, L.B.G., and Murton, B.J., 1992, Upper Cenozoic Volcanic Rocks in the Mariana Forearc Recovered From Drilling at Ocean Drilling Program Site 781: Implications for Forearc Magmatism: J. Geophys. Res., v. 97, p. 15085-15097.

Murton, B.J., Schroth, N., Le Bas, T.P., Van Calsteren, P., Searle, R.C., and Yeo, I., 2012, Formation of oceanic crust at slow spreading ridges by continuous Axial Volcanic Ridge processes: In prep, p. in prep.

Parson, L.M., Murton, B.J., Searle, R.C., Booth, D., Evans, J., Field, P., Keeton, J., Laughton, A., McAllister, E., Millard, N., Redbourne, L., Rouse, I., Shor, A., Smith, D., Spencer, S., Summerhayes, C., and Walker, C., 1993, En-echelon axial volcanic ridges at the Reykjanes Ridge- A life-cycle of volcanism and tectonics Earth and Planetary Science Letters, v. 117, p. 73-87.

Taylor, R.N., Murton, B., and Thirwall, M., 1995, Petrographic and geochemical variation along the Reykjanes Ridge, 57° N–59° N: Journal of the Geological Society, v. 152, p. 1031-1037.

White, W.M., and Schilling, J.-G., 1978, The nature and origin of geochemical variation in Mid-Atlantic Ridge basalts from the Central North Atlantic: Geochimica et Cosmochimica Acta, v. 42, p. 1501-1516.

7.4 Figures

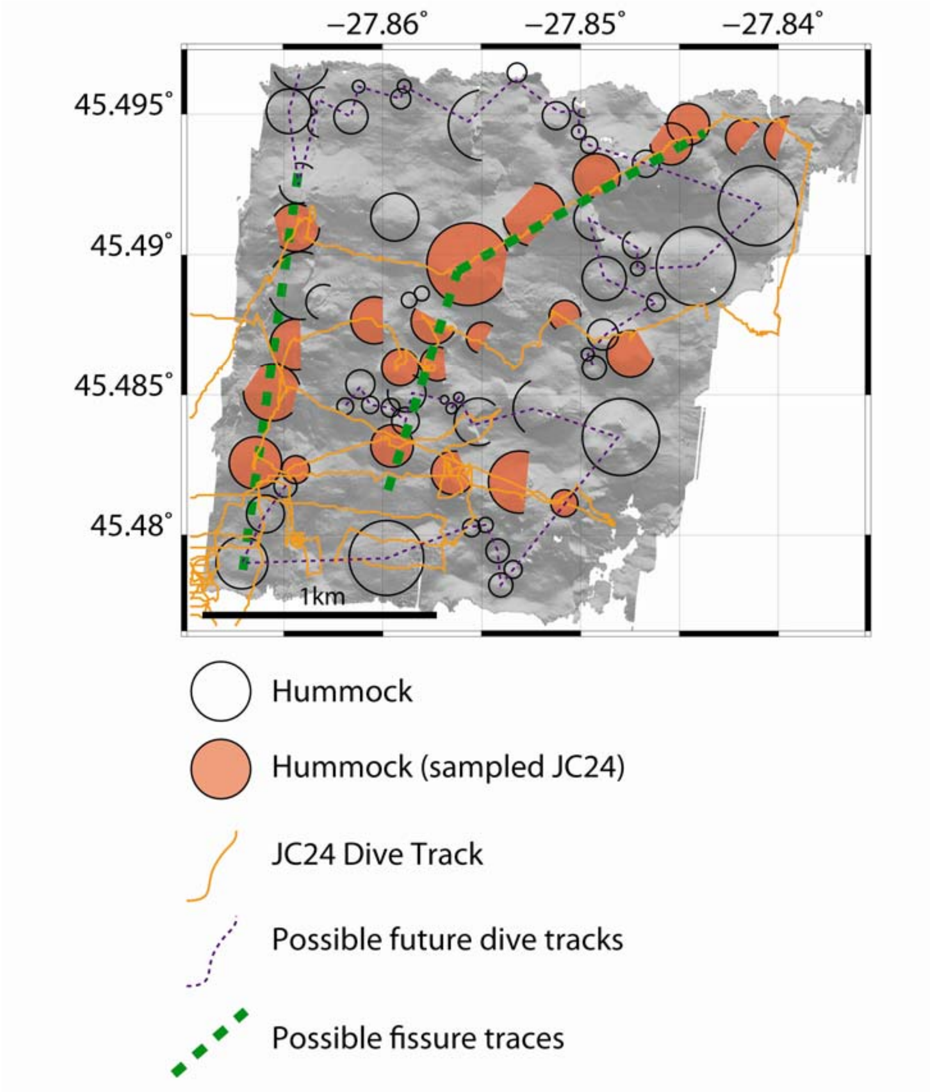

Figure 7.1: Hummocks in the JC24 southern high resolution study area and proposed dive tracks to sample them. Possible fissure traces are shown by green dashed lines.